

DESIGN OF TUNABLE COUPLERS AND INVESTIGATION OF MATERIALS LOSS
MECHANISMS IN SUPERCONDUCTING 2D AND 3D SYSTEMS

by

Nicholas R. Materise

© Copyright by Nicholas R. Materise, 2023

All Rights Reserved

A thesis submitted to the Faculty and the Board of Trustees of the Colorado School of Mines in partial fulfillment of the requirements for the degree of Doctor of Philosophy (Applied Physics).

Golden, Colorado

Date _____

Signed: _____

Nicholas R. Materise

Signed: _____

Dr. Eliot Kapit
Thesis Advisor

Golden, Colorado

Date _____

Signed: _____

Dr. Fred Sarazin
Professor and Department Head
Department of Physics

ABSTRACT

Superconducting qubits are among the leading physical qubit candidates, with coherence times exceeding 100 microseconds and gate times on the order of tens of nanoseconds. At the hardware level, tunable coupling between qubits has enabled fast, high fidelity two qubit gates, the limiting factor for quantum algorithm gate depth. Tunable couplers have played a significant role in scaling these systems and were instrumental in the first quantum advantage demonstration in certifiable random number generation. Parametric operations, such as beam splitter and two-mode squeezing, are activated by oscillating fields applied to a tunable coupler that are resonant with these red and blue sidebands, respectively. Theoretical modeling tools exist for planar geometries and 3D geometries that use capacitive coupling, but ones for galvanic coupling in 3D have not been realized.

This thesis will discuss the design of two novel tunable couplers, one in the planar domain and another in 3D that uses galvanic coupling. In the planar design, a III-V semiconductor heterostructure acts as a tunable capacitor when biased with a negative gate voltage, parting the sea of electrons to modify the geometry of the capacitor. The 3D tunable coupler uses a dc superconducting quantum interference device shunting a 3D cavity and driven at the sum or difference frequencies of cavities to induce beam splitter or two-mode squeezing operations. I will discuss this 3D galvanic coupler and the analysis method developed to estimate beam splitter, two-mode squeezing, and single-mode squeezing rates.

The novel materials comprising the 2DEG coupler spurred experiments to estimate its dielectric losses. These experiments led to the design of cavity-based loss metrology systems, with applications in a variety of materials of interest to the superconducting qubit field, namely bulk dielectric loss in indium phosphide, silicon, and sapphire substrates. I will discuss these cavity loss experiments and 2D resonator loss measurements focused on understanding loss mechanisms in 2D qubits. The materials in the 2D studies include niobium and its oxides and hydrides, tantalum, titanium nitride, and silicon. These studies highlight the importance of designing targeted A/B experiments and collecting sufficient loss statistics with tens of resonators per device variation.

TABLE OF CONTENTS

ABSTRACT	iii
LIST OF SYMBOLS	xvi
LIST OF ABBREVIATIONS	xviii
ACKNOWLEDGMENTS	xx
DEDICATION	xxii
CHAPTER 1 INTRODUCTION	1
1.1 Digital and Analog Quantum Computing	3
1.1.1 Digital Quantum Computing	3
1.1.2 Continuous Variable Quantum Computing	5
1.2 Superconducting Circuits and Circuit QED	6
1.2.1 Classical Circuit Theory and Canonical Quantization	7
1.2.2 Josephson Junctions	9
1.2.3 Circuit QED, Cooper Pair Boxes, and Transmons	11
1.2.4 Circuit QED	11
1.2.5 Cooper Pair Box and Transmons	12
1.3 Circuit QED with 3D Cavities	14
1.3.1 Black-Box Quantization Methods	14
1.3.2 Summary of Black-Box Quantization with the Lossy Foster Decomposition	15
1.3.3 Numerical Idiosyncrasies with Black-Box Quantization	18
1.3.4 Energy Participation Ratio Quantization	20
1.3.5 3D Transmons	21
1.4 Tunable Couplers	22
1.4.1 2D Systems	24
1.4.2 Operating Principles and Coupler Taxonomy	24
1.4.3 Parametric Modulation	26

1.4.4	3D Systems	28
1.5	Superconducting Microwave Resonators	31
1.5.1	Microwave Circuit Theory	31
1.5.2	Microwave Measurement Techniques	35
1.5.3	Loss Mechanisms in Superconducting Resonators	39
1.5.4	Losses from Two Level Systems	40
1.5.5	Losses From the Conductivity of Superconductors	43
CHAPTER 2	TUNABLE CAPACITOR FOR SUPERCONDUCTING QUBITS USING AN INAS/INGAAS HETEROSTRUCTURE	50
2.1	Abstract	50
2.2	Introduction	50
2.3	Methods and Modeling	52
2.3.1	Conceptual Design	52
2.3.2	Classical Modeling	53
2.3.3	Semiconductor 2DEG Calculations	53
2.3.4	Electric Currents Admittance Matrix Calculations	57
2.4	Results	59
2.4.1	Coupler Loss Estimates	60
2.5	Integration with Circuit QED	60
2.5.1	Two Qubit Coupler	60
2.5.2	Energy Participation Ratios and Quantization	61
2.5.3	Extraction of the Exchange Interaction	64
2.5.4	Estimation of Coupler Coherence Limit	65
2.6	Discussion	66
2.7	Conclusion	66
2.8	Acknowledgments	67
2.9	Data Availability	67

CHAPTER 3 FIELD OVERLAP INTEGRAL APPROACH TO ESTIMATE PARAMETRIC RATES BETWEEN SUPERCONDUCTING 3D CAVITIES	68
3.1 Methods	68
3.1.1 Field Overlap Integral Formalism	69
3.1.2 Flux Modulation and Parametric Rates	71
3.2 Discussion	73
3.3 Conclusion	74
CHAPTER 4 GALVANIC COUPLING ELEMENT FOR SUPERCONDUCTING 3D CAVITIES	75
4.1 Two Post Coupler Design and Operation	76
4.1.1 Two Coupler Geometric Studies	78
4.2 Optimized Design Results	79
4.3 Conclusion	80
CHAPTER 5 COPLANAR WAVEGUIDE MICROWAVE LOSS EXPERIMENTS	81
5.1 Loss Budgets	81
5.2 A/B Testing for Comparative Loss Extraction Experiments	84
5.2.1 Niobium Hydride Experiments	84
5.2.2 Capping Studies	86
5.3 Conclusion	89
CHAPTER 6 GRAIN SIZE IN LOW LOSS SUPERCONDUCTING TA THIN FILMS ON C-AXIS SAPPHIRE	90
6.1 Abstract	90
6.2 Introduction	90
6.3 Ta Growth and Characterization	91
6.4 Device Design and Fabrication	95
6.5 Cryogenic Microwave Measurement	95
6.6 Literature Comparison	98
6.7 Discussion	99
6.8 Conclusion	100

6.9	Supplementary Material	100
6.10	Acknowledgements	100
6.11	Author Declarations	100
6.11.1	Conflicts of Interest	100
6.11.2	Commercial Products Disclaimer	100
6.11.3	Author Contributions	101
6.12	Data Availability	101
CHAPTER 7 WAFER-SCALE MICROWAVE DIELECTRIC LOSS EXTRACTION USING A SPLIT-POST SUPERCONDUCTING CAVITY		102
7.1	Methods	102
7.1.1	Cavity Design	104
7.1.2	External Coupling Simulation	105
7.1.3	Wet Chemical Etching of Cavity	107
7.1.4	Cavity Assembly, Mounting, and Wafer Preparation	108
7.2	Results	109
7.2.1	Unetched Cavity Measurements	109
7.3	Discussion and Conclusions	112
CHAPTER 8 CONCLUSIONS AND OUTLOOK		114
8.1	Conclusion	114
8.2	Outlook	115
REFERENCES		118
APPENDIX A TUNABLE CAPACITOR APPENDICES		139
A.1	III-V Ternary Alloy Interpolation Formulas	139
A.2	Charge-Charge Interaction Matrix Element Derivation	140
APPENDIX B BLACK BOX HAMILTONIAN AND CORRESPONDENCE WITH EPR		143
APPENDIX C ANSYS HFSS EIGENVALUE PROBLEM		146
C.1	Maxwell's Equations and Helmholtz Equation	146
C.2	Galerkin Testing	147

APPENDIX D SUPPLEMENTAL MATERIAL OF <i>GRAIN SIZE IN LOW SUPERCONDUCTING TA THIN FILMS ON C-AXIS SAPPHIRE</i>	150
D.1 Ta Grain Size for $T = 600^\circ\text{C}$ Deposition	150
D.2 Wide Scans	150
D.3 Extracted Resonator Parameters	151
D.4 Microwave Setup	154
D.5 Resistance Measurements	154
APPENDIX E PERMISSIONS FOR COPYRIGHTED MATERIAL	157
E.1 Copyright Permissions for Chapter 1	157
E.2 Copyright Permissions for Chapter 2	157
E.3 Copyright Permissions for Chapter 5	157
E.4 Copyright Permissions for Chapter 6 and Appendix D	157

LIST OF FIGURES

Figure 1.1 (a) Bloch sphere representing an arbitrary single qubit state. (b) Energy levels of a superconducting transmon qubit [1].	4
Figure 1.2 Summary of theoretical milestones in superconductivity and superconducting circuits.	7
Figure 1.3 Cross-section of an overlap SIS Josephson junction.	9
Figure 1.4 Summary of experimental milestones in superconductivity and superconducting circuits.	10
Figure 1.5 Dispersive readout. Left: Magnitude of cavity transmission. Right: Phase of cavity transmission. Ground state (blue), excited state (red), bare cavity (gray) with qubit-cavity detuning < 0 . Adapted from [2], see Appendix E.	11
Figure 1.6 Cooper pair box energies as a function of offset charge. (a) Charge qubit regime, (b) typical transmon regime. Energies scaled to $\sqrt{8E_J E_C}$ and shifted from their minima such that the ground state energy at zero charge offset is zero. Adapted from [1], see permissions in Appendix E.	13
Figure 1.7 Lossy Foster series RLC decomposition of a single port network shunted by one Josephson junction with gauge invariant phase difference φ , reproduced with permission from [3].	14
Figure 1.8 Black-box resonance frequencies from (a) zero crossings of the imaginary part of the admittance and (b) lumped port defined by a rectangle representing a Josephson junction.	16
Figure 1.9 Consequences of passivity violations in traditional black-box quantization. (a) The real part of the admittance from a representative superconducting 3D structure showing negative resistance values in gray. Raw data are shifted in blue and smoothed in red to correct for negative resistances. (b) The imaginary part of the admittance shows the resonance frequency locations as the zero crossings of $\text{Im}\{Y(\omega)\}$	18
Figure 1.10 Losses extracted from the admittance data in Figure 1.9 without a correction to the admittance in (a) and with a correction in (b). The black dashed line indicates the loss tangent of sapphire, $\sim 2 \times 10^{-8}$ from [4], as a reference for the scale of the losses for each mode in this device.	19
Figure 1.11 3D transmon in a rectangular cavity [5, 6] including the location of the nodes and antinodes of the lowest frequency cavity modes TE_{101} and TE_{102} in (a) and an exploded view of the assembly to show the two halves of the cavity separated along the E-plane, where currents flow parallel to seam, minimizing seam losses.	22
Figure 1.12 Comparison of tunable coupler two qubit gate fidelities as a function of the number of expected operations in a coherence time (coherence time / gate time). Labels correspond to the following references: Chen 2014 [7], Lu 2017 [8], Gao 2018 [9], Yan 2018 [10], Weiss 2022 [11], Chapman 2023 [12], Jin 2023 [13], Chen 2023 [14], Kubo 2023 [15], Lu 2023 [16].	23
Figure 1.13 2D tunable coupler types.	25

Figure 1.14 State of the art 3D, parametrically activated microwave beam splitters, reproduced with permission from (a) two-tone, four-wave mixing, transmon controlled beam splitter [9], (b) differentially driven SQUID coupler [16], and (c) a single tone, three-wave mixing SNAIL coupler [12].	30
Figure 1.15 Transmission line circuit models. (a) Distributed element circuit model with voltages and currents and (b) the equivalent transmission line circuit shorthand.	31
Figure 1.16 Equivalent resonator coupling networks. (a) Hanger mode, (b) transmission, and (c) single-port reflection mode. Based on and reproduced with permission from [17].	35
Figure 1.17 Simulated resonator responses. (a) Linear point distribution, (b) three segmented point distribution, (c) homophasal point distribution. Resonator parameters are $Q_i = 10^6$, $Q_c = 5 \times 10^5$, $f_c = 5 \text{ GHz}$, $\phi = 0$.	37
Figure 1.18 Circulators and isolators in microwave measurements. (a) A reflection mode measurement taken by measuring S_{21} with a circulator. (b) Three port circulator, (c) isolator and an equivalent circulator with its third port terminated by a 50Ω load (black filled square on port 3).	38
Figure 1.19 DCM fit using the <code>scresonators</code> software package [18] of an Al CPW patterned on InP by W. M. Strickland at New York University.	39
Figure 1.20 Double well potential representing a single TLS. Tunneling rate Δ_0 and asymmetry Δ shown, with the energy splitting between the ground state and first excited state ε . Left and right well-localized eigenstates denoted $ L(R)\rangle$ and energy eigenstates labeled $ \psi_{\pm}\rangle$. Based on and reproduced with permission from [19].	40
Figure 1.21 Coupling between microwave photons and TLS and TLS and phonons. On the far left, a microwave tone is incident on a tapered feedline with frequency ω_0 resonant the resonator on the top right (ω). The inset shows a distribution of TLS coupled to the phonon bath by the interaction Hamiltonian $H_{\text{TLS-PH}}$, indicated by the color gradient arrow. Another bidirectional coupling is shown with the arrows between the TLS and resonator ω_0 with interaction Hamiltonian $H_{\text{TLS-EM}}$. In the small image, we include a scanning electron microscope image of a substrate surface as a representation for the substrate-air or metal-substrate interface hosting TLS.	42
Figure 1.22 Illustration of the Meissner effect and the exponential decay of magnetic fields \mathbf{B} electric supercurrent densities \mathbf{J}_s from the surface of the superconductor as first described by the London equations. This figure is based on a lecture given by de Sousa [20].	46
Figure 1.23 Superconducting gap, normalized to the zero temperature gap Δ_0 as a function of temperature, using the interpolation formula in (1.103).	48
Figure 1.24 Mattis Bardeen fits of temperature sweeps of an Al CPW resonator deposited on InP by W. M. Strickland at New York University. (a) Fractional frequency shift and (b) fractional quality factor shift vs. temperature. (c) Fractional frequency shift vs. $\delta X_s/X_s$ and (d) fractional quality factor vs. $\delta R_s/X_s$.	49
Figure 2.1 Schematic of two transmon qubits and the 2DEG coupler. Blue regions (color online) correspond to low electron concentration or effective dielectrics and red regions correspond to high electron concentration or effective conductors. We use the labeling of the voltage nodes V_i throughout the text, where nodes 1 and 2 correspond to source and drain terminals, and node 3 refers to the gate terminal.	52

Figure 2.2 Schematic of the 2DEG coupler as modeled in COMSOL Multiphysics based on [21]. An aluminum contact deposited on Al_xO_y defines the gate terminal. We abbreviate the fixed composition ternary III-V alloys $\text{In}_{0.81}\text{Ga}_{0.19}\text{As}$ and $\text{In}_{0.81}\text{Al}_{0.19}\text{As}$, as InGaAs and InAlAs, respectively. Not shown or modeled is the superlattice graded buffer layer between InP and InAlAs [22–24].	54
Figure 2.3 Electron concentrations [cm^{-3}] on a base-10 logarithmic scale with source-drain bias $V_{sd} = 0$ V for the fully conducting $V_g = 0$ V, intermediate $V_g = -0.5, -1, -2, -4$ V, and fully depleted $V_g = -5$ V operating points. The horizontal axis is a 300 nm span centered on the gate electrode and the vertical axis starts at the contact–2DEG interface at ~ 117 nm, the 2DEG–InAlAs interface is 18 nm below that, and the InAlAs–InP interface is located at 0 nm. We do not solve for n in the regions where we applied the Electric Charge Conservation equations, i.e. in the Al_xO_y regions not shown, yet the electric fields respect the boundary conditions set by those regions.	56
Figure 2.4 (a) Maxwell capacitance and (b) conductance matrices as computed with the Harmonic Perturbation study of the COMSOL Semiconductor Interface as a function of the gate voltage V_g	59
Figure 2.5 False color geometry of two transmon qubits with the capacitive coupler in between used in the HFSS simulations. Lumped impedances defined in the gold regions of the insets, represent the linear response of the Josephson junctions and capacitive coupling element in the HFSS model.	62
Figure 2.6 Electric field magnitude (dB scale to enhance color contrast) for the first two eigenmode solutions computed with HFSS. (a) 6.0228 GHz and (b) 8.6135 GHz qubits in the fully depleted limit of the coupler.	63
Figure 2.7 Coupling matrix elements in (a) the simplified two node model, (b) the three node parasitic capacitance model, (c) direct comparison of the 1-2 matrix element representing the charge-charge exchange rate between qubits 1 and 2 with the parasitic (para) and simplified (simp) capacitance matrices.	65
Figure 4.1 Two post coupler design. Left: two cavities ω_a, ω_b are coupled to a central cavity ω_c with a SQUID connecting its posts. The coupler itself is encircled with a purple dashed box. Right: common and differential current modes of the lowest two modes of the split post cavity with a SQUID connecting the posts. No current flows through the SQUID ($I_{JJ} = 0$) in the common mode, yet nonzero current flows through the SQUID in the differential mode.	77
Figure 4.2 Geometric studies of tuning range and maximum seam admittance. (a) Coupler pad width sweep and (b) coupler post diameter sweep. Tuning range is calculated as the difference in frequency of the differential mode at $L_J = 1$ nH and $L_J = 10$ nH where the frequency change is linear in L_J . Encircled points indicate the “optimal” design points in Section 4.2 and post diameter, pad width labels indicate the fixed values used in each sweep.	79
Figure 4.3 Optimized design mode tunings (a) and quality factor upper bounds, including radiative and dielectric losses (b) as a function of junction inductance L_J	80
Figure 5.1 Etching of silicon to accentuate interface and bulk losses. MS (a), SA (b), MA (c), and bulk (d) concentrated geometries fabricated with isotropic etching of TiN CPW resonators on silicon. Reproduced with permission from [25].	82

Figure 5.2 (a) Loss budgets of resonators measured in [25] with the highlighted resonators exhibiting the sensitivity to one interface or bulk loss. (b) Simulated isotropic and anisotropic etched device loss tangents to illustrate the increased sensitivity to the MA interface. Reproduced with permission from [25].	83
Figure 5.3 Niobium hydride microwave measurements. (a) Summary of the power dependence of the losses of all resonators. Box and whisker plots of (b) the TLS loss and (c) power independent loss. The labels on the box and whisker plots are as follows: blue box – bottom line is 25th percentile, top line is the 75th percentile; black horizontal lines – minimum / maximum values, excluding outliers; red plus signs – outliers; red horizontal lines – median values; red triangles – 95 % confidence intervals about the median; dashed black lines – “whiskers” extending from the 25th percentile to the minimum and from the maximum to the 75th percentile.	85
Figure 5.4 Aging study of niobium hydride samples following two months of aging in laboratory atmosphere. (a) TLS losses and (b) power independent losses before (black) and after (red) aging.	87
Figure 5.5 Capping studies of devices from multiple groups and fabrication conditions. Rigetti: dc sputtered Nb on high resistivity silicon; NIST Quantum Sensors Group (QSG): HEMEX sapphire prepared with NH ₄ OH, sputtered 200 nm Nb with 10 nm TiN, SF6 etch; Northwestern (NW) / Advanced Microwave Photonics (AMP): sputtered 85 nm of Nb on a-plane sapphire with in situ 10 nm electron beam silicon; NIST Superconductive Electronics Group (SEG) / Fermilab: PVD 160 nm Nb, 10 nm PdAu on crystal systems HEMEX sapphire. Left (light blue) control and right(dark blue) capped resonators.	88
Figure 5.6 Approximate loss budgets constructed from a combination of experimental loss data and simulated device participations. (a) Unscaled data from all Nb control devices from the capping studies on sapphire (Al ₂ O ₃) and silicon, along with Nb control qubits. The thick bar center bars indicate the measured loss data compared to the loss budget estimates. (b) Rescaled Nb on Al ₂ O ₃ losses to account for the difference in substrate air participations between the trenched silicon resonators and untrenched sapphire resonators.	88
Figure 6.1 Structural and chemical characterization of Ta films. (a) X-ray diffraction spectra of 2θ-scans for measurements of the ‘SGS2’ and ‘LGS2’ samples. The inset displays the corresponding spectrum for the ‘LGS2’ sample over a larger angle (Θ) range. The detected diffraction peaks are labeled with the corresponding Miller indices of the α -Ta phase. (b) Atomic force microscopy topographies of the ‘SGS2’ (left) and ‘LGS2’ (right) sample surfaces. (c) Electron binding energy spectra of the Ta 4f core level obtained from X-ray photoelectron spectroscopy measurements at the surface of the ‘SGS2’ and ‘LGS2’ samples. The dominant Ta oxidation states are indicated. (d) Least squares fit (open squares) to an XPS spectrum (solid black line) recorded at the surface of the LGS2 sample. Contributions to the spectrum by the Ta 4f _{5/2} (magenta color) and Ta 4f _{7/2} (green color) core levels of Ta, (solid lines), Ta ³⁺ (dotted lines), and Ta ⁵⁺ (dashed lines) were modeled by using Gaussian profiles.	92
Figure 6.2 Resonator loss power curves with small grain size (left) and larger grain size (right). Total loss δ as a function of average number of photons in the cavity $\langle n_{ph} \rangle$ for all devices measured in this work - SGS1 (light blue), SGS2 (blue), LGS1 (red), and LGS2 (orange) resonators. Lines denote best fits to the TLS model (Eq. (6.4)). 95% confidence intervals for Lorentzian fits to each data point are given, as well as the prediction interval for each TLS-curve fit.	93

Figure 6.3 Optical microscope images of coplanar waveguide resonators. (a) Full chip image of a representative chip. All circuits measured contain eight resonators with identical couplers. (b) Close up of feedline and resonator base. Conductor width is $5.5 \mu m$ and gap is $3.8 \mu m$	96
Figure 6.4 TLS loss in Ta on c-axis sapphire superconducting microwave resonators with smaller and larger grain size. Left: Box and whiskers comparison, indicating median values (red line) and 95% confidence interval of median (red triangles), with outliers shown as crosses. Right: Histogram of TLS loss for all devices in this experiment.	96
Figure 6.5 State-of-the-art literature comparison of TLS ($F\delta_{TLS}^0$) and low-power (δ_{LP}) loss values in CPW resonators. Filling factor F is estimated by plotting loss as a function of CPW gap width g . Grey lines denote lines of constant interface loss. Filled symbols denote TLS loss values, while empty symbols represent low power loss (TLS loss values unavailable).	98
Figure 7.1 (a) Electric field and (b) magnetic field profiles for the target 5.210 GHz mode used to measure the wafer loss.	104
Figure 7.2 Wafer participation design studies. Wafer participation as a function of (a) the post diameter and (b) air-gap between the posts and the wafer. Dashed line in (a) indicates the diameter of wafer. Circled points indicate the maximum participation and designed values. Shaded region in (b) shows the 95 % confidence interval on the exponential fit.	105
Figure 7.3 Quarter wave chokes in waveguides and cavities. (a) Waveguide choke based on [26]. Split post cavity cover choke: (b) top view and (c) cross sectional side view with indium gasket (blue circles) and wafer (red rectangle) positions.	106
Figure 7.4 Coupling quality factor as a function of the pin insertion depth.	107
Figure 7.5 Wet chemical etching processing and results. (a) Transene TM Type A etch of aluminum cavities near the end of the second 2 hour etch, performed by Michael Vissers (MV) at the NIST, Boulder cleanroom facility. (b) Top and bottom cavity halves, post etch. (c) Plastigauge measurement of post separation following the etch.	108
Figure 7.6 Room temperature cavity mechanical tests and mounting. (a) Plastigauge measurement of split post separation. (b) Mounting of two side polished, high resistivity silicon wafer. (c) Mounting of cavity on copper offset bracket in a Bluefors LD 250 dilution refrigerator with a separate Lakeshore RX-102A-CD ruthenium oxide (RuOx) temperature sensor mounted to the copper bracket.	108
Figure 7.7 SMA pin and indium seal. (a) Insertion of the coupling pin into the air gap between the post and the cavity walls. (b) Indium seal made with 4N high purity indium wire, spool shown on the right.	109
Figure 7.8 Preliminary data showing four modes from the SPC before wet chemical etching. Left: Al4N, etched and Al Alloy (6061) results from [27] to give bounds on the expected improvement in $Q_{i,tot}$ after etching. Black dashed lines indicate constant g_{seam} values and the gray dotted line shows the value for the bulk loss of high resistivity silicon (2.5×10^{-7}) as estimated by Woods et al. [25]. Open blue circles and black arrows show best case, expected improvements in Q_i following the SPC etch. Right: representative transmission data of the 5.210 GHz split post resonance.	110
Figure 7.9 Temperature dependent fractional frequency shift in (a) and fractional loss in (b) for the 7.875 GHz resonance of the unetched bare cavity.	111

Figure 7.10 Temperature dependent fractional frequency shift (a) and (b) fractional loss with λ_L , T_c , and p_{cond} as free parameters.	112
Figure A.1 Coupler circuit models. (a) The 2DEG coupler compact representation with a single gate and a pair of transmon qubits compared with (b) the simplified circuit used in the derivation of the charge-charge interaction matrix in the main text. (c) Parasitic capacitance circuit model of the coupler and two transmons; capacitances taken from (2.14) and (2.17).	140
Figure D.1 Typical surface topography recorded with an atomic force microscope of the tantalum film deposited at a substrate temperature of $T=600$ °C.	150
Figure D.2 Correlation of loss metrics. Device-induced intrinsic TLS loss $F\delta_{0,\text{TLS}}$ as a function of three other loss metrics: low power loss δ_{LP} minus power-independent loss δ_{HP} , δ_{HP} , and δ_{LP} . Solid black line indicates a 1:1 relationship between metrics.	151
Figure D.3 Background characterization at -100 dBm. Transmission curves for SGS1 cooldown 2 (light blue) and 4 (blue), LGS1 cooldown 1 (light green) and 3 (green), LGS2 cooldown 4 (purple) and SGS2 cooldown 4 (red) are plotted.	152
Figure D.4 Temperature sweep of resistance of large grain size (LGS) and small grain size (SGS) films. Inset shows similar transition regions for both films and similar T_c 's.	155
Figure D.5 Microwave wiring diagram. Passive and active components at each stage of a Janis JDry250 cryogen-free dilution refrigerator used to measure the devices reported in this work. Radial six-to-one switches, labeled A and B, allow for multiple samples to be measured on one pair of lines during a single cooldown. Red lines indicate the signal path to measure transmission S_{21} through the devices under test (DUT): LGS1, LGS2, SGS1, and SGS2 resonator chips.	156

LIST OF TABLES

Table 1.1	Truth tables for classical logical gates	3
Table 1.2	Truth table of a CNOT quantum logic gate	5
Table 1.3	2D coupler types, control signals, and interaction Hamiltonians	26
Table 1.4	3D coupler types, control signals, and driving schemes	29
Table 1.5	Coupling limits in resonators	36
Table 2.1	Materials parameters used in the COMSOL Semiconductor Module calculations. InGaAs and InAlAs abbreviate $\text{In}_{0.81}\text{Ga}_{0.19}\text{As}$ and $\text{In}_{0.81}\text{Al}_{0.19}\text{As}$. m_0 corresponds to the rest mass of an electron ($0.511 \text{ MeV } c^{-2}$). Out-of-plane effective electron and hole masses of InAs are set to m_0 in the model to simulate 2DEG confinement in the xy-plane. Electron mobilities for InAs, InGaAs, and InAlAs are all set to the same value as extracted from measurements of a similar device at millikelvin temperatures [23]. Values not in parenthesis (in parenthesis) correspond to electron (hole) properties.	54
Table 2.2	Participation ratios p_j , dielectric loss tangents $\tan \delta_j$, layer thicknesses t_j , and estimated dielectric-loss-limited $T_{1,j}$. All $T_{1,j}$ times are referenced to a qubit frequency of $\omega/2\pi = 5 \text{ GHz}$ and $\tan \delta_j^*$ indicates that in the absence of reliable loss tangent data for the individual InAs, InGaAs, InAlAs, and InP layers, we used the low power loss extracted from measurements of an Al patterned CPW resonator on the full III-V stack modeled in this work and measured at 100 mK as an estimate [28].	61
Table 2.3	Eigenmode frequencies and quality factors computed with HFSS in the conducting (c) and depleted (d) limit of the coupler.	63
Table 5.1	Participation matrices for sapphire and silicon Nb control devices.	89
Table 6.1	Relative atomic concentration of different tantalum oxidation states in the 'SGS2' and 'LGS2' samples as obtained from fits to the XPS spectra.	95
Table 6.2	Mean parameter values in A/B grain size comparison.	98
Table 7.1	Unetched cavity estimated wall and seam losses.	112
Table D.1	Parameters extracted from cryogenic microwave measurements of Ta on Al ₂ O ₃ coplanar waveguide (CPW) resonators. Values are given with their 95% confidence intervals where available. f_0 : resonance frequency. $1/Q_{i,\text{HP}}$: inverse high power internal quality factor. $F\delta_{\text{TLS}}^0$: resonator-induced intrinsic TLS loss. $1/Q_{i,\text{LP}}$: inverse low power internal quality factor. $1/Q_c$: inverse coupling quality factor at high power. Surface treatment labels correspond to small grain size (SGS*) and large grain size (LGS*) devices.	153

LIST OF SYMBOLS

Classical Variables

Branch, node, or mode charge variable	q_k
Branch, node, or mode magnetic flux variable	ϕ_k
Elastic dipole moment	γ_e
Electric (magnetic) dipole moment	$\mu_{e(m)}$
Electric displacement field	\mathbf{D}
Electric field	\mathbf{E}
Hamiltonian (classical)	\mathcal{H}
Hamiltonian density (classical)	\mathcal{H}
Lagrangian	\mathcal{L}
Lagrangian density	\mathcal{L}
Magnetic density field	\mathbf{B}
Magnetic field	\mathbf{H}
Strain field	\mathbf{e}

Quantum Mechanical Operators

Bosonic annihilation (creation) operator of mode k	$\hat{a}_k^{(\dagger)}$
Bosonic annihilation (creation) operator of mode k evaluated at a dc control parameter	$\tilde{a}_k^{(\dagger)}$
Branch, node, or mode charge operator	\hat{q}_k
Branch, node, or mode magnetic flux operator	$\hat{\phi}_k$
Electric (magnetic) dipole moment operator	$\hat{\mu}_{e(m)}$
Electric field operator	$\hat{\mathbf{E}}$
Hamiltonian (quantum)	\hat{H}
Magnetic field operator	$\hat{\mathbf{H}}$
Rotating frame transformation unitary	$\hat{U}(t)$

Superconducting Materials Parameters

Coherence length	ξ
London parameter	Λ
London penetration depth	λ_L
Magnetic or conductive participation ratio	α, p_{cond}
Superconducting transition temperature	T_c
Supercurrent density	\mathbf{J}_s
Zero temperature superconducting gap	Δ_0

Physical Constants

Boltzmann's constant	$k_B = 1.38 \times 10^{-23} \text{ J/K}$
Electric permittivity of free space	$\epsilon_0 = 1/36\pi \times 10^{-9} \approx 8.85 \times 10^{-12} \text{ F/m}$
Electron charge	$e = 1.60 \times 10^{-19} \text{ C}$
Magnetic flux quantum	$\Phi_0 = \frac{h}{2e} = 2.07 \times 10^{-15} \text{ Wb}$
Magnetic permeability of free space	$\mu_0 = 4\pi \times 10^{-7} \text{ H/m}$
Planck's constant	$h = 6.63 \times 10^{-34} \text{ Js}$
Reduced Planck's constant	$\hbar = h/2\pi = 1.05 \times 10^{-34} \text{ Js}$
Speed of light in vacuum	$c = 2.98 \times 10^8 \text{ m/s}$
Vacuum impedance	$Z_0 = \sqrt{\frac{\mu_0}{\epsilon_0}} \approx 377 \Omega$

LIST OF ABBREVIATIONS

Axion Dark Matter eXperiment	ADMX
Bardeen, Cooper, and Schrieffer	BCS
Beta-Barium-Borate	BBO
Black-Box Quantization	BBQ
Cavity Quantum Electrodynamics	CQED
Circuit Quantum Acoustodynamics	cQAD
Circuit Quantum Electrodynamics	cQED
Computer Aided Design	CAD
Continuous Variable	CV
Cooper Pair Box	CPB
Cooper Pair Box	CPB
Coplanar Waveguide	CPW
Diameter Correction Method	DCM
Energy Participation Ratio	EPR
Field Overlap Integral	FOI
Five and a half nines (99.9995 %) purity	5N5
Four nines (99.99 %) purity	4N
Gottesman, Kitaev, and Preskill	GKP
High Frequency Structure Simulation	HFSS
Josephson Field Effect Transistor	JOFET or JJFET
Josephson Junction	JJ
Microwave Kinetic Inductance Detector	MKID
Mixing Chamber	MXC
Molecular Beam Epitaxy	MBE
National Quantum Initiative	NQI

Near Term Intermediate Scale Quantum	NISQ
Quantum Electrodynamics	QED
Quantum Phase Slip junction	QPS
Residual Resistance Ratio	RRR
Rotating Wave Approximation	RWA
Single Electron Transistor	SET
Split Post Cavity	SPC
Standard Tunneling Model	STM
Superconducting Nonlinear Asymmetric Inductive eLement	SNAIL
Superconducting Quantum Interference Device	SQUID
Superconducting Quantum Materials and Systems Center	SQMS
Superconducting-Semiconducting	super-semi
Superconductor-Insulator-Superconductor	SIS
Superconductor-Normal-Superconductor	SNS
Transverse Electric, Magnetic	TE, TM
Transverse Electromagnetic	TEM
Two Dimensional Electron Gas	2DEG
Two Level System	TLS
Vector Network Analyzer	VNA
Very Small Logical qubit	VSLQ
Whispering Gallery Mode	WGM
X-ray Diffraction	XRD
X-ray photoelectron spectroscopy	XPS
Zero Point Fluctuation	ZPF

ACKNOWLEDGMENTS

I first want to thank my advisor Eliot Kapit for supporting me and my disparate interests and pivot from computational and theory work to experiments. I appreciated your trust and autonomy that you gave me throughout my PhD. I am grateful for the opportunities that gave me to collaborate with so many different groups and your support in pursuing positions after graduate school, especially the NIST NRC Fellowship and summer schools that I attended before defending. I look forward to continuing to collaborate with you on the experimental side of theory.

To the members of my committee, Paul Martin, Meenakshi Singh, and Mark Lusk, I thank you for your flexibility and support with the administrative and procedural aspects of the program. Before forming my committee, I found your advice and insights as instructors and mentors essential when I was still working through coursework and settling into research.

Among my collaborators, I want to especially thank Corey Rae McRae for accepting me as a member of your experimental group at CU Boulder and NIST. I appreciated your support and investment in me over the last three years. I really enjoyed working with you and look forward to collaborating in the future through SQMS and other organizations.

At the half-way mark of my PhD, Vatsan Chakram and Jens Koch joined my virtual advising team, injecting welcomed skepticism and creative wrinkles to the galvanic coupler project. I have learned so much from both of you and have enjoyed working with Yao Lu who recently joined the project, adding more insight from the 3D cavity and parametric coupler worlds. I look forward to seeing our design come to fruition in experiments over the next few years and see many opportunities to work together again soon.

To my fellow graduate student collaborators, I want to call out David Rodriguez Perez, Eric Jones, and Zhijie Tang. Knowing David from my days at LLNL helped ease the transition to Golden and working with Eliot. I want to especially recognize the team at NYU. Billy Strickland and Joe Yuan, you were excellent virtual supporters. Billy, I really enjoyed our impromptu Zoom meetings to chat about our latest experiments and I look forward to continuing our collaborations when we are on the other side of grad school. At CU Boulder, I had a great time working with John Pitten. You made sure that we went home at a reasonable hour and kept my expectations of opening and closing the fridge in check. I am really excited to see how your projects shape up in the next few years and look forward to working with you again in some capacity. I also want to recognize some exceptional undergraduate (most now graduate) students at Mines and CU Boulder who I had the pleasure of working with: Paul Varosy, Nick Price, Scott Hardman, Lana Doroshevich, Kyle Thompson, and Zach Parrott.

From my PhD cohort, mainly the subset that banded together through teaching, grading, coursework, and off-work gatherings – Paul Niyonkuru, Alan Phillips, and Taylor Wagner – I always enjoyed your company and working through fun math and software problems with vigor and enthusiasm.

There are also the many roommates and neighbors in the Homestake Drive cal-de-sac, notably Gus Floerchinger, Paul Niyonkuru, Bradley Squires, and Jaehyun Suh. It helped having someone to talk to at the end of the day and it certainly made living in Golden more affordable and enjoyable, regardless of what trouble we might have caused with the HOA.

Of course, I want to thank my parents and my sister Raeann for their support through this PhD journey. I appreciate everything that you have done for me and continue to do.

To my family.

CHAPTER 1

INTRODUCTION

Quantum computing, sensing, simulation, and communication promise to deliver solutions in materials design [29], remote sensing [30], quantum chemistry [31, 32], secure information transfer [33, 34], and myriad other settings inaccessible to conventional resources and classical computing. Recent investment in this space has enabled several noisy intermediate scale quantum (NISQ) devices [35] consisting of 20-100 noisy superconducting circuits, trapped ions, and neutral atom gate-based and analog computing platforms, not to mention several thousand lower coherence flux qubits available from D-Wave Systems. Superconducting qubits, developed with tools borrowed from the semiconductor industry, are among the leading physical qubits, with coherence times exceeding $100 \mu\text{s}$ and gate times on the order of tens of ns [36]. Several industry leaders and national laboratories support and provide cloud access to superconducting circuit and ion trap NISQ devices, with teams devoted to hardware, firmware, software, and customer service. At the hardware level, coupling between qubits has enabled fast, high coherence two qubit gates, along with single qubits required to implement a universal gate set (in analog and quantum annealing systems, couplings between qubits limits the size and scope of problems one can study with those systems). Tunable couplers have played a significant role in scaling these systems and were instrumental in the first demonstration of quantum advantage in certifiable random number generation [37].

Superconducting quantum interference devices (SQUIDs) consisting of a superconducting loop interrupted by one or more Josephson junctions, where a local or global magnetic field threads the SQUID loop, act as effective tunable inductors in conventional, flux-tunable couplers [38]. In planar devices, this has been the defacto tunable coupler, allowing fast multi-qubit operations at the expense of flux noise and challenges in minimizing heat dissipation from applied currents [8, 39]. Often these couplers change the effective capacitance between neighboring qubits, rather than the mutual inductance between qubits.¹ One might ask, is there a more direct means of changing the capacitance between qubits without flux bias? We propose voltage or charge control, first explored in Cooper pair box (CPB) charge qubits [40] to address this question. CPBs were quickly replaced by flux tuning, as the transmon qubit with its large shunt capacitor effectively eliminating its sensitive to offset charge noise [1, 41]. This pivot from offset charge dispersion to flux tunability and charge insensitive energies postponed the pursuit of voltage-tunable couplers until the arrival of gatemon qubits with voltage-controlled Josephson junctions [42].

¹See Section 1.4.1 for a systematic organization of coupling types in 2D superconducting qubits.

Superconductor-semiconductor-superconductor (S-Sm-S) junctions, the generalization of superconductor-insulator-superconductor (SIS) and superconductor-normal-superconductor (SNS) junctions used in superconducting qubits and programmable voltage standards [43], respectively, are voltage-controlled with a single gate or array of gate electrodes. The number of mobile charges in the semiconductor underneath the gate (s) changes as a function of the strength and sign of the applied voltage (s). Early interest in Josephson field effect transistors, JOFETs or JJFETs, used in classical digital logic circuits realized such gate-tunable devices in high mobility materials such as GaAs [44] and InGaAs [45]. Unsurprisingly, these materials have garnered attention in the tunable coupler space, with tunable couplings to resonator buses [23, 46, 47], mediated by two-dimensional electron gas (2DEG) based, voltage controlled Josephson junctions.

Our proposed 2DEG coupler changes the effective capacitance seen between neighboring qubits by applying negative voltages to a near surface gate, thereby depleting the 2DEG of electrons, increasing the gap between the conducting regions of the semiconductor, and decreasing the capacitance as a function of the gap size. We emphasize the novelty of this design in Chapter 2, where we quantify the on/off ratio of the coupler (ratio between maximum and minimum capacitance) and extract charge-charge interaction matrix elements relevant to superconducting qubit operations. This work has been condensed into a patent application US Patent App. No. 63/132,831, submitted in late 2020 and recently published in [48], reproduced in Chapter 2. To estimate the losses that a tunable coupler with a large dielectric footprint might add to a conventional superconducting qubit device, we designed an experiment to investigate the losses in the III-V semiconductor materials and other substrates in Chapter 7.

3D cavities pose a different set of challenges when designing and implementing tunable coupling between them. Their high coherence, with single photon lifetimes exceeding one second in Tesla accelerator-inspired niobium cavities [49] and coaxial high purity aluminum cavity lifetimes on order of 10 ms [50], has been partially limited by the coherence of the transmons used to control them. Typically transmon qubits, either fixed frequency or flux-tunable, supply the requisite nonlinearity to address and manipulate cavity states for storage or computation, or the higher levels of the transmon are used as *d*-level *qudits* [51, 52]. The placement of dielectrics in regions of high electric fields leads to additional losses, limiting the lifetime of the composite qubit-cavity system. In an electric field-dipole interaction between a transmon and cavity mode, there are also always-on, static capacitive interactions that require precision cancellation with dc or ac microwave drives. [53] Designing a tunable coupler that is engineered to not have these always-on parasitic couplings with minimal dielectric loss and a high on/off ratio is an active area of research.

In Chapter 4, we propose a galvanic tunable coupler to address the coherence limitations, avoid stray capacitive interactions, increase cavity tunability, and by extension increase the rate of parametrically activated, bilinear interactions. A patent application was submitted for this design, and the associated field integral overlap method discussed in Chapter 3, in early February 2023 based on the work in this thesis.

1.1 Digital and Analog Quantum Computing

This chapter will review the theory of quantum computation, assuming the reader has some previous exposure to quantum mechanics, classical computing, and linear algebra. Contrasting this *digital* framework of quantum computing with one form of *analog* computing, continuous variable (CV) quantum computing, where the work in Chapters 3 and 4 aim to make an impact in the subfield of CV quantum computing using superconducting cavity modes.²

1.1.1 Digital Quantum Computing

To define digital quantum computing, certain aspects of classical computing come to mind, namely digital logical and the fundamental unit of classical information, the bit. A classical bit can represent one of two states, either a logical 0 or logical 1. These states are identified as *high* (1) or *low* (0) analog voltages on transistors. By mapping all voltages less than some threshold to 0 and those above to 1, the underlying analog device approximates a digital system. The number of states that N -bits can represent is N . Hardware (redundant bits) and software (electronic error correction) components ensure that the state of each bit persists and fluctuations in environmental conditions do not modify the state of the bits or do so at a tolerable rate that does not disrupt general computational tasks [55].

Logical operations performed on classical bits include AND, OR, NOT, and combinations of these operations to realize a universal logic, capable of representing any function.³ These operations or *gates* have deterministic truth tables, as in Table 1.1 defining their operations on any single bit or pair of bits.

Table 1.1 Truth tables for classical logical gates

a	b	a AND b	a OR b	NOT a	NOT b
0	0	0	0	1	1
0	1	0	1	1	0
1	0	0	1	0	1
1	1	1	1	0	0

²There are also exciting developments in quantum annealing in the coherent limit performed with the D-Wave machine [54]. Quantum annealing is outside of the scope of this thesis, but it is worth mentioning it as another form of analog quantum computing, along with CV and special-purpose quantum simulators.

³A universal gate set consisting of NAND (not AND) gates alone can implement all possible classical logical operations.

Quantum bits or qubits, in analogy to their classical counterparts, reference logical 0 and 1 states, denoted in the computational basis as $|0\rangle$ and $|1\rangle$, with the Dirac-notation ket $|n\rangle$ and bra $\langle n|$ used as a shorthand for the column and row vectors

$$|0\rangle = \begin{pmatrix} 1 \\ 0 \end{pmatrix}, |1\rangle = \begin{pmatrix} 0 \\ 1 \end{pmatrix}, \quad (1.1)$$

$$\langle 0| = (1, 0), \langle 1| = (0, 1). \quad (1.2)$$

Physically, qubits are electronic states in trapped ions, persistent clockwise and counterclockwise currents in superconducting loops, the presence or absence of microwave photons in a superconducting circuit, as in the transmon qubit [1] energy level diagram in Figure 1.1(b), and many others. Unlike classical bits, the state of a qubit can be a linear superposition of both logical states with complex coefficients α and β as $|\psi\rangle = \alpha|0\rangle + \beta|1\rangle$.

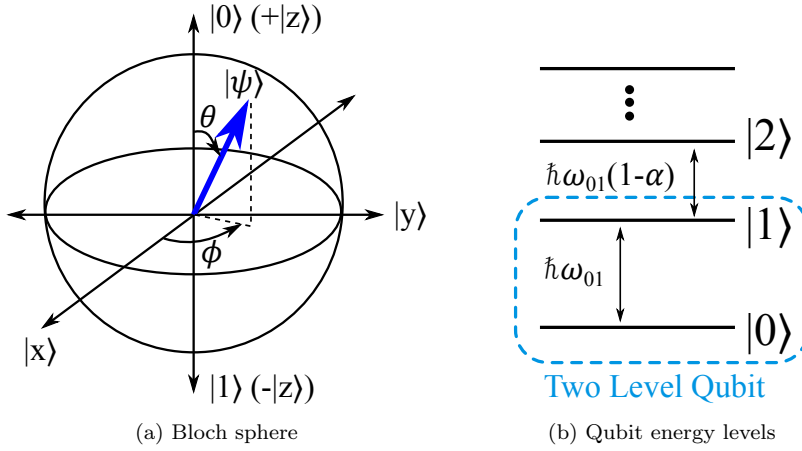


Figure 1.1 (a) Bloch sphere representing an arbitrary single qubit state. (b) Energy levels of a superconducting transmon qubit [1].

The coefficients α and β are the probability amplitudes and the probabilities are the square of these amplitudes, defined in terms of their complex conjugates denoted by the raised asterisk ($\{\cdot\}^*$), e.g. $p_0 = \alpha^*\alpha = |\alpha|^2$ and $p_1 = \beta^*\beta = |\beta|^2$ with the constraint $|\alpha|^2 + |\beta|^2 = 1$ that the total probability is equal to unity. A useful geometric interpretation of a single qubit state is the Bloch sphere (see Figure 1.1(a)), where the qubit state is represented by a point on the surface of the sphere with azimuthal angle ϕ and polar angle θ , $|\psi\rangle = \cos(\theta/2)|0\rangle + e^{i\phi}\sin(\theta/2)|1\rangle$ where $i = \sqrt{-1}$ is the imaginary unit and $|0\rangle, |1\rangle$ are the north and south poles of the Bloch sphere.

As with classical computing, quantum computing uses single (unary) and two qubit (binary) logical gates. These gates act on the state of a single qubit or two qubits, realizing universal computation with the single qubit rotations, controlled NOT (CNOT), SWAP, and Hadamard gates. Logical circuits composed of sequences of single and two qubit gates perform quantum algorithms of varying complexity. One can construct unitary operators, represented as matrices in the computational basis, analogous to the truth tables describing the classical gates.

For example, the CNOT gate or controlled NOT gate, acts on two qubits described by the two component state vector $|ct\rangle = |c\rangle \otimes |t\rangle$, with c the control and t the target qubit. The action of CNOT on two qubits is to flip the state of the target qubit when the control bit is $|1\rangle$, otherwise leave the target qubit state unchanged. In Table 1.2, we give the truth table for a CNOT gate, with the unitary U_{NOT} given by the permutation matrix in the computational basis

$$U_{\text{NOT}} = \begin{pmatrix} 1 & 0 & 0 & 0 \\ 0 & 1 & 0 & 0 \\ 0 & 0 & 0 & 1 \\ 0 & 0 & 1 & 0 \end{pmatrix} \quad (1.3)$$

Table 1.2 Truth table of a CNOT quantum logic gate

$ ct\rangle$	$U_{\text{CNOT}} ct\rangle$
$ 00\rangle$	$ 00\rangle$
$ 01\rangle$	$ 01\rangle$
$ 10\rangle$	$ 11\rangle$
$ 11\rangle$	$ 10\rangle$

The gate depth, denoted by the number of gates in a single quantum circuit, is one measure of the circuit complexity, along with the number of two qubit gates in the circuit. Current NISQ superconducting qubit systems are limited by the error rate of two qubit gates. Reducing the time and error rate of two qubit gates is of great import to achieving fault tolerant quantum computing with superconducting qubits and other modalities.

1.1.2 Continuous Variable Quantum Computing

As alluded to above, *digital* is a misnomer in the NISQ era of quantum computing, where all quantum simulators, annealers, and gate-based quantum computers are still fundamentally analog machines. Calling out a separate heading on analog quantum computing is also necessary to later highlight the role of tunable couplers in CV quantum computing.

The path towards error-corrected, fault-tolerant digital quantum computing has become clearer as planar superconducting circuits recently demonstrated an improvement in error rates by increasing the number of qubits in their surface code scheme [56]. Although this result confirms the theoretical behavior of surface error correction codes [57] at small code distances, the 3D superconducting cavity community has made larger strides with a continuous variables approach.

A continuous variable (CV) quantum system can be used to encode discrete quantum states in a system with continuous quantum degrees of freedom, e.g. the positions and momenta of many modes in a harmonic oscillator [58]. The theoretical proposal for this scheme was presented by Gottesman, Kitaev, and Preskill (GKP) in 2001 [59] and has only been recently realized, to varying degrees, in trapped ions [60] and superconducting 3D cavity circuit QED systems [61, 62]. The GKP code corrects small shifts in the generalized position and momentum of single or multiple modes of an oscillator, and is now a leading error correction candidate to reach fault tolerant quantum computing. Superconducting 3D cavity implementations of GKP state generation and gate operations owe their successes in part to previous efforts to access and control the harmonic oscillator Hilbert space in those cavities [51, 63, 64]. This is part of the motivation behind engineering cavity-nonlinear element couplings, discussed in Chapters 3 and 4, that preserve the base coherence of the cavities, as their bosonic states are tailored to these codes and have relatively long lifetimes compared to individual planar superconducting qubits.

1.2 Superconducting Circuits and Circuit QED

Superconducting circuits, the building blocks of superconducting qubits, have applications that also include astrophysical detectors [65, 66], magnetometry [67], and metrology as in defining the voltage standard. Figure 1.2 chronicles some of the key theoretical milestones and Figure 1.4 summarizes the major demonstrations of superconducting circuit theory, starting with the discovery of superconductivity in mercury [68] and extending to recent significant quantum computing milestones achieved by planar superconducting qubits.

The basic superconducting circuit elements include microwave coplanar waveguide (CPW) structures, lumped element inductors and capacitors, Josephson junctions (JJs) [69], and quantum phase slip junctions (QPSs) [70], each requiring a number of fabrication techniques including photolithography, shadow evaporative deposition, and molecular beam epitaxy (MBE). This section will discuss the classical circuit theory and quantum mechanics used to synthesize and analyze networks of these circuit elements. We review these procedures that arrive at the Hamiltonians encountered in superconducting circuit-based quantum computing. These techniques also underlie the design of tunable couplers discussed in Chapter 1.4 with specific implementations in Chapters 2 and 4.

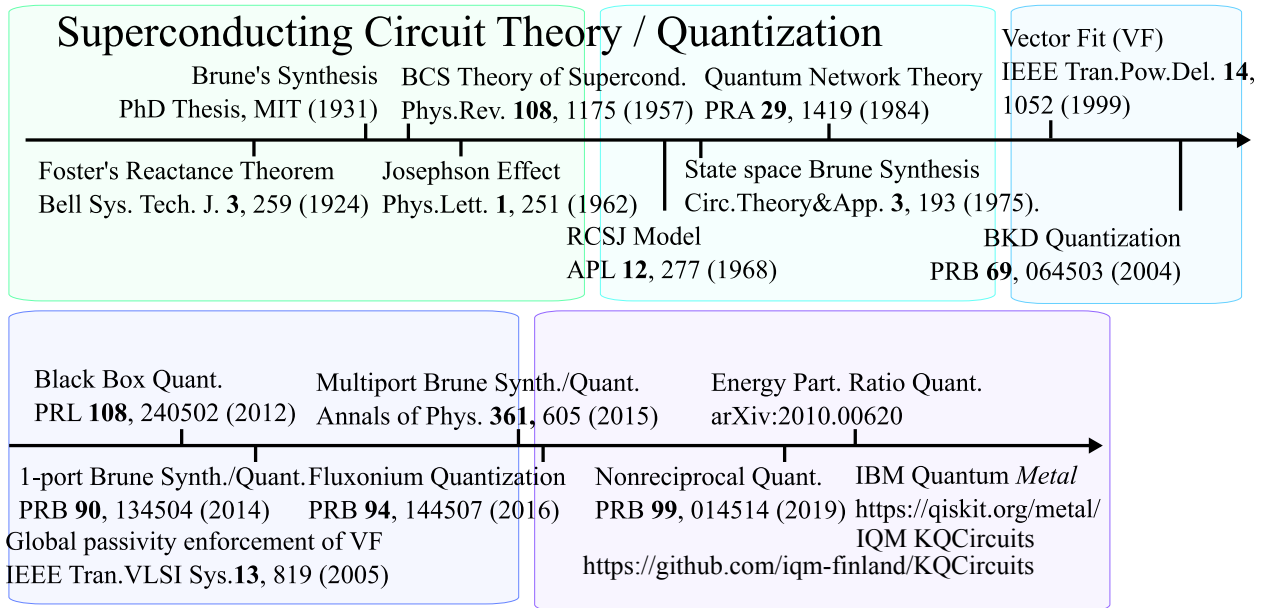


Figure 1.2 Summary of theoretical milestones in superconductivity and superconducting circuits.

1.2.1 Classical Circuit Theory and Canonical Quantization

Superconducting circuit design often starts from a lumped element circuit model to realize a desired Hamiltonian. Circuit quantum electrodynamics (circuit QED or cQED) offers a systematic approach to convert those classical lumped element linear and nonlinear circuit networks into classical Lagrangians in terms of node fluxes ϕ_j and their time derivatives $\dot{\phi}_j$ [71, 72]

$$\mathcal{L}(\{\phi_j\}, \{\dot{\phi}_j\}) = \sum_j \left(\frac{1}{2} C_j \dot{\phi}_j^2 - \frac{1}{2} L_j^{-1} \phi_j^2 \right) \quad (1.4)$$

where C_j and L_j are linear capacitors and inductors in the network. Generalizations of this Lagrangian are ubiquitous in cQED and provide a language to express various interactions between neighboring circuit elements in terms of charges and fluxes. We identify the generalized conjugate momenta as the node charges q_j defined by the classical Lagrangian expressions

$$q_j = \frac{\partial \mathcal{L}}{\partial \dot{\phi}_j} = C_j \dot{\phi}_j \quad (1.5)$$

and the classical Hamiltonian follows from the Legendre transformation

$$\mathcal{H} = \sum_j (q_j \dot{\phi}_j - \mathcal{L}) = \sum_j \left(\frac{1}{2} C_j^{-1} q_j^2 + \frac{1}{2} L_j^{-1} \phi_j^2 \right) \quad (1.6)$$

This Hamiltonian is analogous to a collection of uncoupled harmonic oscillators expressed in terms of generalized positions $\{\phi_j\}$ and momenta $\{q_j\}$. The canonical quantization approach in this context assigns a single harmonic oscillator mode to each LC pair or node flux / charge pair [73].

To quantize the circuit, the node charge and flux variables are promoted to operators with commutation relations given by

$$[\hat{\phi}_j, \hat{q}_k] = \hat{\phi}_j \hat{q}_k - \hat{q}_k \hat{\phi}_j = i\hbar \delta_{jk} \quad (1.7)$$

(1.8)

where $\delta_{jk} = 1, j = k, \delta_{jk} = 0, j \neq k$ is the Kronecker delta.⁴ These operators can then be expressed as linear combinations of bosonic creation and annihilation operators $\hat{a}_j, \hat{a}_j^\dagger$, whose commutation relations $[\hat{a}_j, \hat{a}_k^\dagger] = \delta_{jk}$ follow from (1.7)

$$q_j \rightarrow \hat{q}_j = -iq_j^{\text{ZPF}} (\hat{a}_j - \hat{a}_j^\dagger), \quad \phi_j \rightarrow \hat{\phi}_j = \phi_j^{\text{ZPF}} (\hat{a}_j + \hat{a}_j^\dagger) \quad (1.9)$$

The resonance frequency associated with the j th bosonic mode is $\omega_j = (L_j C_j)^{-1/2}$, $Z_j = (L_j C_j^{-1})^{1/2}$ is the mode impedance, and $\phi_j^{\text{ZPF}}, q_j^{\text{ZPF}}$ are the zero point fluctuations of the mode, defined by

$$q_j^{\text{ZPF}} = \sqrt{\frac{\hbar}{2Z_j}} = \sqrt{\frac{\hbar\omega_j C_j}{2}} = \sqrt{\frac{\hbar}{2\omega_j L_j}} \quad (1.10)$$

$$\phi_j^{\text{ZPF}} = \sqrt{\frac{\hbar Z_j}{2}} = \sqrt{\frac{\hbar\omega_j L_j}{2}} = \sqrt{\frac{\hbar}{2\omega_j C_j}} \quad (1.11)$$

Physically, these fluctuations are related to the vacuum expectation values of the square of the charge and flux operators or the variances as

$$\begin{aligned} \langle \hat{\phi}_j^2 \rangle &= \langle 0_j | \hat{\phi}_j^2 | 0_j \rangle \\ &= (\phi_j^{\text{ZPF}})^2 \langle 0_j | (\hat{a}_j^2 + \hat{a}_j^{\dagger 2} + \hat{a}_j^\dagger \hat{a}_j + \hat{a}_j \hat{a}_j^\dagger) | 0_j \rangle = (\phi_j^{\text{ZPF}})^2 \end{aligned} \quad (1.12)$$

$$\langle \hat{q}_j^2 \rangle = \langle 0_j | \hat{q}_j^2 | 0_j \rangle = (q_j^{\text{ZPF}})^2 \quad (1.13)$$

Note, we have written all of the possible expressions for zero point fluctuations and will choose each definition throughout this thesis depending on its suitability to the problem at hand. For most applications, choosing the first or second definitions in (1.10) and (1.11) is the natural choice, unless one is interested in expressing couplings in terms of mode impedances, then the first pair of definitions is preferred.

⁴Note, the classical Hamiltonian in (1.6) is of a symplectic form, i.e. the Poisson bracket $\{\phi_j, q_k\} = \delta_{jk} \Rightarrow [\hat{\phi}_j, \hat{q}_k] = i\hbar \delta_{jk}$. In Ref. [74], the authors present a more general prescription to arrive at a Hamiltonian of this form that guarantees the ϕ_j and q_k are canonically conjugate variables and thus $\hat{\phi}_j$ and \hat{q}_k are canonically conjugate operators.

Each expression is equivalent and the first is the most compact, but some authors will choose one form over another to compare capacitance with mass and inductance with an inverse spring constant in mechanical oscillators.

The bosonic operator description for the linear elements in a given superconducting circuit lends itself to analogies with cavity QED (CQED), i.e. atoms in cavities and interactions of the Jaynes-Cummings [75] type, where Josephson junctions act as artificial atoms and LC 's act as cavity modes [41, 76].

1.2.2 Josephson Junctions

The nonlinear elements alluded to in the previous section are Josephson junctions and quantum phase slip junctions. For the purposes of this thesis, we will omit QPSs and focus on Josephson junctions. These junctions are typically superconducting-insulator-superconductor (SIS) or superconductor-normal metal-superconductor (SNS) structures. The lumped element model of SIS junctions was first described by Josephson [69] in 1962, with the behavior of such a device depending on the phase difference $\varphi = \varphi_2 - \varphi_1$ of the wavefunctions of the two superconducting leads. Figure 1.3 shows a conceptual model of these wavefunctions plotted on a cross-section of an overlap SIS Josephson junction.

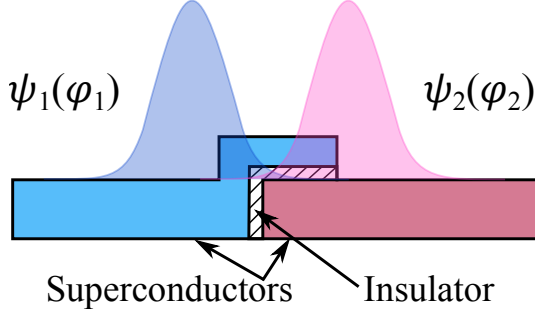


Figure 1.3 Cross-section of an overlap SIS Josephson junction.

Two consequences of the overlapping macroscopic quantum wavefunctions of the two superconducting leads of the Josephson junction are the dc and ac Josephson effects relating φ to the supercurrent I_s ⁵ flowing across the junction and the voltage across the junction V_J

$$I_s = I_c \sin \varphi \quad (1.14)$$

$$\frac{\Phi_0}{2\pi} \frac{d\varphi(t)}{dt} = V_J(t) \quad (1.15)$$

⁵This is related to the supercurrent density J_s described in more detail in Section 1.5.5 by the junction area.

In (1.15), $\Phi_0 = h/2e$ is the magnetic flux quantum, and (1.15) has the correct sign resulting from the derivation outlined in [67] rather than the minus sign in Faraday's law of a similar form due to the relationship between the phases of superconducting leads.

The dc Josephson effect in (1.14) describes the nonlinear behavior of the junction current, which can be treated as a nonlinear inductor with inductance L_J [77]

$$V_J = \frac{1}{I_c \cos \varphi} \frac{\Phi_0}{2\pi} \frac{dI_s}{dt} = L_J \frac{dI_s}{dt} \quad (1.16)$$

$$L_J = \frac{\Phi_0}{2\pi} \frac{1}{I_c \cos \varphi} = \frac{L_{J_0}}{\cos \varphi} \quad (1.17)$$

The ac Josephson effect in (1.15) is a statement of flux-voltage transformation, useful in the development of the superconducting Josephson junction-based voltage standard at NIST [78] and to circuit quantization involving external voltage sources.

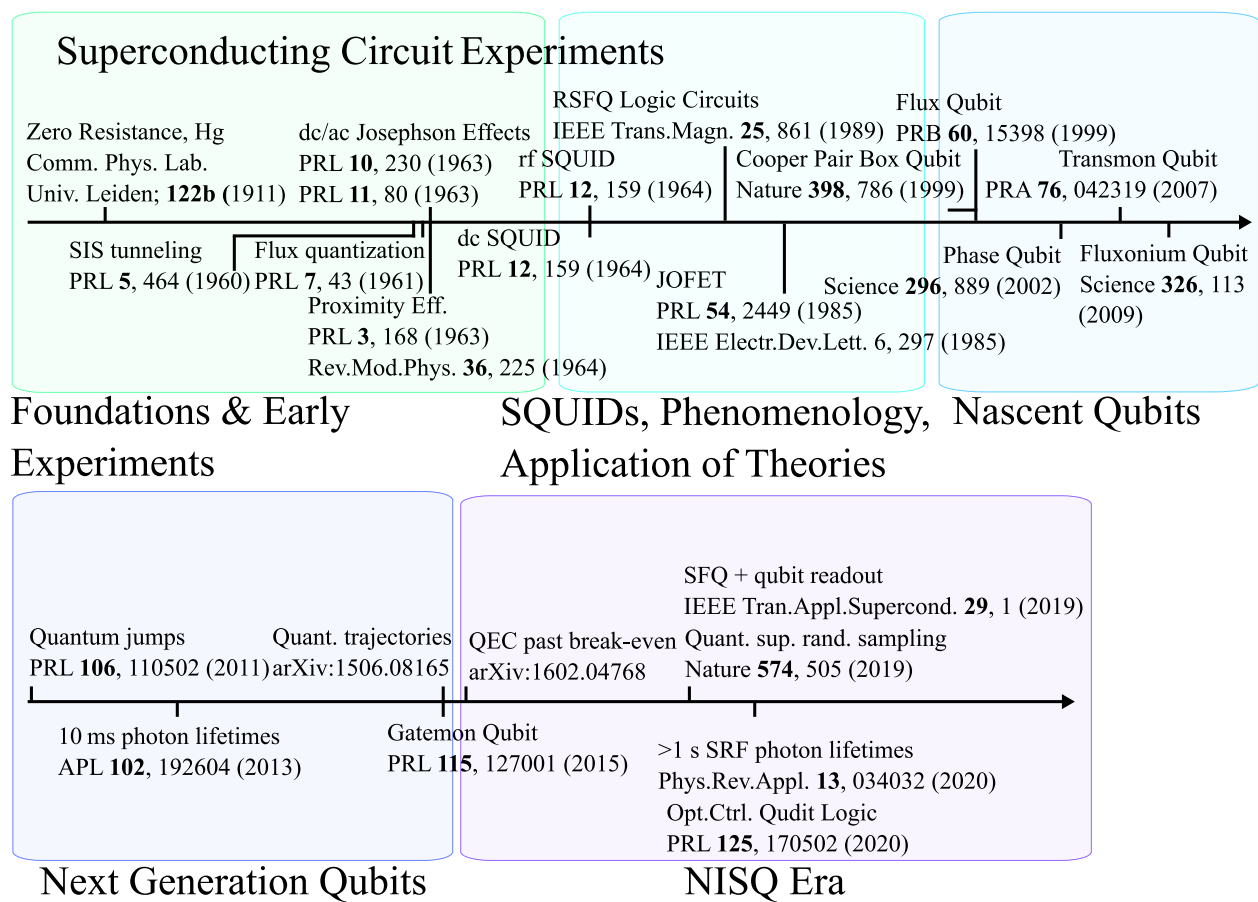


Figure 1.4 Summary of experimental milestones in superconductivity and superconducting circuits.

1.2.3 Circuit QED, Cooper Pair Boxes, and Transmons

With the addition of Josephson junctions to the circuit quantization toolbox, superconducting circuits could realize (in the appropriate parameter regimes) physics from cavity QED. Unlike naturally occurring atomic systems, artificial atoms and cavities in superconducting circuits can be designed to have much stronger couplings and richer energy spectra depending on the choice of circuit topologies and values. This is both a feature and a concern, as no two superconducting qubits can be fabricated to have exactly the same energy spectra, although recent work at IBM has improved the precision of their qubit frequencies using a laser annealing process to adjust the junction inductance of their qubits, leading to an imprecision of 0.15 % in frequency [79]. This is still a relatively large uncertainty on the qubit frequency; for a 5 GHz qubit, this amounts to an uncertainty of 7.5 MHz, much larger than the linewidth κ of a transmon with a $100 \mu\text{s}$ T_1 time and corresponding $\kappa/2\pi = 1.6 \text{ kHz}$.

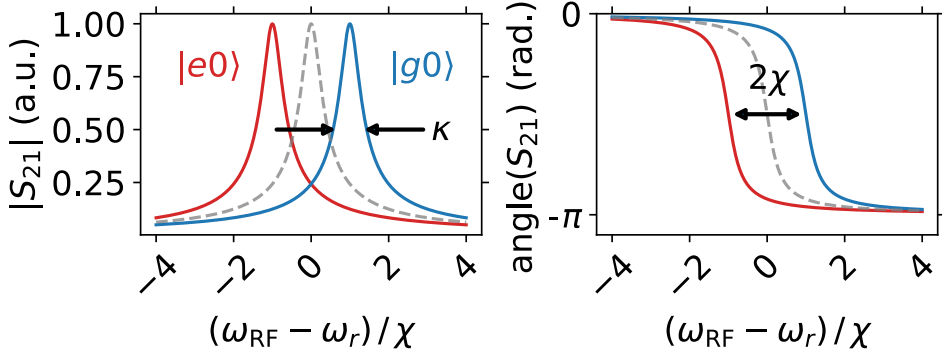


Figure 1.5 Dispersive readout. Left: Magnitude of cavity transmission. Right: Phase of cavity transmission. Ground state (blue), excited state (red), bare cavity (gray) with qubit-cavity detuning < 0 . Adapted from [2], see Appendix E.

1.2.4 Circuit QED

As mentioned above, circuit QED or cQED is the circuit analog to CQED. The prototype Hamiltonian in the cavity (CQED) case is that of the Jaynes-Cummings model [75] which consists of a two level atom with a dipole coupling to the electric field operator $\hat{\mathbf{E}}$ (single mode with frequency ω_c and bosonic operators \hat{a}, \hat{a}^\dagger) of a cavity [80]

$$\begin{aligned}\hat{H}_{\text{JC}} &= \frac{1}{2}\hbar\omega_a\hat{\sigma}_z + \hbar\omega_c(\hat{a}^\dagger\hat{a} + 1/2) - \hat{\boldsymbol{\mu}}_e \cdot \hat{\mathbf{E}} \\ &= \frac{\hbar\omega_a\hat{\sigma}_z}{2} + \hbar\omega_c(\hat{a}^\dagger\hat{a} + 1/2) - i\hbar g(\hat{a}\hat{\sigma}_+ - \hat{a}^\dagger\hat{\sigma}_- - \hat{\sigma}_+\hat{a}^\dagger + \hat{\sigma}_-\hat{a}) \\ &\approx \frac{\hbar\omega_a\hat{\sigma}_z}{2} + \hbar\omega_c(\hat{a}^\dagger\hat{a} + 1/2) - i\hbar g(\hat{a}\hat{\sigma}_+ - \hat{a}^\dagger\hat{\sigma}_-) \end{aligned} \quad (1.18)$$

The first term in (1.18) gives the energy of a single atom with ground to excited state transition frequency ω_a and electric dipole moment operator $\hat{\mu}_e$. The second term gives the energy of a single mode of the cavity with resonance frequency ω_c and the third term gives the dipole coupling between the electric field of the cavity and atom. Between the second and third lines in (1.18), we discarded the terms that do not conserve photon number, $\hat{\sigma}_+ \hat{a}^\dagger + \hat{\sigma}_- \hat{a}$ by applying the rotating wave approximation (RWA).

The RWA follows from rewriting the Schrödinger-picture Hamiltonian in (1.18) in the interaction picture and discarding terms with phase factors $e^{\pm i(\omega_c + \omega_a)t}$, as these terms oscillate rapidly relative to the terms with $e^{\pm i(\omega_c - \omega_a)t}$ and their time averages go to zero, provided that the atom-cavity detuning satisfies $\Delta_{ac} = |\omega_c - \omega_a| \ll |\omega_c + \omega_a|$. In the field integral overlap method reported in Chapter 3, both photon number conserving and non-conserving terms will be retained and can be activated by applying external fields at the sum or difference frequencies. The dispersive limit, $g \ll \Delta_{ac}$, permits a unitary transformation of this Hamiltonian known as the Schrieffer-Wolf transformation that highlights two important features of cQED systems: dispersive readout and photon number-state dependent qubit dephasing [41, 81]. Ignoring the vacuum energy term in (1.18), we have, to order g^2/Δ_{ac}

$$\hat{H}_{\text{disp}} \approx \frac{1}{2} \hbar \omega'_a \sigma_z + \hbar \omega_c \hat{a}^\dagger \hat{a} + \hbar \chi_{ac} \hat{a}^\dagger \hat{a} \hat{\sigma}_z \quad (1.19)$$

where $\omega'_a = \omega_a + \chi_{ac}$, $\chi_{ac} = g^2/\Delta_{ac}$, and the last two terms are often grouped together as $\hbar(\omega_c + \chi_{ac} \hat{\sigma}_z) \hat{a}^\dagger \hat{a}$ to illustrate the qubit state-dependent shift of the cavity frequency as shown in Figure 1.5. Similarly, the qubit state can shift with a change in the number of photons in the cavity by grouping the first and last terms $\hbar(\omega'_a + \chi_{ac} \hat{a}^\dagger \hat{a}) \hat{\sigma}_z$. This latter grouping has applications in quantum sensing, where single photons are counted by measuring shifts in the qubit frequency or by measuring the photon number parity [82].

1.2.5 Cooper Pair Box and Transmons

To realize a Hamiltonian such as (1.18) or (1.19) with superconducting circuits, one starts from the classical descriptions in Section 1.2.1 with an additional energy term for the Josephson junctions of the form $(-E_J \cos \varphi)$ [41]

$$H_{\text{CPB}} = E_C(n - n_g)^2 - E_J \cos \varphi \quad (1.20)$$

where n is the number of Cooper pairs on the superconducting island forming the so-called Cooper pair box qubit [40], n_g is the offset charge on the island, and φ is the gauge-invariant superconducting phase difference across the Josephson junction.

The quantized version of (1.20) in the Cooper-pair number basis reads [83]

$$\hat{H}_{\text{CPB}} = E_C(\hat{n} - n_g)^2 - \frac{1}{2}E_J \sum_{n \in \mathbb{Z}} (|n\rangle \langle n+1| + |n+1\rangle \langle n|) \quad (1.21)$$

with its energies depending on the offset charge n_g . The transmon qubit operates in the charge-insensitive limit, where $E_J/E_C \gg 1$ and the energy levels no longer strongly depend on the offset charge n_g [1, 41]. Figure 1.6 illustrates this offset charge dependence, with the figures produced using the open source Python package `scqubits` [84, 85].

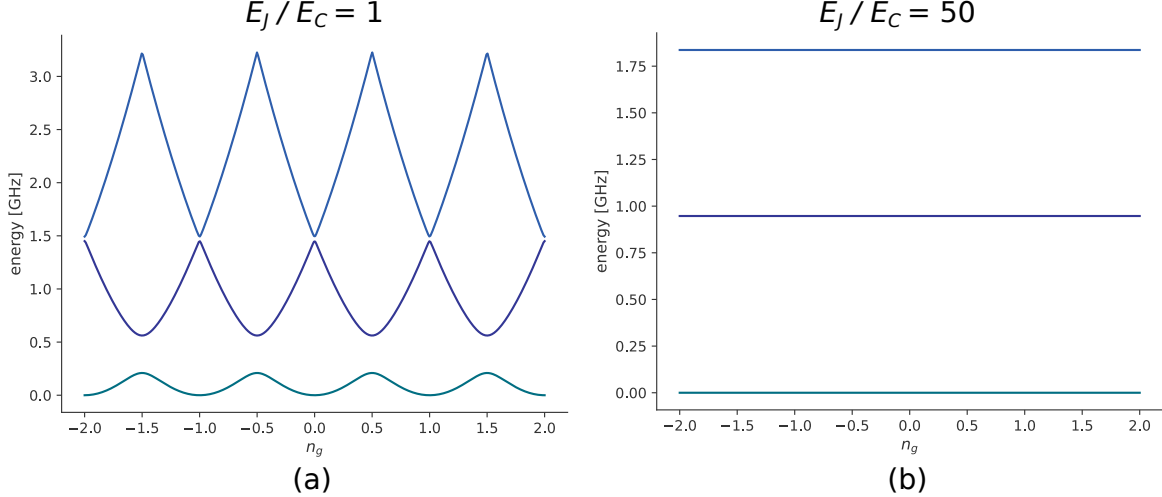


Figure 1.6 Cooper pair box energies as a function of offset charge. (a) Charge qubit regime, (b) typical transmon regime. Energies scaled to $\sqrt{8E_JE_C}$ and shifted from their minima such that the ground state energy at zero charge offset is zero. Adapted from [1], see permissions in Appendix E.

This insensitivity to offset charge fluctuations leads to a suppression of charge noise dephasing, that is proportional to $\partial E_{01}/\partial \lambda = \langle 0 | \partial \hat{H}_{\text{CPB}}/\partial \lambda | 0 \rangle - \langle 1 | \partial \hat{H}_{\text{CPB}}/\partial \lambda | 1 \rangle$, with $\lambda = n_g$, i.e. [1]

$$T_{2,1/\text{f charge}} \sim \frac{\hbar}{A} \left| \frac{\partial E_{01}}{\partial n_g} \right|^{-1} \quad (1.22)$$

where $A \sim 10^{-4}e$ is a typical charge fluctuation amplitude from experiments at the time of writing in Ref. [1]. There is a tradeoff to achieve this exponential suppression in charge dispersion, that is an algebraic reduction in the anharmonicity, the departure of the level spacings from equally-spaced, harmonic oscillator-like levels. In practical transmon implementations, an E_J/E_C ratio of 50 is achieved with an $E_J = 15$ GHz and $E_C = 300$ MHz. This anharmonicity is sufficiently large to individually address the 0-1 transition, and often the 1-2 transition, as it is much larger than the qubit linewidth and easily realized with micron sized shunt capacitor pads.

The large shunt capacitor in the transmon differentiates it from the Cooper pair box qubit, resulting in a large E_J/E_C ratio with a large capacitance ($E_C = e^2/2E_\Sigma$, C_Σ is the total capacitance of the Josephson junction and shunt capacitor).

1.3 Circuit QED with 3D Cavities

In Section 1.2, we saw that given a circuit network, one can write down the Lagrangian and Hamiltonian to arrive at a quantum description for the circuit. For some 3D structures such as individual modes of rectangular cavities, it is possible to write down an approximate equivalent circuit model. However, general microwave structures, either planar or 3D, require other methods to convert the frequency response of the linear circuit to an equivalent circuit that can then be quantized by the methods described in the Section 1.2 or other approaches described below.

Prior to the writing of this thesis, the two primary approaches to quantizing 3D structures were the blackbox approach and associated Brune synthesis and quantization methods, and the energy participation ratio (EPR) method. In Chapter 3, we will introduce the field overlap integral method that generalizes a subset of the EPR approach to enable the analysis of 3D structures with galvanic shunts such as the tunable coupler described in Chapter 4.

1.3.1 Black-Box Quantization Methods

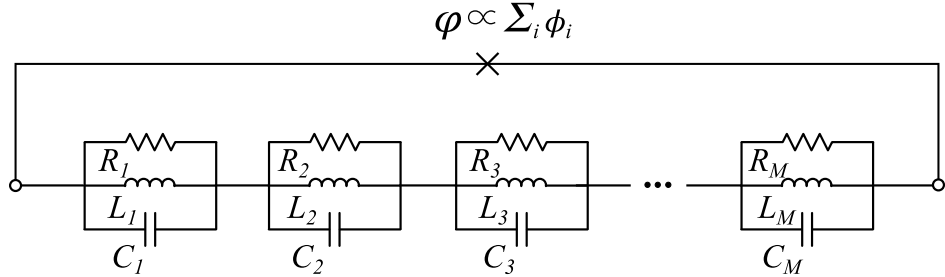


Figure 1.7 Lossy Foster series RLC decomposition of a single port network shunted by one Josephson junction with gauge invariant phase difference φ , reproduced with permission from [3].

The starting points for all driven modal, black-box circuit quantization approaches are semi-automated circuit extraction methods that approximate the multiport impedance \mathbf{Z} or admittance \mathbf{Y} as a series of LC circuits or other more general cascaded, passive linear networks. The LC ladder network normal mode expansion of the structure is based on Foster's reactance theorem [86]. This theorem states that any passive, linear, and purely reactive network can be expressed as a series combination of parallel LC sections or a parallel combination of series LC sections. The addition of resistors approximates the losses in the system, but the *lossy* Foster form cannot exactly reproduce the impedance of the underlying network.

Otto Brune developed a single port synthesis method that exactly represents the impedance of any linear passive network satisfying the positive-real conditions, i.e. that the impedance function must have positive, real values for all complex frequencies s with $\text{Re}\{s\} > 0$ [87]. This is a statement of passivity itself, that resistances must be non-negative and energy is conserved. The multiport version of this circuit synthesis method followed from the work of Anderson and Moylan [88], where state space methods improved the numerical and algorithmic implementation of the synthesis procedure. Solgun quantized the single port Brune circuit [90] and generalized the procedure to the multiport Brune circuit from the state space description of the circuit by Anderson and Moylan [88] in his PhD thesis [89].

The latter procedure, purported to be a general method to circuit synthesis and quantization of 2D and 3D structures, is extremely sensitive to passivity violations in the parametrized impedance matrices computed by Vector Fitting algorithms [91, 92] and the development of postprocessing techniques to correct those violations is an active area of research. These methods fall under the larger class of black-box impedance quantization methods, but the details of Vector Fitting and Brune synthesis are outside of the scope of this thesis.

1.3.2 Summary of Black-Box Quantization with the Lossy Foster Decomposition

The black-box quantization method, in the lossy Foster approximation, treats cavity modes and Josephson junctions separately. The lossy Foster approach treats the electromagnetic fields of the passive, linear elements in the system as a collection of damped harmonic oscillators or cascaded RLC sections, as in Figure 1.7. In the absence of loss (modes with infinite quality factor), Foster's reactance theorem maps the poles and residues of the impedance matrix or zeros and derivatives of the imaginary part of the admittance matrix to LC sections corresponding to the resonant frequencies of a passive, linear N -port network [86].

Foster's reactance theorem, together with circuit QED, considers an N -port network whose terminals are shunted by N -Josephson junctions. The driving point [93] admittances (the diagonal entries of the admittance matrix calculated by Ansys HFSS or a similar full-wave electromagnetic finite element solver) captures the linear, classical response of the circuit, with the nonlinearity of the k -th junction added to the k -th driving point admittance, “by hand”^{6,7}

$$Y_{kk}(\omega) \rightarrow Y_{kk}(\omega) + i\omega C_{J,k} + \frac{1}{i\omega L_{J,k}} + \frac{1}{R_{J,k}} \quad (1.23)$$

⁶When we say “by hand”, we mean that the Josephson junction inductance and its nonlinearity are added to the admittance function $Y_{kk}(\omega)$ extracted from HFSS as a post-processing step. Some practitioners prefer to include the linear part of the inductance as a lumped element boundary condition across the port where $Y_{kk}(\omega)$ is calculated. All calculations performed and referenced in this thesis use the “by hand” approach.

⁷We use i instead of j for the imaginary unit to agree with the notation used throughout this thesis.

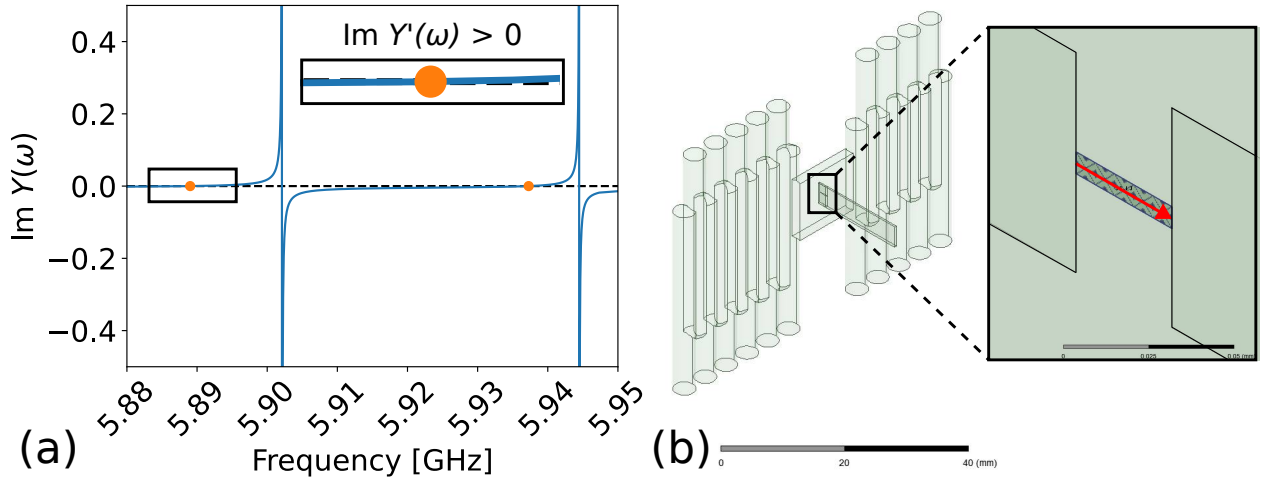


Figure 1.8 Black-box resonance frequencies from (a) zero crossings of the imaginary part of the admittance and (b) lumped port defined by a rectangle representing a Josephson junction.

In (1.23) $Y_{kk}(\omega)$ is the driving point admittance, the response of the system at port k driven by a driving voltage V_k resulting in an output current I_k , with all other ports short circuited,

$Y_{kk}(\omega) = I_k/V_k|_{V_{j \neq k}=0}$. $C_{J,k}$ is k -th junction capacitance, and $L_{J,k}^{-1}$ is the k -th junction inductance. The resistor $R_{J,k}$ is an optional parameter to estimate the coherence limit of the entire structure by including losses from experiments. For example, one can assume that the junction acts as a transmon with a Purcell-limited T_1 [94] set by

$$T_{1,\text{Purcell}} = \frac{C_J}{\text{Re}\{Y_{JJ}(\omega)\}} \Rightarrow R_{J,k} = \frac{C_J}{T_{1,\text{Purcell}}} \quad (1.24)$$

In practice, HFSS calculates the driving point impedances Z_{kk} with a lumped port defined by a rectangular sheet at the location of the k -th Josephson and the direction of the driving current I_k specified by the user (typically oriented along the longest dimension of the rectangular sheet, centered along the shortest dimension) generating an output voltage V_k . The driving point admittances are computed by inverting the driving point impedances,⁸ $Y_{kk} = Z_{kk}^{-1}$ [93].

In the single port picture, we have one driving point admittance, $Y_{11} = Y(\omega)$, with resonance frequencies ω_p located at the zero crossings of $\text{Im}\{Y_{kk}(\omega)\}$ (see Figure 1.8) and mode inductances L_p , capacitances C_p , and impedances Z_p defined by [95]

$$C_p = \frac{1}{2} \frac{d\text{Im}\{Y(\omega)\}}{d\omega} \Big|_{\omega=\omega_p}, \quad L_p = \frac{1}{\omega_p^2 C_p}, \quad Z_p = \sqrt{\frac{L_p}{C_p}} \quad (1.25)$$

⁸Note this does not apply to the transfer impedances and transfer admittances, i.e. the off-diagonal entries of the corresponding matrices, where $Y_{mn} \neq Z_{mn}^{-1}$, $m \neq n$.

$\text{Im}\{\cdot\}$ gives the imaginary part of a complex valued function. All passive networks have resonances where $d\text{Im}\{Y(\omega)\}/d\omega > 0$, as shown in the inset of Figure 1.8a, resulting in positive capacitances in (1.25). The Hamiltonian associated with the combination of mode inductors and capacitors is given by [41]

$$\begin{aligned} H_0 &= \sum_p \left(\frac{Q_p^2}{2C_p} + \frac{\Phi_p^2}{2L_p} \right) \\ &= \sum_p \left(4E_{C,p}N_p^2 + \frac{1}{2}E_{L,p}\varphi_p^2 \right) \end{aligned} \quad (1.26)$$

$$N_p = \frac{Q_p}{2e}, \quad \varphi_p = \left(\frac{2\pi}{\Phi_0} \right) \Phi_p \quad (1.27)$$

$$E_{L,p} = \left(\frac{\Phi_0}{2\pi} \right)^2 \frac{1}{L_p}, \quad E_{C,p} = \frac{e^2}{2C_p} \quad (1.28)$$

where Q_p is the charge operator, N_p is the Cooper pair number operator, Φ_p is the flux operator, φ_p is the 2π -periodic phase operator, $\Phi_0 = h/2e$ is the magnetic flux quantum, $2e$ is the electronic charge of a Cooper pair, $E_{L,p}$ is the inductive energy, and $E_{C,p}$ is the charge energy, each referenced to a normal mode with index p . The Hamiltonian in Eq. (1.26) is equivalent to a harmonic oscillator Hamiltonian

$$\hat{H}_0 = \sum_p \hbar\omega_p (\hat{a}_p^\dagger \hat{a}_p + 1/2) \quad (1.29)$$

where $\omega_p = (L_p C_p)^{-1/2}$ and $[\hat{a}_p, \hat{a}_q^\dagger] = \delta_{pq}$. For a detailed derivation of the quantization of this Hamiltonian and the relationship between the black-box zero point fluctuations and the energy participation ratios described in Section 1.3.4, see Appendix B.

To accurately compute the above quantities, the admittances are calculated with full-wave electromagnetic finite element simulations. These simulations are performed as frequency sweeps, where the excitation (input voltage) frequency is swept densely near each resonance and sparsely away from resonance. Typically, Ansys High Frequency Structure Simulation (HFSS) acts as the finite element solver with a driven modal solution type as the frequency sweep driver. These frequency sweeps increase the runtime of the simulation, limiting the speed with which geometric parameter sweeps can be performed to optimize a given device design. The frequency refinement is a user-controlled process, leading to significant variability between resonance frequency identification from user-to-user. There are other limitations of this analysis, including the modeling of loss. In the next section, we discuss some of these pitfalls and heuristics to remove unphysical simulation artifacts from quantities derived from black-box calculations. In Section 1.3.4, the energy participation ratio approach addresses both the frequency sweep and loss problems by solving a simpler eigenvalue problem.

1.3.3 Numerical Idiosyncrasies with Black-Box Quantization

The black-box quantization methods have subtle numerical problems that can lead to nonphysical results. These concerns are compounded by other theoretical concerns in how to properly handle the truncation of the infinite modal expansion to a finite set of modes, the discussion of which can be found in Chapter 2.5 of Nicholas Frattini's thesis [96].

One of the challenges in both impedance and admittance based black-box quantization methods is the enforcement of passivity. HFSS guarantees the resulting S -parameters derived from a driven modal simulation are passive to some threshold. One expression of passivity is that the scattering matrix S must be unitary, i.e. its singular values must be no greater than one, or equivalently, the norm of $S \leq 1$ [97]. Small violations of the passivity constraint can occur with varying severity over a broad frequency range, with the largest violations often observed near resonances. These violations can halt the Brune synthesis procedure [87, 88], an alternative circuit synthesis method with exact reproduction of the original impedance matrix, which was rigorously explored and quantized in the work by Solgun [89]. There is an entire subfield in the electrical engineering community [98, 99] devoted to addressing this problem in the context of Vector Fitting [91, 92] and model order reduction. Few groups use the Brune synthesis approach for the reasons mentioned above, but the traditional black-box or lossy Foster method is not immune to these passivity violations.

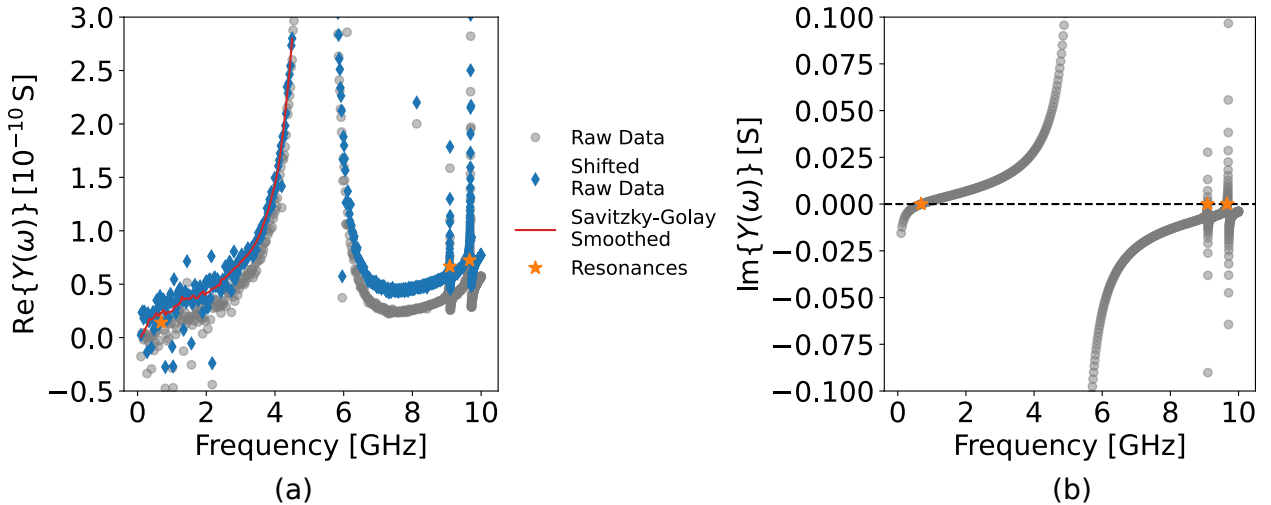


Figure 1.9 Consequences of passivity violations in traditional black-box quantization. (a) The real part of the admittance from a representative superconducting 3D structure showing negative resistance values in gray. Raw data are shifted in blue and smoothed in red to correct for negative resistances. (b) The imaginary part of the admittance shows the resonance frequency locations as the zero crossings of $\text{Im}\{Y(\omega)\}$.

The consequences of these passivity violations in the traditional black-box approach do not result in the same catastrophic failures as in the Brune, but manifest in subtle ways when estimating the mode losses.

These losses, $Q_p^{-1} = \omega_p R_p C_p$ depend on the real part of the admittance, R_p^{-1} , and the derivative of the imaginary part of the admittance, C_p . The former is particularly sensitive to passivity violations, especially those occurring near resonances, where violations are most common. The latter is sensitive to the slope of the admittance at the zero crossings. Using a combination of a simple zero crossing detector, essentially a sign change detector, and a root finding algorithm applied to the neighborhood around the position returned by the sign change method, we have developed a robust zero crossing detector. On the issue of passivity violations, there are systematic methods to correct them with minimal changes to the entire admittance spectrum [98, 99] and countless heuristics that minimally modify the driving point admittances, but would otherwise significantly change the admittance matrix.⁹

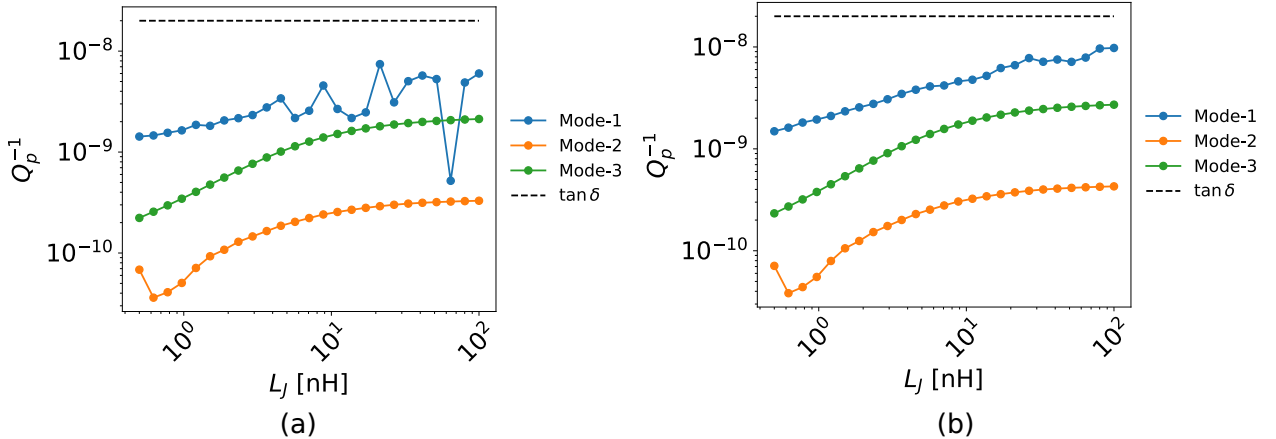


Figure 1.10 Losses extracted from the admittance data in Figure 1.9 without a correction to the admittance in (a) and with a correction in (b). The black dashed line indicates the loss tangent of sapphire, $\sim 2 \times 10^{-8}$ from [4], as a reference for the scale of the losses for each mode in this device.

For example, the resistance can be small in high Q systems, dropping below zero and leading to nonphysical, negative losses. The admittance can also have high frequency numerical noise that can lead to artificial variations in losses as well. We added a small offset to the resistances in the neighborhood of the problematic resonances to compensate for the negative resistances, usually at low frequencies and near resonances, then we applied a smoothing routine [100–102] to reduce the roughness of the real part of Y . Figure 1.9 shows an example frequency response of $\text{Re}\{Y(\omega)\}$ with the raw data, shifted data, and smoothed data.

⁹Recall that the driving point admittances refer to the diagonal entries in the admittance matrix, which are the only quantities considered in the lossy Foster black-box approach. Adding a vertical shift to the real part of $Y(\omega)$ does not significantly change the magnitude of derived quantities, such as Q_p^{-1} , but can change their sign. The Brune synthesis uses information from the entire admittance or impedance matrix, thus ad hoc shifts to one or more of the diagonal matrix elements can have an outsized effect on the spectrum of the \mathbf{Y} or \mathbf{Z} matrices, affecting the values of extracted circuit elements.

The peaks correspond to the resonances observed in the imaginary part of the admittance, where the resistances are extracted, i.e. at frequencies $\{\omega_p\}$, the orange stars in Figure 1.9 (b). In Figure 1.10, we see that the losses of the lowest frequency mode become particularly sensitive to the variations in $\text{Re}\{Y\}$, especially at high values of L_J . Here, L_J is the junction inductance “added by hand” to the admittance calculated by HFSS to represent a flux-tunable transmon or dc-SQUID as in (1.23). We will return to this example in Chapters 3 and 4, where we add an inductance to the admittance to represent a nonlinear inductor (dc-SQUID) used in the 3D galvanic tunable coupler.

1.3.4 Energy Participation Ratio Quantization

The energy participation ratio (EPR) quantization method, developed by Minev et al. [103], bypasses the problem of model identification in the black-box methods by extracting the linear, normal-mode Hamiltonian from ratios of capacitive and inductive energies. Driven modal simulations are replaced with eigenmode simulations that give the electric and magnetic field solutions to the time harmonic Maxwell’s equations subject to boundary conditions of the geometry under study. Unlike the driven modal case where the Josephson junctions are replaced by ports and later added to the admittance outside of HFSS, EPR defines the junctions as lumped element inductors with a finite area represented by a rectangular sheet in the eigenmode solver. Care must be taken in meshing these structures, as they are often several orders of magnitude smaller than the largest structures in the model. Seeding the initial mesh, i.e. applying a fixed length surface mesh to the junctions and surrounding pad structures often improves the convergence of the adaptive meshing routine in the eigenmode solver.

Along with addressing the numerical concerns of BBQ, the EPR method also places lossy objects on the same footing as lossless ones with participation ratios associated with dielectric losses, radiative losses, and seam losses [103]. This formulation emphasizes energies over admittances or impedances, forgoing the numerical derivative expressions to calculate the mode capacitances and zero crossing detectors with integrals and eigenvalue problems that have more favorable convergence properties.

Starting with the expression for the (inductive) EPR of the j -th Josephson junction in mode m [103]

$$\begin{aligned} p_{mj} = p_{mj}^L &:= \frac{\text{Inductive energy stored in the } j\text{-th junction}}{\text{Inductive energy stored in the } m\text{-th mode}} \\ &= \frac{\langle \psi_m | \frac{1}{2} E_{J_j} \varphi_j^2 | \psi_m \rangle}{\langle \psi_m | \frac{1}{2} H_0 | \psi_m \rangle} = \frac{\frac{1}{2} E_{J_j} \langle \varphi_{mj}^2 \rangle}{\frac{1}{4} \hbar \omega_m} = \frac{2 E_{J_j} \langle \varphi_{mj}^2 \rangle}{\hbar \omega_m} \end{aligned} \quad (1.30)$$

$E_{J_j} = \left(\frac{\Phi_0}{2\pi}\right)^2 L_{J_j}^{-1}$ is the Josephson energy associated with the j -th junction. In the last line of Eq. (1.30), we took the vacuum expectation value, $|\psi_m\rangle = |0\rangle_m$, as we did in (1.12) and (1.13) to compute the zero point flux and charge fluctuations.

Next, we define analogous capacitive EPRs in terms of the zero point Cooper pair number fluctuations

$$\begin{aligned} p_{mj}^C &:= \frac{\text{Capacitive energy stored in the } j\text{-th junction}}{\text{Capacitive energy stored in the } m\text{-th mode}} \\ &= \frac{\langle \psi_m | 4E_{Cj} N_j^2 | \psi_m \rangle}{\langle \psi_m | \frac{1}{2} H_0 | \psi_m \rangle} = \frac{4E_{Cj} \langle N_{mj}^2 \rangle}{\frac{1}{4} \hbar \omega_m} = \frac{16E_{Cj} \langle N_{mj}^2 \rangle}{\hbar \omega_m} \end{aligned} \quad (1.31)$$

where we have introduced the Josephson charging energy $E_{Cj} = \frac{e^2}{2C_j}$, with C_j being the self-capacitance of the j -th Josephson junction.

The Hamiltonian of a multimode system with N_{JJ} Josephson junctions or Josephson dipoles is given by a combination of a linear component and a nonlinear component written in terms of a power series in the phase operators φ_j [103]

$$\begin{aligned} \hat{H} &= \hat{H}_{\text{lin}} + \hat{H}_{\text{nlin}} \\ &= \sum_{m=1}^{N_M} \hbar \omega_m \hat{a}_m^\dagger \hat{a}_m + \sum_{j=1}^{N_{JJ}} \sum_{p=4}^{\infty} c_{jp} E_j \hat{\varphi}_j^p \end{aligned} \quad (1.32)$$

$$\hat{\varphi}_j = \sum_{m=1}^{N_M} \varphi_{mj} (\hat{a}_m + \hat{a}_m^\dagger) \quad (1.33)$$

where N_M is the number of modes and the c_{jp} are given by

$$c_{jp} = \begin{cases} \frac{(-1)^{p/2+1}}{p!}, & p \text{ even} \\ 0, & p \text{ odd} \end{cases} \quad (1.34)$$

1.3.5 3D Transmons

The techniques described above were developed to model 3D structures, but what are these 3D structures and why did they emerge when there was reason to believe that 2D structures offer a straightforward path to scalability in superconducting circuit-based quantum computers? To address the first question, we review part of the historical progression of 3D qubits, starting with the first 3D transmon [5].

This first 3D transmon resembled the rectangular cavity in Figure 1.11, with a slight modification—the qubit chip was centered along the length of the cavity to maximize the coupling between the qubit and the fundamental TE_{101} mode used for readout. Later iterations of the rectangular design [104] shifted the location of the qubit slightly off-center to couple to the readout mode and the next highest mode, the TE_{102} mode, referred to as the *storage mode*, that was used in early experiments to stabilize integer photon number Fock states using engineered dissipation [51] among other demonstrations of cavity-based cQED.

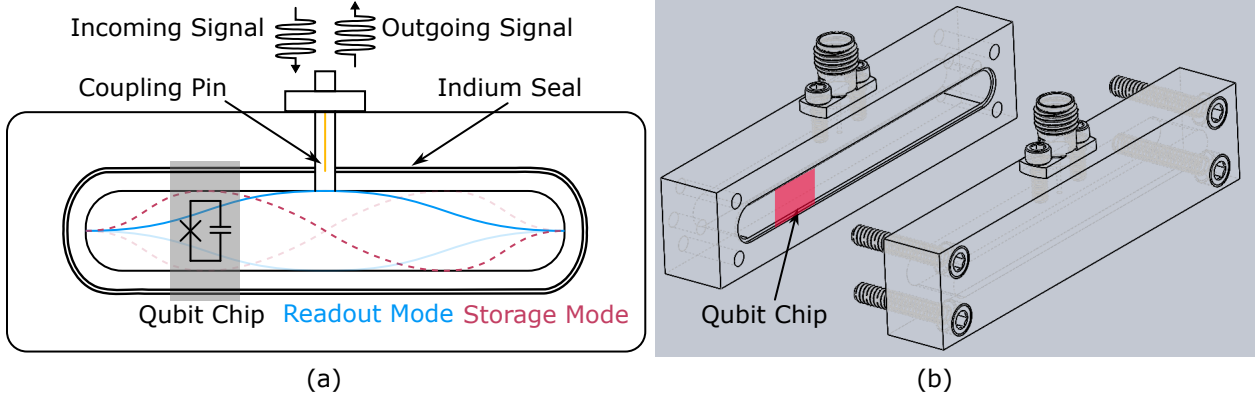


Figure 1.11 3D transmon in a rectangular cavity [5, 6] including the location of the nodes and antinodes of the lowest frequency cavity modes TE_{101} and TE_{102} in (a) and an exploded view of the assembly to show the two halves of the cavity separated along the E-plane, where currents flow parallel to seam, minimizing seam losses.

Compared to the planar transmons, the 3D implementations have much larger capacitor pads to compensate for the reduced coupling between the transmon dipole moment and the cavity electric field. These larger pads move the qubit fields away from the surface and into the bulk of the substrate and vacuum, reducing its sensitivity to interface losses and surface two level system (TLS) loss, discussed in Section 1.5.4. The rectangular cavity design also has an E-plane seam between the two cavity halves in Figure 1.11 (b), presenting the seam with parallel currents to minimize seam loss.

Subsequent iterations of 3D transmons used a $\lambda/4$ superconducting reentrant post cavity, where the fields of the fundamental mode are confined to the region near the top of the post, falling off exponentially above and below the top of the post. With a lid at the top of the cavity where the fields are exponentially attenuated, this was one of the first cavities to have a seamless design, where the currents at the seam are negligible [105]. Similar to the rectangular design, the transmon dipole moment is oriented parallel to the radial electric field between the post and the cavity wall.

Another seamless design involved intersecting drill holes to define rectangular and, in principle, arbitrary shaped cavities in the overlapping hole regions [106]. The holes are of a radius and a depth such that, away from the overlapping regions, the field is evanescent in those sub-cutoff cylindrical cavities, similar to the reentrant cavity with negligible seam loss.

1.4 Tunable Couplers

Quantum computers are limited by their two qubit gate performance, regardless of their physical realization. Early coupling schemes of superconducting qubits used fixed capacitive or mutual inductive coupling between qubits.

To perform gates, either the qubit frequencies were tuned in resonance with one another and energy was resonantly exchanged between them or a control qubit was driven at the resonance frequency of a target, enacting the so-called cross-resonance gates [107]. Although the hardware requirements for cross resonance gates are much lower than their tunable coupling counterparts, the latter continues to outperform the former in gate speeds and fidelities.¹⁰ There is a tradeoff between gate speed and qubit coherence, with increased tunability there is an increase in the number of control lines and loss mechanisms from flux or charge used to control the tunable element compared with fixed coupling schemes.

In Figure 1.12, we summarize several recent tunable coupler architectures in both 2D superconducting circuits and 3D superconducting cavities. As expected, the general trend over time is towards higher gate fidelity, or lower gate infidelity (1 - fidelity), and an increasing number of gate operations. We will return to this figure when considering the three coupling modalities in the next section, highlighting the galvanic couplers and capacitive couplers which this thesis presents novel designs for both.

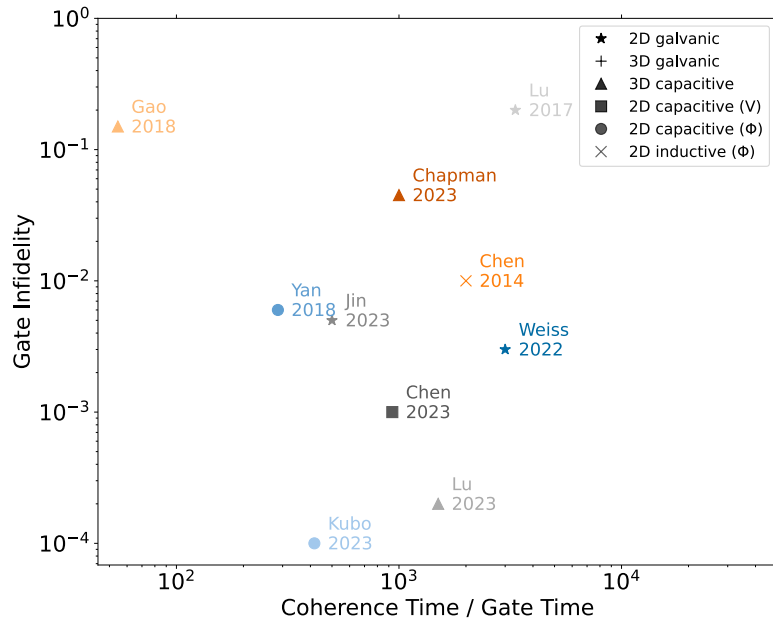


Figure 1.12 Comparison of tunable coupler two qubit gate fidelities as a function of the number of expected operations in a coherence time (coherence time / gate time). Labels correspond to the following references: Chen 2014 [7], Lu 2017 [8], Gao 2018 [9], Yan 2018 [10], Weiss 2022 [11], Chapman 2023 [12], Jin 2023 [13], Chen 2023 [14], Kubo 2023 [15], Lu 2023 [16].

¹⁰We separate gate speed from fidelity here, as a figure of merit when evaluating quantum computing platforms with disparate, dominant error models as the number of operations performed before the quantum state has dissipated or dephased is a more fair comparison between different architectures.

1.4.1 2D Systems

We start with a brief survey of the 2D coupler landscape, discussing the advantages and disadvantages of the three coupling types. In Figure 1.13, we give three example circuits illustrating coupling between two fixed frequency or tunable frequency transmon qubits. Figure 1.12 subdivides the coupling types based on the control signals used (V for voltage or charge and Φ for flux bias or current). This distinction is necessary to separate the errors induced by stray control line coupling, charge and flux noise on the control line, and noise seen by the individual qubits. Table 1.3 organizes the coupling types and control signals, along with the form of the physical interaction Hamiltonian between charge or flux degrees of freedom.

1.4.2 Operating Principles and Coupler Taxonomy

The operating principles of the three coupler types are summarized as follows. A capacitive coupler of the form drawn in Figure 1.13 mediates a charge-charge interaction between qubits in contact with an effective capacitor. The capacitance is tuned by applying a gate voltage to a superconducting-semiconducting (super-semi) structure or threading magnetic flux through a SQUID that is itself capacitively coupled to the two qubits. The mutual inductive coupler is a superconducting loop interrupted by one or more Josephson junctions¹¹ that couples nearby qubits by mutual inductances between the coupler and two qubits. Threading a magnetic flux through the superconducting loop modifies the coupling between the qubits and coupler, modifying the coupling between the qubits.

The capacitive coupling type leads to purely charge-charge like interactions and the inductive coupling leads to flux-flux interactions. In both flux-driven couplers, the inductive and capacitive couplers in the first and third lines of Table 1.3, the coupler and connected qubits are susceptible to stray magnetic fields and $1/f$ -like flux noise on the coupler control line. The purely charge-driven coupler is only sensitive to charge noise on the control line, but charge noise sensitivity is exponentially suppressed in transmon qubits, as was discussed in Section 1.2.5. In Chapter 2, we will present a coupler design with the same materials as [14], with estimates of its coherence limits based on detailed multiscale modeling of the semiconductor physics, electrostatics of the coupler itself, and the full-wave electromagnetic behavior of the coupler embedded in a typical two-transmon qubit microwave circuit [48].

In the galvanic coupler, due to details of the geometry in [8], both charge and flux interactions are present.

¹¹A superconducting loop interrupted by one junction is an rf-SQUID and a loop interrupted by two Josephson junctions is a dc-SQUID. See [67] for a complete treatment of the theory, operation, and applications of SQUIDs.

The consequences of this type of coupling are highlighted in [8]: (1) stronger coupling relative to purely inductive or capacitive coupling by currents shared between the qubit and cavity, (2) an interaction that combines both red and blue sidebands, aptly named the “purple” sideband with higher fidelity in stabilizing states than either sideband enacted alone, and (3) the possibility of realizing non-stoquastic Hamiltonians, whose ground states cannot be easily simulated with quantum Monte Carlo¹² [108].

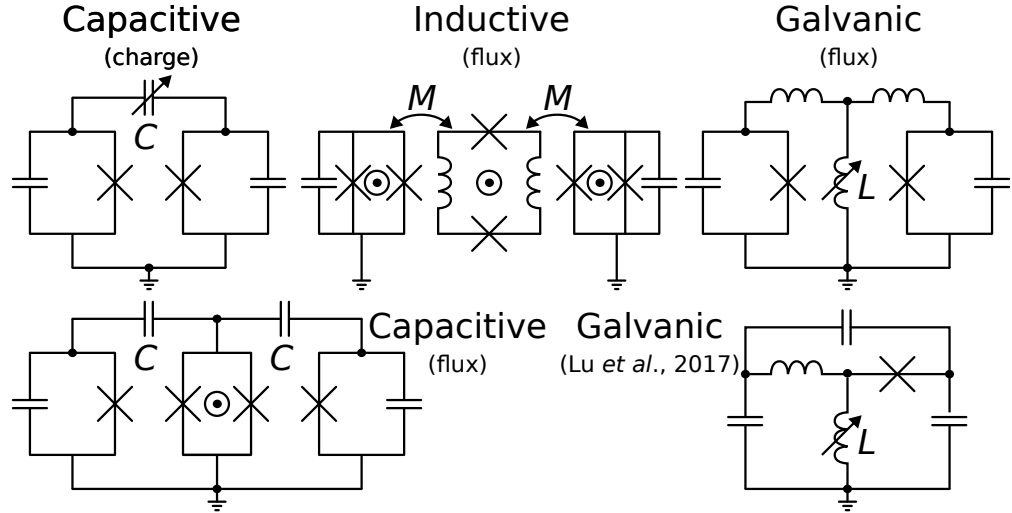


Figure 1.13 2D tunable coupler types.

To generate the red and blue sidebands, or any parametric process for that matter, it is helpful to review rotating frame transformations. Given a Hamiltonian describing a circuit with two nodes corresponding to two nodal flux variables ϕ_1 and ϕ_2 , couplings in both charge and flux as in the last row of Table 1.3, and all Josephson junctions replaced by linear inductors for simplicity, we have

$$\hat{H} = \frac{1}{2} (L_1^{-1} \phi_1^2 + L_2^{-1} \phi_2^2 + C_1^{-1} q_1^2 + C_2^{-1} q_2^2 + 2M_{12}\phi_1\phi_2 + 2C_{12}^{-1}q_1q_2) \quad (1.35)$$

For the sake of introducing the rotating frame transformation and reviewing the mechanics of driving red and blue sidebands rather than dwelling on the procedure of constructing the Hamiltonian from a circuit Lagrangian, we assert that the charges and fluxes are canonically conjugate, i.e. $[\hat{\phi}_j, \hat{q}_k] = i\hbar\delta_{jk}$ and they can be represented with bosonic creation and annihilation operators, as in Section 1.2.1 ($\hat{\phi}_j = \phi_j^{\text{ZPF}} (\hat{a}_j + \hat{a}_j^\dagger)$, $\hat{q}_j = -iq_j^{\text{ZPF}} (\hat{a}_j - \hat{a}_j^\dagger)$) and rewrite (1.35) in terms of \hat{a}_j , \hat{a}_j^\dagger .

¹²Hamiltonians that cannot be simulated by classical methods such as quantum Monte Carlo are considered good candidates for quantum simulators that do not suffer from the Fermi sign problem as classical computers do.

The resulting Hamiltonian then takes the form

$$\begin{aligned}\hat{H} = & \sum_{j=1,2} \left\{ \left[L_j^{-1} (\phi_j^{\text{ZPF}})^2 + C_j^{-1} (q_j^{\text{ZPF}})^2 \right] (\hat{a}_j^\dagger \hat{a}_j + 1/2) \right. \\ & + \frac{1}{2} \left[L_j^{-1} (\phi_j^{\text{ZPF}})^2 - C_j^{-1} (q_j^{\text{ZPF}})^2 \right] (\hat{a}_j^2 + \hat{a}_j^{\dagger 2}) \Big\} \\ & + (M_{12} \phi_1^{\text{ZPF}} \phi_2^{\text{ZPF}} + C_{12}^{-1} q_1^{\text{ZPF}} q_2^{\text{ZPF}}) (\hat{a}_1^\dagger \hat{a}_2 + \hat{a}_1 \hat{a}_2^\dagger) \\ & + (M_{12} \phi_1^{\text{ZPF}} \phi_2^{\text{ZPF}} - C_{12}^{-1} q_1^{\text{ZPF}} q_2^{\text{ZPF}}) (\hat{a}_1 \hat{a}_2 + \hat{a}_1^\dagger \hat{a}_2^\dagger)\end{aligned}\quad (1.36)$$

Using the definitions of the zero point fluctuations from (1.11) and (1.10), $\phi_j^{\text{ZPF}} = (\hbar \omega_j L_j / 2)^{1/2}$, $q_j^{\text{ZPF}} = (\hbar \omega_j C_j / 2)$, $\omega_j = (L_j C_j)^{-1/2}$, we rewrite (1.36) in a more suggestive form

$$\begin{aligned}\hat{H} = & \sum_{j=1,2} \hbar \omega_j (\hat{a}_1^\dagger \hat{a}_1 + 1/2) + \frac{\hbar}{2} (\omega_1 \omega_2)^{1/2} \left[M_{12} (L_1 L_2)^{1/2} + C_{12}^{-1} (C_1 C_2)^{1/2} \right] (\hat{a}_1^\dagger \hat{a}_2 + \hat{a}_1 \hat{a}_2^\dagger) \\ & + \frac{\hbar}{2} (\omega_1 \omega_2)^{1/2} \left[M_{12} (L_1 L_2)^{1/2} - C_{12}^{-1} (C_1 C_2)^{1/2} \right] (\hat{a}_1 \hat{a}_2 + \hat{a}_1^\dagger \hat{a}_2^\dagger) \\ = & \sum_{j=1,2} \hbar \omega_j (\hat{a}_1^\dagger \hat{a}_1 + 1/2) + \hbar g_{\text{BS},12} (\hat{a}_1^\dagger \hat{a}_2 + \hat{a}_1 \hat{a}_2^\dagger) + \hbar g_{\text{TMS},12} (\hat{a}_1 \hat{a}_2 + \hat{a}_1^\dagger \hat{a}_2^\dagger)\end{aligned}\quad (1.37)$$

where we identify the beam splitter g_{BS} and two mode squeezing rates g_{TMS} . We note that the $(\hat{a}_j^2 + \hat{a}_j^{\dagger 2})$ single mode squeezing terms exactly canceled with each other and control of M_{12} , C_{12}^{-1} could cancel the beam splitter or two-mode squeezing terms or give couplings that are negative [8].

Table 1.3 2D coupler types, control signals, and interaction Hamiltonians

Coupling type	dc bias	ac bias	\hat{H}_{int}	Reference
Capacitive	flux	flux	$\frac{1}{2} C_{12}^{-1} q_1 q_2$	Yan et al. (2018) [10]
Capacitive	charge	charge	$\frac{1}{2} C_{12}^{-1} q_1 q_2$	Chen et al. (2023) [14]
Inductive	flux	flux	$\frac{1}{2} M_{12} \phi_1 \phi_2$	Chen et al. (2014) [7]
Galvanic	flux	flux	$\frac{1}{2} M_{12} \phi_1 \phi_2 + \frac{1}{2} C_{12}^{-1} q_1 q_2$	Lu et al. (2017) [8]

1.4.3 Parametric Modulation

Next, we consider modulating the inductive and capacitive couplings M_{12} and C_{12}^{-1} in time as $M_{12} \rightarrow \bar{M}_{12} + \delta M_{12} \sin(\omega_{\text{sb}} t)$ and $C_{12}^{-1} \rightarrow \bar{C}_{12}^{-1} + \delta C_{12}^{-1} \sin(\omega_{\text{sb}} t)$ which, in turn, modulates the beam splitter and two mode squeezing interaction strengths. The δ 's indicate the modulation amplitudes, treated as small perturbations to the dc values \bar{M}_{12} and \bar{C}_{12}^{-1} .

Expanding $g_{\text{BS},12}$ and $g_{\text{TMS},12}$ about $M_{12} = \bar{M}_{12}$ and $C_{12}^{-1} = \bar{C}_{12}^{-1}$ to first order^{13,14}

$$\begin{aligned}
g_{\text{BS},12}(M_{12}, C_{12}^{-1}) &\approx g_{\text{BS},12}(\bar{M}_{12}, \bar{C}_{12}^{-1}) + \delta M_{12} \sin(\omega_{\text{sb}}t) \frac{\partial g_{\text{BS},12}}{\partial M_{12}} \Big|_{M_{12}=\bar{M}_{12}} \\
&\quad + \delta C_{12}^{-1} \sin(\omega_{\text{sb}}t) \frac{\partial g_{\text{BS},12}}{\partial C_{12}^{-1}} \Big|_{C_{12}^{-1}=\bar{C}_{12}^{-1}} \\
&= \frac{1}{2} (\omega_1 \omega_2)^{1/2} \left\{ \left[\bar{M}_{12} (L_1 L_2)^{1/2} + \bar{C}_{12}^{-1} (C_1 C_2)^{1/2} \right] \right. \\
&\quad \left. + \left[\delta M_{12} (L_1 L_2)^{1/2} + \delta C_{12}^{-1} (C_1 C_2)^{1/2} \right] \sin(\omega_{\text{sb}}t) \right\} \\
&= \bar{g}_{\text{BS},12} + \epsilon_{g_{\text{BS},12}} \sin(\omega_{\text{sb}}t)
\end{aligned} \tag{1.38}$$

Similar algebra gives the two mode squeezing strength as

$$\begin{aligned}
g_{\text{TMS},12}(M_{12}, C_{12}^{-1}) &\approx \frac{1}{2} (\omega_1 \omega_2)^{1/2} \left\{ \left[\bar{M}_{12} (L_1 L_2)^{1/2} - \bar{C}_{12}^{-1} (C_1 C_2)^{1/2} \right] \right. \\
&\quad \left. + \left[\delta M_{12} (L_1 L_2)^{1/2} - \delta C_{12}^{-1} (C_1 C_2)^{1/2} \right] \sin(\omega_{\text{sb}}t) \right\} \\
&= \bar{g}_{\text{TMS},12} + \epsilon_{g_{\text{TMS},12}} \sin(\omega_{\text{sb}}t)
\end{aligned} \tag{1.39}$$

Now we introduce a rotating frame transformation that is a generalization of Eq. (8) of the supplemental information of [109] defined by the unitary operator $\hat{U}(t) = \exp \left[i \sum_{j=1,2} (\omega_j t) \hat{a}_j^\dagger \hat{a}_j \right]$ acting on the Hamiltonian in (1.37) with the time-dependent couplings as in [109, 110]

$$\hat{H}(t) \rightarrow \hat{H}' = \hat{U}(t) \hat{H}(t) \hat{U}(t)^\dagger - i\hbar \hat{U}(t) \partial_t \hat{U}^\dagger(t) \tag{1.40}$$

To ease the calculation of (1.40), we write down the action of \hat{U} on the operators \hat{a}_j , \hat{a}_j^\dagger using the Baker-Campbell-Hausdorff formula and calculate the Berry's phase term $-i\hat{U}(t)\partial_t \hat{U}(t)$ below

$$\begin{aligned}
\hat{U}(t) \hat{a}_k \hat{U}^\dagger(t) &= e^S \hat{a}_k e^{-S} = \hat{a}_k + [S, \hat{a}_k] + \frac{1}{2} [S, [S, \hat{a}_k]] + \dots +, \quad S = \sum_{j=1,2} \omega_j \hat{a}_j^\dagger \hat{a}_j \\
&= \hat{a}_k + (-i\omega_k t) \hat{a}_k + \frac{1}{2} (-i\omega_k t)^2 \hat{a}_k + \dots + = \hat{a}_k e^{-i\omega_k t}
\end{aligned} \tag{1.41}$$

$$-i\hat{U}(t)\partial_t \hat{U}^\dagger(t) = - \sum_{j=1,2} \hbar \omega_j \hat{a}_j^\dagger \hat{a}_j \tag{1.42}$$

¹³In this example, $g_{\text{BS},12}$ and $g_{\text{TMS},12}$ are linear in M_{12} and C_{12}^{-1} . We can evaluate these derivatives analytically and higher order derivatives vanish, as well as mixed derivatives such as $\partial^2 g_{\text{BS}(\text{TMS}),12} / \partial M_{12} \partial C_{12}^{-1} = 0$. Of course, this does not hold in the general case, as we will see in the field overlap integral method presented in Chapter 3.

¹⁴There are alternative ways to express coupler and frequency modulation, separately, which are discussed at length in Lu's thesis [77] and elsewhere [109–111]. We chose this approach because in Chapter 3, we found that this scheme works in the case where both the mode frequencies and couplings are modulated simultaneously. In fact, we could perform a change of basis where that is the case in this setting, but chose this basis instead to focus on the coupling modulation.

Applying the transformation in (1.40) to (3.16), we see that the Berry's phase contribution in (1.42) cancels the resonant term, up to the ground state energy $\sum_{j=1,2} \hbar\omega_j/2$ which we drop here and arrive at the modulated Hamiltonian in the rotating frame

$$\begin{aligned}\hat{H}/\hbar &= (\bar{g}_{\text{BS},12} + \epsilon_{g_{\text{BS},12}} \sin(\omega_{\text{sb}}t)) \left(\hat{a}_1^\dagger \hat{a}_2 e^{-i(\omega_2 - \omega_1)t} + \text{h.c.} \right) \\ &\quad + (\bar{g}_{\text{TMS},12} + \epsilon_{g_{\text{TMS},12}} \sin(\omega_{\text{sb}}t)) \left(\hat{a}_1 \hat{a}_2 e^{i(\omega_2 + \omega_1)t} + \text{h.c.} \right)\end{aligned}\quad (1.43)$$

Setting the modulation frequency ω_{sb} to the sum or difference frequency ($\omega_2 \pm \omega_1$) makes either the two mode squeezing term or the beam splitter term stationary, with the remaining terms oscillating rapidly relative to the stationary terms, averaging to zero over time. The terminology of red and blue sidebands is evident, as the terms with phase factors containing the difference frequencies (longer wavelength) are referred to as "red" and the terms with sum frequency phase factors (shorter wavelength) are labeled "blue." We note that with this type of coupling it is possible to engineer multiple drives to simultaneously activate both processes, with a multi-tone modulation scheme.

1.4.4 3D Systems

Many of the concepts from the 2D tunable couplers transfer to 3D systems, with the physical implementation and packaging approaches significantly varying. We will also discuss how the form of the nonlinearity plays a role in realizing a particular process such as beam splitting. In Table 1.4, we organize the three 3D couplers in Figure 1.14 by their coupling, control signals, and the form of the driving scheme used to induce parametric operations. Unlike in the 2D case where the tunable couplers were used as general purpose coupling elements or to stabilize arbitrary quantum states, couplers in 3D have been used primarily as high fidelity beam splitters. The primary motivations behind focusing on beam splitting at this point in 3D cavity development are (1) to demonstrate high fidelity SWAPs and entangling gates for digital and continuous variable quantum computing and (2) to support dual rail qubit encodings [112, 113].

In Table 1.3, the coupling types are limited to capacitive and inductive/capacitive, depending on how one defines coupling. There are practical reasons for the lack of inductive or galvanic coupling in 3D. Until recently, the most obvious and simplest way to couple a transmon or another nonlinear Josephson junction-based or kinetic inductance-based object to electric fields in a cavity with cylindrical symmetry is by an antenna or dipole-like coupling. The analogy with cavity QED and 2D capacitive coupling is clear and straightforward to implement: orienting the transmon or other nonlinear object parallel to the electric field of a cavity mode provides sufficiently strong coupling, with a clear trade-off between the coupling strength and dielectric loss depending on the insertion depth of the chip into the cavity.

In short, the deeper the chip protrudes into the cavity field, the stronger the coupling between the coupler and the cavity, yet there is a commensurate increase in the dielectric loss with insertion depth.¹⁵

Table 1.4 3D coupler types, control signals, and driving schemes

Coupling type	dc bias	ac bias	Driving Scheme	Reference
Capacitive	-	charge	2-tone, 4 wave mixing	Gao et al. (2018) [9]
Capacitive	flux	charge	1-tone, 3 wave mixing	Chapman et al. (2023) [12]
Inductive/Capacitive	flux	charge	2-tone	Lu et al. (2023) [16]

The beam splitter in the first row of Table 1.4 differs from the 2D couplers discussed in 1.4.2 in that it does not have a dc bias. This early realization of a microwave beam splitter used a fixed frequency transmon driven with two charge drives with frequencies ω_1 and ω_2 . The beam splitter interaction is activated when the difference between the two drives is equal to the difference between the two cavity frequencies by a 4 wave mixing (4WM) process inherent in the quartic nonlinearity of the Josephson junction cosine potential of the transmon coupler. In this driving scheme, the beam splitter coupling $g(t) = \sqrt{\chi_{ac}\chi_{bc}}\xi_1(t)\xi_2(t)$, where χ_{jc} is the cross-Kerr coupling between the j -th cavity mode and the coupler and $\xi_j(t)$ is the j -th classical, time-varying drive amplitude. Although the coupling strength is proportional to the drive strength, the cross-Kerr's are small relative to the capacitive or inductive coupling achieved in 2D systems [9]. The typical g 's achieved in 2D devices are on the order of hundreds of MHz, whereas the 3D beam splitter had a g on the order of tens of kHz (a few μ s in time to enact one beam splitter operation), which was large compared to the bare coupling between the cavities and the coherence time of the cavities was hundreds of μ s [9].

Following the transmon-based beam splitter, a similar capacitive coupling between a Superconducting Nonlinear Asymmetric inductive eLement (SNAIL) and two cavities achieved a beam splitter rate on the order of hundreds of kHz, with the number of operations relative to the coherence time exceeding 10^3 [12], more than an order of magnitude improvement over [9]. The SNAIL enables a 3 wave mixing (3WM) process when dc-biased such that only odd terms of its Josephson potential are enhanced and unwanted, parasitic fourth-order processes are suppressed. Applying a single charge drive to the coupler at the difference frequency of the cavities activates the beam splitter operation as opposed to two tones in the 4WM transmon coupler. The combination of higher coherence cavities, a faster beam splitter rate, suppression of unwanted fourth order processes, and single tone rather than two tone control sets this coupler [12] apart from the previous iteration with a transmon [9].

¹⁵There is another regime relevant to cavity control, where the coupling is comparable to the loss rates of the qubit and cavity, the weak dispersive regime. Under these conditions, the echoed conditional displacement gate converts the weak 4 wave mixing interaction into an enhanced 3 wave mixing, circumventing both the interaction limit of $2\pi/\chi$ while reducing the participation of the transmon and its substrate with the cavity fields [114].

The form of coupling, capacitive, as in all other 3D transmon and related 3D qubit implementations, remained unchanged until a recent experiment explored an inductive coupling scheme.

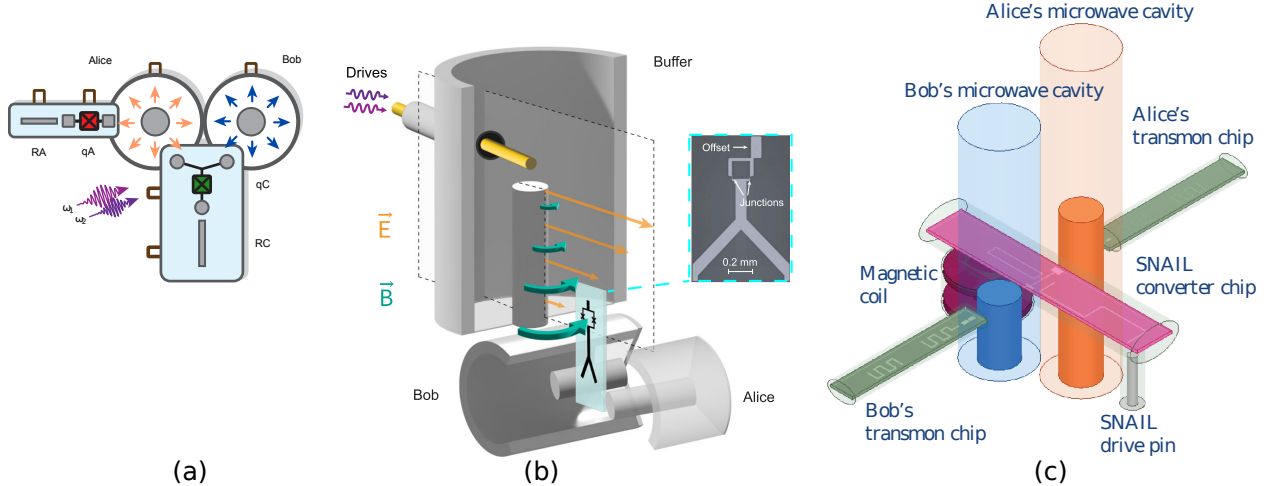


Figure 1.14 State of the art 3D, parametrically activated microwave beam splitters, reproduced with permission from (a) two-tone, four-wave mixing, transmon controlled beam splitter [9], (b) differentially driven SQUID coupler [16], and (c) a single tone, three-wave mixing SNAIL coupler [12].

Lu et al. [16] devised a tunable coupler where a SQUID is located near the bottom of and oriented parallel to the axis of a reentrant $\lambda/4$ post cavity. This orientation serves two purposes: first, to allow magnetic fields from the cavity to thread the SQUID and thereby supply an ac flux bias with a charge drive and second, to orient the SQUID dipole moment to be perpendicular to the electric field of the cavity, minimizing Purcell losses. The lowered position of the SQUID in the cavity takes full advantage of the asymmetry in electric and magnetic field intensities in $\lambda/4$ post cavities, where the electric fields are minimized and the magnetic fields are maximized near the bottom of the cavity, as illustrated in Figure 1.14 (b).

There is additional parity protection in this design, as the common mode of the SQUID couples to the cavities, but the magnetic fields only couple to the differential mode. By common and differential modes, we refer to the orientation of the currents across the two Josephson junctions of the SQUID. The common mode refers to the parallel current orientation and the differential mode refers to the antiparallel current orientation. This separation of coupler and “accuator” modes minimizes coupler *heating* or populating the coupler mode with photons from the drive when performing beam splitter operations [16].

To activate beam splitter interactions, the differential mode of the SQUID is driven with two tones that are detuned by the same amount as the detunings between the two coupled cavity mode frequencies. The buffer cavity that supplies the ac magnetic fields to the SQUID is designed to have a bandwidth close to the detuning of the cavities and the coupler mode is placed much higher in frequency than the buffer cavity and the cavities involved in the beam splitter operation to further suppress Purcell loss [94]. Finally, compared to the two other beam splitters discussed above, this implementation achieved a beam splitter rate on the order of 5 MHz, a significant improvement over the previous iterations, yet well below the highest equivalent rates achieved in 2D systems.

The steady improvement in coupling strengths achieved with 3D beam splitters over the last five years is impressive, given that the strongest known coupling from the 2D superconducting qubit community has not been explored. In Chapter 4, we present a coupler that borrows features of the differentially driven SQUID coupler and the galvanic 2D coupler, both developed by the same lead author. We will highlight the strengths and challenges of this design compared to previous 3D designs and 2D designs, as well as apply the field analysis techniques presented in Chapter 3 to estimate beam splitter, single-mode, and two-mode squeezing rates.

1.5 Superconducting Microwave Resonators

This section attempts to consolidate the relevant theoretical and experimental techniques related to the investigation of materials loss mechanisms in superconducting circuits and cavities.

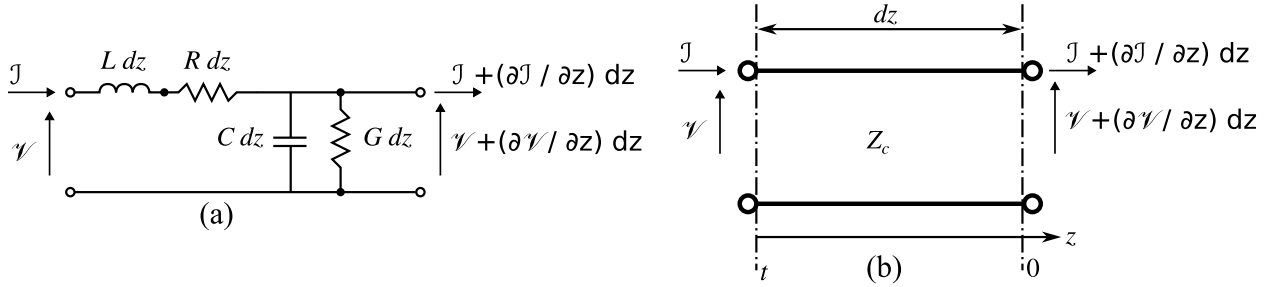


Figure 1.15 Transmission line circuit models. (a) Distributed element circuit model with voltages and currents and (b) the equivalent transmission line circuit shorthand.

1.5.1 Microwave Circuit Theory

We would be remiss if there was no coverage of microwave circuit theory, namely the tools that this thesis references in both the tunable coupler design and loss measurement thrusts. There are a number of texts that give a more thorough treatment than what can be covered here, including the defacto Pozar [115], its predecessor Collin [116], the lesser known Harvey [117], and many other others.

This section will follow Chapter 3 and 4 of Collin [118, 119], introducing impedances, admittances, and scattering parameters related to passive, linear networks. These concepts will follow from the transmission line circuit model, which we will use to derive the Telegrapher's equations and introduce voltage and current phasors (see V^\pm in Figure 1.15 (a)).

Applying Kirchhoff's voltage law to the loop in Figure 1.15 (a), including the input voltage, series resistor, series inductor, and output voltage gives

$$\begin{aligned}\mathcal{V} &= R\mathcal{I}dz + L\frac{\partial\mathcal{I}}{\partial t}dz + \left(\mathcal{V} + \frac{\partial\mathcal{V}}{\partial z}dz\right) \\ -\frac{\partial\mathcal{V}}{\partial z} &= R\mathcal{I} + L\frac{\partial\mathcal{I}}{\partial t}\end{aligned}\quad (1.44)$$

where in the second line of (1.44) we divided through by dz , $dz \rightarrow 0$. Kirchhoff's current law applied to the shunt elements gives

$$\begin{aligned}\mathcal{I} &= G\mathcal{V}dz + C\frac{\partial\mathcal{V}}{\partial t}dz + \left(\mathcal{I} + \frac{\partial\mathcal{I}}{\partial z}dz\right) \\ -\frac{\partial\mathcal{I}}{\partial z} &= G\mathcal{V} + C\frac{\partial\mathcal{V}}{\partial t}\end{aligned}\quad (1.45)$$

Differentiating (1.44) by z and (1.45) by t gives the pair of second order partial differential equations

$$-\frac{\partial^2\mathcal{V}}{\partial z^2} = R\frac{\partial\mathcal{I}}{\partial z} + L\frac{\partial^2\mathcal{I}}{\partial t\partial z}\quad (1.46)$$

$$-\frac{\partial^2\mathcal{I}}{\partial z\partial t} = G\frac{\partial\mathcal{V}}{\partial t} + C\frac{\partial^2\mathcal{V}}{\partial t^2}\quad (1.47)$$

Eliminating the mixed derivative terms and taking \mathcal{I} to be a continuous, twice differentiable function¹⁶

$$\frac{\partial^2\mathcal{V}}{\partial z^2} = RG\mathcal{V} + (RC + LG)\frac{\partial\mathcal{V}}{\partial t} + LC\frac{\partial^2\mathcal{V}}{\partial t^2}\quad (1.48)$$

As we alluded to above, \mathcal{I} satisfies the same equation as \mathcal{V} and can be derived by differentiating (1.44) by t and (1.45) by z and eliminating the mixed derivative term to find

$$\frac{\partial^2\mathcal{I}}{\partial z^2} = RG\mathcal{I} + (RC + LG)\frac{\partial\mathcal{I}}{\partial t} + LC\frac{\partial^2\mathcal{I}}{\partial t^2}\quad (1.49)$$

¹⁶We can exchange the order of partial derivatives, which is a valid assumption as we will see it is a solution to the same second order partial differential equation as \mathcal{V} .

We use the ansatz for $\mathcal{V} = \text{Re}\{Ve^{i\omega t}\}$ and $\mathcal{I} = \text{Re}\{Ie^{i\omega t}\}$, with i the imaginary unit $i = \sqrt{-1}$, and substitution of these expressions into the first order partial differential equations, (1.44) and (1.45) gives

$$-\frac{\partial V}{\partial z} = (R + i\omega L) I \quad (1.50)$$

$$-\frac{\partial I}{\partial z} = (G + i\omega C) V \quad (1.51)$$

The phasors V and I are complex, time-independent functions of z that are themselves linear combinations of left and right propagating waves of the form

$$V = V^+ e^{-\gamma z} + V^- e^{\gamma z} \quad (1.52)$$

$$I = I^+ e^{-\gamma z} - I^- e^{\gamma z} \quad (1.53)$$

where $\gamma = \alpha + i\beta$ is the complex propagation constant with α the attenuation constant and β the phase constant. Substituting the expression for the voltage in terms of the phasors from (1.52) into the wave equation in (1.48) and eliminating the common $e^{j\omega t}$ factors gives

$$[\gamma^2 - (RG - \omega^2 LC) - i\omega(RC + LG)] (V^+ e^{-\gamma z} + V^- e^{\gamma z}) = 0 \quad (1.54)$$

For arbitrary V^\pm the bracketed expression vanishes and the propagation constant is equal to

$$\begin{aligned} \gamma &= [RG - \omega^2 LC + i\omega(RC + LG)]^{1/2} \\ &= [(R + i\omega L)(G + i\omega C)]^{1/2} \end{aligned} \quad (1.55)$$

From the expressions for the propagation constant, the voltage and current phasors, and first order equations for V and I , (1.50) and (1.51), the voltage and current amplitudes are related by

$$I = \frac{\gamma}{R + i\omega L} (V^+ e^{-\gamma z} - V^- e^{\gamma z}) \quad (1.56)$$

Here we have shown how the full wave problem, in terms of electric and magnetic fields, reduces to a distributed element description in terms of V^\pm , I^\pm whose ratios are the characteristic impedance of the line, i.e. $Z_c = V^+/V^- = I^+/I^- = [(R + i\omega L)/(G + i\omega C)]^{1/2}$, $Z_c = (L/C)^{1/2}$ in the lossless case.

If now we consider an N -port network, with a port defined as a pair of conducting terminals, the phasor¹⁷ currents and voltages I_j , V_j at the j -th port are related to the impedances Z_{ij} by

$$\begin{pmatrix} V_1 \\ V_2 \\ \vdots \\ V_N \end{pmatrix} = \begin{pmatrix} Z_{11} & Z_{12} & \dots & Z_{1N} \\ Z_{21} & Z_{22} & \dots & Z_{2N} \\ \vdots & \vdots & \ddots & \vdots \\ Z_{N1} & Z_{N2} & \dots & Z_{NN} \end{pmatrix} \begin{pmatrix} I_1 \\ I_2 \\ \vdots \\ I_N \end{pmatrix} \quad (1.57)$$

and $Y = Z^{-1}$ the admittance matrix, is related to the currents and voltages by

$$\begin{pmatrix} I_1 \\ I_2 \\ \vdots \\ I_N \end{pmatrix} = \begin{pmatrix} Y_{11} & Y_{12} & \dots & Y_{1N} \\ Y_{21} & Y_{22} & \dots & Y_{2N} \\ \vdots & \vdots & \ddots & \vdots \\ Y_{N1} & Y_{N2} & \dots & Y_{NN} \end{pmatrix} \begin{pmatrix} V_1 \\ V_2 \\ \vdots \\ V_N \end{pmatrix} \quad (1.58)$$

where the matrix elements of Z and Y are calculated by ratios of currents and voltages at ports i and j with the remaining ports either open or short circuit terminated, i.e.

$$Z_{ij} = \left. \frac{V_i}{I_j} \right|_{I_{j \neq k}=0} \quad (1.59)$$

$$Y_{ij} = \left. \frac{I_i}{V_j} \right|_{V_{j \neq k}=0} \quad (1.60)$$

In Section 1.3.1, we referenced impedance and admittance matrices to design superconducting circuits and study loss in superconducting resonators, but expound on them here for completeness. These quantities, namely the voltages and currents, are not easily measurable at microwave frequencies, but the amplitude and phase of transmitted and reflected waves can be obtained from instruments such as vector network analyzers. A third set of parameters described by the matrix S relate incident waves V^+ to scattered waves V^- in an N -port network by

$$\begin{pmatrix} V_1^+ \\ V_2^+ \\ \vdots \\ V_N^+ \end{pmatrix} = \begin{pmatrix} S_{11} & S_{12} & \dots & S_{1N} \\ S_{21} & S_{22} & \dots & S_{2N} \\ \vdots & \vdots & \ddots & \vdots \\ S_{N1} & S_{N2} & \dots & S_{NN} \end{pmatrix} \begin{pmatrix} V_1^- \\ V_2^- \\ \vdots \\ V_N^- \end{pmatrix} \quad (1.61)$$

Unlike in the impedance and admittance parameter conditions where all ports besides the port being excited are either open or short circuited, the scattering parameters are measured when all other ports besides the active port are terminated with a matched load. This is a preferred termination over open or short circuited terminations that are either not possible or undesirable for certain microwave devices.

¹⁷We will omit the phasor qualifier for the remainder of this chapter as it is understood that I and V refer to phasors.

The Z , Y , and S parameters all pertain to linear, passive networks used throughout this thesis, with nonlinear elements treated by separate means.¹⁸ There are generalizations of the S parameters, namely the X -parameters, that describe nonlinear devices. These parameters are particularly useful in the design and analysis of amplifiers and have recently entered the superconducting qubit and circuit communities in the design of near-quantum-limited, broadband parametric amplifiers [120].

1.5.2 Microwave Measurement Techniques

In the previous section, we introduced the theory of scattering parameters to preface a discussion of commonly performed transmission and reflection measurements. Vector network analyzers (VNAs) are the workhorse of these measurements, capable of measuring the N^2 matrix elements of the S -matrix in a passive, linear N -port network. Either S_{11} , the reflection coefficient of a single port network, or S_{21} the transmission coefficient of a two port network, are measured to extract the total (or loaded) Q_l , internal Q_i , and coupling (or external) Q_c quality factors of microwave resonators, as well as to characterize microwave circuits in general.

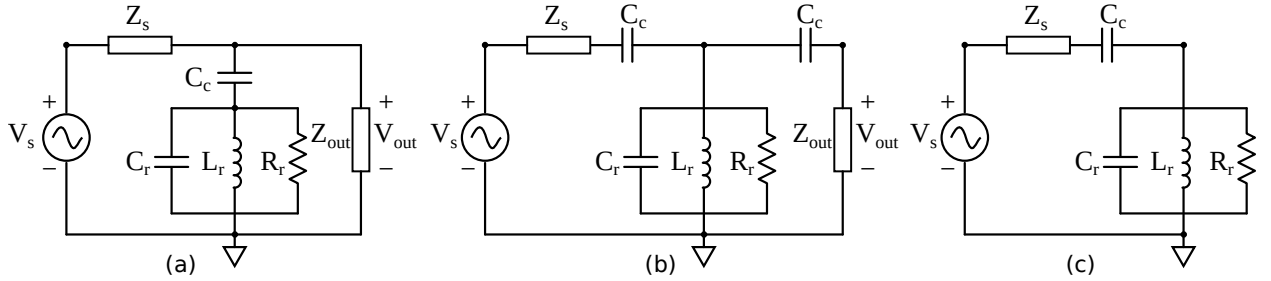


Figure 1.16 Equivalent resonator coupling networks. (a) Hanger mode, (b) transmission, and (c) single-port reflection mode. Based on and reproduced with permission from [17].

There are several models that describe the frequency response of a resonator circuit depending on the coupling geometry (See Figure 1.16) and the S -parameter being measured. The transmission and reflection coefficients, S_{21} and S_{11} , respectively, depend on the resonance frequency ω_0 , the quality factors, and a parameter describing the asymmetry of the resonance, i.e. the degree of departure of the lineshape of the resonance from a symmetric Lorentzian. Among these models is the diameter correction method (DCM), where the transmission coefficient is given by [121]

$$S_{21}(\omega) = (1 + \hat{\epsilon}) \left(1 - \frac{Q_l |\hat{Q}_c^{-1}| e^{i\phi}}{1 + 2iQ_l \frac{\omega - \omega_0}{\omega_0}} \right) \quad (1.62)$$

¹⁸See the black-box quantization [95] and energy participation ratio [103] methods in Sections 1.3.1 and 1.3.4

In (1.62) \hat{Q}_c is a complex expression related to the magnitude of the coupling quality factor Q_c and the phase angle capturing the asymmetry of the resonance. The complex factor $\hat{\epsilon}$ is a function of the input impedance of the total measurement circuit, including the resonator and its coupling to a transmission line [121]. In practice, it is assumed to be small in magnitude ($|\hat{\epsilon}| \ll 1$) and fit as a free parameter in the model. Figure 1.19 shows an example of this fit without the complex $(1 + \hat{\epsilon})$ prefactor. The loaded quality factor Q_l is related to the coupling and internal quality factor Q_i in this model by [121]

$$Q_l^{-1} = Q_i^{-1} + \operatorname{Re} \left\{ \hat{Q}_c^{-1} \right\} \quad (1.63)$$

This is analogous to the typical expression $Q_l^{-1} = Q_i^{-1} + Q_c^{-1}$ where all Q 's are real-valued and add as resistors in parallel, as losses (inverse quality factors) in this setting are additive. There are three coupling regimes, summarized in Table 1.5, with the critically coupled and undercoupled limits preferred for loss extraction experiments over the overcoupled limit. As we will discuss below, the error on the DCM fit of Q_i is a quadratic function of Q_i/Q_c , minimized at $Q_i/Q_c = 1$ and of a few percent in fractional error up to one order of magnitude above and below critical coupling [122].

Table 1.5 Coupling limits in resonators

Limit	Condition	Consequence
$Q_c \ll Q_i$	Overcoupled	Sensitivity to Q_c
$Q_c \sim Q_i$	Critically coupled	Equal Q_c, Q_i extraction
$Q_c \gg Q_i$	Undercoupled	Sensitivity to Q_i

Transmission measurements of coplanar waveguide (CPW) resonators are among the most common high-throughput measurements used in superconducting materials loss studies. We will discuss methods to improve the speed and accuracy of transmission measurements modeled by the DCM and the same model without the complex $(1 + \hat{\epsilon})$ prefactor, omitting techniques related to the other measurement modes in Figure 1.16. Recent work by Baity et al. [122] investigated the sensitivity of the DCM fit on the frequency point distribution in the $\operatorname{Im} \{S_{21}\}, \operatorname{Re} \{S_{21}\}$ complex plane as in the left panel of Figure 1.19. Baity et al. showed that a linear point distribution can lead to biases in the errors of the extracted Q_i values as the ratio between the linewidth $\kappa/2\pi = f_c/Q_l$ of the resonance and the span of the measurement δf exceeds approximately 18, i.e. when the span is more than 18 linewidths wide. Typical measurements with linear point distributions have spans of approximately 21 linewidths, ten on either side of the resonance with one near resonance, at high power and fewer as the power decreases and the linewidth increases until it saturates when the TLS loss saturates at powers on the order of a few photons per second.

Baity et al. considered the phase-frequency relationship that Gao [66] stated and Probst et al. [123] separately investigated

$$\theta(f) = \theta_0 + 2 \arctan(2Q_l(1 - f/f_c)) \quad (1.64)$$

$$f(\theta) = f_c \left(1 - \frac{1}{2Q_l} \tan\left(\frac{\theta - \theta_0}{2}\right) \right) \quad (1.65)$$

where the phase $(\theta - \theta_0) \in (-\pi, \pi)$ and θ_0 is chosen to be $\pi/32$ in the **scresonators** implementation of what is referred to as a homophasal point distribution [18]. This uniform distribution in phase, hence homophasal, leads to a uniform spacing of points in the complex plane of S_{21} . In Figure 1.17, we simulated three point distributions to illustrate the effect of the distributions on the error of the estimated Q_i . We added white Gaussian noise with a standard deviation of -20 dB to both the real and imaginary parts of the signal using a pseudorandom number generator with independent seeds for the two quadratures (real and imaginary parts).

A compromise between the full homophasal and the linear point distribution is shown in Figure 1.17 (b), where we have defined three linear segments (the lengths and locations of the segments are indicated in the shaded regions of the magnitude of S_{21}) of different point densities to approximate the homophasal distribution. This segmented sweep improves the error on the fit to Q_i compared to the linear point distribution and does not require knowledge of the loaded quality factor as in the homophasal point distribution. We recently became aware of similar segmented sweeps implemented by Satzinger et al. [124], where three linear frequency segments were used, two sparse segments off-resonance and one dense segment on-resonance.

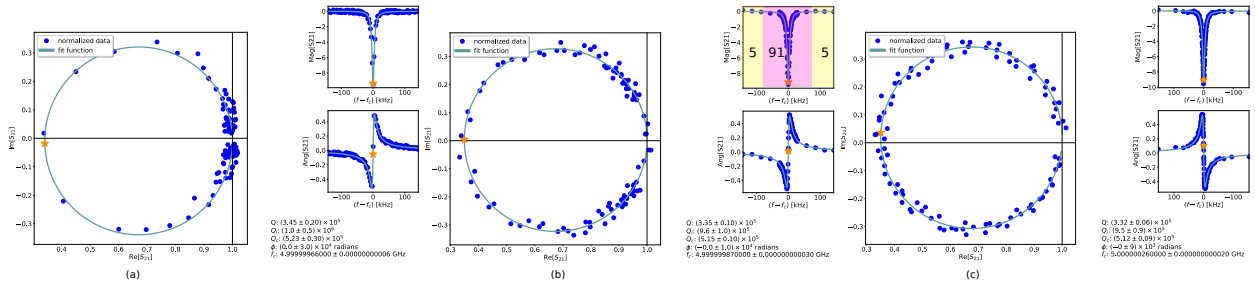


Figure 1.17 Simulated resonator responses. (a) Linear point distribution, (b) three segmented point distribution, (c) homophasal point distribution. Resonator parameters are $Q_i = 10^6$, $Q_c = 5 \times 10^5$, $f_c = 5$ GHz, $\phi = 0$.

Along with transmission measurements, there are reflection-based measurements involving single port devices where the same port acts as the input and output of the measurement.

Signals are routed to the device with a single cable, as in Figure 1.16 (c) or a circulator, a three-port non-reciprocal device as in Figure 1.18, that preferentially transmits signals between ports in the sequence $1 \rightarrow 2 \rightarrow 3 \rightarrow 1$.

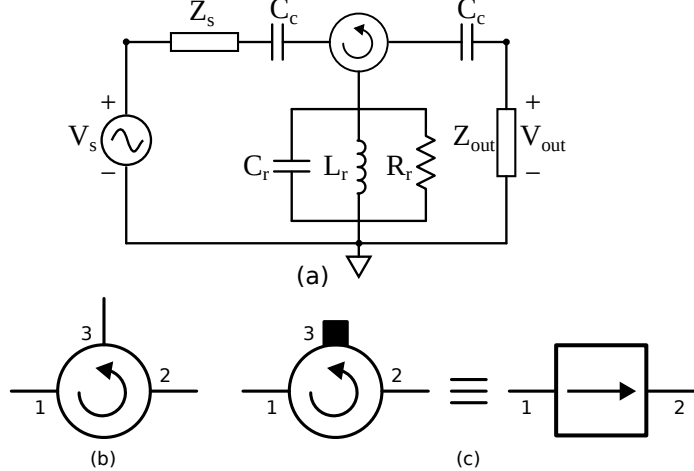


Figure 1.18 Circulators and isolators in microwave measurements. (a) A reflection mode measurement taken by measuring S_{21} with a circulator. (b) Three port circulator, (c) isolator and an equivalent circulator with its third port terminated by a 50Ω load (black filled square on port 3).

The ideal circulator scattering matrix is given by [115]

$$S_{\text{circ}} = \begin{pmatrix} 0 & 0 & 1 \\ 1 & 0 & 0 \\ 0 & 1 & 0 \end{pmatrix} \quad (1.66)$$

Often circulators contain an anisotropic ferrite material that presents incident electromagnetic waves with a different magnetic permeability, depending on the waves' direction of propagation. This difference in magnetic permeability leads to directional wave propagation and approximates the ideal circulator scattering parameters. The departures from this ideal include signals being transmitted in the reverse direction (quoted as isolation or the degree to which leakage does not occur), losses from resistive elements in the device, and variations in the frequency response that differ from the frequency-independent, ideal case in (1.66).

Recent work by Rieger et al. [125] showed that unaccounted for signal paths, e.g. signals propagating in the reverse direction of what a circulator is designed to support, can lead to interference between the forward and reverse signals, giving rise to Fano interference [126, 127]. The hallmark of Fano interference is an observed asymmetry in the lineshape of a resonance, which is accounted for in the DCM model by the phase angle ϕ .

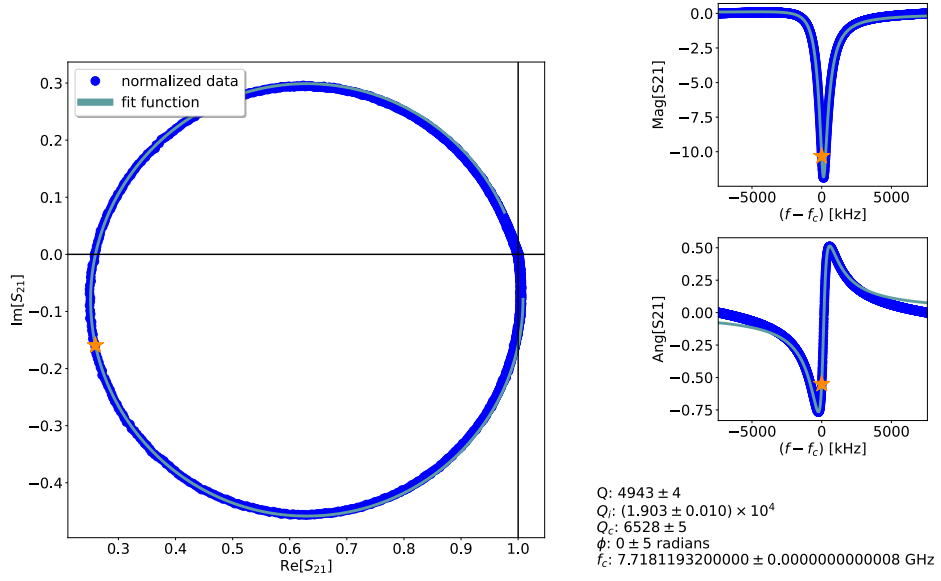


Figure 1.19 DCM fit using the `scresonators` software package [18] of an Al CPW patterned on InP by W. M. Strickland at New York University.

A model similar to the DCM describes the signal S_{21} measured with a circulator connected to a device in reflection-mode, referred to as the DCM reflection model [18]

$$S_{21}(\omega) = 1 - \frac{2Q_l/Q_c e^{i\phi}}{1 + 2iQ_l \frac{\omega - \omega_0}{\omega_0}} \quad (1.67)$$

1.5.3 Loss Mechanisms in Superconducting Resonators

Superconducting resonators, fabricated as monolithic 3D structures or integrated microwave circuits, are subject to the noise power spectral density of their microwave transmitter/receiver chain, surface and interface defect composition and density, infrared radiation, ionizing radiation, magnetic vortices, and thermally-induced quasiparticle generation, i.e. the temperature dependent behavior of the superconducting complex conductivity. The following sections will focus on the dominant intrinsic, materials sources of noise in superconducting qubits described by an ensemble of two level systems (TLS) and temperature dependent loss described by the Mattis-Bardeen theory that connects the surface impedance of superconductors to the internal quality factor and resonance frequency of a given resonator.

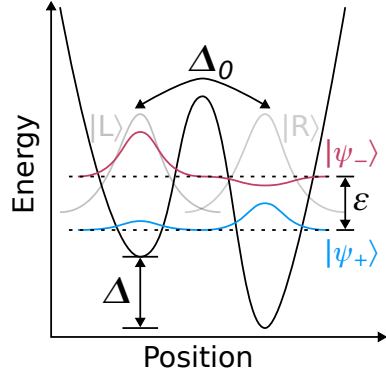


Figure 1.20 Double well potential representing a single TLS. Tunneling rate Δ_0 and asymmetry Δ shown, with the energy splitting between the ground state and first excited state ε . Left and right well-localized eigenstates denoted $|L(R)\rangle$ and energy eigenstates labeled $|\psi_{\pm}\rangle$. Based on and reproduced with permission from [19].

1.5.4 Losses from Two Level Systems

In Gao's thesis [66], he traces the history of the development of noise models in superconducting resonators and qubits to his experiments with microwave kinetic inductance detectors (MKIDs [65]) and observations from the single electron transistor (SET) community of correlated charge noise between neighboring SETs [128]. MKIDs are superconducting resonators that respond to radiation deposited on them with energy large enough to break Cooper pairs and generate quasiparticles (normal electrons). The next section on losses from the conductivity of superconductors describes the relationship between a change in temperature, either by the environment or photons depositing their energy in the substrate, and a shift in the resonance frequency of a superconducting resonator or MKID. This shift gives information about the energy of the incident photon, with a sensitivity bounded by the rate of quasiparticle generation-recombination. The large disparity between the quality factors (inverse losses) of the resonators in Gao's experiments and that expected by quasiparticle dynamics motivated a systematic investigation of the noise observed in superconducting resonators which became the focus of his PhD thesis [66].

Hints that this excess noise had a material origin came when aluminum resonators patterned on sapphire substrates had significantly lower noise than those patterned on silicon. The SET experiment [128] and work by the superconducting qubit community [129] further corroborated this materials source of noise in amorphous dielectrics. Earlier investigations of the behavior of glasses [130–132] presented a model that resembled the losses reported by [133], among others, that is referred to as the standard tunneling model (STM) of two level systems (TLSs) [19].

A prototypical model for a TLS is a particle in a double well potential (see Figure 1.20) with asymmetry¹⁹ Δ and a barrier large enough that thermally activated hopping between the wells is suppressed and quantum tunneling between the wells dominates with tunneling matrix element Δ_0 [19, 66].

The Hamiltonian for a single TLS in the basis referencing states localized to the left and right wells $\{|L\rangle, |R\rangle\}$ is given by

$$\begin{aligned}\hat{H}_{\text{TLS}} &= \frac{1}{2}\Delta\hat{\sigma}_z + \frac{1}{2}\Delta_0\hat{\sigma}_x \\ &= \begin{pmatrix} \Delta & \Delta_0 \\ \Delta_0 & -\Delta \end{pmatrix}\end{aligned}\quad (1.68)$$

where $\hat{\sigma}_z = (|R\rangle\langle R| - |L\rangle\langle L|)$ and $\hat{\sigma}_x = (|R\rangle\langle L| + |L\rangle\langle R|)$ [19]. The energy eigenbasis $\{\psi_+, \psi_-\}$ is related to the local basis by the unitary transformation

$$\begin{pmatrix} |\psi_+\rangle \\ |\psi_-\rangle \end{pmatrix} = \begin{pmatrix} \sin(\theta/2) & \cos(\theta/2) \\ \cos(\theta/2) & -\sin(\theta/2) \end{pmatrix} \begin{pmatrix} |L\rangle \\ |R\rangle \end{pmatrix}\quad (1.69)$$

with $|\psi_+\rangle$ the ground state and $|\psi_-\rangle$ the first excited state, $\tan\theta = \Delta_0/\Delta$, and energy eigenvalues $E_{\pm} = \pm\varepsilon/2 = \pm\sqrt{\Delta_0^2 + \Delta^2}/2$.

Now that we have established the energies of the bare TLS, we now consider two dipole couplings between the TLS and the strain and electric fields. Figure 1.21 depicts these couplings with some notion of how they manifest in superconducting resonator and qubit devices. The two interaction Hamiltonians, represented by the bidirectional arrows with color gradients, determine how energy is exchanged between the TLS and electromagnetic fields, $\hat{H}_{\text{TLS-EM}}$, and TLS and phonons, $\hat{H}_{\text{TLS-PH}}$ [66]

$$\hat{H}_{\text{TLS-EM}} = (\mathbf{d}_0 \cdot \mathbf{E}) (\Delta\hat{\sigma}_z + \Delta_0\hat{\sigma}_x) / \varepsilon\quad (1.70)$$

$$\hat{H}_{\text{TLS-PH}} = (\boldsymbol{\gamma}_e \cdot \mathbf{e}) (\Delta\hat{\sigma}_z + \Delta_0\hat{\sigma}_x) / \varepsilon\quad (1.71)$$

where \mathbf{d}_0 is the electric dipole moment of a single TLS, $\boldsymbol{\gamma}_e$ is the elastic dipole moment, and \mathbf{e} is the strain field. We direct the reader to the remainder of the derivation by Gao [66] connecting these microscopic models for the single TLS to ensembles of TLS with Δ and Δ_0 being uniformly and log uniformly distributed and the macroscopic discription of the dielectric function varying with applied microwave fields and temperatures.

¹⁹We will use the notation in Gao's thesis [66] for coefficients and the notation in [19] to label eigenstates, as the former is more readily used in the TLS community and the latter is more intuitive from the illustration of the double well potential in Figure 1.20.

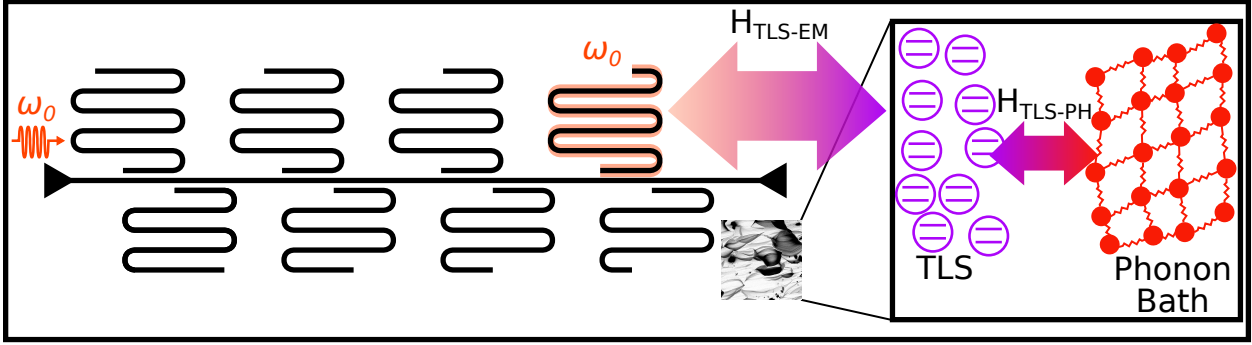


Figure 1.21 Coupling between microwave photons and TLS and phonons. On the far left, a microwave tone is incident on a tapered feedline with frequency ω_0 resonant with the resonator on the top right (ω). The inset shows a distribution of TLS coupled to the phonon bath by the interaction Hamiltonian $H_{\text{TLS-PH}}$, indicated by the color gradient arrow. Another bidirectional coupling is shown with the arrows between the TLS and resonator ω_0 with interaction Hamiltonian $H_{\text{TLS-EM}}$. In the small image, we include a scanning electron microscope image of a substrate surface as a representation for the substrate-air or metal-substrate interface hosting TLS.

The result of a temperature and power-dependent dielectric function $\epsilon(\omega, T, P) = \epsilon'(\omega, T, P) - j\epsilon''(\omega, T, P)$ is a loss tangent $\tan \delta = \text{Im}\{\epsilon\} = \epsilon''$ that is also a function of power and temperature. In the strong or general field limit that is relevant to the experiments performed in this thesis, the loss tangent $\tan \delta \simeq \delta = Q_i^{-1}$ is equal to the inverse internal quality factor of a given resonance at ω_0 [17, 66, 134]

$$Q_{i,\text{TLS}}^{-1}(\omega_0, T, n) = \delta_{\text{TLS}} = F \delta_{\text{TLS}}^0 \frac{\tanh(\hbar\omega_0/k_B T)}{\left(1 + \frac{\langle n \rangle}{n_c}\right)^\beta} \quad (1.72)$$

where n_c is the critical photon number equal to the photon power at the onset of TLS saturation. β is an exponent interpolating between the non-interacting TLS model $\beta = 1/2$ and interacting TLS model $\beta < 1/2$ [130, 135, 136], δ_{TLS}^0 is the intrinsic TLS loss, F is the geometry-dependent filling factor defined by the ratio of electric field energy stored in the dielectric compared to the total electric field energy

$$F_j = \frac{\frac{1}{2}\epsilon_j \int_{V_j} |\mathbf{E}|^2 d^3x}{\sum_k \frac{1}{2}\epsilon_k \int_{V_k} |\mathbf{E}|^2 d^3x} \quad (1.73)$$

The filling factor here is labeled with index j to include a multi-component TLS model [17], where multiple TLS “species” participate in the loss, each characterized by a quadruplet $(\beta_j, n_{c,j}, F_j, \delta_{\text{TLS},j}^0)$, and the total TLS loss being the sum $\delta_{\text{TLS, total}} \sum_j \delta_{\text{TLS},j}$, with the j -th loss term described by (1.72).

We have also made the substitution of power P for average number of photons in the resonator $\langle n \rangle$, which is related to the external and total quality factors by [137]

$$\langle n \rangle = \frac{Z_0}{Z_r} \frac{Q_l^2}{Q_c} \frac{2}{\hbar \omega_0^2} P \quad (1.74)$$

where Z_0/Z_r is the impedance mismatch between the resonator Z_r and the characteristic impedance of the microwave chain Z_0 , assuming no other mismatches, (Z_0 is typically 50Ω), $Q_l^{-1} = Q_i^{-1} + Q_c^{-1}$ is the loaded quality factor, Q_c is the external or coupling quality factor, and P is the power applied to the resonator.

1.5.5 Losses From the Conductivity of Superconductors

Conventional superconductors follow the theory presented by Bardeen, Cooper, and Schrieffer (BCS) [138]. Before citing the results of their theory and the subsequent work by Mattis and Bardeen [139], it is worth reviewing the phenomenological model of superconductivity that preceded the BCS theory to develop some intuition for the length scales involved in the Mattis-Bardeen theory. This phenomenological model is described by the London equations [140], and captures a number of experimentally observed properties of superconductors, including the Meissner effect, which was not predicted by competing theories at the time that the London brothers presented their theory. Following the treatment by Gross et al. [141], a brief review of the probability current in single particle quantum mechanics will give the necessary ingredients to arrive at the supercurrent density at the heart of the London equations. Let's start from the classical equation of the motion of a charged particle moving in an electromagnetic field [141]

$$\frac{d\mathbf{p}}{dt} = -\nabla \left\{ qV - \frac{q}{m}(\mathbf{p} \cdot \mathbf{A}) + \frac{q^2}{2m}(\mathbf{A} \cdot \mathbf{A}) \right\} = -\nabla U \quad (1.75)$$

where q is the charge of the particle, V is the electric scalar potential, \mathbf{p} is the momentum of the particle, \mathbf{A} is the magnetic vector potential, m is the mass of the particle, and U is the generalized potential of the system. Taking the kinetic energy as $\mathbf{p} \cdot \mathbf{p}/2m$, the total energy of the system can be written as

$$E = \frac{1}{2m} (\mathbf{p} - q\mathbf{A}) \cdot (\mathbf{p} - q\mathbf{A}) + qV \quad (1.76)$$

and making the replacement $\mathbf{p} \rightarrow -i\hbar\nabla$ in (1.76), we have the Hamiltonian of the system and Schrödinger equation as

$$\hat{H}_L = \frac{1}{2m} (-i\hbar\nabla - q\mathbf{A})^2 + qV \quad (1.77)$$

$$i\hbar \frac{\partial \Psi}{\partial t} = \left\{ \frac{1}{2m} (-i\hbar\nabla - q\mathbf{A})^2 + qV \right\} \Psi \quad (1.78)$$

The probability $\rho(\mathbf{x}, t)$ of finding a particle at position \mathbf{x} and time t is given by the square of the wavefunction,²⁰ $\rho(\mathbf{x}, t) = \Psi(\mathbf{x}, t)^* \Psi(\mathbf{x}, t) = |\Psi(\mathbf{x}, t)|^2$ with the normalization condition [141]

$$\int_V \Psi(\mathbf{x}, t)^* \Psi(\mathbf{x}, t) d^3\mathbf{x} = 1 \quad (1.79)$$

The time evolution of the probability follows from multiplying (1.78) on the left by Ψ^* , taking the complex conjugate of (1.78) and multiplying on the right by Ψ , then taking the difference of the two expressions.

This gives the time derivative of $\rho = \Psi^* \Psi$ constructed from the two components of the product rule of differentiation, i.e. $\partial_t(\Psi^* \Psi) = \Psi^* \partial_t \Psi + \Psi \partial_t \Psi^*$. The result, after some differential and algebraic manipulation, is a partial differential equation for ρ

$$\frac{\partial \rho}{\partial t} = -\nabla \cdot \left\{ \frac{\hbar}{2mi} (\Psi^* \nabla \Psi - \Psi \nabla \Psi^*) \right\} = -\nabla \cdot \mathbf{J}_\rho \quad (1.80)$$

where the right hand side is rewritten to resemble that of a continuity equation, with a probability current density \mathbf{J}_ρ in analogy with the classical electric current density and charge density.

It is worth emphasizing that this expression applies to a single particle, whereas the supercurrent density of superconductors involves a macroscopic number of particles. This macroscopic wavefunction is described by a dynamical phase $\theta(\mathbf{x}, t)$ and amplitude $\Psi_0(\mathbf{x}, t)$, $\Psi(\mathbf{x}, t) = \Psi_0(\mathbf{x}, t) e^{i\theta(\mathbf{x}, t)}$. In the superconducting context, the square of the wavefunction corresponds to the *local* number density $n_s^*(\mathbf{x}, t)$ of superelectrons or Cooper pairs and the normalization condition is modified to account for the total number of Cooper pairs N_s [141]

$$\int_V \Psi^*(\mathbf{x}, t) \Psi(\mathbf{x}, t) d^3\mathbf{x} = N_s \quad (1.81)$$

The continuity equation for the probability $|\Psi(\mathbf{x}, t)|^2 = n_s(\mathbf{x}, t)$ results in a current density \mathbf{J}_s referred to as the supercurrent that is no longer a probability current density, but one that describes the flow of Cooper pairs in the superconductor [141]. Thus, $\Psi(\mathbf{x}, t) = \sqrt{n_s^*(\mathbf{x}, t)} e^{i\theta(\mathbf{x}, t)}$ and \mathbf{J}_s is given by [141]

$$\mathbf{J}_s = \frac{q^* \hbar}{2m^* i} (\Psi^* \nabla \Psi - \Psi \nabla \Psi^*) - \frac{q^{*2}}{2m^*} \Psi \Psi^* \mathbf{A} \quad (1.82)$$

where $q^* = 2e$ and $m^* = 2m_e$ are the charge and mass of the Cooper pairs, consisting of two paired electrons of opposite spin and momentum.²¹

²⁰This should not be confused with the density matrix or density operator $\hat{\rho}$ whose diagonal entries are the probabilities of occupying a state in a particular basis and off-diagonal elements are the coherences.

²¹At the level of the two-fluid theory of superconductivity discussed here, the mechanism that leads to the pairing of electrons described by the BCS theory of superconductivity has not been introduced, nor will it be discussed in subsequent sections [138]. Later, the results of the BCS theory will be quoted when discussing the temperature dependence and frequency dependence of the conductivity and superconducting gap described by the Mattis-Bardeen theory.

Substituting $\Psi = \sqrt{n_s^*} e^{i\theta}$ into (1.82), gives

$$\mathbf{J}_s = \frac{q^* \hbar n_s^*}{m^*} \left(\nabla \theta - \frac{q^*}{\hbar} \mathbf{A} \right) = \frac{\hbar}{q^* \Lambda} \boldsymbol{\gamma} \quad (1.83)$$

$$\Lambda = \frac{m^*}{n_s^* q^{*2}} \quad (1.84)$$

$$\lambda_L = \sqrt{\frac{m^*}{\mu_0 n_s^* q^{*2}}} \quad (1.85)$$

$$\boldsymbol{\gamma} = \nabla \theta - \frac{q^*}{\hbar} \mathbf{A} \quad (1.86)$$

where Λ is the London parameter, λ_L is the London penetration depth and $\boldsymbol{\gamma}$ is a gauge invariant phase gradient. This form of the gradient leaves the supercurrent density unchanged under gauge transformations of the magnetic vector potential and phase of the form $\mathbf{A} \rightarrow \mathbf{A} + \nabla \chi$ and $\theta \rightarrow \theta + q^*/m^* \chi$ [141].

Taking the curl of both sides of the first form of (1.83) and using the property $\nabla \times \nabla \theta = 0$ gives the relationship between the magnetic field $\mathbf{B} = \nabla \times \mathbf{A}$ and supercurrent density as London's second relation [20]

$$\begin{aligned} \nabla \times \mathbf{A} &= \mathbf{B} = -\Lambda (\nabla \times \mathbf{J}_s) \\ \Rightarrow \mathbf{J}_s &= -\frac{1}{\Lambda} \mathbf{A}, \quad \nabla \cdot \mathbf{A} = 0 \end{aligned} \quad (1.87)$$

where in the second line we applied the London gauge ($\nabla \cdot \mathbf{A} = 0$).

From Ampère's law, the current density is related to the magnetic field by $\mathbf{J}_s = \mu_0^{-1} \nabla \times \mathbf{B}$ and taking the curl of this equation gives

$$\begin{aligned} \nabla \times \mathbf{J}_s &= -\frac{1}{\Lambda} \mathbf{B} = \mu_0^{-1} \nabla \times \nabla \times \mathbf{B} \\ &= \mu_0^{-1} \left(\nabla (\nabla \cdot \mathbf{B}) - \nabla^2 \mathbf{B} \right) \\ \Rightarrow \nabla^2 \mathbf{B} &= \frac{\mu_0}{\Lambda} \mathbf{B} = \frac{1}{\lambda_L^2} \mathbf{B} \end{aligned} \quad (1.88)$$

In one dimension, as drawn in Figure 1.22, the magnetic field is taken to be $\mathbf{B} = B(y)\mathbf{z}$ directed out of the page and (1.88) reduces to $\partial_{yy} B = \lambda_L^{-2} B$ with the exponential decay solution plotted in the right hand panel of Figure 1.22. Similarly, the exponential decay of the current density in the xy -plane, orthogonal to the \mathbf{B} field is drawn in Figure 1.22 (c), which can be derived from similar arguments as above, arriving at an equation of motion for the supercurrent as $\nabla^2 \mathbf{J}_s = \lambda_L^{-2} \mathbf{J}_s$, from $\nabla \cdot \mathbf{J}_s = 0$ and $\partial_t n_s^* = 0$.

The first London equation requires additional calculations, using the Schrödinger equation in (1.78) with the charge and mass replaced by their effective counterparts (with superscripted asterisks) and taking the number density n_s^* to be constant.

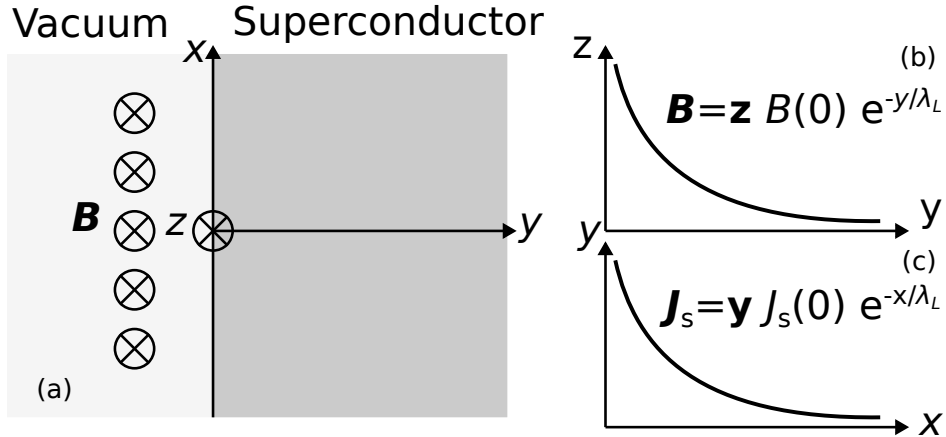


Figure 1.22 Illustration of the Meissner effect and the exponential decay of magnetic fields \mathbf{B} electric supercurrent densities \mathbf{J}_s from the surface of the superconductor as first described by the London equations. This figure is based on a lecture given by de Sousa [20].

Differentiating (1.82) with respect to time and substituting $\Psi = \sqrt{n_s^*} e^{i\theta(\mathbf{x}, t)}$ gives

$$\partial_t \mathbf{J}_s = -\frac{1}{\Lambda} \left\{ \partial_t \mathbf{A} - \frac{\hbar}{q^*} \nabla \partial_t \theta \right\} \quad (1.89)$$

$$-\hbar \partial_t \theta = \frac{q^{*2}}{2m^*} \left\{ \mathbf{A} - \frac{\hbar}{q^*} \nabla \theta \right\}^2 + q^* V \quad (1.90)$$

Rearranging the first term in (1.90) and substituting the expression for the gauge invariant gradient $\boldsymbol{\gamma}$, a relationship between $\partial_t \theta$ and \mathbf{J}_s emerges

$$-\hbar \partial_t \theta = \frac{\hbar^2}{2m^*} \boldsymbol{\gamma}^2 = \frac{q^{*2}}{2m^*} \Lambda^2 \mathbf{J}_s^2 = \frac{1}{n_s^*} \Lambda \mathbf{J}_s^2 \quad (1.91)$$

Substituting this result into (1.89) and using $\mathbf{E} = -\partial_t \mathbf{A} - \nabla V$, we arrive at the first London equation

$$\partial_t \mathbf{J}_s = \frac{1}{\Lambda} \mathbf{E} - \nabla \frac{1}{2n_s^* q^*} \mathbf{J}_s^2 \quad (1.92)$$

This is the full nonlinear expression relating the supercurrent density and the electric field. The second term is typically small compared to the first, giving the linear relationship $\partial_t \mathbf{J}_s = \Lambda^{-1} \mathbf{E}$, stating that time-independent currents flow without dissipation in superconductors.

These expressions describe the local relationship between the electric field and supercurrent density [66], but work by Pippard and Bragg [142] showed that a nonlocal relationship captures the experimental observation of a London penetration depth that varies with the coherence length ξ of the material, which itself is a function of the purity of the superconductor.

The coherence length is a measure of the size of a Cooper pair in a superconductor and is combination of a pure superconductor term $\xi_0 = \hbar v_0 / \pi \Delta_0$, where v_0 is the Fermi velocity of the metal and Δ_0 is the superconducting gap at zero temperature, and a term proportion to the electron mean free path l , i.e. $\xi^{-1} = \xi_0^{-1} + (\alpha_p l)$, where α_p is an empirical constant of proportionality [66].

This brings us to the starting point for the Mattis-Bardeen theory of the temperature and frequency dependence of the complex-valued conductivity of superconductors. Gao [66] gives a thorough derivation of the Mattis-Bardeen theory [139] starting from the nonlocal supercurrent density motivated by similar expressions for the classical (normal) current density $J_n(\mathbf{r})$ that describes variations in the skin depth with the electron mean free path l [66]

$$J_n(\mathbf{r}) = \frac{3\sigma_{dc}}{4\pi l} \int_V \frac{\mathbf{R}(\mathbf{R} \cdot \mathbf{E}(\mathbf{r}')) e^{-R/l}}{R^4} d^3\mathbf{r}' \quad (1.93)$$

$$J_s(\mathbf{r}) = -\frac{3}{4\pi\xi_0\lambda_L^2} \int_V \frac{\mathbf{R}(\mathbf{R} \cdot \mathbf{A}(\mathbf{r}')) e^{-R/\xi}}{R^4} d^3\mathbf{r}' \quad (1.94)$$

where $\mathbf{R} = \mathbf{r}' - \mathbf{r}$ and we used London's second equation in the London gauge ($\nabla \cdot \mathbf{A} = 0$), then substituted the coherence length for the mean free path, analogous with the normal current expression. Mattis and Bardeen developed a modified form of (1.94) [139]

$$J_{s,MB} = \frac{3}{4\pi^2 v_0 \hbar \lambda_L^2} \int_V \frac{\mathbf{R}(\mathbf{R} \cdot \mathbf{A}(\mathbf{r}')) I(\omega, R, T) e^{-R/l}}{R^4} \quad (1.95)$$

with the kernel $I(\omega, R, T) e^{-R/l}$ encoding the physics of the BCS theory of conventional superconductivity, the form of which is given in [66]. Gao discusses several limits of expressions resulting from (1.95), namely the surface impedance $Z_s = R_s + jX_s$, where R_s is the surface resistance, and X_s is the surface reactance of the superconductor, which is itself related to the frequency shift and quality factor shift as a function of temperature by [66]

$$\frac{\delta f}{f} = \frac{f(T) - f(0)}{f(0)} = -\frac{\alpha}{2} \frac{\delta X_s}{X_s} = -\frac{\alpha}{2} \frac{X_s(T) - X_s(0)}{X_s(0)} \quad (1.96)$$

$$\delta \frac{1}{Q_i}(T) = \frac{1}{Q_i(T)} - \frac{1}{Q_i(0)} = \alpha \frac{\delta R_s}{X_s} = \alpha \frac{R_s(T) - R_s(0)}{X_s(0)} \quad (1.97)$$

where α , also referred to as a conductive participation ratio p_{cond} or magnetic participation ratio, is defined by

$$\alpha = \frac{\lambda_L \int_S |\mathbf{H}|^2 d^2\mathbf{x}}{\int_V |\mathbf{H}|^2 d^3\mathbf{x}} \quad (1.98)$$

In the superconducting bulk aluminum cavities studied in this work, the effective London penetration depth is $50 \text{ nm} < \lambda_{\text{eff}} < 65 \text{ nm}$, [50] placing them firmly in the dirty or local limit $\lambda_{\text{eff}} \gg l, \xi_0$, ($l \approx 19 \text{ nm}$ [143]) with the surface impedance related to the complex conductivity $\sigma = \sigma_1 - i\sigma_2$ by [66]

$$Z_s(\omega, T) = \sqrt{\frac{i\mu_0\omega(T)}{\sigma_1(T) - i\sigma_2(T)}} \quad (1.99)$$

where the conductivities have the form referenced to the normal conductance of the material σ_n by [66, 139, 144]

$$\begin{aligned} \frac{\sigma_1(\omega, T)}{\sigma_n} &= \frac{2}{\hbar\omega} \int_{\Delta}^{\infty} \frac{(f(E) - f(E + \hbar\omega))(E^2 + \Delta^2 + \hbar\omega E)}{\sqrt{E^2 + \Delta^2} \sqrt{(E + \hbar\omega)^2 - \Delta^2}} dE \\ &\quad + \frac{1}{\hbar\omega} \int_{\Delta - \hbar\omega}^{-\Delta} \frac{(1 - 2f(E + \hbar\omega))(E^2 + \Delta^2 + \hbar\omega E)}{\sqrt{E^2 + \Delta^2} \sqrt{(E + \hbar\omega)^2 - \Delta^2}} dE \end{aligned} \quad (1.100)$$

$$\frac{\sigma_2(\omega, T)}{\sigma_n} = \frac{1}{\hbar\omega} \int_{\max\{\Delta - \hbar\omega, -\Delta\}}^{\Delta} \frac{(1 - 2f(E + \hbar\omega))(E^2 + \Delta^2 + \hbar\omega E)}{\sqrt{E^2 + \Delta^2} \sqrt{(E + \hbar\omega)^2 - \Delta^2}} dE \quad (1.101)$$

where $f(E) = (1 + \exp(E/k_B T))^{-1}$ is the Fermi-Dirac distribution function and $\Delta = \Delta(T)$ is the superconducting gap whose temperature dependence is given by the integral expression

$$\frac{1}{N(0)V} = \int_0^{\hbar\omega_c} \frac{\tanh\left(\frac{\sqrt{\xi^2 + \Delta^2}}{2k_B T}\right)}{\sqrt{\xi^2 + \Delta^2}} d\xi \quad (1.102)$$

where $\omega_c = \omega_D$ is an upper cutoff frequency, taken to be the Debye frequency, $N(0)$ is the number of Cooper pairs at zero temperature, and V is the BCS interaction strength.

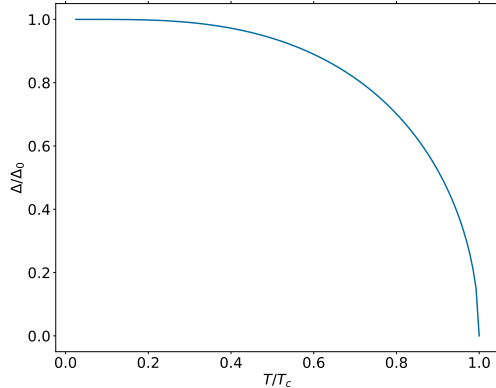


Figure 1.23 Superconducting gap, normalized to the zero temperature gap Δ_0 as a function of temperature, using the interpolation formula in (1.103).

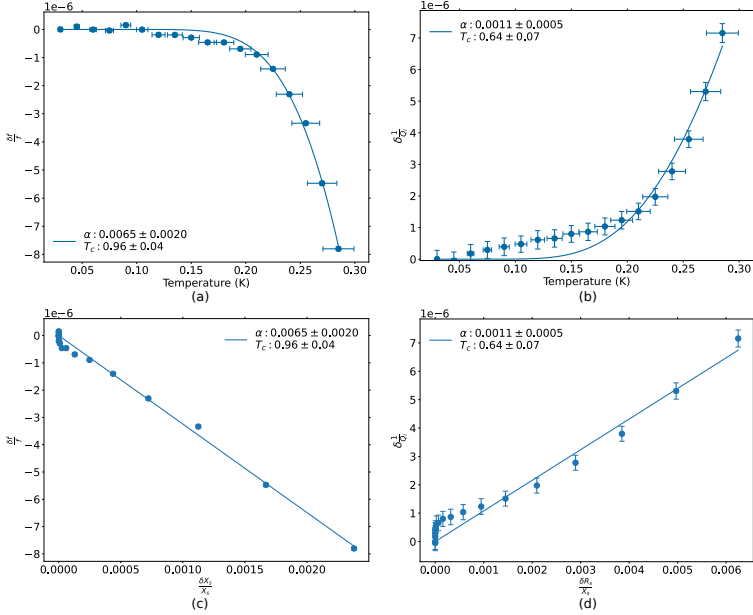


Figure 1.24 Mattis Bardeen fits of temperature sweeps of an Al CPW resonator deposited on InP by W. M. Strickland at New York University. (a) Fractional frequency shift and (b) fractional quality factor shift vs. temperature. (c) Fractional frequency shift vs. $\delta X_s/X_s$ and (d) fractional quality factor vs. $\delta R_s/X_s$.

There are a number of interpolation formulas that approximate the gap function in the region of interest to experiments $0 < T < T_c/3$, with the following used in this thesis and **scresonators** [18]

$$\Delta(T) \approx \Delta_0 \tanh(\sqrt{T_c/T - 1}) \quad (1.103)$$

and shown in Figure 1.23. Other software tools use similar approximation schemes, including the *Supermix* package [145]

$$\Delta(T) \approx \Delta_0 \exp\left[-\frac{2\pi k_B T}{\Delta_0} e^{-\frac{\Delta_0}{k_B T}}\right] \quad (1.104)$$

Gao et al. gives asymptotic expressions for the conductivities in the limit where $\hbar\omega \ll \Delta$, $k_B T \ll \Delta$, and $e^{-E/k_B T} \ll 1$ which are valid in all experimental settings of interest in this work [146]

$$\frac{\sigma_1(\omega, T)}{\sigma_n} = \frac{4\Delta}{\hbar\omega} e^{-\Delta/k_B T} \sinh(\zeta) K_0(\zeta), \quad \zeta = \frac{\hbar\omega}{k_B T} \quad (1.105)$$

$$\frac{\sigma_2(\omega, T)}{\sigma_n} = \frac{\pi\Delta}{\hbar\omega} \left[1 - 2e^{-\Delta/k_B T} e^{-\zeta} I_0(\zeta) \right] \quad (1.106)$$

where $I_0(\zeta)$ and $K_0(\zeta)$ are 0-th order modified Bessel functions of the first and second kind, respectively. Figure 1.24 shows example temperature sweeps fit using the approximate expressions for the superconducting gap in (1.103) and the conductivities in (1.105) and (1.106).

CHAPTER 2

TUNABLE CAPACITOR FOR SUPERCONDUCTING QUBITS USING AN INAS/INGAAS HETEROSTRUCTURE

Reproduced with permission from [48] published in *Quantum Science and Technologies*.

Nicholas Materise,^{*,22} Matthieu C. Dartiallh,²³ William M. Strickland,²³ Javad Shabani,²³ and Eliot Kapit²²

2.1 Abstract

Adoption of fast, parametric coupling elements has improved the performance of superconducting qubits, enabling recent demonstrations of quantum advantage in randomized sampling problems. The development of low loss, high contrast couplers is critical for scaling up these systems. We present a blueprint for a gate-tunable coupler realized with a two-dimensional electron gas in an InAs/InGaAs heterostructure. Rigorous numerical simulations of the semiconductor and high frequency electromagnetic behavior of the coupler and microwave circuitry yield an on/off ratio of more than one order of magnitude. We give an estimate of the dielectric-limited loss from the inclusion of the coupler in a two qubit system, with coupler coherences ranging from a few to tens of microseconds.

2.2 Introduction

Tunable couplers for superconducting qubits, previously thought of as long-term investments in future quantum computers and building blocks towards demonstrating high fidelity two qubit gates [8, 39], are now center-pieces of large scale superconducting qubit-based quantum computers. The early quantum advantage demonstration [37] owes its success, in part, to the two-qubit gate fidelities across the chip facilitated by fast, tunable couplers. Often tunable couplers are realized as mutual inductances or effective capacitances between nearest-neighbor qubits and tuned by flux-biased superconducting quantum interference devices (SQUIDs), naturally integrating with both fixed and flux-tunable superconducting qubit fabrication capabilities [38].

Advancements in the growth of superconductor-semiconductor (super-semi) structures for use in gate-tunable Josephson junctions have led to proposals [46, 147] and experimental demonstrations of voltage-controlled coupling schemes, superconducting quantum storage units [148], and readout resonator buses [47].

^{*}Primary and corresponding author, nick.materise@gmail.com

²²Department of Physics, Colorado School of Mines, 1500 Illinois St., Golden, CO 80401 USA

²³Center for Quantum Information Physics, Department of Physics, New York University, NY 10003, USA

Unlike their conventional transmon qubit [1] counterparts, whose energies are either fixed by their shunt capacitors or tuned with magnetic fluxes threading SQUID loops [149], these hybrid quantum systems consist of epitaxial III-V semiconductor layers whose properties are tunable with precise composition control and applied electric fields.

Challenges in optimizing materials and fabrication processes remain to realize high coherence gatemon [42] qubits and other voltage-tunable super-semi devices. These gatemon qubits differ from their flux-tunable and fixed frequency transmon counterparts in that their Josephson junctions are formed by superconductor-semiconductor-superconductor junctions and their Josephson energies E_J are tunable by an external electric potential. Although achieving coherences of two dimensional electron gas (2DEG)-based gatemon qubits at parity with conventional transmon-like qubits remains an open area of research, similar systems acting as low participation couplers still offer fast, high contrast control with a tolerable reduction in system coherence. Recent experimental demonstrations of tunable resonators using the same materials stack, achieved an on/off coupling ratio between resonators of one order of magnitude, a promising first step towards realizing fast, voltage-tunable couplers [150].

We propose a voltage-controlled capacitive coupling element between neighboring superconducting qubits using a III-V semiconductor 2DEG in an InAs/InGaAs heterostructure. The capacitance of the coupler tunes as a function of a gate voltage or series of gate voltages applied to the 2DEG, repelling electrons away from the region underneath the gates. By “parting the sea of electrons” in the quantum well, the coupler straddles two limits – fully conducting and fully depleted or insulating. In the intermediate region, the area of the depleted charges acts as an effective dielectric of some width d , and the capacitance of the coupler decreases with increasing width, as one might expect a parallel plate capacitor to behave as the separation between the plates increases. From this simple operational principle and reduction in sensitivity to bias line fluctuations, we expect such a coupler to be a drop-in replacement for SQUID-based inductive couplers [21].

Additional capacitors between the coupler and the qubits may minimize unwanted electric field coupling to other qubits. This is an improvement over SQUID-based couplers, where stray magnetic fields can lead to classical cross-talk between qubits [151]. We suspect that the 2DEG coupler may introduce more charge noise than the inductive couplers through the voltage control lines, yet transmon qubits, our initial targets for qubit-coupler integration testing, are exponentially insensitive to this charge noise.

The structure of the paper is as follows. We start by presenting a conceptual design of the coupler in Section 2.3.1. In Section 2.3.2, we formulate rigorous numerical models of the 2DEG coupler, starting with COMSOL semiconductor electron density calculations, followed by additional electrostatic and frequency-domain COMSOL simulations of the capacitance and admittance matrices, respectively.

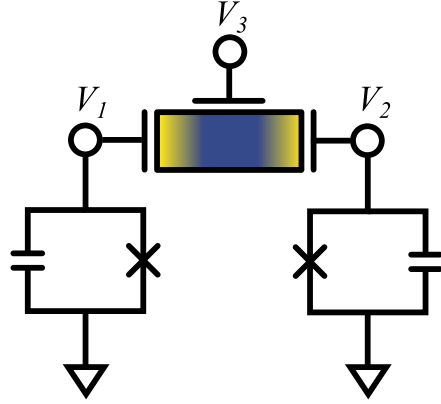


Figure 2.1 Schematic of two transmon qubits and the 2DEG coupler. Blue regions (color online) correspond to low electron concentration or effective dielectrics and red regions correspond to high electron concentration or effective conductors. We use the labeling of the voltage nodes V_i throughout the text, where nodes 1 and 2 correspond to source and drain terminals, and node 3 refers to the gate terminal.

That section concludes with a summary of the dielectric and other loss mechanisms present in the III-V semiconductor and dielectric materials in the coupler. Section 2.5 details our ANSYS high frequency simulation software (HFSS) simulations of a prototypical two transmon qubit circuit coupled by a lumped element capacitor representing the 2DEG coupler. We apply energy participation ratio techniques [103] to extract the Hamiltonian matrix elements in the dispersive regime, and extend these calculations to compute the charge-charge interaction matrix elements between the two transmon qubits. These analyses give similar results when considering a single lumped element variable capacitor representing the coupler compared to a full parasitic capacitance model of the coupler from our electrostatic COMSOL simulations.

2.3 Methods and Modeling

2.3.1 Conceptual Design

Inspired by textbook parallel plate capacitors, our coupler design relies on electronic control of the carrier concentration between two contacts to modify the effective parallel plate capacitor geometry seen by neighboring qubits. We consider a proximitized semiconductor [152] sandwiched between two transmon-like qubits with large capacitor plates patterned on top and a metal-oxide gate separating the two plates. Applying a negative gate voltage decreases the carrier concentration directly below the gate, modifying the capacitor geometry by increasing the effective separation of the parallel plates. The high electron mobility of the carriers in the 2DEG, exceeding $14\,000 \text{ cm}^2\text{V}^{-1}\text{s}^{-1}$ at 20 mK, [23] allows for fast gating, enabling parametric interactions with rapidly oscillating gate voltages.

This concept generalizes to multiple gates, where each region of low electron concentration corresponds to an effective dielectric and each region with high electron concentration acts a conductor.

The effective capacitance seen by the two qubits is the series combination of the individual capacitances defined by alternating effective dielectrics and conductors. Similar gating schemes have been proposed for nonreciprocal devices [153], tunable quantum buses [47], and controlled-Z gates [46].

Apart from the aforementioned experimental demonstrations of these devices, few modeling efforts, if any, have explored the practical considerations of realizing such couplers. The following numerical simulations aim to address those concerns by estimating the capacitive tuning range in the presence and absence of parasitic capacitances, calculating relevant interaction matrix elements, and providing an upper bound on the losses inherited by the system from the dielectric materials of the coupler.

2.3.2 Classical Modeling

2.3.3 Semiconductor 2DEG Calculations

To estimate the capacitance of the 2DEG coupler, we compute the electron concentrations in the active region of the device (InGaAs/InAs/InGaAs layers) using the COMSOL Multiphysics Semiconductor Module [154]. Equilibrium solutions to the drift-diffusion equations with Fermi-Dirac statistics serve to identify regions of high depletion under the gate(s) when applying negative voltages on the order of a few volts, overcoming the work function of the aluminum gate contact.

We use a layer structure typical of gatemon qubits as in figure Figure 2.2 and refer to this structure as the “device stack” [22–24, 155]. To model the device stack in COMSOL, we specified the following electronic properties of the semiconductor materials and the dielectric constant of the gate oxide: electron and hole effective conduction band masses $m_{n(p),c}^*$, low-field mobilities $\mu_{n(p)}^{lf}$, band gap energies E_g , conduction band offsets ΔE_c between neighboring semiconductors, dielectric constants ϵ_r , and effective densities of states for the conduction and valence bands $N_{c(v)}$. Taking the electron affinity χ for InAs as given by the COMSOL material library, we calculated the remaining affinities using Anderson’s affinity rule and the conduction band offsets of each material [156]. As in reference [155], we included a silicon delta-doping 6 nm below the interface between the InAlAs and lower InGasAs layers. COMSOL approximates such a doping profile with the Geometry Doping profile, which we select a Gaussian profile with a width of 0.1 nm. Table Table 2.1 gives a summary of the material parameters used in these semiconductor simulations; see A for detailed calculations of the energy gaps, effective masses, and conduction band offsets for $In_xGa_{1-x}As$ and $In_xAl_{1-x}As$ as functions of the composition parameter (x).

We specify the geometry in Figure 2.2 using the native COMSOL CAD editor to define domains (surfaces or planes) and boundaries (lines or edges), solving for the electron density in the domains and on the boundaries. Electronic properties assigned to each domain follow from table Table 2.1.

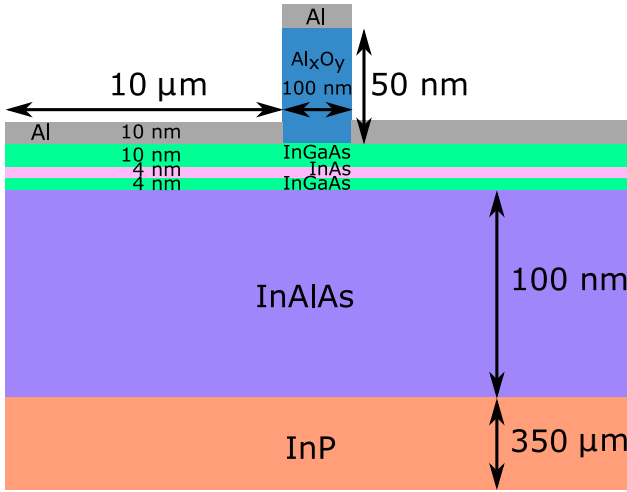


Figure 2.2 Schematic of the 2DEG coupler as modeled in COMSOL Multiphysics based on [21]. An aluminum contact deposited on Al_xO_y defines the gate terminal. We abbreviate the fixed composition ternary III-V alloys $\text{In}_{0.81}\text{Ga}_{0.19}\text{As}$ and $\text{In}_{0.81}\text{Al}_{0.19}\text{As}$, as InGaAs and InAlAs, respectively. Not shown or modeled is the superlattice graded buffer layer between InP and InAlAs [22–24].

Table 2.1 Materials parameters used in the COMSOL Semiconductor Module calculations. InGaAs and InAlAs abbreviate $\text{In}_{0.81}\text{Ga}_{0.19}\text{As}$ and $\text{In}_{0.81}\text{Al}_{0.19}\text{As}$. m_0 corresponds to the rest mass of an electron ($0.511 \text{ MeV } c^{-2}$). Out-of-plane effective electron and hole masses of InAs are set to m_0 in the model to simulate 2DEG confinement in the xy-plane. Electron mobilities for InAs, InGaAs, and InAlAs are all set to the same value as extracted from measurements of a similar device at millikelvin temperatures [23]. Values not in parenthesis (in parenthesis) correspond to electron (hole) properties.

	InAs	InGaAs	InAlAs	InP
E_g [eV]	0.354	0.473	0.752	1.344
ΔE_c [eV]	-	0.200	0.201	0.12
ϵ_r	15.15	14.03	13.13	12.9
N_c [cm^{-3}]	6.6E18	1.4E17	2.1E17	
N_v [cm^{-3}]	8.73E16	6.4E18	7.8E18	
χ [eV]	4.9	4.7	4.5	4.38
$\mu_{n(p)}^{\text{lf}}$ [$\text{cm}^2\text{V}^{-1}\text{s}^{-1}$]	14.4E3 (500)	14.4E3 (450)	14.E3 (384)	5.4E3 (200)
$m_{n(p),c}^*$ [m_0]	0.023 (1.00)	0.03 (0.25)	0.04 (0.31)	0.08 (0.60)

We model the terminals (source – 1, drain – 2, gate – 3, as in Figure 2.1) as Terminal boundary conditions with voltages V_1 , V_2 , V_3 and contact work functions $\Phi_{c,1}$, $\Phi_{c,2}$, $\Phi_{c,3} = 4 \text{ V}$ [154].

We selected the density gradient discretization scheme [157] in COMSOL to approximate the quantum confinement effects in the 2DEG more efficiently than a self-consistent Schrödinger-Poisson equation calculation.

The density gradients modify the equilibrium electron (n) and hole (p) concentrations by [154]

$$n = N_c F_{1/2} \left(\frac{E_{fn} - E_c + qV_n^{DG}}{k_B T} \right) \quad (2.1)$$

$$p = N_v F_{1/2} \left(\frac{E_v - E_{fp} + qV_p^{DG}}{k_B T} \right) \quad (2.2)$$

$$N_{c(v)} = \left(\frac{2m_{n(p)}^* \pi k_B T}{\hbar^2} \right)^{3/2} \quad (2.3)$$

where $E_{c(v)}$ is a given material's conduction (valence) band edge, $E_{fn(p)}$ are the electron (hole) quasi-Fermi level energies, $F_{1/2}(\eta)$ is the Fermi-Dirac integral [158], k_B is Boltzmann's constant, T is the temperature of the device (approximate temperature of the mixing chamber stage of typical dilution refrigerators ~ 10 mK), and q is the charge of an electron or hole. The quantum potentials $V_{n(p)}^{DG}$ are defined in terms of the density gradients by [154]

$$\nabla \cdot (\mathbf{b}_n \nabla \sqrt{n}) = \frac{1}{2} \sqrt{n} V_n^{DG} \quad (2.4)$$

$$\nabla \cdot (\mathbf{b}_p \nabla \sqrt{p}) = \frac{1}{2} \sqrt{p} V_p^{DG} \quad (2.5)$$

with the density gradient tensors $\mathbf{b}_{n(p)}$ for electrons (holes) expressed in terms of the effective mass tensors $\mathbf{m}_{n(p)}^*$

$$\mathbf{b}_n = \frac{\hbar^2}{12q} [\mathbf{m}_n^*]^{-1} \quad (2.6)$$

$$\mathbf{b}_p = \frac{\hbar^2}{12q} [\mathbf{m}_p^*]^{-1} \quad (2.7)$$

Note the distinction between the scalar effective masses $m_{n(p)}^*$ and, the effective mass tensors $\mathbf{m}_{n(p)}^*$.

Anisotropy in the effective mass tensors emulates the quantum confinement effects in the 2DEG, constraining electron movement to one plane.

For the remaining materials, Al₂O₃ and air, we used the Electric Charge Conservation interface, including the following constitutive relations for each dielectric in terms of its electric permittivity tensor $\boldsymbol{\epsilon}$ [154]

$$\mathbf{D} = \epsilon_0 \boldsymbol{\epsilon} : \mathbf{E} \quad (2.8)$$

where \mathbf{D} is the electric displacement field, ϵ_0 is the permittivity of free space, \mathbf{E} is the electric field, and $\boldsymbol{\epsilon} : \mathbf{E}$ is a tensor contraction (matrix vector product) between $\boldsymbol{\epsilon}$ and \mathbf{E} .

Modeling these regions as pure dielectrics reduces the size of the system of equations relative to a drift-diffusion calculation applied to the materials that behave as perfect insulators, air and oxide layers.

We excluded the superlattice graded buffer between the InAlAs and InP, as we expect the electric fields and carrier concentrations to be negligible in those regions and the additional computational cost (number of degrees of freedom solved for in the COMSOL model) would not improve the accuracy of our estimates of the capacitances and conductances of the coupler that will be largely determined by the charge dynamics in and near the active region (InGaAs/InAs/InGaAs).

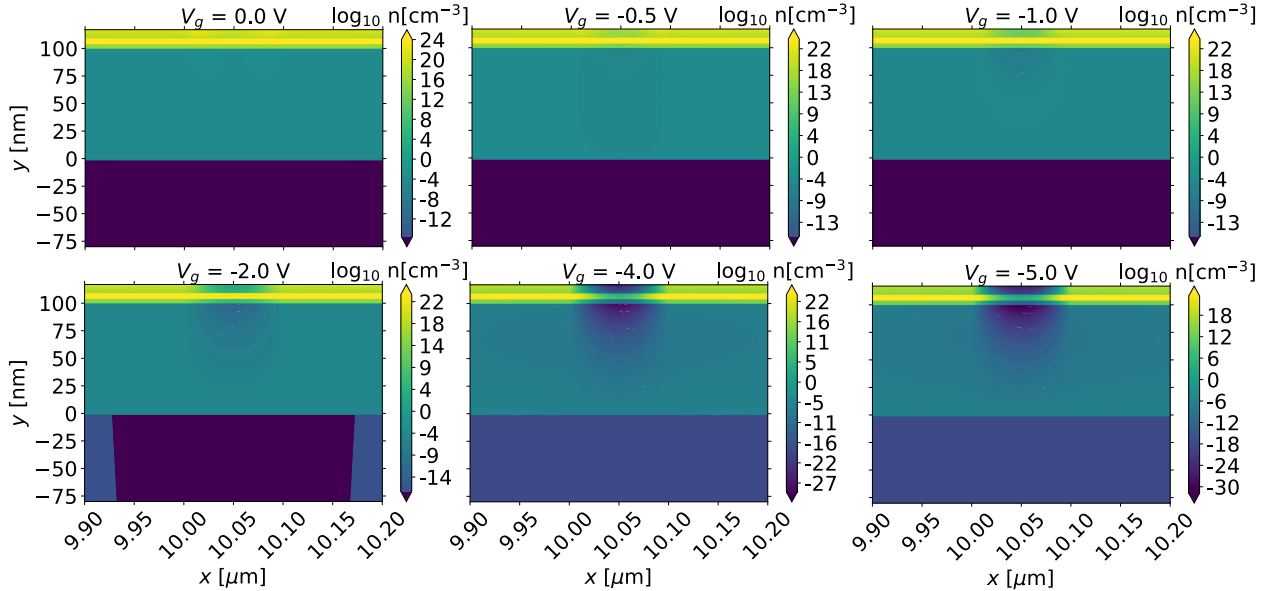


Figure 2.3 Electron concentrations [cm^{-3}] on a base-10 logarithmic scale with source-drain bias $V_{\text{sd}} = 0 \text{ V}$ for the fully conducting $V_g = 0 \text{ V}$, intermediate $V_g = -0.5, -1, -2, -4 \text{ V}$, and fully depleted $V_g = -5 \text{ V}$ operating points. The horizontal axis is a 300 nm span centered on the gate electrode and the vertical axis starts at the contact-2DEG interface at $\sim 117 \text{ nm}$, the 2DEG-InAlAs interface is 18 nm below that, and the InAlAs-InP interface is located at 0 nm. We do not solve for n in the regions where we applied the Electric Charge Conservation equations, i.e. in the Al_xO_y regions not shown, yet the electric fields respect the boundary conditions set by those regions.

2.3.4 Electric Currents Admittance Matrix Calculations

To extract the conductance matrix and verify the capacitance matrix of the device under high frequency excitation agrees with the electrostatic result, we use the Harmonic Perturbation option in the COMSOL Semiconductor module to compute the admittance matrix \mathbf{Y} defined in terms of the N terminal voltages V_k and currents I_k [159]

$$\begin{pmatrix} I_1 \\ I_2 \\ \vdots \\ I_N \end{pmatrix} = \begin{pmatrix} Y_{11} & Y_{12} & \dots & Y_{1N} \\ Y_{21} & Y_{22} & \dots & Y_{2N} \\ \vdots & \vdots & & \vdots \\ Y_{N1} & Y_{N2} & \dots & Y_{NN} \end{pmatrix} \begin{pmatrix} V_1 \\ V_2 \\ \vdots \\ V_N \end{pmatrix} \quad (2.9)$$

In the frequency domain, the voltages and currents become phasors of the form $\tilde{V}_k e^{i\omega t}$ and $\tilde{I}_k e^{i\omega t}$, with the admittance matrix given by

$$\mathbf{Y} = \mathbf{G} + i\omega\mathbf{C}, \quad (2.10)$$

where \mathbf{G} and \mathbf{C} are the conductance and capacitance matrices, $i = \sqrt{-1}$, and ω is the angular frequency [159]. Both matrices are nearly symmetric for our nonlinear, three-terminal device in figure Figure 2.1.

The Harmonic Perturbation option applies a small AC signal with angular frequency ω to each terminal after a DC operating point has been calculated by the semiconductor solver with some voltage applied to the gate, source, and drain contacts. At each DC operating point (linearization point), COMSOL computes the currents and voltages by differentiating the perturbed solution. To compute the admittance matrix above, we compute the ratio of the current and voltage at each terminal, i.e. [154]

$$Y_{ij} = \left. \frac{I_i}{V_j} \right|_{V_k \neq j=0} \quad (2.11)$$

We compute these currents at each terminal, given voltage source excitations, as a function of frequency ω in the band of 4–8 GHz relevant to superconducting qubit and resonator frequencies, and extracted the conductance matrix as the real, frequency-independent part of \mathbf{Y} and the capacitance matrix as the derivative of the imaginary part of \mathbf{Y} from (2.10)

$$G_{ij} = \text{Re}\{Y_{ij}(\omega)\} \quad (2.12)$$

$$C_{ij} = \text{Im} \left\{ \frac{dY_{ij}(\omega)}{d\omega} \right\} \quad (2.13)$$

$dY_{ij}(\omega)/d\omega$ is a constant in our case, as we omit the junction inductance L_{J_0} leading to discontinuities at resonance frequencies proportional to $(C_{ij}L_{J_0})^{-1/2}$ [95]. The capacitance and conductance matrices in the fully conducting limit \mathbf{C}_c and \mathbf{G}_c read

$$\mathbf{C}_c[\text{fF}] = \begin{pmatrix} 13.2 & -13.0 & -0.17 \\ -13.0 & 13.2 & -0.17 \\ -0.17 & -0.17 & 0.34 \end{pmatrix} \quad (2.14)$$

$$\mathbf{G}_c[\mu\text{S}] = \begin{pmatrix} 23.3 & -23.3 & -6.38\text{E}-4 \\ -23.3 & 23.3 & -6.38\text{E}-4 \\ -6.38\text{E}-4 & -6.38\text{E}-4 & 1.28\text{E}-3 \end{pmatrix} \quad (2.15)$$

$$(2.16)$$

Similarly, in the fully depleted limit we have

$$\mathbf{C}_d[\text{fF}] = \begin{pmatrix} 15.5 & -0.32 & -0.16 \\ -0.32 & 15.5 & -0.16 \\ -0.06 & -0.06 & 0.33 \end{pmatrix} \quad (2.17)$$

$$\mathbf{G}_d[\mu\text{S}] = \begin{pmatrix} 38.3 & 0.532 & -3.09\text{E}-4 \\ 0.532 & 38.3 & -3.09\text{E}-4 \\ 7.74\text{E}-3 & 7.74\text{E}-3 & 6.49\text{E}-4 \end{pmatrix} \quad (2.18)$$

We include the resistance matrices $\mathbf{R}_{c(d)} = \mathbf{G}_{c(d)}^{-1}$, for later use in Section 2.5 where we perform coupled two qubit simulations with HFSS and reference the $R_{c(d),12}$ matrix elements in the lumped element representation of the coupler.

$$\mathbf{R}_c[\Omega \times 10^9] = \begin{pmatrix} 93.3 & 93.3 & 93.3 \\ 93.3 & 93.3 & 93.3 \\ 93.3 & 93.3 & 94.1 \end{pmatrix} \quad (2.19)$$

$$\mathbf{R}_d[\Omega] = \begin{pmatrix} 2.61\text{E}+4 & -3.65\text{E}+2 & 1.23\text{E}+4 \\ -3.65\text{E}+2 & 2.61\text{E}+4 & 1.23\text{E}+4 \\ -3.07\text{E}+5 & -3.07\text{E}+5 & 1.54\text{E}+9 \end{pmatrix} \quad (2.20)$$

Note that the capacitance, conductance, and resistance matrices away from the fully conducting operating point are not symmetric. The departure of the capacitance matrices from symmetry likely stems from numerical imprecision. The conductance discrepancies we attribute to the observed frequency dependence of the real part of \mathbf{Y} . In the symmetric setting, we expect $\text{Re}\{\mathbf{Y}(\omega)\}$ to be constant with respect to ω , but we find that it varies linearly with ω . This frequency dependence we model as $\text{Re}\{\mathbf{Y}(\omega)\} = \omega\mathbf{g}$ and report $\mathbf{G} = \mathbf{g}\Delta\omega$, where \mathbf{g} has units of $\Omega^{-1}s$ and $\Delta\omega$ is the frequency step used by the Harmonic Perturbation study.

The matrix elements of interest, $C_{12} = C_{21}$, $G_{12} = G_{21}$, and $R_{12} = R_{21}$ represent the effective capacitance, conductance, and resistance between the source and drain terminals.

These terminals form capacitive contacts with any pair of qubits. The capacitance tuning ratio r , or on/off contrast of the 2DEG coupler is given by $r_C = C_{c,12} / C_{d,12} \approx 40$. Similarly, the ratio of conductances is $r_G = G_{c,12} / G_{d,12} \approx 43$. A back of the envelope calculation of the charge concentration in the 2DEG between the source and drain contacts, using expressions for the conductivity $\sigma = \mu_n e n$ and conductance $G_{12}/d_0 = \sigma$ gives

$$n_{c,\text{eff}} = \frac{G_{c,12}}{\mu_n e d_0} = 2.0\text{E+17 cm}^{-3} \quad (2.21)$$

$$n_{d,\text{eff}} = \frac{G_{d,12}}{\mu_n e d_0} = 4.6\text{E+15 cm}^{-3} \quad (2.22)$$

These *effective* charge concentrations agree with figure Figure 2.3 and link the change in capacitance and conductance with a change in carrier concentration between the source and drain contacts.

2.4 Results

Summary of the modeling results of the 2DEG tunable coupler.

We report the gate voltage dependence of the capacitance and conductance matrices computed in the previous section at intermediate DC operating points between the fully conducting ($V_g = 0 \text{ V}$) and fully depleted ($V_g = -5 \text{ V}$) limits. Figure Figure 2.4 shows that the source-drain capacitance $C_{12} = C_{21}$ saturates quickly, as $V_g < -1 \text{ V}$. This is a desired feature for practical tunable couplers, as lower operating voltages are preferred to reduce the active heat load from DC control signals [160]. The conductances $G_{12} = G_{21}$ follow a similar trend, with the other matrix elements following a different V_g -dependence than the capacitance matrix elements.

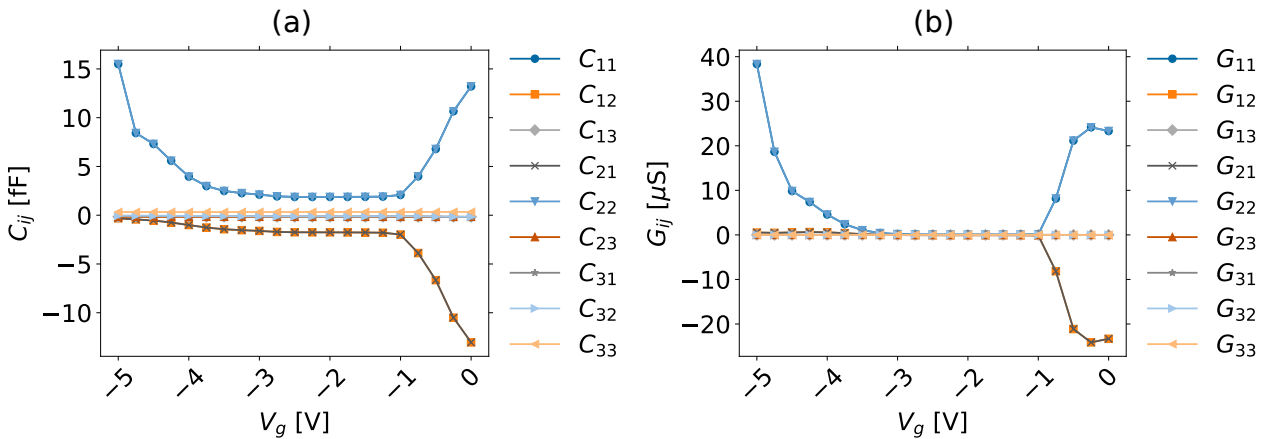


Figure 2.4 (a) Maxwell capacitance and (b) conductance matrices as computed with the Harmonic Perturbation study of the COMSOL Semiconductor Interface as a function of the gate voltage V_g .

2.4.1 Coupler Loss Estimates

We give bounds on the losses introduced by the 2DEG coupler from experimental measurements of the high participating gate dielectrics and InGaAs upper layer, along with the other layers in the device stack. In table Table 2.2, we compute the electric field participation ratios p_j following the procedure developed by [161, 162]. The relaxation time T_1 at a given angular frequency ω , as a function of the dielectric material properties and geometric factors, reads [162]

$$T_1^{-1} = \frac{\omega}{Q} = \omega \sum_j \frac{p_j}{Q_j} + \Gamma_0 \quad (2.23)$$

$$Q_j^{-1} = \tan \delta_j \quad (2.24)$$

$$p_j = W_e^{-1} t_{\text{oxide}} \varepsilon_{1,j} \int_{S_j} |\mathbf{E}|^2 dS \quad (2.25)$$

$$W_e = \int_V |\mathbf{E}|^2 dV \quad (2.26)$$

W_e is the electric field energy density stored in the volume of the entire geometry V , Q_j are the quality factors, $\tan \delta_j$ are the loss tangents, $\varepsilon_{1,j}$ are the real parts of the dielectric function, and t_{oxide} is the thickness of the participating lossy surface, assumed to be 3 nm for all materials [162]. The participation ratios give the fraction of the electrical energy stored in a given surface S_j relative to the total electrical energy stored in the entire volume of the device. The last term in (2.23), Γ_0 , includes all other loss mechanisms contributing to T_1 besides dielectric loss [162]. Note, these participation ratios differ from those in subsequent calculations involving *energy* participation ratios referenced to a given mode rather than a particular surface.

Other sources of loss relevant to III-V semiconductor materials, but not considered in this study, include piezoelectricity [163], non-equilibrium quasiparticles [164], cosmic ray muon flux [165], and, to a lesser extent, stray magnetic fields [166].

2.5 Integration with Circuit QED

2.5.1 Two Qubit Coupler

In figure Figure 2.5 we have a microwave circuit model of two transmon qubits coupled by a lumped impedance $Z_{\text{JJ}_c}(\omega) = 1/(1/R + i\omega C)$, where R and C take the values of R_{12} and C_{12} in either the fully conducting or fully depleted limits of the 2DEG coupler. In the conducting limit, where some current can flow across the coupler and act like a Josephson junction, one might consider adding an inductance to the coupler lumped element model.

Table 2.2 Participation ratios p_j , dielectric loss tangents $\tan \delta_j$, layer thicknesses t_j , and estimated dielectric-loss-limited $T_{1,j}$. All $T_{1,j}$ times are referenced to a qubit frequency of $\omega/2\pi = 5$ GHz and $\tan \delta_j^*$ indicates that in the absence of reliable loss tangent data for the individual InAs, InGaAs, InAlAs, and InP layers, we used the low power loss extracted from measurements of an Al patterned CPW resonator on the full III-V stack modeled in this work and measured at 100 mK as an estimate [28].

Depleted	t_j [nm]	$p_{j,\text{norm}}$	$\tan \delta_j^*$	T_1 [μs]
InGaAs (Top)	10	4.19E-2	4.1E-4	1.85E+0
InAs	4	1.03E-2	4.1E-4	7.53E+0
InGaAs (Bottom)	4	7.85E-3	4.1E-4	9.89E+0
InAlAs	100	2.92E-2	4.1E-4	2.67E+0
Al_2O_3 [167]	50	9.04E-1	5E-3	6.87E-3
InP	3.5E3	6.97E-3	4.1E-4	8.95E+0
Total	-	1	7.3E-3	6.81E-3
Conducting	t_j [nm]	$p_{j,\text{norm}}$	$\tan \delta_j^*$	T_1 [μs]
InGaAs (Top)	10	1.01E-8	4.1E-4	7.69E+6
InAs	4	3.73E-9	4.1E-4	2.08E+7
InGaAs (Bottom)	4	4.03E-9	4.1E-4	1.93E+7
InAlAs	100	1.10E-9	4.1E-4	7.06E+7
Al_2O_3 [167]	50	9.9999E-1	5E-3	6.24E-3
InP	3.5E3	1.41E-5	4.1E-4	4.43E+3
Total	-	1	7.3E-3	6.24E-1

Taking R_{12} to be the normal resistance of a Josephson junction and computing the junction inductance with the Ambegaokar-Baratoff formula [168], the junction inductances would be very small, on the order of a few aH to tens of fH, resulting in high coupler mode frequencies, far outside of the frequency band of the finite element electromagnetic field solver, Ansys HFSS. For this reason and expected small modifications to qubit-qubit interactions, we omit these inductances in our model and use Ansys HFSS to compute the lowest electromagnetic eigenmodes of the device with the two transmon qubits, indexed by j , defined as parallel LC lumped elements, $Z_{\text{JJ}_{q,j}} = 1 / (1/(i\omega L_{q,j}) + i\omega C_{q,j})$. In the following section, we use these eigenmode solutions to estimate the Hamiltonian matrix elements corresponding to qubit-qubit mode and qubit-coupler mode coupling strengths. We will differentiate between this modal coupling from direct capacitive coupling in the final part of this section, where we calculate the direct charge-charge interaction matrix elements.

2.5.2 Energy Participation Ratios and Quantization

To extract the coupling matrix elements between the qubits in our microwave device layout, we employ the energy participation ratio (EPR) method developed by Minev [169]. This approach goes beyond the larger family of black box quantization methods [90, 95], where the Hamiltonian describes a collection of Josephson junction-based qubits interacting with any number of harmonic modes separates into linear and nonlinear terms.

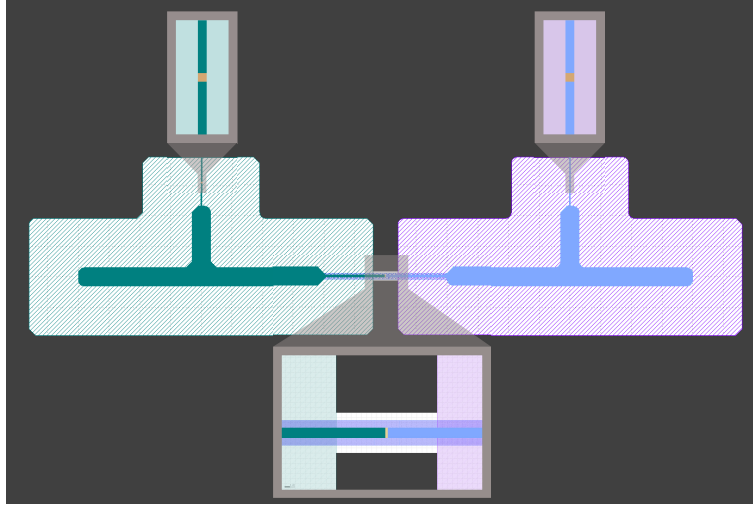


Figure 2.5 False color geometry of two transmon qubits with the capacitive coupler in between used in the HFSS simulations. Lumped impedances defined in the gold regions of the insets, represent the linear response of the Josephson junctions and capacitive coupling element in the HFSS model.

One can relate the modal decomposition of the classical electromagnetic response, e.g. impedance, admittance, or electromagnetic energies, with the linear parts of the Hamiltonian. Additional inputs describing the Josephson junction energy scales, E_J and E_C , related to the inductive and capacitive energies of the junction, account for the nonlinear terms. The total Hamiltonian, accounting for M modes, in the dispersive regime and under the rotating wave approximation, reads

$$H = H_{\text{lin}} + H_{\text{nl}} \quad (2.27)$$

$$H_{\text{lin}}/\hbar = \sum_{m=1}^M \omega_m a_m^\dagger a_m \quad (2.28)$$

$$\begin{aligned} H_{\text{nl}}/\hbar &= - \sum_{m=1}^M \left(\Delta_m a_m^\dagger a_m + \frac{1}{2} \alpha_m a_m^\dagger a_m^2 \right) \\ &+ \frac{1}{2} \sum_{m \neq n} \chi_{mn} a_m^\dagger a_m a_n^\dagger a_n \end{aligned} \quad (2.29)$$

where the Lamb shifts Δ_m , cross-Kerr coefficients χ_{mn} , and anharmonicities α_m are given by [169]

$$\Delta_m = \frac{1}{2} \sum_{n=1}^M \chi_{mn} \quad (2.30)$$

$$\chi_{mn} = - \sum_{j \in J} \frac{1}{2} \frac{\hbar \omega_m \omega_n}{4E_{J_j}} \quad (2.31)$$

$$\alpha_m = \frac{1}{2} \chi_{mm} \quad (2.32)$$

The cross- and self-Kerr (anharmonicities) coefficients extracted with the pyEPR Python package [103, 169] are given by the entries of the $\chi_{c(d)}$ matrix in the conducting (c) and depleted (d) limits of the coupler

$$\frac{1}{2\pi}\chi_c \text{ [MHz]} = \begin{pmatrix} 223 & 67.1 \\ 67.1 & 223 \end{pmatrix} \quad (2.33)$$

$$\frac{1}{2\pi}\chi_d \text{ [MHz]} = \begin{pmatrix} 129 & 1.02 \\ 1.02 & 129 \end{pmatrix} \quad (2.34)$$

The rows and columns of $\chi_{c(d)}$ correspond to qubits 1 and 2. Note that the diagonal entries include the $1/2$ factor in the definition of the anharmonicities as in (2.32). The eigenfrequencies and quality factors are recorded in table Table 2.3 and follow from the HFSS eigenmode solutions.

Table 2.3 Eigenmode frequencies and quality factors computed with HFSS in the conducting (c) and depleted (d) limit of the coupler.

Qubit Index	$\omega/2\pi$ [GHz]	Q
1 (d)	6.0228	1.7E7
2 (d)	8.6135	5.1E9
1 (c)	6.0228	4.5E8
2 (c)	8.6135	1.3E9

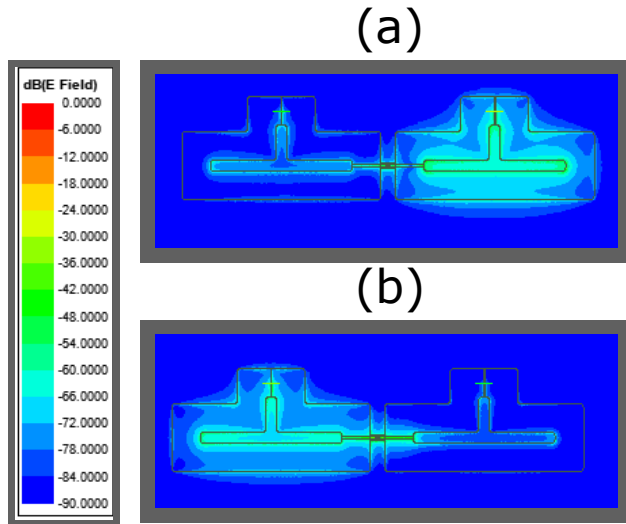


Figure 2.6 Electric field magnitude (dB scale to enhance color contrast) for the first two eigenmode solutions computed with HFSS. (a) 6.0228 GHz and (b) 8.6135 GHz qubits in the fully depleted limit of the coupler.

2.5.3 Extraction of the Exchange Interaction

To compute the charge-charge interaction strength between the transmon qubits in our HFSS model, we consider the capacitance matrix associated with a persistent current or flux qubit following the derivation by Orlando [170]. For details on the derivation of the capacitance matrix, see A.2. The Hamiltonian for the coupled two transmons, written in terms of the Josephson junction phases φ_j and node charges q_j , is given by

$$H = \frac{1}{2} \mathbf{Q}^T \mathbf{C}^{-1} \mathbf{Q} + U(\varphi) \quad (2.35)$$

$$U(\varphi) = \sum_j E_{J_j} (1 - \cos \varphi_j) \quad (2.36)$$

$$\mathbf{C} = \begin{pmatrix} C_1 + C_3 & -C_3 \\ -C_3 & C_2 + C_3 \end{pmatrix} \quad (2.37)$$

In (2.35), the charge-charge matrix elements are one half the entries of the inverse of the capacitance matrix. We numerically inverted \mathbf{C} in (2.37) using values for C_1 , C_2 obtained from (A.19) and $C_3 = C_{12}(V_g)$ in the depleting and conducting limits. This matrix $\frac{1}{2}e^2 \mathbf{C}_{c(d)}^{-1}$ is given by

$$\frac{1}{2}e^2 \mathbf{C}_c^{-1} [\text{MHz}] = \begin{pmatrix} 179 & 21.3 \\ 21.3 & 179 \end{pmatrix} \quad (2.38)$$

$$\frac{1}{2}e^2 \mathbf{C}_d^{-1} [\text{MHz}] = \begin{pmatrix} 200 & 0.66 \\ 0.66 & 200 \end{pmatrix} \quad (2.39)$$

The ratio of the off diagonal elements in (2.38) and (2.39) recovers an on/off interaction ratio of more than one order of magnitude, $r_{\text{int}} \approx 32$.

We emphasize here that the off-diagonal charge-charge interaction matrix elements give a more accurate description of the coupling between the qubits mediated by the 2DEG coupler than the EPR calculations of the cross-Kerr coefficients.

A more detailed treatment of the coupler including the parasitic capacitances from the Maxwell capacitance matrices in (2.14) and (2.17) give three-by-three coupling capacitance matrices in the Lagrangian of the form in (A.24). The modified charge-charge interaction matrix elements in the full parasitic capacitance model is given by

$$\frac{1}{2}e^2 \mathbf{C}_{c,\text{para}}^{-1} [\text{MHz}] = \begin{pmatrix} 159 & 16.9 & 44.1 \\ 16.9 & 108 & 44.1 \\ 44.1 & 44.1 & 2.86E+4 \end{pmatrix} \quad (2.40)$$

$$\frac{1}{2}e^2 \mathbf{C}_{d,\text{para}}^{-1} [\text{MHz}] = \begin{pmatrix} 172 & 0.552 & 43.0 \\ 0.552 & 113 & 43.0 \\ 43.0 & 43.0 & 2.99E+4 \end{pmatrix} \quad (2.41)$$

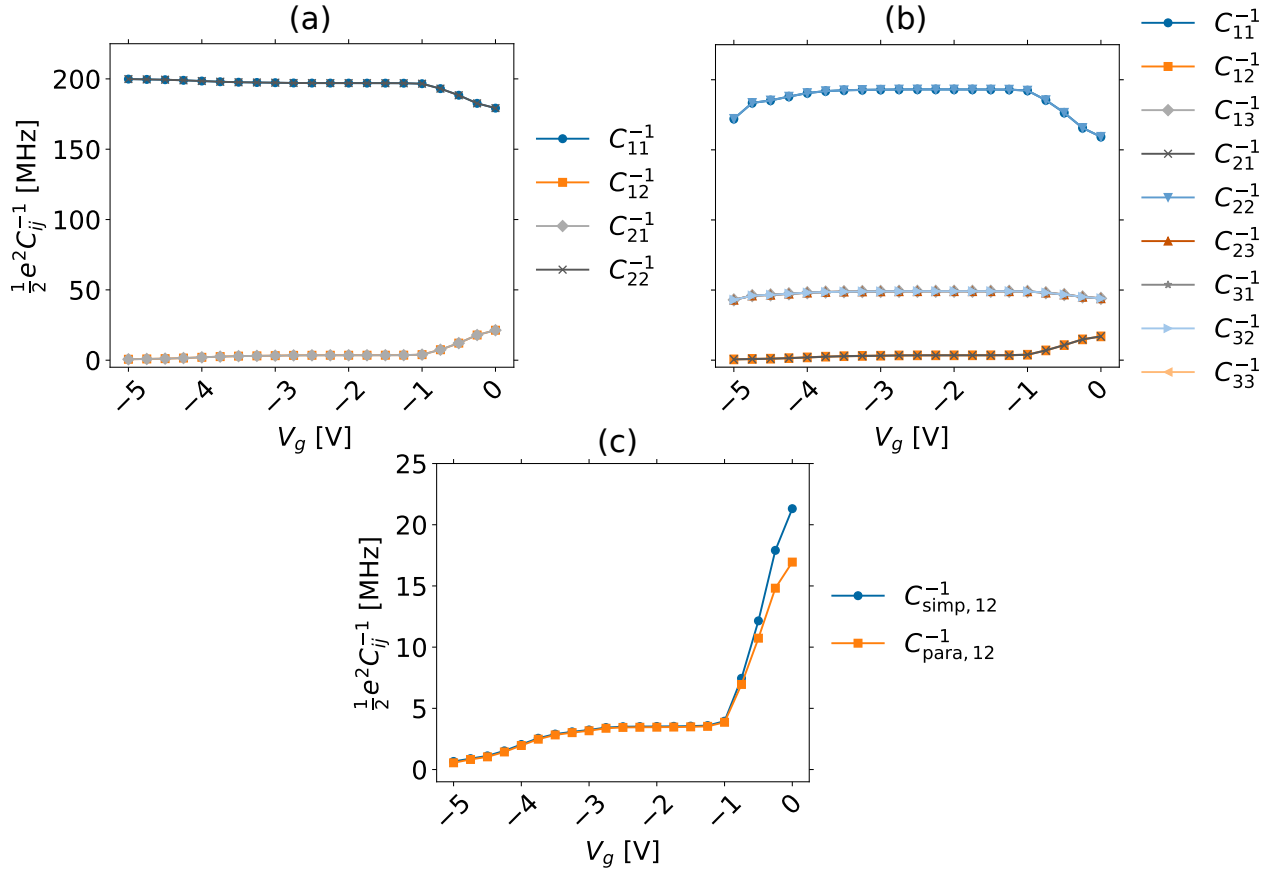


Figure 2.7 Coupling matrix elements in (a) the simplified two node model, (b) the three node parasitic capacitance model, (c) direct comparison of the 1-2 matrix element representing the charge-charge exchange rate between qubits 1 and 2 with the parasitic (para) and simplified (simp) capacitance matrices.

In the parasitic capacitance model, we find an on/off interaction ratio of $r_{\text{int}} \approx 31$. Figure Figure 2.7 illustrates the excellent agreement between the simplified and parasitic capacitances as a function of the gate voltage. Although the simplified model does not account for the parasitic capacitances C_{13} , C_{31} , C_{23} , and C_{32} , it captures the behavior of the charge-charge exchange matrix elements accurately, as the parasitic contributions do not significantly change the values of C_{12}^{-1} .

2.5.4 Estimation of Coupler Coherence Limit

To estimate the total coherence limit of our coupler in the two qubit device in figure Figure 2.6, a back-of-the-envelope calculation of the energy stored in the coupler surface, in either qubit mode, gives an electric field participation ratio on the order of 10^{-3} , resulting in a coherence limit of a few to tens of μs , when considering the loss to be dominated by the gate dielectric and the top InGaAs layer.

This is consistent with previous studies of transmon qubits whose participations are near unity in their given mode [95, 103] and gives us further confidence that a coupler of a similar geometry could support fast parametric operations with moderate coherence.

2.6 Discussion

From our COMSOL simulations of the 2DEG semiconductor physics, electrostatic and electric current analyses, we modeled a tunable capacitor with an order of magnitude on/off contrast. The numerical results agree with the schematic picture of modulating a parallel plate geometry by gating a high mobility 2DEG. At the level of estimating the lumped capacitance and resistance inputs to HFSS, our models incorporate 2D semiconductor behavior in greater detail than previous mixed experimental/computational reports [21, 23].

Two models of the coupler, with and without the parasitic capacitances extracted from COMSOL, give similar on/off interaction ratios and absolute interaction strengths. By simulating the full capacitance matrix of the multi-terminal coupler device, we motivating the choice of single gate over multi-gate coupler designs [171]. Both the simplified and parasitic capacitance estimates of the interaction strengths fall between hundreds of kHz to tens of MHz of coupling, on the same order of magnitude as flux-tunable couplers [37, 151].

Our coherence estimates further emphasize that incorporating our coupler design with existing transmon qubit designs comes at a modest reduction in system coherence. With coupler coherences limiting the system coherence to tens of μ s and expected improvements in the base coherences of the coupler materials, we are optimistic that future couplers using a similar operational principle as 2DEG coupler may incur a lower system coherence penalty with the same low participation as modeled here.

This work has implications in the quantum annealing context, where both inductive and capacitive coupling may lead to nonstoquastic Hamiltonians, those that cannot be simulated by quantum Monte Carlo techniques due to the sign problem [108]. By coupling conjugate degrees of freedom, charge and flux, gate-based superconducting qubit systems also stand to benefit from a richer native gate set, e.g. XX, YY, and ZZ [172, 173].

2.7 Conclusion

We simulated a 2DEG-based, voltage-controlled tunable coupler compatible with superconducting qubits. With an estimated tuning ratio of one order of magnitude and similarly reduced conductance in the off state, our proposed design is an excellent candidate for capacitively coupling superconducting qubits.

HFSS simulations and subsequent capacitance matrix inversion analysis suggest that the coupling matrix elements exhibit the same range of tunability, and estimates of the loss suggest that the gate oxides limit the lifetime of the coupler to nearly ten μ s and the top InGaAs layer limits coupler lifetimes to several tens of μ s. Low loss gate dielectrics such as tantalum oxide [174] and hexagonal boron nitride [175], along with improvements in the fabrication of the III-V stack may increase these coherence limits in the near term. Subsequent design iterations may look to reduce the parasitic capacitances with geometric optimization techniques to maximize contrast and minimize stray interactions [6]. A tunable capacitive element may also serve a complementary role with tunable inductive elements to realize nonstoquastic Hamiltonians in quantum annealing systems [108]. Our tuning and coherence estimates, coupled with the benefit of exponential suppression of charge noise over first order sensitivity flux noise in SQUID-based couplers, give us confidence that voltage-controlled coupling elements of the form developed here have the potential to supplant and complement their inductive counterparts in superconducting qubit systems.

2.8 Acknowledgments

We acknowledge funding from NSF Grant PHY-1653820 and Army Research Office Grant Nos. W911NF-18-1-0125 and W911NF-18-1-0067. N. M. acknowledges funding from the Graduate Fellowships for STEM Diversity and W. M. S. acknowledges funding from the Army Research Office QuaCGR Fellowship. We would like to thank Bradley Llyod, Chien Liu, Paul Niyonkuru, Alan Phillips, John Rose, Meenakshi Singh, and David Young for many insightful discussions.

2.9 Data Availability

The data that support the findings of this study are openly available at the following DOI:
<https://doi.org/10.5281/zenodo.8125613>.

CHAPTER 3

FIELD OVERLAP INTEGRAL APPROACH TO ESTIMATE PARAMETRIC RATES BETWEEN SUPERCONDUCTING 3D CAVITIES

Superconducting circuits and cavities are on the cusp of achieving both the coherence and control needed to implement error correction schemes with biased error noise models, which have shown favorable scaling and improved error thresholds over the surface code and other systems with unbiased noise models [113]. The realization of high fidelity parametric operations with tunable couplers has accelerated this development, especially with the advent of parametrically activated beam splitters [9, 16]. In designing these 3D tunable couplers, full-wave electromagnetic simulations are necessary to predict their performance using the methods of black-box quantization (BBQ) and the energy participation ratio (EPR) approach. These methods typically give a reasonable estimate of parametric coupling rates and bare, geometric coupling rates in the degenerate coupled mode case when the nonlinear element that is used to induce parametric operations is capacitively coupled to a cavity mode or collection of modes. The general problem of estimating the bare and parametric coupling rates for capacitively coupled, inductively coupled, and galvanically coupled nonlinear elements in the nondegenerate case requires a new modeling framework. We present such a framework using a generalization of EPR, where the parametric rates are functions of field overlap integrals evaluated at different mode numbers and control parameters.

3.1 Methods

The starting point for our analysis is the assumption that the electric and magnetic field eigenmode solutions from Ansys HFSS each form a complete orthonormal basis. A derivation of the finite element problem solved by HFSS in Appendix C gives a sketch of a proof that the electric fields are orthogonal and the magnetic fields are likely orthogonal, but their normalization is not accessible at the user level, i.e. the values of the eigenvectors in the eigenvalue problem resulting from the weak form of the Helmholtz equation, subject to boundary conditions, are not exposed to users. However, the electric and magnetic field solutions are available at the user level and we will use them as a basis functions to expand the electric and magnetic field operators.

3.1.1 Field Overlap Integral Formalism

We write the classical Hamiltonian as the total energy stored in the electric and magnetic fields in the volume V including all vacuum and dielectric regions of the device.

$$H = \frac{1}{2}\epsilon \int_V \mathbf{E}(\mathbf{x}) \cdot \mathbf{E}(\mathbf{x}) d^3\mathbf{x} + \frac{1}{2}\mu \int_V \mathbf{H}(\mathbf{x}) \cdot \mathbf{H}(\mathbf{x}) d^3\mathbf{x} \quad (3.1)$$

Then, we expand the electric and magnetic fields in terms of the eigenmode fields $\{\mathbf{E}_k, \mathbf{H}_k\}$ which are solutions to the Helmholtz equation at particular wavenumbers k subject to boundary conditions applied to the modeled structure, e.g. perfect electric conductor boundary conditions on the surfaces of all vacuum regions and vacuum impedance boundary conditions²⁴ where appropriate. These solutions are the output of an eigenmode solution type simulation performed with the Ansys HFSS finite element method software. The expansion coefficients $\{q_k, \phi_k\}$ are suggestive of dimensionless charge and flux operators²⁵

$$\mathbf{E}(\mathbf{x}) = \sum_k q_k \mathbf{E}_k(\mathbf{x}) = \sum_k \tilde{q}_k \tilde{\mathbf{E}}_k(\mathbf{x}) \quad (3.2)$$

$$\mathbf{H}(\mathbf{x}) = \sum_k \phi_k \mathbf{H}_k(\mathbf{x}) = \sum_k \tilde{\phi}_k \tilde{\mathbf{H}}_k(\mathbf{x}) \quad (3.3)$$

where the tilde functions denote solutions evaluated at a particular static parameter value, e.g. $L_J = L_{J_0}$, referring to dc flux bias applied to a dc-SQUID with an effective inductance L_{J_0} . Substituting these expansions into the Hamiltonian in (3.1) gives

$$\begin{aligned} H &= \frac{1}{2} \sum_{kk'} \left[\epsilon q_k q_{k'} \int_V \mathbf{E}_k(\mathbf{x}) \cdot \mathbf{E}_{k'}(\mathbf{x}) d^3\mathbf{x} + \mu \phi_k \phi_{k'} \int_V \mathbf{H}_k(\mathbf{x}) \cdot \mathbf{H}_{k'}(\mathbf{x}) d^3\mathbf{x} \right] \\ &= \sum_k (q_k^2 \mathcal{E}_k^E + \phi_k^2 \mathcal{E}_k^H) \end{aligned} \quad (3.4)$$

In the second line of (3.4) we used the orthogonality of the electric field eigenfunctions, and recognize the terms in the integrals are equivalent to the magnetic field and electric field energies $\mathcal{E}_k^E, \mathcal{E}_k^H$

$$\mathcal{E}_k^E = \frac{1}{2}\epsilon \int_V \mathbf{E}_k(\mathbf{x}) \cdot \mathbf{E}_k(\mathbf{x}) d^3\mathbf{x} \quad (3.5)$$

$$\mathcal{E}_k^H = \frac{1}{2}\mu \int_V \mathbf{H}_k(\mathbf{x}) \cdot \mathbf{H}_k(\mathbf{x}) d^3\mathbf{x} \quad (3.6)$$

We recall that these are the energies used to compute the participations in the energy participation ratio approach [103].

²⁴Here, a vacuum impedance boundary condition refers to an impedance boundary condition, described in Appendix C with an impedance $Z = \sqrt{\mu_0/\epsilon_0} \approx 337\Omega$.

²⁵We do not use hats to denote operators here in anticipation of the tilde notation used below to differentiate between L_J and L_{J_0} operators. The charge and flux operators do not have the corresponding zero fluctuation prefactors to lump all units into the eigenmode fields exported from HFSS.

The following derivation will show that these energies will be scaled by the field overlap integrals.

Before arriving at scaled field energy result, we would like to express the Hamiltonian in terms of the field eigenfunctions and operators evaluated at $L_J = L_{J_0}$. We relate the fields \mathbf{E}_k to $\tilde{\mathbf{E}}_k$ by

$$\tilde{\mathbf{E}}_k(\mathbf{x}) = \sum_{k''} A_{kk''}^E \mathbf{E}_{k''}(\mathbf{x}) \quad (3.7)$$

and multiplying both sides by $\mathbf{E}_{k'}$ then integrating over the volume V gives

$$\sum_{k''} A_{kk''}^E \int_V \mathbf{E}_{k'}(\mathbf{x}) \cdot \mathbf{E}_{k''}(\mathbf{x}) d^3\mathbf{x} = \int_V \mathbf{E}_{k'}(\mathbf{x}) \cdot \tilde{\mathbf{E}}_k(\mathbf{x}) d^3\mathbf{x} \quad (3.8)$$

Using the orthogonality of the electric field eigenfunctions, we can write the coefficients $A_{kk'}^E$ in terms of an overlap term and an electric field energy contribution

$$\begin{aligned} A_{kk'}^E \int_V \mathbf{E}_{k'}(\mathbf{x}) \cdot \mathbf{E}_{k'}(\mathbf{x}) d^3\mathbf{x} &= \int_V \mathbf{E}_{k'}(\mathbf{x}) \cdot \tilde{\mathbf{E}}_k(\mathbf{x}) d^3\mathbf{x} \\ \Rightarrow A_{kk'}^E &= \frac{2}{\epsilon \mathcal{E}_{k'}^E} \int_V \mathbf{E}_{k'}(\mathbf{x}) \cdot \tilde{\mathbf{E}}_k(\mathbf{x}) d^3\mathbf{x} \end{aligned} \quad (3.9)$$

Similarly, the magnetic eigenmode fields are related by

$$\tilde{\mathbf{H}}_k(\mathbf{x}) = \sum_{k''} A_{kk''}^H \mathbf{H}_{k''}(\mathbf{x}) \quad (3.10)$$

with the form of the expansion coefficients $A_{kk'}^H$ given by

$$A_{kk'}^H = \frac{2}{\mu \mathcal{E}_{k'}^H} \int_V \mathbf{H}_{k'}(\mathbf{x}) \cdot \tilde{\mathbf{H}}_k(\mathbf{x}) d^3\mathbf{x} \quad (3.11)$$

The matrices A^E and A^H are generalizations of the electric and magnetic field participation ratios defined in [103], evaluated at different mode number and junction inductance (or any control parameter in general). We will refer to these matrices as field overlap integrals or FOIs for short.

Next, we use the linear transformations connecting the electric and magnetic fields at L_J and L_{J_0} to relate the charges and fluxes at different inductances. Dropping the explicit \mathbf{x} -dependence of the fields, we have

$$\begin{aligned} \mathbf{E} &= \sum_{k'} \tilde{\mathbf{E}}_{k'} \tilde{q}_{k'} = \sum_{k'} \left[\sum_k A_{k'k}^E \mathbf{E}_k \right] \tilde{q}_{k'} = \sum_k \left[\sum_{k'} A_{k'k}^E \tilde{q}_{k'} \right] \mathbf{E}_k = \sum_k q_k \mathbf{E}_k \\ \Rightarrow q_k &= \sum_{k'} A_{k'k}^E \tilde{q}_{k'} \end{aligned} \quad (3.12)$$

Similarly, the fluxes are related by $\phi_k = \sum_{k'} A_{k'k}^H \tilde{\phi}_{k'}$. Substituting these expressions into the Hamiltonian in (3.1) gives

$$H = \sum_k \left\{ \mathcal{E}_k^E \sum_{k'k''} A_{k'k}^E A_{k''k}^E \tilde{q}_{k'} \tilde{q}_{k''} + \mathcal{E}_k^H \sum_{k'k''} A_{k'k}^H A_{k''k}^H \tilde{\phi}_{k'} \tilde{\phi}_{k''} \right\} \quad (3.13)$$

Exchanging indices in (3.13) we identify frequency terms associated with the electric and magnetic fields, $\Omega_{kk'}^E$, $\Omega_{kk'}^H$ as the bracketed terms, up to a factor of \hbar , in the first line below

$$\begin{aligned} H &= \sum_{kk'} \left\{ \left[\sum_{k''} \mathcal{E}_{k''}^E A_{kk''}^E A_{k''k'}^E \right] \tilde{q}_k \tilde{q}_{k'} + \left[\sum_{k''} \mathcal{E}_{k''}^H A_{kk''}^H A_{k''k'}^H \right] \tilde{\phi}_k \tilde{\phi}_{k'} \right\} \\ &= \sum_{kk'} \left\{ \hbar \Omega_{kk'}^E \tilde{q}_k \tilde{q}_{k'} + \hbar \Omega_{kk'}^H \tilde{\phi}_k \tilde{\phi}_{k'} \right\} \end{aligned} \quad (3.14)$$

Now we make the replacements $\tilde{q}_k = -i(\tilde{a}_k - \tilde{a}_k^\dagger)$ and $\tilde{\phi}_k = (\tilde{a}_k + \tilde{a}_k^\dagger)$, with $[\tilde{a}_k, \tilde{a}_{k'}] = \delta_{kk'}$ and we arrive at the beam splitter, single mode, and two mode squeezing Hamiltonian

$$H/\hbar = \sum_{kk'} \left[\Omega_{kk'}^H (\tilde{a}_k + \tilde{a}_k^\dagger) (\tilde{a}_{k'} + \tilde{a}_{k'}^\dagger) - \Omega_{kk'}^E (\tilde{a}_k - \tilde{a}_k^\dagger) (\tilde{a}_{k'} - \tilde{a}_{k'}^\dagger) \right] \quad (3.15)$$

$$\begin{aligned} &= \sum_k \left[2\tilde{\omega}_k (\tilde{a}_k^\dagger \tilde{a}_k + 1/2) + g_{\text{SMS},k} (\tilde{a}_k^2 + \tilde{a}_k^{\dagger 2}) \right] \\ &\quad + \sum_{k \neq k'} \left[g_{\text{BS},kk'} (\tilde{a}_k^\dagger \tilde{a}_{k'} + \tilde{a}_k \tilde{a}_{k'}^\dagger) + g_{\text{TMS},kk'} (\tilde{a}_k^\dagger \tilde{a}_{k'}^\dagger + \tilde{a}_k \tilde{a}_{k'}) \right] \end{aligned} \quad (3.16)$$

where the frequencies $\tilde{\omega}_k$, single mode squeezing $g_{\text{SMS},k}$, two mode squeezing $g_{\text{TMS},kk'}$, and beam splitter rates $g_{\text{BS},kk'}$ are given by

$$\tilde{\omega}_k = \Omega_{kk}^H + \Omega_{kk}^E \quad (3.17)$$

$$g_{\text{SMS},k} = \Omega_{kk}^H - \Omega_{kk}^E \quad (3.18)$$

$$g_{\text{TMS},kk'} = \Omega_{kk'}^H - \Omega_{kk'}^E \quad (3.19)$$

$$g_{\text{BS},kk'} = \Omega_{kk'}^H + \Omega_{kk'}^E \quad (3.20)$$

From these expressions, we see that beam splitter interactions are possible when the total energy is equally or unequally divided among the electric and magnetic field energies, whereas the single and two mode squeezing terms are nonzero only when there is an imbalance between the two field energies.

3.1.2 Flux Modulation and Parametric Rates

To induce parametric beam splitter, single mode, and two mode squeezing operations, we modulate the junction inductance such that $L_J \rightarrow L_{J_0} + \delta L_J \sin(\omega_{\text{sb}} t)$. Modulating L_J will modulate the resonance frequencies and couplings.

Expanding these functions about $L_J = L_{J_0}$ to first order in the modulation strength δL_J gives

$$\tilde{\omega}_k(L_J, L_{J_0}) \approx \tilde{\omega}_k(L_{J_0}, L_{J_0}) + \delta L_J \frac{d\tilde{\omega}_k}{dL_J} \Big|_{L_J=L_{J_0}} \sin(\omega_{sb}t) = \omega_k(L_{J_0}) + \epsilon_k \sin(\omega_{sb}t) \quad (3.21)$$

$$g_{\text{BS},k'k''}(L_J, L_{J_0}) \approx \underbrace{g_{\text{BS},k'k''}(L_{J_0}, L_{J_0})}_{0} + \delta L_J \frac{dg_{\text{BS},k'k''}}{dL_J} \Big|_{L_J=L_{J_0}} \sin(\omega_{sb}t) = \epsilon_{g_{\text{BS},k'k''}} \sin(\omega_{sb}t) \quad (3.22)$$

$$\begin{aligned} g_{\text{SMS},k'}(L_J, L_{J_0}) &\approx g_{\text{SMS},k'(L_{J_0}, L_{J_0})} + \delta L_J \frac{dg_{\text{SMS},k'}}{dL_J} \Big|_{L_J=L_{J_0}} \sin(\omega_{sb}t) \\ &= g_{\text{SMS},k'}^0 + \epsilon_{g_{\text{SMS},k'}} \sin(\omega_{sb}t) \end{aligned} \quad (3.23)$$

$$g_{\text{TMS},k'k''}(L_J, L_{J_0}) \approx \underbrace{g_{\text{TMS},k'k''}(L_{J_0}, L_{J_0})}_{0} + \delta L_J \frac{dg_{\text{TMS},k'k''}}{dL_J} \Big|_{L_J=L_{J_0}} \sin(\omega_{sb}t) = \epsilon_{g_{\text{TMS},k'k''}} \sin(\omega_{sb}t) \quad (3.24)$$

where we used the orthogonality of the eigenfunctions, i.e. $A_{k'k''}^E(L_{J_0}, L_{J_0}) = 0$ and $A_{k'k''}^H(L_{J_0}, L_{J_0}) = 0$ when $k' \neq k''$, to show that the first terms in the expansions of the couplings vanish.

To cancel the time dependence in the frequencies, we go to the rotating frame described by the unitary [110]

$$U(t) = \exp \left\{ i \sum_m \left[\left(\omega_m t - \frac{\epsilon_m}{2\omega_{sb}} \cos(\omega_{sb}t) \right) \tilde{a}_m^\dagger \tilde{a}_m \right] \right\} \quad (3.25)$$

whose action on the operators $\tilde{a}_{k'}$ is given by

$$\begin{aligned} U(t)\tilde{a}_{k'}U^\dagger(t) &= \tilde{a}_{k'} \exp \left[-i \left(\omega_{k'} t - \frac{\epsilon_{k'}}{2\omega_{sb}} \cos(\omega_{sb}t) \right) \right] \\ &= \tilde{a}_{k'} e^{-i\omega_{k'} t} e^{i\frac{\epsilon_{k'}}{2\omega_{sb}} \cos(\omega_{sb}t)} \end{aligned} \quad (3.26)$$

$$U(t)\tilde{a}_{k'}^\dagger(L_{J_0})U^\dagger(t) = \tilde{a}_{k'}^\dagger e^{i\omega_{k'} t} \sum_{m=-\infty}^{\infty} i^m J_m \left(\frac{\epsilon_{k'}}{2\omega_{sb}} \right) e^{im\omega_{sb}t} \quad (3.27)$$

We used the Jacobi-Anger expansion [176] of the second term (3.26) to express the exponentiated cosine in terms of Bessel functions of the first kind $J_m(z)$

$$e^{\pm iz \cos(x)} = \sum_{m=-\infty}^{\infty} i^{\pm m} J_m(z) e^{\pm imx} \quad (3.28)$$

Substituting the modulated frequencies and couplings into the Hamiltonian in (3.16) and going to the rotating frame defined by the unitary in (3.25), we find

$$\begin{aligned}
\mathcal{H}(t) \rightarrow \mathcal{H}' &= U(t)\mathcal{H}(t)U^\dagger(t) - iU(t)\partial_t U^\dagger(t) \\
&= \sum_{k'} \left[\tilde{a}_{k'}^2 \left(g_{\text{SMS},k}^0 + \epsilon_{g_{\text{SMS},k'}} \sin(\omega_{\text{sb}}t) \right) e^{-i2\omega_{k'} t} \right. \\
&\quad \times \sum_{m,n=-\infty}^{\infty} i^{(m+n)} J_m \left(\frac{\epsilon_{k'}}{2\omega_{\text{sb}}} \right) J_n \left(\frac{\epsilon_{k'}}{2\omega_{\text{sb}}} \right) e^{i(m+n)\omega_{\text{sb}}t} + \text{h.c.} \Big] \\
&\quad + \sum_{k' \neq k''} \left[\tilde{a}_{k'} \tilde{a}_{k''} \epsilon_{g_{\text{TMS},k'k''}} \sin(\omega_{\text{sb}}t) e^{-i\Sigma_{k'k''} t} \right. \\
&\quad \times \sum_{m,n=-\infty}^{\infty} i^{(m+n)} J_m \left(\frac{\epsilon_{k'}}{2\omega_{\text{sb}}} \right) J_n \left(\frac{\epsilon_{k''}}{2\omega_{\text{sb}}} \right) e^{i(m+n)\omega_{\text{sb}}t} + \text{h.c.} \Big] \\
&\quad + \sum_{k' \neq k''} \left[\tilde{a}_{k'}^\dagger \tilde{a}_{k''} \epsilon_{g_{\text{BS},k'k''}} \sin(\omega_{\text{sb}}t) e^{-i\Delta_{k'k''} t} \right. \\
&\quad \times \sum_{m,n=-\infty}^{\infty} i^{(m-n)} J_m \left(\frac{\epsilon_{k'}}{2\omega_{\text{sb}}} \right) J_n \left(\frac{\epsilon_{k''}}{2\omega_{\text{sb}}} \right) e^{i(m-n)\omega_{\text{sb}}t} + \text{h.c.} \Big] \tag{3.29}
\end{aligned}$$

where $\Sigma_{k'k''} = \omega_{k'} + \omega_{k''}$ and $\Delta_{k'k''} = \omega_{k'} - \omega_{k''}$ are the sum and difference frequencies between modes k' and k'' . By driving the coupler at $\omega_{\text{sb}} = \Delta_{kk'}$, the beam splitter terms with mode indices k, k' became stationary and the remaining terms rapidly oscillate, averaging to zero. Similarly, if take $\omega_{\text{sb}} = \Sigma_{kk'}$ or $\omega_{\text{sb}} = 2\omega_k$, then we enact the two or single mode squeezing operations. As with other parametric schemes such as [110, 111], the strength of the interaction is proportional to drive the strengths ($\epsilon_{g_{\text{BS}}}, \epsilon_{g_{\text{SMS}}}, \epsilon_{g_{\text{TMS}}}$) which is a function of the bare coupling strengths and the magnitude of the inductance modulation δL_J or equivalently, flux modulation.

3.2 Discussion

Prior to the BBQ quantization method, there were only a handful of 3D superconducting transmon qubits and the tools developed to analyze microwave circuits with cQED that had not been fully ported to the 3D domain. When the EPR method arrived, the black-box prescription had become exactly that, the default method to describe 3D cavity-Josephson junction systems, although the driven modal Ansys HFSS simulations in BBQ were fraught with ambiguities in identifying resonance frequencies and estimating losses²⁶ with expensive, fine frequency sweeps. EPR shifted the problem from driven modal frequency sweeps to obtain impedances or admittances to an eigenvalue problem centered around ratios of energies.

²⁶See Section 1.3.3 for a discussion of the subtleties encountered in those calculations.

With the advent of open source tools such as Qiskit Metal and KQCircuits, one can now drag and drop predefined graphical representations of superconducting circuits and generate a design ready for photolithography and electron beam deposition with predictive modeling tools that leverage EPR and BBQ for the quantum calculations.

This work looks to complement EPR and BBQ rather than supplanting them by generalizing the energy participation ratio approach to include the cross terms, or field overlap integrals, at different mode numbers and control or geometric parameters. We expect this technique to be closer to a first principles approach to estimate both parametric and bare coupling rates in general 2D and 3D systems. This method also holds applications in estimating loss rates to box modes and other parasitic resonances as a function of geometric and external control parameters [177].

3.3 Conclusion

We presented a novel design and analysis approach to estimating parametric and bare coupling rates in 3D superconducting cavity systems with an external tunable element. The method agrees with the BBQ and EPR analysis methods that have previously been shown to predict experimental Hamiltonian parameters within a few percent. An open source software package is under development to share our approach with the larger community of groups working on parametric tunable couplers and 3D superconducting qubits.

CHAPTER 4

GALVANIC COUPLING ELEMENT FOR SUPERCONDUCTING 3D CAVITIES

The continuous variable (CV) quantum computing field has expanded in the last five years with the first demonstrations of GKP states, as discussed in Section 1.1.2, in trapped ions [60] in 2019 and superconducting 3D cavity circuit QED systems shortly thereafter [61, 62]. Superconducting 3D cavity implementations of GKP state generation and gate operations owe their successes in part to precision control of harmonic oscillator states with nonlinear elements such as fixed and tunable frequency transmon qubits.

Another promising cavity-based qubit is the dual-rail qubit, where logical states $|0_L\rangle$, $|1_L\rangle$ map to the single photon subspace given by the presence of a photon in cavity a ($|0_L\rangle = |10\rangle$) or b ($|1_L\rangle = |01\rangle$). The original use of this encoding was in the optical domain [178], when beam splitters were readily available to generate superposition states, and nonlinearities were sourced from Kerr-media such as beta-barium-borate (BBO) [179]. With the arrival of high-coherence, parametrically activated microwave beam splitters [9, 12, 16], a dual rail qubit encoded in two superconducting microwave cavities has been demonstrated in [112, 113].

We highlight the role of the high-coherence beam splitters and general tunable couplers in realizing both dual rail qubit encodings and enacting gates on GKP states through parametrically activated interactions between two modes (a, b) of the form: $H_{\text{int}} = g_{\text{BS}}ab^\dagger + \text{h.c.}$ for frequency conversion (or beam splitter operations) and $H_{\text{int}} = g_{\text{TMS}}ab + \text{h.c.}$ for amplification (or two mode squeezing) [58]. With the exception of the work by Lu et al. [16], these tunable couplers have relied on capacitive coupling to a fixed frequency transmon, tunable transmon (or SQUID), or Superconducting Nonlinear Asymmetric Inductive eElement (SNAIL). To that end, we present a new tunable coupler design based on a galvanic coupling element inspired by earlier planar realizations [8, 11, 180]. Estimates of the coupler loss channels indicate that it preserves the base coherence of the buffer cavity and is at least competitive with the latest 3D couplers in interaction strengths.

Here we present the first step towards a galvanic 3D tunable coupler, a linear tunable element that minimally reduces the base coherence of the host cavity. We give a description of its operating principles, estimate its tuning range and contributions to loss from contact resistance, radiation losses, dielectric loss tangent, and wall losses.

4.1 Two Post Coupler Design and Operation

The two post coupler is a derivative of the earlier single post $\lambda/4$ cavity whose fundamental mode is set by the post height. As with other $\lambda/4$ resonances, the first harmonic is a factor of three higher in frequency ($3\lambda/4$), which can be advantageous when trying to isolate a single mode, but undesirable if one is interested in manipulating multiple cavity modes [106]. The single post design's success is due to its simplicity and negligible seam loss, as the post is embedded in a cylindrical cavity with a length much larger than the post such that the electric fields and the surface currents are exponentially suppressed at the top of the cavity where there is a seam [50, 144]. An essentially “seamless” design, the single post cavity is the preferred first choice for 3D transmon realizations, where the transmon and control signals are inserted into the high electric field region near the post, maximizing the dipole coupling between the transmon and cavity fields [105]. Strong electric fields also couple to the dielectric substrate, typically chosen to be sapphire for its relatively low bulk dielectric loss tangent $\tan \delta = 1.9 \times 10^{-8}$ [4].

One might ask, is it possible to couple cavity fields with a nonlinear element such as a transmon or SQUID without placing the substrate in a high electric field region? Lu et al. [16] answered this question in the affirmative with a SQUID coupled to the high magnetic fields near the bottom of a single post cavity where the electric fields are suppressed. Our design takes this idea one step further, moving the SQUID to the boundary of a two post cavity, coupling it to the cavity currents by direct, galvanic contact between its pads and the two posts. The two lowest modes of the two post coupler are high- Q , similar to the single post in that the electric fields fall off exponentially from the posts, minimizing seam loss at the top of the cavity.

To make contact between the posts and the SQUID capacitor pads, a slot is cut between and underneath the two posts to interrupt the current flowing between the posts in the differential mode shown in the right panel of Figure 4.1. This mode is the first harmonic of the two post cavity, while the fundamental mode is referred to as the common mode as the electric fields and surface currents on both posts point in the same direction. It follows that the differential mode will change as the inductance of the SQUID changes with dc flux bias. The common mode will not tune with flux as there is a current node at the location of the SQUID. All other higher low- Q modes do not participate with the SQUID in electric fields, magnetic fields, or surface currents and will not tune.

The SQUID can be modeled as an effective nonlinear inductor whose inductance is a function of the flux threaded through the SQUID loop [77]

$$L_J(\Phi) = \frac{L_{J_0}}{\cos(2\pi\Phi/\Phi_0)} \quad (4.1)$$

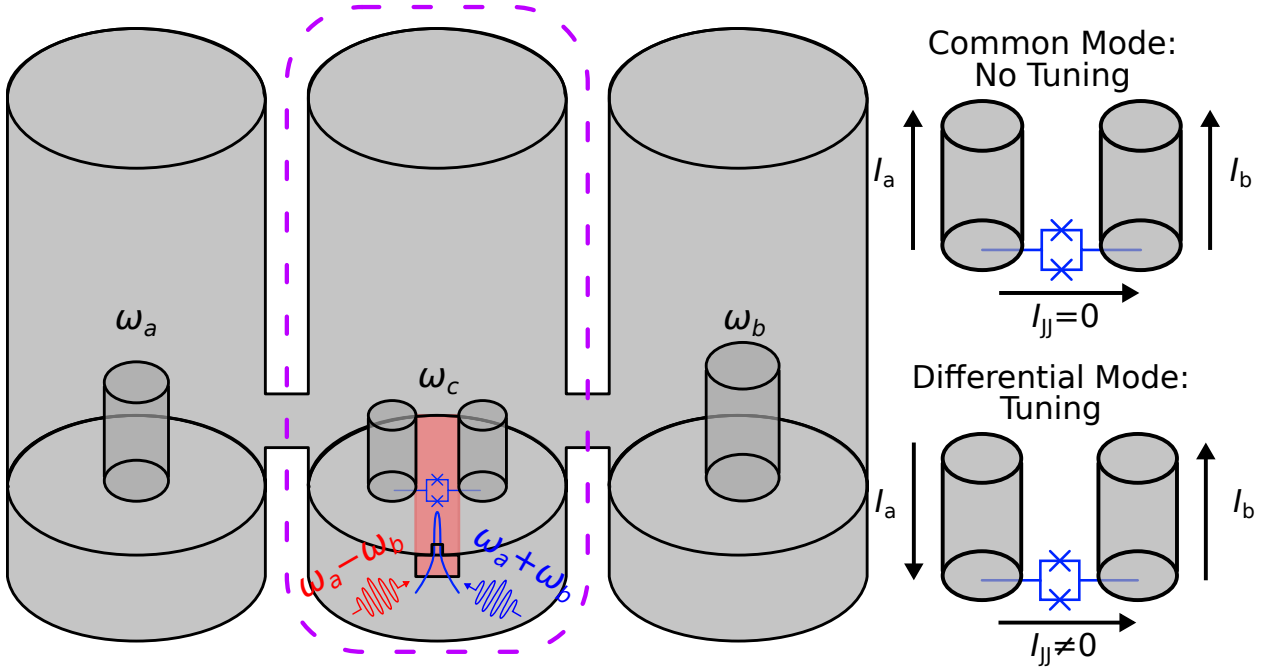


Figure 4.1 Two post coupler design. Left: two cavities ω_a , ω_b are coupled to a central cavity ω_c with a SQUID connecting its posts. The coupler itself is encircled with a purple dashed box. Right: common and differential current modes of the lowest two modes of the split post cavity with a SQUID connecting the posts. No current flows through the SQUID ($I_{JJ} = 0$) in the common mode, yet nonzero current flows through the SQUID in the differential mode.

Replacing the SQUID with a variable inductor simplifies the analysis and allows us to express the coupling strengths in terms of electric and magnetic field overlap integrals as was discussed in Chapter 3. The couplings are parametrically activated by applying an ac flux bias at the sum (blue sideband) and difference (red sideband) frequencies of the cavities a and b in Figure 4.1. These interactions are also referred to as the beam splitter $H_{BS} = g_{BS}ab^\dagger + \text{h.c.}$ and two mode squeezing $H_{TMS} = g_{TMS}ab + \text{h.c.}$ terms. To arrive at these interactions, we briefly summarize the results of the work in Chapter 3 relating the quadratic Hamiltonian for an arbitrary structure with electric and magnetic field energies defined by the integrals

$$H = \frac{1}{2}\epsilon \int_V \mathbf{E}(\mathbf{x}) \cdot \mathbf{E}(\mathbf{x}) d^3x + \frac{1}{2}\mu \int_V \mathbf{H}(\mathbf{x}) \cdot \mathbf{H}(\mathbf{x}) d^3x \quad (4.2)$$

Expanding the electric and magnetic fields in terms of their eigenmode solutions at a given inductance L_J and expressing those fields as linear combinations of fields at a fixed inductance L_{J_0} , we arrive at a Hamiltonian in the L_{J_0} basis (operators and eigenmode fields with tildes).

This Hamiltonian, with all operators, electric, and magnetic eigenmode solutions with tildes, whose coefficients are functions of field overlaps at different mode numbers and inductances is given by

$$H/\hbar = \sum_k \left[\tilde{\omega}_k \left(\tilde{a}_k^\dagger \tilde{a}_k + 1/2 \right) + g_{\text{SMS},k} \left(\tilde{a}_k^2 + \tilde{a}_k^{\dagger 2} \right) \right] \\ + \sum_{k \neq k'} \left[g_{\text{BS},kk'} \left(\tilde{a}_k^\dagger \tilde{a}_{k'} + \tilde{a}_k \tilde{a}_{k'}^\dagger \right) + g_{\text{TMS},kk'} \left(\tilde{a}_k^\dagger \tilde{a}_{k'}^\dagger + \tilde{a}_k \tilde{a}_{k'} \right) \right] \quad (4.3)$$

The ultimate goal of this work is to calculate the magnitude of the beam splitter, single mode squeezing, and two mode squeezing coefficients, $g_{\text{BS},kk'}$, $g_{\text{SMS},k}$, $g_{\text{TMS},kk'}$ using EPR, BBQ, and the field overlap integral method developed as part of this thesis. Before performing those calculations, we will survey the geometric parameter landscape of the coupler to gain intuition into the design trade-offs between loss mechanisms and tuning range which directly translates to bare and parametric coupling strengths.

4.1.1 Two Coupler Geometric Studies

We studied a subset of the geometric design parameters of the coupler as a coarse-grained search of the larger parameter space to discern the interplay between losses and coupling strengths in this design. There are reasons to suspect, a priori, that coupling and seam loss will track with one another, as the tuning of the differential mode in this galvanic design should depend on the amount of current flowing across the junction (SQUID, referred to interchangeably as the junction hereon) and the seam loss goes as the square of the current across a seam [27, 181]

$$Q_{\text{seam}}^{-1} = G_{\text{seam}}^{-1} \frac{L \int_{\gamma_{\text{seam}}} |\mathbf{J} \times \mathbf{l}|^2 d\mathbf{l}}{\omega \mu_0 \int_V |\mathbf{H}|^2 d^3\mathbf{x}} = \frac{y_{\text{seam}}}{g_{\text{seam}}}. \quad (4.4)$$

We will focus on the numerator of (4.4), as the denominator is a material-dependent factor, whose value can range by orders of magnitude depending on the materials used and the clamping force at the joint. Unlike in the split post cavity in Chapter 7 and other applications where microwave transmission lines or cavities encounter a seam and y_{seam} can be engineered to be small,²⁷ we want to maximize the amount current flowing across the junction. By convention, the seam loss is calculated at the smallest, innermost intersection between two metallic contacts [182], which happens to be where the junction pads contact the bottom of the posts.

In Figure 4.2, we report the geometric sweeps, focusing on the pad width and post diameter that change the length of the post-pad intersection where the seam loss is calculated. We see that the seam admittance is sensitive to the pad width, and to a lesser extent to the post diameter.

²⁷For example, one can select a seam along a plane where there are no currents perpendicular to the seam for the mode of interest, or quarter wave chokes can create a current node at the location of the seam.

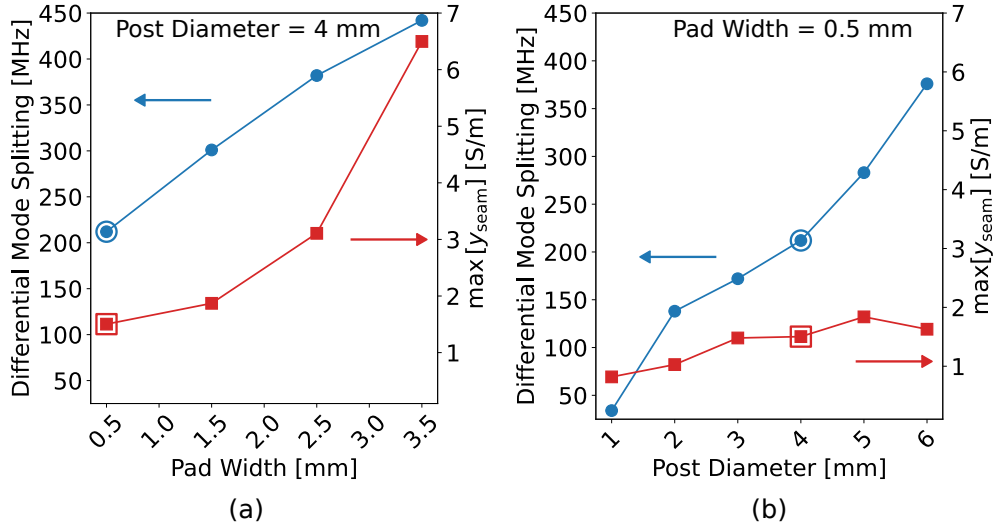


Figure 4.2 Geometric studies of tuning range and maximum seam admittance. (a) Coupler pad width sweep and (b) coupler post diameter sweep. Tuning range is calculated as the difference in frequency of the differential mode at $L_J = 1$ nH and $L_J = 10$ nH where the frequency change is linear in L_J . Encircled points indicate the “optimal” design points in Section 4.2 and post diameter, pad width labels indicate the fixed values used in each sweep.

4.2 Optimized Design Results

Following the geometric studies, we converged on a candidate design in the two post configuration with large tuning and bounded loss. We note that this is not an optimal design in the sense of a local minimum of a cost function and there are additional experimental limitations, such as the actual range of L_J .

In Figure 4.3, we see that the differential mode (Diff) tunes by hundreds of MHz, with a linear tuning range between 1 and 10 nH, achievable with contemporary dc-SQUID static flux biases. As expected, the common mode (Comm) does not tune with L_J . We fit the differential mode response to a phenomenological model accounting for the change in inductance and a vertical offset ω_0

$$\omega_{\text{Diff}} = \omega_0 + \frac{1}{\sqrt{(L + L_J)C}} \quad (4.5)$$

where C is the capacitance of the mode and L is related to the bare mode frequency by C .

The mode quality factors reported are the upper bounds, as the finite element model only includes dielectric and radiative losses in the calculation of the mode quality factors. We observe that the due to negligible participation of the junction in the common mode, the common mode does not vary with L_J . The differential mode Q_i , however, decreases by an order of magnitude, from 3×10^9 at low L_J to 2×10^8 at $L_J = 10$ nH, in the desired linear range of tuning. This sets a stringent requirement on the seam conductance on the order of 10^8 – 10^9 S/m to recover the radiation and dielectric loss limit of the coupler.

The highest seam conductance reported in the literature is $g_{\text{seam}} > 10^{10}$ S/m in indium-indium bump bonds and g_{seam} approaching 10^9 S/m in indium cavities, and high purity aluminum cavities (4N) with currents perpendicular to seams have $g_{\text{seam}} \sim 10^4$ S/m [181].

This analysis might suggest that the coupler quality factor is limited to $Q_i \sim 10^4$ – 10^5 , three to four orders of magnitude less than the upper bound given by the dielectric and radiation loss calculations. Recent work in sputtering $1.6\ \mu\text{m}$ aluminum thin films onto diamond-turned 6061-Al cavities gave a $g_{\text{seam}} = 5.9 \times 10^7$ S/m [182]. The more likely solution for this design is a form of indium bump bonding, with indium hemispheres deposited onto the SQUID pads. Contact is made by pressing the chip with the pads and indium bump bonds into the posts with a clamp from the bottom of the cavity.

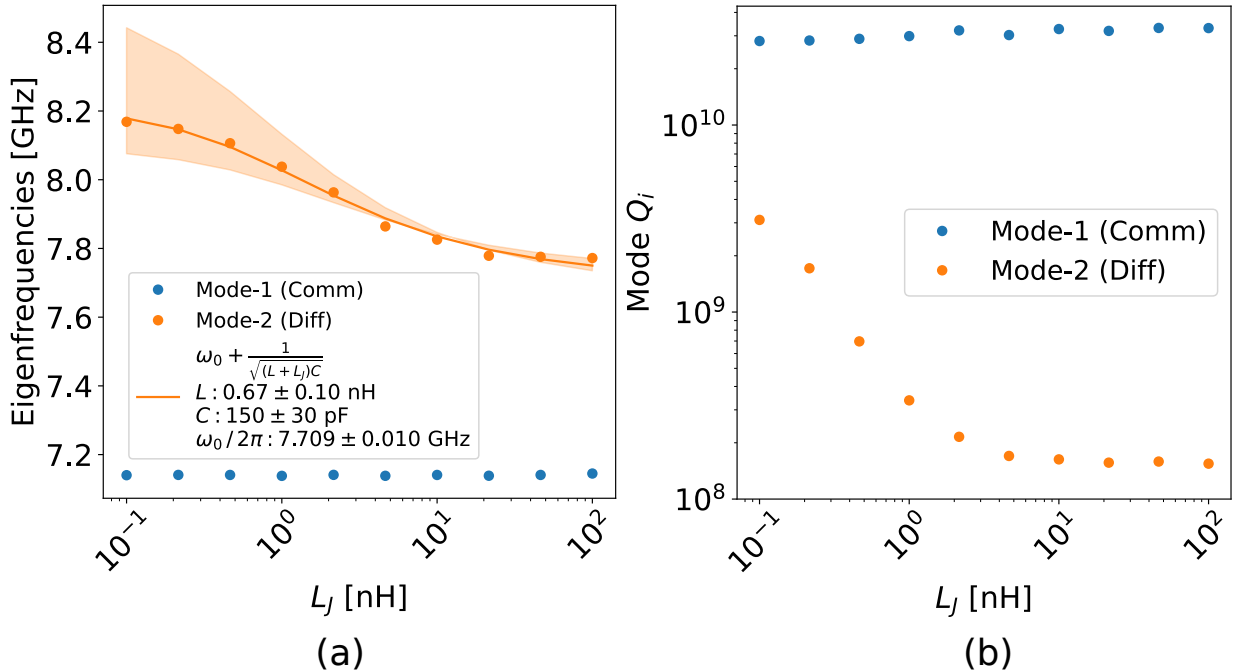


Figure 4.3 Optimized design mode tunings (a) and quality factor upper bounds, including radiative and dielectric losses (b) as a function of junction inductance L_J .

4.3 Conclusion

We designed a 3D galvanic tunable coupler with estimated tuning of hundreds of MHz over a range of SQUID inductances of 1 to 10 nH. The losses of this coupler are dominated by the high seam admittance where the SQUID pads contact the cavity posts. The radiative and dielectric losses of the differential mode that tunes are one to two orders of magnitude higher than the stationary common mode. Future calculations aim to estimate the parametric coupling rates with the field integral overlap method, as well as detailed simulations of the losses incurred by introducing a flux line into the coupler cavity.

CHAPTER 5

COPLANAR WAVEGUIDE MICROWAVE LOSS EXPERIMENTS

The performance of superconducting qubits, and all solid state qubits for that matter, is bounded by the intrinsic loss properties of their constituent materials. As we discussed in Section 1.5, Gao [66] identified the primary excess noise source in superconducting resonator as surface and interface states modeled by a distribution of two level systems. Superconducting qubits are subject to the same noise sources [129], and superconducting resonators have long been a proxy for investigating those losses that manifest in qubits.

5.1 Loss Budgets

A recent series of systematic studies performed by Calusine et al. [183], Woods et al. [25], and Melville et al. [184] used trenching and isotropic etching of coplanar waveguide resonators to disentangle losses from each interface of the resonators – substrate-air (SA), metal-air (MA), metal-substrate (MS), and bulk substrate.²⁸ Each interface is assigned an electric field participation p_j which is a ratio of the electric field energy stored in that interface region with volume V_j and dielectric constant ϵ_j relative to the electric energy stored in the entire device, including relevant vacuum regions

$$p_j = \frac{\frac{1}{2}\epsilon_j \int_{V_j} |\mathbf{E}|^2 d^3\mathbf{x}}{U_{E,tot}} \quad (5.1)$$

$$U_{E,tot} = \sum_j \frac{1}{2}\epsilon_j \int_{V_j} |\mathbf{E}|^2 d^3\mathbf{x} \quad (5.2)$$

where $\epsilon_j = \epsilon_0 \epsilon_{r_j}$ and the sum defining the total electric field energy $U_{E,tot}$ runs over all objects considered in a finite element simulation of the resonator. These participations are calculated with either a full-wave 3D finite element electromagnetic simulation or a 2D cross-sectional electrostatic simulation of a section of CPW resonator, e.g. all vacuum and dielectric regions. The 2D cross-sectional electrostatic simulations assume that the electric fields are constant over the thickness $t_{ox,j}$ defining the interface region, replacing the numerator in (5.1) with

$$p_j = \frac{\frac{1}{2}\epsilon_j t_{ox,j} \int_{S_j} |\mathbf{E}|^2 d^3\mathbf{x}}{U_{E,tot}} \quad (5.3)$$

where S_j is the surface of the interface. Each interface is assigned a thickness extracted from cross-sectional transmission electron microscopy (TEM) imaging or estimated to be on the order of 3 nm, in most cases for Nb and Al thin films and bulk, etched metals [4, 185].

²⁸The bulk substrate loss is attributed to the volume of the substrate and not an interface.

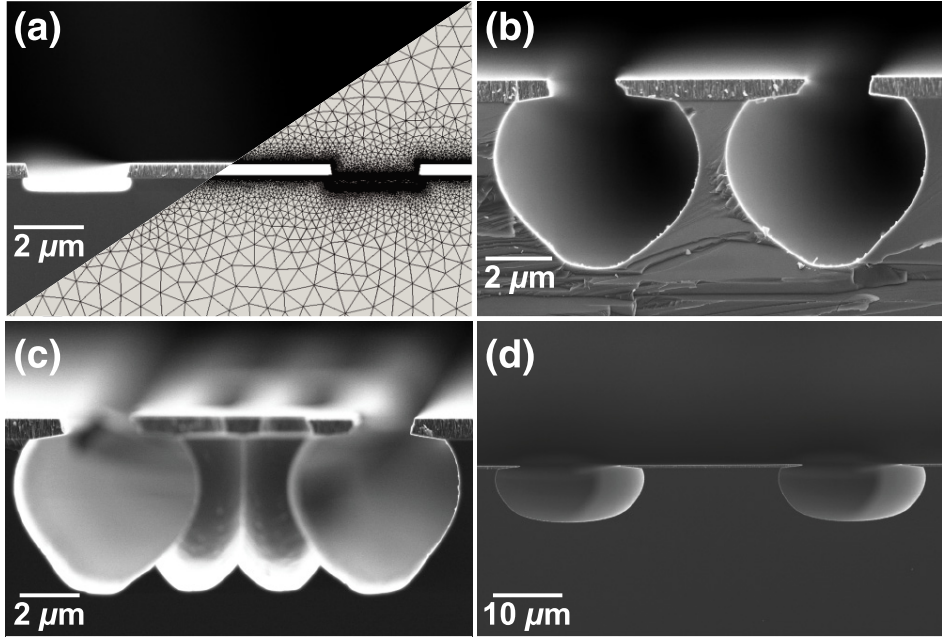


Figure 5.1 Etching of silicon to accentuate interface and bulk losses. MS (a), SA (b), MA (c), and bulk (d) concentrated geometries fabricated with isotropic etching of TiN CPW resonators on silicon. Reproduced with permission from [25].

In Figure 5.1, we highlight the work of Woods et al. [25], illustrating the extreme geometries needed to separate the three interface and bulk losses. Using an isotropic etch of silicon in Figure 5.1, Woods et al. fabricated four sets of resonators that are sensitive to the three interface types and the bulk substrate, separately. Extracting the loss contributions from these four regions requires measuring hundreds of resonators to accumulate statistics for each loss contribution. These measurements are combined with simulations of the participations for each region and the loss contribution from each region is extracted by solving the linear system of equations [25]

$$\begin{pmatrix} p_{MS,1} & p_{SA,1} & p_{MA,1} & p_{Si,1} \\ p_{MS,2} & p_{SA,2} & p_{MA,2} & p_{Si,2} \\ p_{MS,3} & p_{SA,3} & p_{MA,3} & p_{Si,3} \\ p_{MS,4} & p_{SA,4} & p_{MA,4} & p_{Si,4} \end{pmatrix} \begin{pmatrix} x_{MS} \\ x_{SA} \\ x_{MA} \\ x_{Si} \end{pmatrix} = \begin{pmatrix} 1/Q_{TLS,1} \\ 1/Q_{TLS,2} \\ 1/Q_{TLS,3} \\ 1/Q_{TLS,4} \end{pmatrix} \quad (5.4)$$

where the right hand side is a column vector of measured TLS losses for each resonator, the left hand side matrix is the participation matrix with columns corresponding to the interface and bulk participations and rows corresponding to the values simulated for the four resonator geometries, and the column vector of x 's is the normalized loss factors for each interface and the bulk.

These loss factors are proportional to the dielectric loss tangent associated with each interface, normalized to the simulated (nom or nominal) and measured interface thicknesses (without the nom subscript) [25]

$$x_j = \begin{cases} \frac{t_j/t_{\text{nom},j}}{\epsilon_{\text{nom},j}/\epsilon_j} \tan \delta_j, & \text{if } \mathbf{E} \parallel \text{to interface} \\ \frac{t_j/t_{\text{nom},j}}{\epsilon_j/\epsilon_{\text{nom},j}} \tan \delta_j, & \text{if } \mathbf{E} \perp \text{to interface} \end{cases} \quad (5.5)$$

The ideal participation matrix is the identity matrix, with a condition number²⁹ equal to one. Extreme geometries lead to a participation matrix that approximates the identity by concentrating the electric field energy in one interface (or in the bulk).

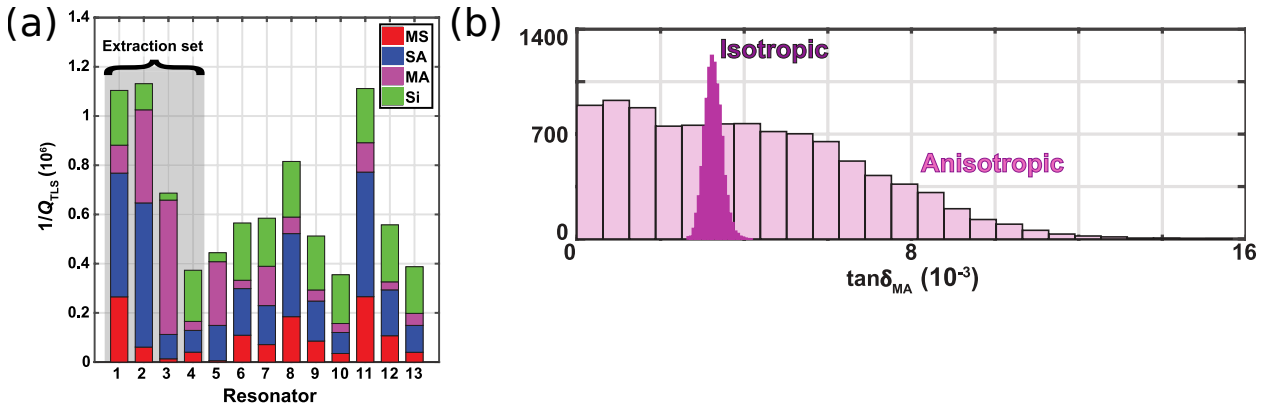


Figure 5.2 (a) Loss budgets of resonators measured in [25] with the highlighted resonators exhibiting the sensitivity to one interface or bulk loss. (b) Simulated isotropic and anisotropic etched device loss tangents to illustrate the increased sensitivity to the MA interface. Reproduced with permission from [25].

Figure 5.2 (a) shows a series of loss budgets with the individual loss contributions for each resonator adding to the total measured TLS loss. The highlighted resonators, starting from the left, exhibit high sensitivity to the SA, MA, and bulk silicon losses. Not shown, is a resonator that is more sensitive to MS interface losses as in the geometry from Figure 5.1 (c). In Figure 5.2 (b), two histograms of simulated anisotropically and isotropically etched devices clearly illustrates the necessity for these extreme geometries, as well as the large disparity between the condition numbers of the participation matrices for each etching process, 100000 vs. 2000 in the anisotropic and isotropic geometries, respectively [25].

In Chapter 7, we will discuss experiments tailored to extracting bulk losses in three inch wafers. This complementary measurement technique aims to screen wafers from various vendors, processed under different conditions that are not as easily accessible to CPW measurement approaches.

²⁹The condition number is a measure of the difficulty of inverting a matrix. Depending on the definition, it is the ratio of the maximum and minimum singular values, the ratio of largest and smallest eigenvalues, or the product of the norms of the matrix and its inverse or pseudoinverse. The identity matrix has a condition number of one and all other matrices are greater than one, with larger condition number corresponding to a more difficult linear system to solve.

We summarized the work by Woods et al. [25] and the companion papers from MIT Lincoln Laboratory to give context to the other loss measurements reported in this chapter and to contrast with the cavity measurements in Chapter 7. The next section will review another class of techniques where the geometry of the CPW resonators is fixed, but the materials or fabrication conditions are changed to observe changes due to those materials rather than separating contributions from all interfaces rigorously in every experiment.

5.2 A/B Testing for Comparative Loss Extraction Experiments

The set of materials and fabrication controls in superconducting resonators and qubits is large, yet finite. There are only so many elemental superconductors and related alloys that have the transition temperatures, and by extension superconducting gaps, that are compatible with microwave control and millikelvin temperature dilution refrigerators. Among these are aluminum (Al), niobium (Nb), tantalum (Ta), and their alloys with titanium (Ti) and nitrogen (N). There are other materials including the oxides that form Josephson junction tunnel barriers, as well as the III-V semiconductors used in the super-semi-gatemon qubits and tunable couplers discussed in Chapter 2, but the focus of this chapter will be on Al, Nb, Ta, and their alloys. The space of fabrication controls is much larger and interdependent, including but not limited to substrate temperatures, electron beam and sputtering energies, etching processes and acids, argon ion milling, liftoff processes, and countless others outside of the scope of this thesis [41, 186].

In Chapter 6, we will discuss the role of grain size in superconducting resonator loss, specifically on Ta thin films growth on c-axis sapphire. The next section will address the effects of hydrofluoric (HF) acid etching on the loss of Nb resonators, along with definitive aging comparisons. A subsequent section will review a series of capping studies where superconducting resonators are capped with normal metals, other superconductors, or dielectrics to modify the MA interface. In each study, the A/B comparison is between a control (A), an untreated Nb or Ta resonator and (B) a device with a capping layer or chemical treatment. The comparisons focus on TLS losses and power independent (PI) or losses due to the conductivity of the superconductor.

5.2.1 Niobium Hydride Experiments

This section is based on unpublished work performed with Northwestern, University of Colorado Boulder, NIST Boulder, and other collaborators in the Superconducting Quantum Materials and Systems (SQMS) National Quantum Initiative (NQI) Center [187]. The experiment involved six devices with eight Nb resonators per device, fabricated with the “white paper mask” [188] on intrinsic silicon substrates.

Each device received a different wet chemical etch treatment with the labels: CTRL (control, untreated Nb), HF2p (2 % HF), HF5p (5 % HF), HF8p (8 % HF), NH4F (ammonium fluoride or NH₄F), and BOE (buffered oxide etch, 5:1 NH₄F:HF). These etchants are used throughout typical semiconductor fabrication process steps that have been adapted for superconducting qubits and resonators. HF, in particular, has been shown to remove the lossy niobium pentoxide, Nb₂O₅ that is associated with increased TLS loss and that oxide, along with the Nb₂O₃ and NbO suboxides that have been the focus of other studies led by the SQMS center [189].

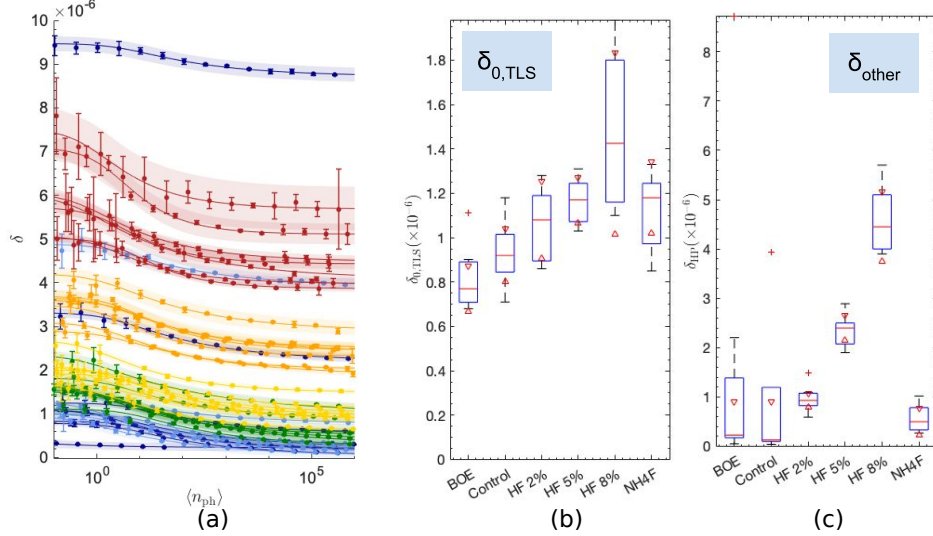


Figure 5.3 Niobium hydride microwave measurements. (a) Summary of the power dependence of the losses of all resonators. Box and whisker plots of (b) the TLS loss and (c) power independent loss. The labels on the box and whisker plots are as follows: blue box – bottom line is 25th percentile, top line is the 75th percentile; black horizontal lines – minimum / maximum values, excluding outliers; red plus signs – outliers; red horizontal lines – median values; red triangles – 95 % confidence intervals about the median; dashed black lines – “whiskers” extending from the 25th percentile to the minimum and from the maximum to the 75th percentile.

Although HF and other fluorine-based etchants effectively strip oxides from the Nb surfaces and silicon substrate, hydrogen can incorporate into the bulk of the Nb film after the Nb₂O₅ is removed, producing niobium hydrides NbH_x of various phases. The presence of these hydrides was first observed in superconducting Nb cavities tailored to particle accelerator applications following similar wet chemical treatments that led to significant reductions in the internal quality factors of those cavities [190]. The SQMS study with six devices tracked two phases of NbH_x, the α -NbH_x superconducting phase with a lower T_c than Nb and the β -NbH_x phase that does not exhibit superconductivity, at least down to 1.3 K [191].

The α phase is body centered cubic (BCC) with interstitial hydrogen occupying a tetrahedral site in the Nb metal, while the β phase is face centered orthorhombic (FCO) on tetrahedral sites at higher hydrogen concentrations [192]. As the concentration of HF in the acids increases, so does the hydrogen content in the Nb film and the number of hydrides in the film. The room temperature materials characterization of these films is outside of the scope of this thesis, but we note that it correlated the presence of hydrides at room temperature with the microwave loss measurements results that are the focus of this chapter.

We expect that the T_c will decrease for the films with high HF concentration, leading to more thermal equilibrium quasiparticles and power independent losses. To investigate the link between increased hydrides from HF and other fluoride-based acidic treatments, we performed microwave transmission measurements, extracting the power independent and TLS losses for each device. In Figure 5.3, we summarize the microwave loss measurements, with the TLS curves in (a) of all resonators across the six devices, and the TLS loss and power independent losses in (b) and (c). There is a distinct increase in the power independent loss with increasing HF concentration, consistent with the materials characterization findings indicating that more hydrogen incorporates into the Nb film forming the lower T_c and non-superconducting α and β phases of NbH_x . We observe a weak dependence with HF concentration and TLS loss, with a notable increase in the spread of the losses.

After exposing the devices to atmosphere for two months on a laboratory bench, we repeated our microwave measurements to study the effects of aging on oxide growth and hydrogen loading. In Figure 5.4, we report the TLS and power independent losses before and after aging. Power independent losses did not appreciably change due to aging, consistent with the connection made between hydrogen loading and power independent losses, as the only change expected from aging is an increase in oxide thickness on the metal-air and substrate air interfaces. The hydrogen content in the Nb film should not change with time, as the resident hydrogen in the bulk is likely trapped by the surface oxide which also prevents further incorporation of hydrogen with prolonged exposure to atmosphere. TLS losses increased across all six samples, consistent with previous aging studies [193] and the correlation between surface oxide thickness and TLS loss. Our results may also contradict other studies linking hydrides with variations in loss from cooldown-to-cooldown and changes in TLS losses with aging [194].

5.2.2 Capping Studies

As we have discussed in the previous sections, the interfaces, especially the metal air (MA) or the surface of the superconductor, affect the loss of resonators due to the presence of oxides and hydrides. To change the MA interface, one might consider adding a capping layer to the metal superconductor to either prevent oxides of that metal from forming or use a metal with a less lossy oxide, such as Ta.

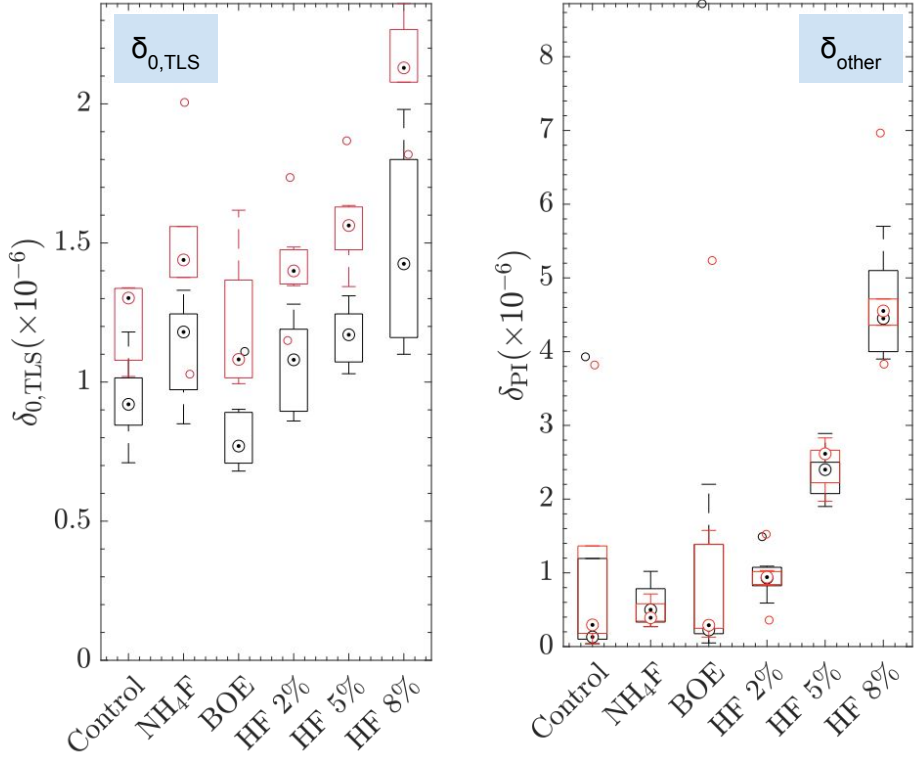


Figure 5.4 Aging study of niobium hydride samples following two months of aging in laboratory atmosphere. (a) TLS losses and (b) power independent losses before (black) and after (red) aging.

Such a study of capped qubits was recently performed by [195] where Nb qubits were capped with Al, TiN, and Ta. This work is under review and some of our recent measurements agree with their results that, on average, these capping strategies lead to minimal changes in the loss between the capped and control devices.

Figure 5.5 summarizes the capped devices with Ta, TiN, Si, and PdAu fabricated at Rigetti Computing, NIST Quantum Sensors Group, Northwestern University, and Fermilab. The results show minimal improvement, if any, over the control devices with capping for the power independent and TLS losses. There are differences among the Nb control devices when considering the substrate used, silicon or sapphire, where the silicon devices have significantly lower TLS losses. This difference can be accounted for by considering the difference in trenching of the silicon substrate from the etch that is not present in sapphire devices, as the etchants used do not significantly etch the sapphire. The silicon trenching reduces the SA participation of the resonators deposited on silicon relative to those patterned on sapphire. Rescaling the loss of the sapphire in Figure 5.6 by the ratio of participations for the trenched silicon and the untrenched sapphire gives a similar total loss for both substrates across the totality of control samples.

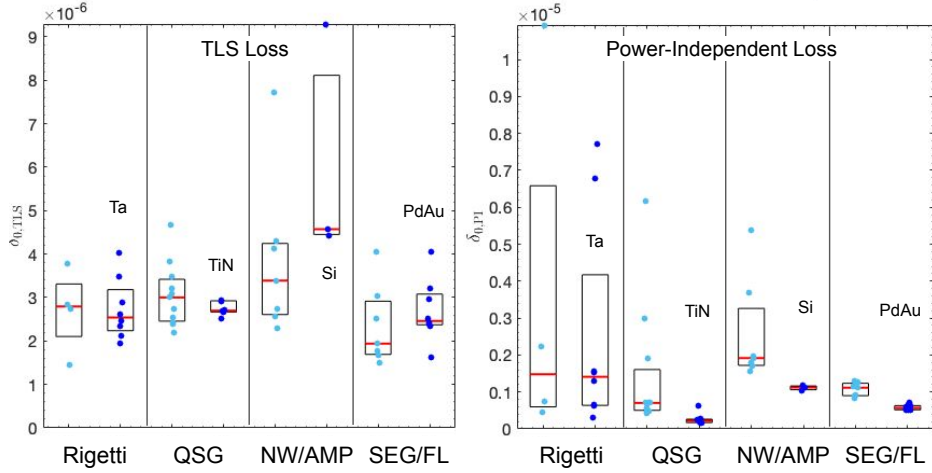


Figure 5.5 Capping studies of devices from multiple groups and fabrication conditions. Rigetti: dc sputtered Nb on high resistivity silicon; NIST Quantum Sensors Group (QSG): HEMEX sapphire prepared with NH_4OH , sputtered 200 nm Nb with 10 nm TiN, SF6 etch; Northwestern (NW) / Advanced Microwave Photonics (AMP): sputtered 85 nm of Nb on a-plane sapphire with in situ 10 nm electron beam silicon; NIST Superconductive Electronics Group (SEG) / Fermilab: PVD 160 nm Nb, 10 nm PdAu on crystal systems HEMEX sapphire. Left (light blue) control and right(dark blue) capped resonators.

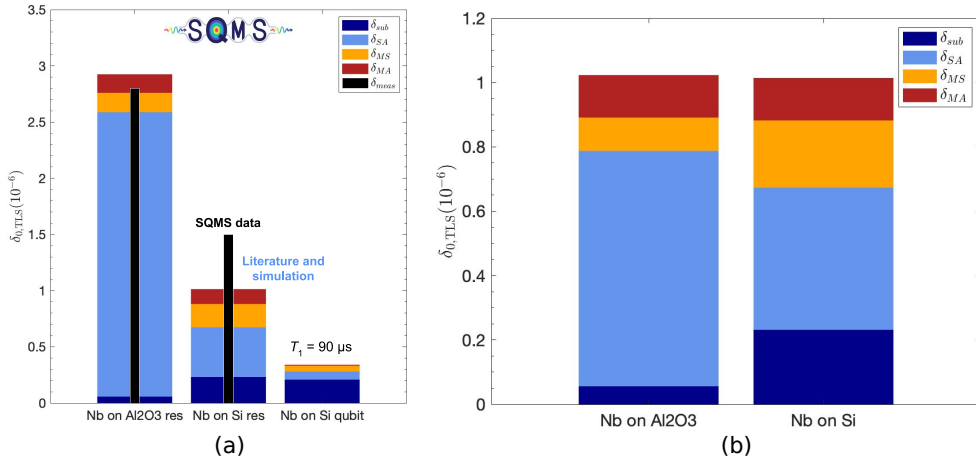


Figure 5.6 Approximate loss budgets constructed from a combination of experimental loss data and simulated device participations. (a) Unscaled data from all Nb control devices from the capping studies on sapphire (Al_2O_3) and silicon, along with Nb control qubits. The thick bar center bars indicate the measured loss data compared to the loss budget estimates. (b) Rescaled Nb on Al_2O_3 losses to account for the difference in substrate air participations between the trenched silicon resonators and untrenched sapphire resonators.

Figure 5.6 shows the approximate loss budgets constructed from participation ratio simulations and multiple Nb control resonator devices.

The least squares problem associated with this two device-type study is given by

$$\begin{pmatrix} p_{MS,1} & p_{SA,1} & p_{MA,1} & p_{Si,1} \\ p_{MS,2} & p_{SA,2} & p_{MA,2} & p_{Si,2} \end{pmatrix} \begin{pmatrix} x_{MS} \\ x_{SA} \\ x_{MA} \\ x_{Si} \end{pmatrix} = \begin{pmatrix} 1/Q_{TLS,1} \\ 1/Q_{TLS,2} \end{pmatrix} \quad (5.6)$$

where the indices 1 and 2 refer to the silicon and sapphire devices. The numerical entries of this participation matrix are given in Table 5.1. The condition number of this participation matrix is reasonably small enough (~ 500 by a ratio of its singular values) to solve the least squares, but the matrix $\tilde{P}^T \tilde{P}$ that defines the covariance matrix $C = (\tilde{P}^T \tilde{P})^{-1}$ of the least squares problem in (5.6) might be poorly conditioned in this case, where $\tilde{P}_{ij} = P_{ij}/\sigma_{Q_{TLS,i}^{-1}}$ and $\sigma_{Q_{TLS,i}^{-1}}$ is the uncertainty on the i -th measured TLS loss [4].

Table 5.1 Participation matrices for sapphire and silicon Nb control devices.

Substrate	p_{SA}	p_{MS}	p_{MA}	p_{Si}
Sapphire	0.0045	0.0043	0.0001	0.9
Silicon	0.0013	0.0026	0.00008	0.89

5.3 Conclusion

We presented two sets of A/B resonator loss studies to emphasize the utility of such studies in quickly evaluating the effect of changes in fabrication processes and materials to device performance. This is contrasted with the systematic participation-guided studies by Woods et al.. There are proposed hybrid studies on the horizon, where devices that are particularly sensitive to MA loss are used to study the efficacy of capping strategies. The split post cavity discussed in Chapter 7 is another example of a device that is extremely sensitive to bulk losses. There are alternative CPW geometries that can target the MS interface being discussed to replace the isotropic etching approach from [25]. A combination of these techniques could improve the accuracy of future loss budgets and obviate the need for isotropic etching to achieve accurate loss extraction of the three interface and bulk loss contributions. More work is needed to explore the mechanisms behind the effects of capping and other loss reduction strategies, especially those that lead to reductions in power independent losses where they are not expected, such as the silicon capping results in Figure 5.5.

CHAPTER 6

GRAIN SIZE IN LOW LOSS SUPERCONDUCTING TA THIN FILMS ON C-AXIS SAPPHIRE

Reproduced with permission from [196] published in *Journal of Applied Physics*.

Sarah Garcia Jones,^{30,31,32} Nicholas Materise,^{30,22} Ka Wun Leung,^{30,33} Joel C. Weber,³⁴ Brian D. Isakov,³¹ Xi Chen,³³ Jiangchang Zheng,³³ András Gyenis,³¹ Berthold Jaeck,^{35,33} and Corey Rae H. McRae^{36,31,32,34}

6.1 Abstract

In recent years, the implementation of thin-film Ta has led to improved coherence times in superconducting circuits. Efforts to further optimize this materials set have become a focus of the subfield of materials for superconducting quantum computing. It has been previously hypothesized that grain size could be correlated with device performance. In this work, we perform a comparative grain size experiment with α -Ta on *c*-axis sapphire. Our evaluation methods include both room-temperature chemical and structural characterization and cryogenic microwave measurements, and we report no statistical difference in device performance between smaller- and larger-grain-size devices with grain sizes of 924 nm² and 1700 nm², respectively. These findings suggest that grain size is not correlated with loss in the parameter regime of interest for Ta grown on *c*-axis sapphire, narrowing the parameter space for optimization of this materials set.

6.2 Introduction

Superconducting qubits are a promising avenue for scalable quantum computing devices due to their high-fidelity operation [197–200]. Recent advances in qubit design, packaging, and control have shrunk the gap toward their practical use [35, 201]. Still, dielectric losses due to bulk substrates, surface oxides, and amorphous or defect-ridden material interfaces limit the coherence of superconducting qubits and ancillary devices [4, 202, 203].

³⁰These authors contributed equally to this work.

³¹Department of Electrical, Computer, and Energy Engineering, University of Colorado Boulder, Boulder, Colorado 80309, USA

³²Department of Physics, University of Colorado, Boulder, Colorado 80309, USA

³³Department of Physics, The Hong Kong University of Science and Technology, Clear Water Bay, Kowloon, Hong Kong SAR, China

³⁴National Institute of Standards and Technology, Boulder, Colorado 80305, USA

³⁵Corresponding author, bjaeck@ust.hk

³⁶Corresponding author, coreyrae.mcrae@colorado.edu

Microscopically, materials loss is largely associated with the excitation of two-level systems (TLS) that dominate microwave losses in the technologically relevant range of low temperatures and single-photon numbers [17, 19]. Materials engineering has been identified as a leading route for improvement of superconducting qubit coherence by reducing the effect of TLS [204].

Recent works demonstrate improved qubit performance when α -phase tantalum (Ta) replaces niobium (Nb) as the superconducting thin film base layer for device fabrication [202, 205]. These findings are further supported by loss measurements of superconducting microwave resonators [203, 206–208] and it is believed that the loss reduction is afforded by the simple oxide structure of the Ta film surface [202]. Further evidence for this is suggested by recent work capping Nb films with Ta for improved qubit performance [195].

A detailed materials study of Nb-based qubits links the bulk properties of the polycrystalline films to qubit losses [209]. Smaller crystalline grain sizes were found to correlate with increased qubit losses, which could arise from TLS present at the subsurface grain boundary oxides in Nb films [209]. Hence, the grain size of the superconducting base layer has recently been debated as a promising process parameter to further minimize microwave losses in Ta films. Moreover, controlled A/B-testing studies would be desirable to firmly establish this relation and it remains unknown whether grain size effects on microwave losses extend to resonators based on Ta films, whose surface and subsurface oxide structure differs from that of Nb films.

The goal of this work is to probe the relationship between grain size and microwave losses for α -Ta films grown on *c*-axis sapphire, a substrate commonly used for Ta growth [202, 206]. To this end, we perform microwave loss measurements of coplanar waveguide resonators made from magnetron-sputtered α -Ta films with large and small grain sizes. We compare the losses of both types of films across thirty resonators from multiple chips and report no statistical difference between the performance of films with small and larger grain sizes. In combination with results from the chemical and crystallographic thin film characterizations, our observations indicate that grain size does not play a significant role in microwave losses for α -Ta films across the tested parameter regime.

6.3 Ta Growth and Characterization

Ta films of nominal 200 nm thickness were deposited on *c*-axis sapphire wafers (2" diameter, 550 μm thickness, from Hefei Keijing Materials Technology) using dc magnetron sputtering. Prior to deposition, the as-purchased substrates were cleaned via ultrasonication in acetone, isopropanol, and deionized water for 5 min each and blown dry with nitrogen of purity 4N.

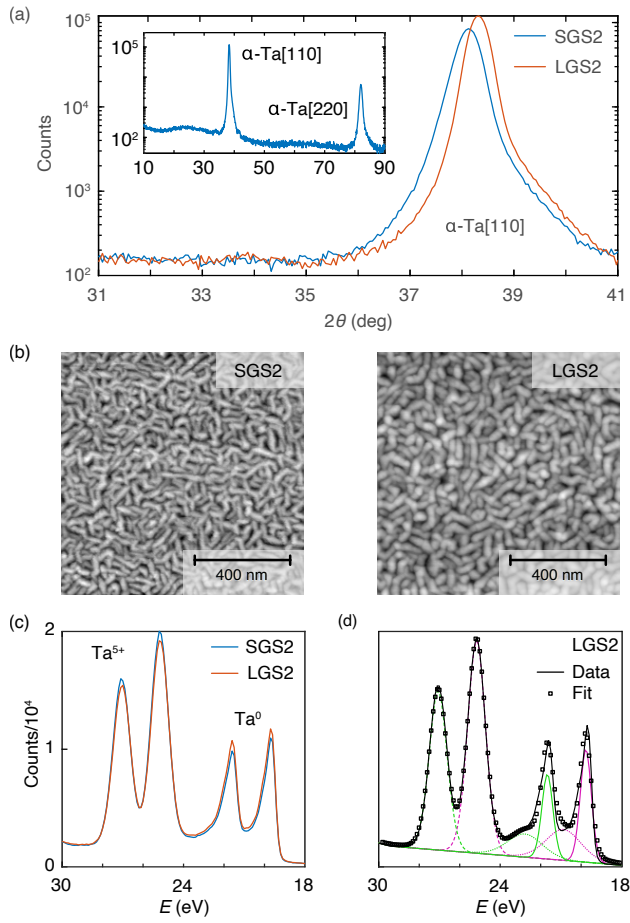


Figure 6.1 Structural and chemical characterization of Ta films. (a) X-ray diffraction spectra of 2θ -scans for measurements of the ‘SGS2’ and ‘LGS2’ samples. The inset displays the corresponding spectrum for the ‘LGS2’ sample over a larger angle (Θ) range. The detected diffraction peaks are labeled with the corresponding Miller indices of the α -Ta phase. (b) Atomic force microscopy topographies of the ‘SGS2’ (left) and ‘LGS2’ (right) sample surfaces. (c) Electron binding energy spectra of the Ta 4f core level obtained from X-ray photoelectron spectroscopy measurements at the surface of the ‘SGS2’ and ‘LGS2’ samples. The dominant Ta oxidation states are indicated. (d) Least squares fit (open squares) to an XPS spectrum (solid black line) recorded at the surface of the LGS2 sample. Contributions to the spectrum by the Ta 4f_{5/2} (magenta color) and Ta 4f_{7/2} (green color) core levels of Ta, (solid lines), Ta³⁺ (dotted lines), and Ta⁵⁺ (dashed lines) were modeled by using Gaussian profiles.

To deposit thin films with different grain sizes, two different substrate temperatures $T = 400^\circ\text{C}$ (sample label ‘SGS’ or ‘smaller grain size’) and $T = 500^\circ\text{C}$ (sample label ‘LGS’ or ‘larger grain size’) during the deposition were chosen, while other deposition parameters (background pressure $\leq 1 \times 10^{-7}$ Torr, argon pressure 3 mTorr, deposition power 150 W, deposition rate 3.6 nm/min) were not changed. The deposition was carried out without the use of a seed layer. A $T = 600^\circ\text{C}$ sample was also grown, but no increase in grain size was detected, so this sample is not included in the detailed film comparison.

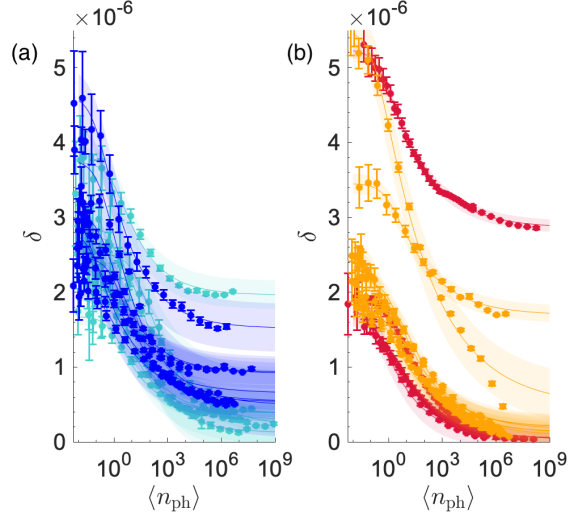


Figure 6.2 Resonator loss power curves with small grain size (left) and larger grain size (right). Total loss δ as a function of average number of photons in the cavity $\langle n_{\text{ph}} \rangle$ for all devices measured in this work - SGS1 (light blue), SGS2 (blue), LGS1 (red), and LGS2 (orange) resonators. Lines denote best fits to the TLS model (Eq. (6.4)). 95% confidence intervals for Lorentzian fits to each data point are given, as well as the prediction interval for each TLS-curve fit.

The large-scale diffraction spectrum of the films (Figure 6.1(a) inset) is dominated by a set of two peaks, which can be associated with diffraction at the [110] and [220] planes of the α -Ta[220] phase. A comparably small diffraction signal, which rises just above the background signal, is detected at $2\Theta \approx 33.7^\circ$ that can be associated with the [002]-diffraction of the tantalum β -phase. Our observations indicate the Ta films prepared for this study predominantly nucleate in the α -Ta phase. This finding is consistent with previous reports on 200 nm thick α -Ta films on *c*-axis sapphire, which were deposited under comparable conditions [202]. The close-up view of the α -Ta[110] peaks for the 'SGS2' and 'LGS2' samples is shown in the main panel of Figure 6.1(a). The diffraction peak of the 'LGS2' sample ($\sigma = 0.4^\circ$) has a smaller full-width-half-maximum σ compared to that of the 'SGS2' sample ($\sigma = 0.5^\circ$). While this observation is indicative of a larger average grain size in the 'LGS2' sample, we note that the Scherrer equation is less suited to quantitatively analyze the grain size in this case, owing to the grain shape anisotropy and significant grain size variations (see AFM measurements below). We further observed a small deviation in the [110]-diffraction angle both between the 'SGS2' ($2\Theta = 38.1^\circ$) and 'LGS2' ($2\Theta = 38.3^\circ$) sample, as well as with respect to the nominal bulk value ($2\Theta = 38.505^\circ$). This can be attributed to the presence of strain in the thin film structure, which appears slightly more pronounced in the 'SGS2' sample.

To characterize the crystalline grain size of the Ta films deposited at different substrate temperatures, we carried out atomic force microscopy (AFM) measurements (tapping mode).

The resulting AFM topographies for samples ‘SGS2’ and ‘LGS2’ are shown in Figure 6.1(b). Both topographies are characterized by elongated crystalline grains oriented along the hexagonal basal plane of the sapphire surface, consistent with previous reports [206]. Moreover, the grains of ‘LGS2’ exhibit a visibly larger grain size area G than those of ‘SGS2’, consistent with our expectations in light of the substrate temperatures during deposition. To quantify these grain size differences, we applied a watershed algorithm [210] to determine G , which is an average across several $1 \mu\text{m}^2$ surface areas per sample and several samples for each deposition condition. This approach was previously applied to quantify grain sizes of Nb films [209]. We obtain $G = (924 \pm 51) \text{ nm}^2$ for the ‘SGS2’ and $G = (1700 \pm 29) \text{ nm}^2$ for the ‘LGS2’ sample, respectively. Interestingly, the average grain size $G = (1732 \pm 92) \text{ nm}^2$ of samples deposited at a substrate temperature $T = 600^\circ\text{C}$ is comparable to that of the $T = 500^\circ\text{C}$ deposition [211].

To detect the possible influence of the crystalline grain size on the surface oxide structure, we performed X-ray photoelectron spectroscopy (XPS) measurements (Kraxios Ultra DLD; X-ray source: Al $\text{K}\alpha$ line $E = 1486.6 \text{ eV}$) on the ‘SGS2’ and ‘LGS2’ samples. We note that these samples did not undergo surface treatment to remove native surface oxides prior to XPS measurements. The resulting XPS spectra in Figure 6.1(c) show the photo-electron count as a function of the electron binding energy for the Ta-4f core level. The spectra are dominated by a four peak structure, which is predominantly composed of the spin-orbit split Ta^0 and Ta^{5+} doublets that can be assigned to the metallic Ta bulk and the Ta_2O_5 at the film surface, respectively [212, 213].

We quantify the relative contributions of the different Ta oxidation states to the observed XPS spectra by applying a least-squares fit based on Gaussian profiles. We find a three doublet structure composed of six Gaussians, as shown in Figure 6.1(d), can most accurately describe these spectra. The additional third doublet exhibits a core level shift of $\approx 1.1 \text{ eV}$ and can be assigned to the Ta^{3+} oxidation state of the Ta_2O_3 suboxide [213]. The resulting relative contributions of Ta, Ta^{3+} , and Ta^{5+} obtained from these fits are shown in Table 6.1 and reveal a near identical chemical structure of the tantalum film surface for both samples. this is consistent with their almost identical XPS spectra (*cf.* Figure 6.1(c)). The relative spectral weight of the Ta^0 and Ta^{5+} peaks at the given incident X-ray energy is in close agreement with that found in previous XPS studies of tantalum films and indicates a surface oxide thickness of approximately 2 nm [202].

In addition to structural and chemical analyses, we measured the electrical resistance R as a function of temperature T (see the supplementary material for R versus T data). We extracted the residual resistance ratio (RRR) and superconducting transition temperature T_c of the two films (Table 6.2).

We compare this result with the Nb study by Premkumar et al., where a reduction in the grain size by a factor of two corresponded to a similar reduction in RRR, and to a lesser extend, a reduction in T_c , attributed to oxides forming in the grain boundaries of the smallest grain size Nb films. [209] In contrast, here we see no significant difference in T_c , and a small decrease in RRR.

Table 6.1 Relative atomic concentration of different tantalum oxidation states in the 'SGS2' and 'LGS2' samples as obtained from fits to the XPS spectra.

Oxidation state	Smaller grain size atomic %	Larger grain size atomic %
Ta ⁰	18	20
Ta ³⁺	17	18
Ta ⁵⁺	65	62

6.4 Device Design and Fabrication

All devices are coplanar waveguide resonators fabricated using the same designs as reported by Kopas et al. [188]. Nominally identical designs and fabrication procedures were used for all samples. Prior to etching, the samples were cleaned via ultrasonication in toluene, acetone, methanol, and isopropanol, then patterned using optical lithography and AZ-P4330-RS photoresist. The films were etched in a single 4 minute CF₄/N₂ Inductively Coupled Plasma – Reactive Ion Etch (Panasonic E640). Since the Ta films were deposited on sapphire substrates, the etches did not produce any trenching into the substrate. After etching, the resist was submerged in AZ 300 T stripper at 80 °C for 1 hour. After stripping, the samples were diced and again cleaned ultrasonically in toluene, acetone, methanol, and isopropanol before being wire bonded for cryogenic microwave measurement. Optical images of the resonators are shown in Figure 6.3.

Inverse coupling quality factors, $1/Q_c$, of the fabricated resonators are presented in Supplementary Materials Table 1 and range from 1.18×10^{-6} to 6.61×10^{-6} across all devices. This is a larger spread of values with a trend towards smaller coupling factors than the simulated $1/Q_c$ values of these designs, which ranged from 1.95×10^{-6} to 2.02×10^{-6} . [188] This variation is likely due to a slight over etch of the devices during fabrication, which is congruent with a thinner measured conductor width than the lithography designs used (design: $6\mu\text{m}$, measured: $5.5\mu\text{m}$).

6.5 Cryogenic Microwave Measurement

We perform transmission measurements on CPW resonators mounted to the mixing chamber (MXC) plate of a FormFactor (formerly Janis) JDry 250 dilution refrigerator (DR) at a mixing chamber temperature of ~ 10 mK using a Keysight PNA N5222B vector network analyzer (VNA).

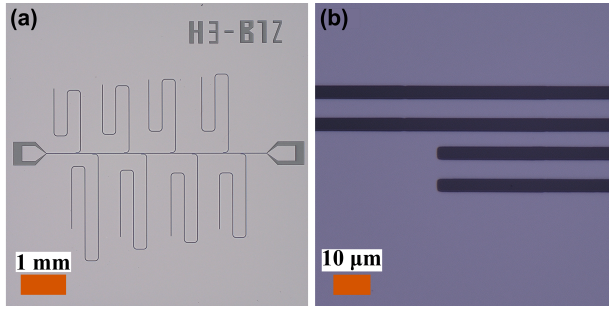


Figure 6.3 Optical microscope images of coplanar waveguide resonators. (a) Full chip image of a representative chip. All circuits measured contain eight resonators with identical couplers. (b) Close up of feedline and resonator base. Conductor width is $5.5 \mu\text{m}$ and gap is $3.8 \mu\text{m}$.

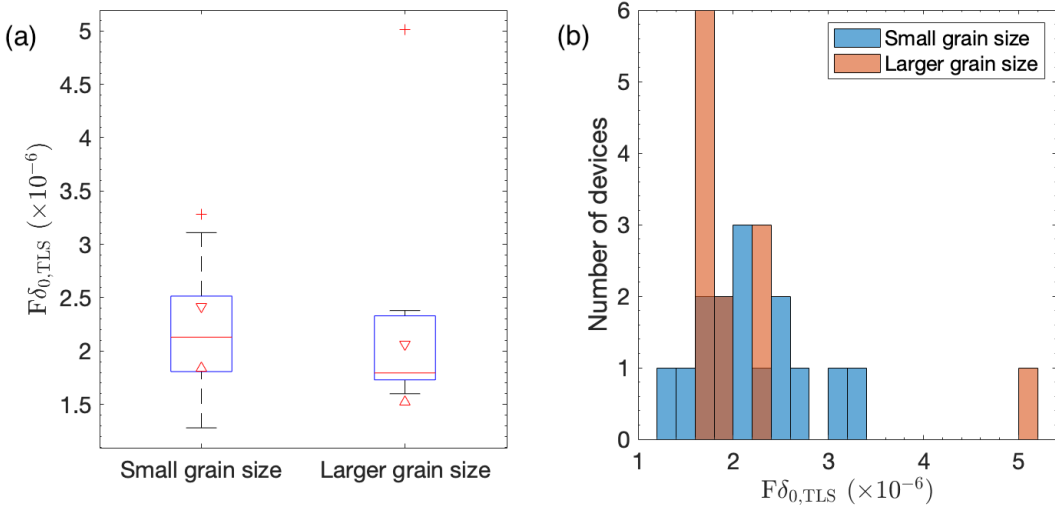


Figure 6.4 TLS loss in Ta on c-axis sapphire superconducting microwave resonators with smaller and larger grain size. Left: Box and whiskers comparison, indicating median values (red line) and 95% confidence interval of median (red triangles), with outliers shown as crosses. Right: Histogram of TLS loss for all devices in this experiment.

The input power is varied over ten orders of magnitude in estimated photon power to accurately extract the dominant two level system (TLS) loss [66]. Nominally identical gold-plated oxygen-free high conductivity copper sample boxes house the resonator chips and are mounted to a plate perpendicular to the MXC plate with additional mu-metal shielding surrounding all samples. Two Radiall R583 six-way microwave switches allow multiple samples to be measured on the same pair of coaxial input and output lines.

The transmission data for each resonator (S_{21} of the two-port S -parameter matrix measured by the VNA) is first normalized with a circle fit [123], and then fit to a diameter-corrected asymmetric Lorentzian model of the form [121]

$$S_{21}(f) = 1 - \frac{(Q_l / Q_c) e^{i\phi}}{1 + 2iQ_l \frac{f-f_0}{f_0}} \quad (6.1)$$

$$Q_i^{-1} = Q_l^{-1} - \text{Re} \left\{ \hat{Q}_c^{-1} \right\} \quad (6.2)$$

$$\hat{Q}_c^{-1} = Q_c^{-1} e^{i\phi} \quad (6.3)$$

where f_0 is the resonance frequency, ϕ is the asymmetry angle, Q_c is coupling quality factor, Q_l is the loaded quality factor, and Q_i is the internal quality factor. These parameters are fit with their corresponding 95% confidence intervals from a least squares fitting routine [18]. A secondary fit of the loss $\delta = Q_i^{-1}$ as a function of average number of photons $\langle n_{\text{ph}} \rangle$ and fixed temperature T follows from the sum of the TLS loss contribution δ_{TLS} and an offset term $1/Q_{\text{HP}}$ that accounts for power-independent losses dominating at higher powers [17]

$$\delta(\langle n_{\text{ph}} \rangle, T) = \delta_{\text{TLS}}(\langle n_{\text{ph}} \rangle, T) + 1/Q_{\text{HP}} \quad (6.4)$$

$$\delta_{\text{TLS}}(\langle n_{\text{ph}} \rangle, T) = F \delta_{\text{TLS}}^0 \frac{\tanh\left(\frac{\hbar\omega_0}{2k_B T}\right)}{\left(1 + \frac{\langle n_{\text{ph}} \rangle}{n_c}\right)^\beta} \quad (6.5)$$

where n_c is the critical photon number at which TLS saturate at low power, $\omega_0 = 2\pi f_0$ is the angular resonance frequency, β is an exponent interpolating between the non-interacting TLS model $\beta = 1/2$ and interacting TLS model $\beta < 1/2$ [130, 135, 136], δ_{TLS}^0 is the intrinsic TLS loss, F is the geometry-dependent filling factor, \hbar is the reduced Planck constant, and k_B is the Boltzmann constant.

In Figure 6.2, we plot the loss power dependence for all larger and smaller grain size devices used in this work. The high power losses are subtracted to emphasize the similar power dependence (line shape) and low power loss (TLS saturation loss) between the two samples, without the confounding factor of high-power losses which are known to be caused by a myriad of sources external to the device materials [17]. Figure 6.4 further highlights this point, as the medians from the box and whisker plots of the intrinsic TLS losses for the larger and smaller grain size Ta films coincide with one another and their respective histograms give similar variances.

Table 6.2 Mean parameter values in A/B grain size comparison.

	Smaller grain size	Larger grain size
Grain area (nm ²)	924 ± 51	1700 ± 29
$F\delta_{TLS}^0 (\times 10^{-6})$	2.19 ± 0.07	2.17 ± 0.03
RRR	2.584 ± 0.001	2.895 ± 0.001
T_c (K)	4.063 ± 0.005	4.056 ± 0.004

6.6 Literature Comparison

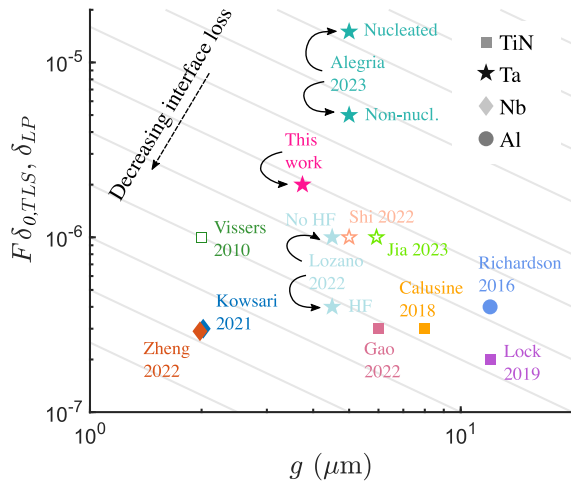


Figure 6.5 State-of-the-art literature comparison of TLS ($F\delta_{TLS}^0$) and low-power (δ_{LP}) loss values in CPW resonators. Filling factor F is estimated by plotting loss as a function of CPW gap width g . Grey lines denote lines of constant interface loss. Filled symbols denote TLS loss values, while empty symbols represent low power loss (TLS loss values unavailable).

Mean parameter values for the two resonator populations are summarized in Tab. Table 6.2. Though our small-geometry resonators are very sensitive to TLS losses from surfaces and interfaces, we see no statistical difference in TLS loss between the small-grain and large-grain devices, despite the difference in grain size (with the large grain size devices being almost twice as big in area). This difference in grain size is similar to that seen in Nb films in Ref. [209], where a difference in grain size of a factor of two was correlated with a difference in qubit T_1 of almost two, and a difference in resonator TLS loss was also detected.

We refer to recent studies, especially the work by Lozano et al. [208], to estimate the number of devices required to adequately sample the device-to-device variation in $F\delta_{TLS}^0$. With more than ten devices of each grain size, we exceed the number of devices for each variation (choice of control parameter value) in Refs. Crowley et al. [203], Alegria et al. [206], Lozano et al. [208], Jia et al. [214].

The median values of the losses for the untreated Ta resonators on silicon in Ref. Lozano et al. [208] are comparable to the large- and small-grain size median losses reported in Figure 6.4(a).

Figure 6.5 shows that the difference between the large- and small-grain size losses in this study is imperceptible on the same scale as other A/B comparisons, e.g. Refs. Alegria et al. [206], Lozano et al. [208].

6.7 Discussion

An enduring hypothesis in the superconducting qubit community has been that larger grain size in superconducting thin films is an indication of improved device performance. The simple and stable oxide structure of Ta differs from that of Nb, where Premkumar et al. [209] reported that smaller grain size films exhibited higher concentrations of suboxides in interface regions, resulting in measurably higher losses in their Nb resonators. In this study, we show that smaller grain size does not induce significant low power loss in Ta thin films grown between 400 and 500 °C on *c*-axis sapphire.

Microwave measurements of low power loss suggest that there is no statistically significant difference between the intrinsic TLS losses of the two grain size Ta thin films. Chemical and structural analysis support this interpretation, as the surface chemistry obtained by XPS is nearly identical for the two films. This distinguishes densely packed Ta films with their simple Ta₂O₅ surface oxide structure [202] from Nb films [209] for which subsurface grain boundary oxides contribute a grain size dependent TLS channel.

Following this train of thought, we expect qubits and resonators fabricated from Ta films to exhibit more uniform microwave losses than those fabricated from Nb. At the same time, non-negligible concentrations of Ta³⁺ species found in our XPS measurements indicates the presence of Ta₂O₃ suboxides at the Ta metal-Ta₂O₅ interface consistent with a recent report [215]. Interestingly, we also detect practical limits within which to tune the grain size of [110]-oriented α -Ta films deposited on *c*-axis sapphire: Deposition at substrate temperatures below 400 °C favors the formation of the unwanted β -phase [216, 217] whereas grain size does not respond to an increase of substrate temperature in excess of 500 °C in our study. Thus, it would be interesting to explore other substrates or sapphire surface orientations to promote larger grain sizes up to the formation of single-crystalline Ta films.

On the other hand, our study suggests more sophisticated materials engineering efforts that focus on the reduction of TLS losses at the immediate metal-air surface rather than on the optimization of bulk properties, such as grain size, are required to further reduce microwave losses below those reported in this and other recent studies [203, 206, 208, 214]. These efforts will benefit from targeted A/B testing studies, such as is presented here, to address the vast materials and processing parameter space in order to maximize state-of-the-art superconducting qubit performance.

6.8 Conclusion

We performed millikelvin microwave transmission measurements of α -phase Ta microwave resonators with both larger- and smaller-grain size sputter-deposited on c-axis sapphire at two different growth temperatures. Structural and chemical analysis reveal that the films differ only in their grain size and not in their surface oxide types and concentrations, and crystal structure. The extracted intrinsic TLS losses show no statistical difference between the two film types, suggesting that, in this materials regime, grain size does not significantly affect millikelvin, ultralow power dielectric loss. We encourage future A/B experimentation to continue to reduce the fabrication parameter space and to identify correlations between other room-temperature materials characterization parameters and low-power, low-temperature microwave performance of devices.

6.9 Supplementary Material

Please see the supplementary material for more information on the 600 °C deposited sample, as well as 4-8 GHz wide scans of the microwave background of each measured chip, a table of all extracted resonator parameters, further detail on the microwave set-up, superconducting thin film resistances as a function of temperature, and details of the T_c and RRR measurements.

6.10 Acknowledgements

The authors would like to thank Qiming Shao and Jiacheng Liu for their assistance with the sputter deposition, and Carlos Torres Castanedo, David Garcia, Dominic Goronzy, Tony McFadden, and Michael Vissers for helpful discussions and feedback on the manuscript. N.M. acknowledges funding from the Graduate Fellowships for STEM Diversity. B.J. acknowledges funding from the Croucher Foundation. A. G. and S. G. J. acknowledge funding from the University of Colorado Research & Innovation Seed Grant Program.

6.11 Author Declarations

Conflicts of interest, disclaimers, and contributions.

6.11.1 Conflicts of Interest

The authors have no conflicts to disclose.

6.11.2 Commercial Products Disclaimer

Certain commercial instruments are identified to specify the experimental study adequately. This does not imply endorsement by NIST or that the instruments are the best available for the purpose.

6.11.3 Author Contributions

Sarah Garcia Jones: Resonator sample fabrication (lead), Writing - review & editing; *Nicholas Materise*: Writing - original draft (lead), Writing - review & editing (supporting), Data acquisition (equal), Software (equal); *Ka Wun Leung*: Materials fabrication (lead) ; *Brian D. Isakov*: Writing - review & editing; *Chen Xi*: Materials characterization (lead); *Jiangchang Zheng*: Materials characterization (supporting); *András Gyenis*: Writing - review & editing, Resonator sample fabrication; *Bertold Jaeck*: Conceptualization (equal), Writing - review & editing (lead), Visualization (equal), Formal analysis (equal), Methodology (lead); *Corey Rae H. McRae*: Conceptualization (equal), Writing - review & editing (lead), Visualization (equal), Formal analysis (equal), Methodology (lead).

6.12 Data Availability

The data that support the findings of this study are openly available at
<https://zenodo.org/record/8161535>, reference number 10.5281/zenodo.8161535.[218]

CHAPTER 7

WAFER-SCALE MICROWAVE DIELECTRIC LOSS EXTRACTION USING A SPLIT-POST SUPERCONDUCTING CAVITY

Superconducting qubits are a promising candidate to build quantum computers. Their lifetimes now extend into the millisecond range [185, 219] and beyond [220], with gate times on the order of a few to tens of nanoseconds. These achievements are due to efforts to minimize field intensities in high loss regions, engineer states with disjoint support [221, 222], and encode information in bosonic states [112]. Alongside these efforts, systematic materials studies have expanded the understanding and mitigation of losses resulting from interface and surface states in niobium and tantalum-based superconducting qubits [174, 189, 215]. Yet there remains an upper limit on the coherence of superconducting qubits deposited on dielectric substrates: the bulk loss of the substrate. Multiple precision measurements of bulk losses have been performed using superconducting cavities including silicon substrates [223], lithium niobate [224] and sapphire [4]. This last measurement set an upper bound on the loss of HEMEX sapphire as $1.9(6) \times 10^{-8}$ [4], with corresponding T_1 on the order of ms, which recent experiments with planar superconducting qubits are quickly approaching [185]. We note that this limit assumes unity participation in the bulk of the substrate, which is on the order of 0.8 to 0.9 in planar qubits and in 3D qubits can be as high as tens of percent.

In the above measurements of bulk loss, the substrate in question was modified to accommodate the conditions of the experiment (diced, milled, etc.), but measurements of bulk losses in whole, unaltered wafers have not been performed until now. Borrowing from the whispering gallery mode (WGM) experiments [225, 226], we design a split post, reentrant cavity to measure three inch wafers with a near unity dielectric participation in the wafer. Similar to the work by Read et al. [4], we perform a differential measurement of the dielectric loss tangent by first measuring the cavity without a wafer, then loaded with a wafer, extracting the wafer loss from the bare and loaded measurements.

7.1 Methods

We use a high purity 4N Al superconducting cavity to extract the bulk loss of a 3 inch wafer with a differential measurement technique. The losses are extracted from transmission measurements, where the frequency response of a high order quasi-transverse magnetic (TM) mode is fit to an asymmetric Lorentzian with the diameter correction method (DCM) described in [121] and implemented in [18].

First, we measure the losses of the bare cavity before and after wet chemical etching. The losses of the cavity are the sum of the wall or conductive losses and the seam loss, given by [27, 50]

$$Q_{\text{walls}}^{-1} = \frac{R_s}{X_s} \frac{\lambda_L \int_S |\mathbf{H}|^2 d^2\mathbf{x}}{\int_V |\mathbf{H}|^2 d^3\mathbf{x}} = \frac{R_s}{X_s} p_{\text{cond}} \quad (7.1)$$

$$Q_{\text{seam}}^{-1} = G_{\text{seam}}^{-1} L \frac{\int_{\gamma_{\text{seam}}} |\mathbf{J} \times \mathbf{l}|^2 dl}{\omega \mu_0 \int_V |\mathbf{H}|^2 d^3\mathbf{x}} = \frac{y_{\text{seam}}}{g_{\text{seam}}} \quad (7.2)$$

where R_s is the surface resistance, X_s is the surface reactance, λ_L is the London penetration depth, and p_{cond} is the conductive participation ratio in the expression for the wall loss. The seam loss is calculated on \mathbf{l} , the vector tangent to the curve γ_{seam} defining the seam, G_{seam} is the conductance of the seam, $g_{\text{seam}} = G_{\text{seam}}/L$ is the conductance per unit length, L is the length of the seam, and y_{seam} is the admittance per unit length of the seam, defined by the ratio of the current and magnetic field integrals. Similar to the dielectric loss, the seam loss separates into a geometric factor (y_{seam}) and a material-dependent factor (g_{seam}).

The losses associated with the bulk of the wafer follow from the phenomenological single species, standard two level system (TLS) model [66, 130, 132]

$$Q_{\text{wafer}}^{-1} = \delta_{\text{wafer}} = \delta_{\text{PI}} + F \delta_{\text{TLS}}^0 \frac{\tanh(\hbar\omega/2k_B T)}{\left(1 + \frac{\langle n \rangle}{n_c}\right)^\beta} \quad (7.3)$$

$$F = \frac{\frac{1}{2}\epsilon_{\text{wafer}} \int_{V_{\text{wafer}}} |\mathbf{E}|^2 d^3\mathbf{x}}{\frac{1}{2}\epsilon \int_V |\mathbf{E}|^2 d^3\mathbf{x}} \quad (7.4)$$

where δ_{PI} is a power-independent loss term, F is the electric filling factor, a ratio of the electric field energy stored in the wafer compared to all space, δ_{TLS}^0 is the intrinsic TLS loss, ω is the resonance frequency of the mode we are measuring, $\langle n \rangle$ is the average number of photons in the cavity, n_c is the critical photon number marking the onset of the TLS saturation, and β is a parameter $0 < \beta < 1$, with $\beta = 1/2$ denoting the noninteracting TLS limit and $\beta < 1/2$ the interacting TLS limit. We have written the denominator of (7.4) in a shorthand that can be rewritten as a sum over the vacuum and wafer volumes with $\epsilon = \epsilon_r \epsilon_0$ in the case of the wafer with its dielectric constant ϵ_r and $\epsilon = \epsilon_0$ for the vacuum.

Measuring multiple resonances of the bare cavity, we can extract the wall losses and seam losses. With these losses characterized, a measurement of the loaded cavity gives an indirect measurement of the wafer loss. To extract the wafer loss, we subtract the bare cavity losses from the total loss, given by

$$Q_{\text{loaded,tot}}^{-1} = Q_{\text{wafer}}^{-1} + Q_{\text{bare,tot}}^{-1} = Q_{\text{wafer}}^{-1} + Q_{\text{walls}}^{-1} + Q_{\text{seam}}^{-1} \quad (7.5)$$

For high dielectric participations, we see that to distinguish losses of the cavity from the wafer a much lower quality factor cavity can be used to achieve a similar sensitivity of a higher Q , lower participating cavity. Previous attempts to separate bulk losses from surface losses in coplanar waveguide resonators required isotropically etching into a silicon substrate [25]. This process is nontrivial to implement and does not transfer to all substrates, especially sapphire which is difficult to etch at all, let alone isotropically.

7.1.1 Cavity Design

The split post design maximizes the electric field participation of the wafer in a high order quasi-TM cylindrical mode, in analogy with the WGM boule experiments. This high order mode has multiple antinodes distributed across the wafer, shown in Figure 7.1, probing local defects with higher sensitivity than an isotropic TM_{01} or similar mode with cylindrical symmetry might.

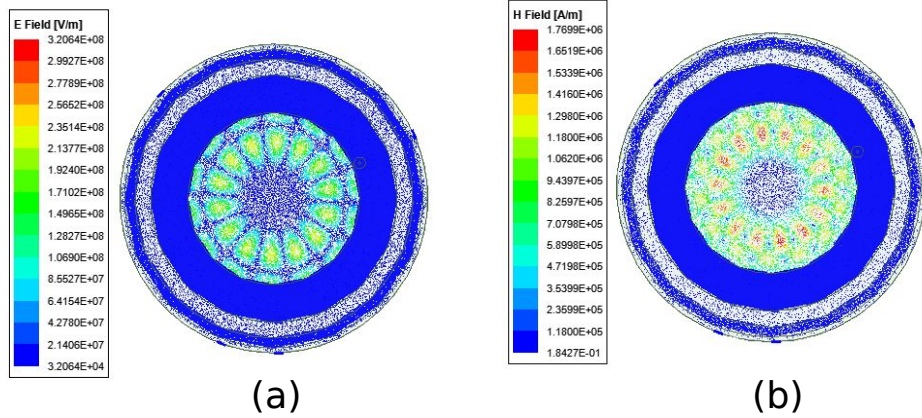


Figure 7.1 (a) Electric field and (b) magnetic field profiles for the target 5.210 GHz mode used to measure the wafer loss.

The resulting electric field participation of this mode is sensitive to the boundary conditions between the wafer and the posts. We studied this sensitivity by sweeping the air gap between the wafer and the posts in simulation, anticipating that machining tolerances could limit the participation of the wafer. Figure 7.2 (a) shows a region of relative insensitivity to post diameter, just less than the wafer diameter. In Figure 7.2 (b), we highlight the exponential dependence of wafer participation on the air gap between the posts and wafer. This motivated a design that uses a seam along the H-plane, where the currents are perpendicular to the seam, maximizing the geometric contribution of the seam loss [27] from (7.2).

In micromachined rectangular cavities with H-plane seams, Brecht [181] showed three orders of magnitude improvement in the quality factor by introducing a quarter-wavelength “cavity cover choke.” Quarterwave chokes have a long history of minimizing leakage currents at the interfaces of rectangular and circular waveguides [26], as in Figure 7.3 (a).

These chokes are achieved by introducing a circular trench $\lambda/4$ in depth and $\lambda/4$ away from the cavity with a radial waveguide connecting the trench to the cavity. At the bottom of the trench the current is maximized, creating a microwave short circuit, whereas at the top of the trench (the interface between the mating faces of the cavity or waveguide) the current is minimized.

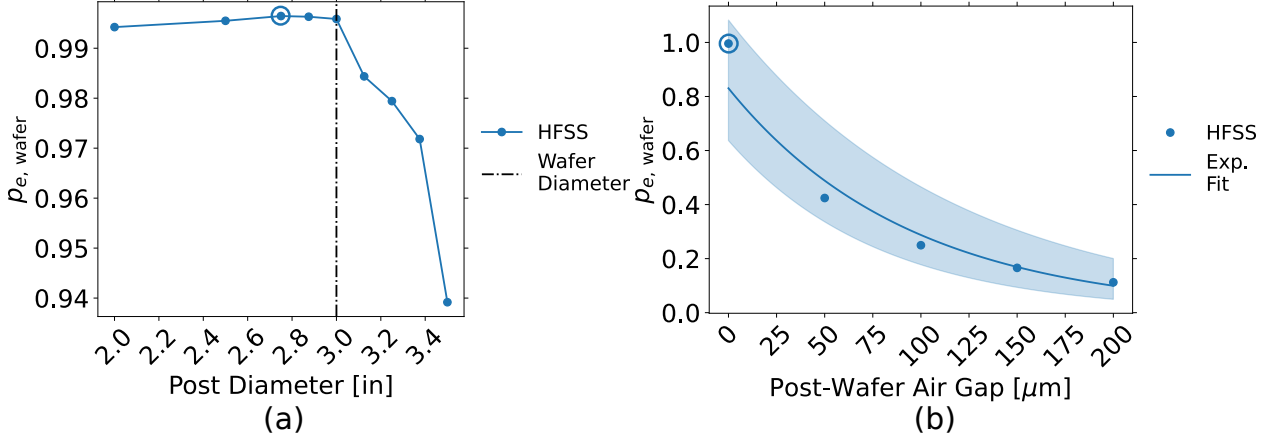


Figure 7.2 Wafer participation design studies. Wafer participation as a function of (a) the post diameter and (b) air-gap between the posts and the wafer. Dashed line in (a) indicates the diameter of wafer. Circled points indicate the maximum participation and designed values. Shaded region in (b) shows the 95 % confidence interval on the exponential fit.

We employed a similar design to the “cavity cover choke” in the split post cavity (cover shown in Figure 7.3 (b)). A cross section of the two cavity halves in Figure 7.3 (c) shows the size and location of the $\lambda/4$ circular channel with respect to the posts. The design also ensures that the posts make contact with wafers of various thicknesses. This feature potentially allows for extraction of losses from the wafer surface by using wafers of different thicknesses from the same boule as in [4].

A raised ring structure makes contact with the bottom of the $\lambda/4$ groove before the outside of the cavity walls connect, leaving a gap that is partially filled by an indium gasket (blue circles near the outside edge of the cavity walls in Figure 7.3 (c)). We also used two indium gaskets, recessed in grooves on the post surfaces, to prevent cracking of fragile wafers such as silicon and to adhere the wafer to the post surfaces.

7.1.2 External Coupling Simulation

To predict the range of coupling quality factors, we simulated the total quality factor as a function of pin insertion depth into the cavity. In the absence of other losses, except for a vacuum impedance boundary condition applied to the outside boundary of the coupling pin, the total quality factor $Q_l = Q_c$ varies with the pin insertion depth z_{pin} .

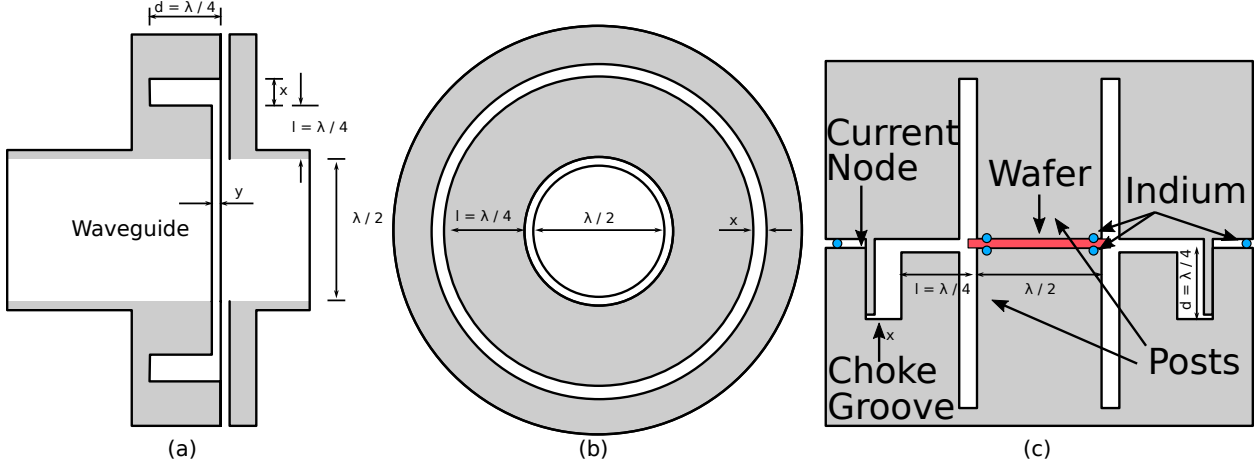


Figure 7.3 Quarter wave chokes in waveguides and cavities. (a) Waveguide choke based on [26]. Split post cavity cover choke: (b) top view and (c) cross sectional side view with indium gasket (blue circles) and wafer (red rectangle) positions.

Zero is referenced to the interior cavity wall, with positive values corresponding to in the cavity volume and negative values recessed from the cavity volume, into the circular coupling pin hole. In Figure 7.4 the exponential fit agrees with the reported trend by Reagor [144], where the coupling quality factor scales as $Q_c \propto e^{-2i\beta_{TM_{01}} z_{pin}}$, with $\beta_{TM_{01}}$ the complex propagation constant of the fundamental TM_{01} mode of the circular waveguide of the coupling pin hole given by [144]

$$\beta_{TM_{0m}} = \sqrt{k^2 - \left(\frac{p_{0m}}{r_0}\right)^2} \quad (7.6)$$

where the wavenumber $k = \omega/c$, the radius of the coupling pin hole r_0 , and the m -th zero of the zero-th order Bessel function of the first kind, $J_0(p_{0m}) = 0$ combine to set the cutoff frequency of the waveguide, $\omega_c = p_{0m}c/r_0$. Frequencies below this cutoff are exponentially attenuated in the waveguide which leads to the exponential decay of the coupling quality factor Q_c . This exponential dependence on the pin length gives coupling quality factors that span orders of magnitude, yet achieving critical coupling $Q_c \approx Q_i$ is difficult with this coupling scheme. In practice, we set Q_c to be within an order of magnitude of Q_i , where the error on the fit of Q_i is tolerable [122], preferably an order of magnitude larger, such that the pin is undercoupled to the cavity and $Q_l \approx Q_i$ and measurements of transmission through an SMA tee coupled to the cavity port are sensitive to Q_i by changes in the resonance linewidth.

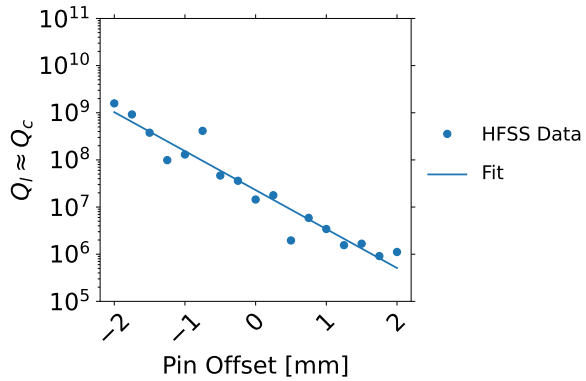


Figure 7.4 Coupling quality factor as a function of the pin insertion depth.

7.1.3 Wet Chemical Etching of Cavity

To reduce the London penetration depth of the cavity surfaces,³⁷ which has been shown to give up to an order of magnitude improvement in Q_i [50, 144], we performed a wet chemical etch of the cavity following the recipe outlined in [227]. The etching recipe is as follows. Before etching, titanium screws were threaded into the tapped holes to prevent the etchant from modifying the threads. The etchant used does not significantly etch titanium and screws are readily available from McMaster Carr and other hardware vendors that are made of grade-2 titanium.³⁸ Once the titanium screws are threaded into the tapped cavity holes, a 6 inch glass container (shown in Figure 7.5 (a)) was filled with Transene™ Type A aluminum etchant (phosphoric-, nitric-, and acetic-acid with a proprietary surfactant) and heated on a hot plate inside a fume hood until reaching a temperature of 50 °C. Then the cavity halves are added to the acid bath and etched for 2 hours. After 2 hours, the cavity halves were removed from the bath and submerged into deionized water. A fresh etchant was heated to 50 °C and the cavity was etched for another 2 hours. The etch rate for this acid at 50 °C is $\sim 100 \text{ \AA/s}$, removing $\approx 150 \mu\text{m}$ of material from the surface of the cavity halves [227]. Following the etch, the cavities were briefly submerged in deionized water, twice, then cleaned in an ultrasonic cleaner with acetone, then isopropanol, each for 5 minutes, and dried with a nitrogen gun. Michael Vissers at the National Institute of Standards and Technology (NIST), Boulder performed this recipe on short notice and we are eternally grateful for his assistance in this chemical processing procedure.

³⁷There is also evidence from subsurface transmission electron microscopy of 5N5 aluminum before and after etching indicating that the surface oxide following the etch is more uniform and thinner than before the etch [182].

³⁸Other groups use teflon screws and have observed similar white residues forming after etching, likely biproducts of the etch, e.g. aluminum phosphates, nitrates, and acetates. Private communication with Srivatsan Chakram and Yao Lu.

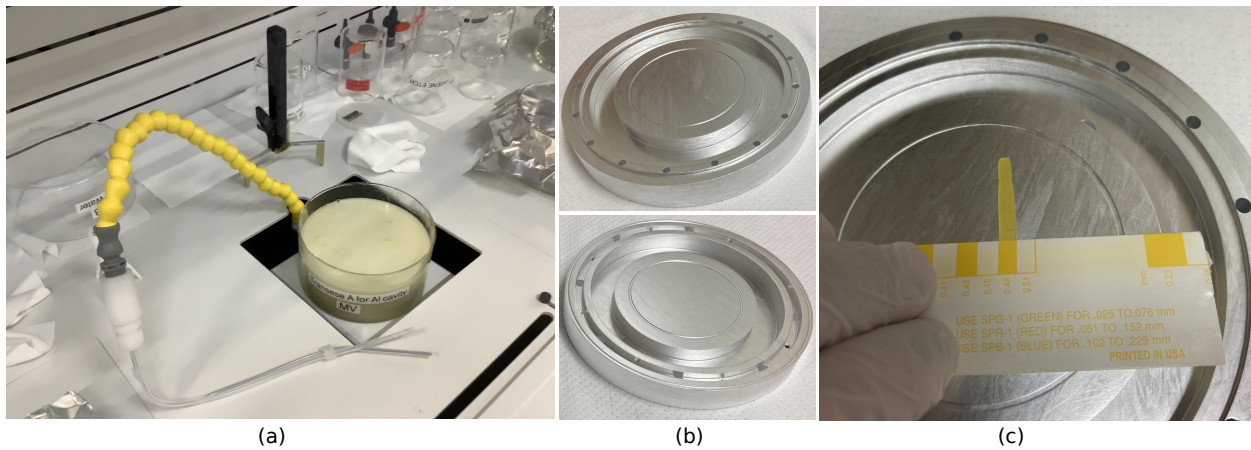


Figure 7.5 Wet chemical etching processing and results. (a) Transene™ Type A etch of aluminum cavities near the end of the second 2 hour etch, performed by Michael Vissers (MV) at the NIST, Boulder cleanroom facility. (b) Top and bottom cavity halves, post etch. (c) Plastigauge measurement of post separation following the etch.

7.1.4 Cavity Assembly, Mounting, and Wafer Preparation

Before measuring the bare or loaded cavity, we verified that the machining and assembly of the two cavity halves led to an air gap close to the design goal of $500\text{ }\mu\text{m}$. We used Plastigauge, a precision polymer gauge used to measure clearances in automotive and other mechanical systems by squeezing the polymer between two surfaces and measuring the clearance based on the spreading of the polymer compared to a gauge provided by the manufacturer (see Figure 7.6).

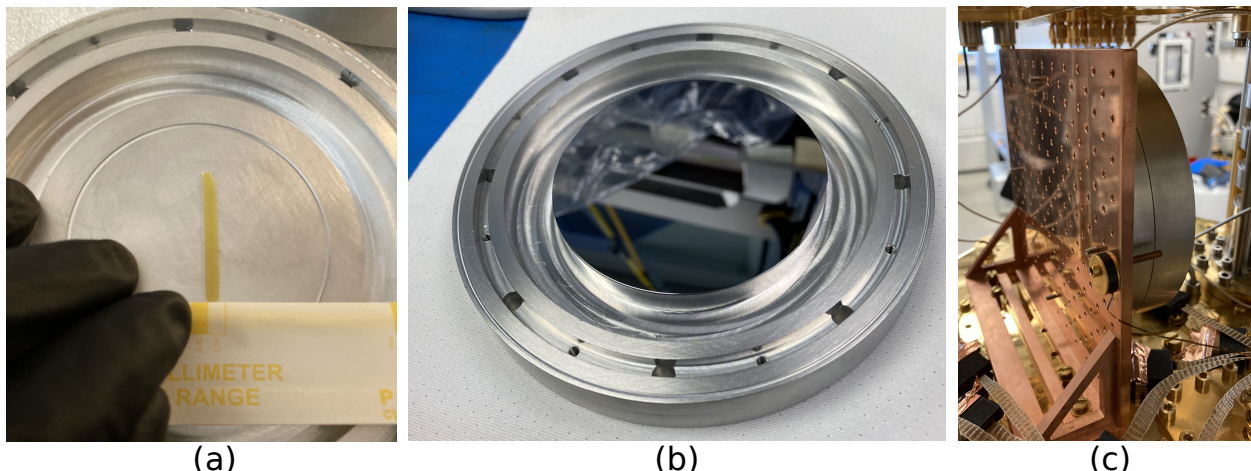


Figure 7.6 Room temperature cavity mechanical tests and mounting. (a) Plastigauge measurement of split post separation. (b) Mounting of two side polished, high resistivity silicon wafer. (c) Mounting of cavity on copper offset bracket in a Bluefors LD 250 dilution refrigerator with a separate Lakeshore RX-102A-CD ruthenium oxide (RuOx) temperature sensor mounted to the copper bracket.

We controlled the coupling to the split post mode by changing the insertion depth of a pin connected to an SMA jack. To seal the cavity along the H-plane of the high order TM mode between the posts, we used 1.0 mm diameter 4N (99.99 %) high purity indium wire, shown in Figure 7.7.



Figure 7.7 SMA pin and indium seal. (a) Insertion of the coupling pin into the air gap between the post and the cavity walls. (b) Indium seal made with 4N high purity indium wire, spool shown on the right.

7.2 Results

We report preliminary measurements of the unetched and etched bare cavity losses using experimental and computational results to separate seam losses from wall losses. The differential loss extraction of bulk silicon was performed with the etched cavity, marking the first measurement of a 3 inch wafer at millikelvin temperatures and single photon powers.

7.2.1 Unetched Cavity Measurements

We initially measured the unetched cavity, as low temperature microwave characterization facilities became available sooner than wet chemical etching access. The goal of these measurements was to set the coupling quality factor, extract the internal quality factor of the measurement mode and other modes, and estimate the surface resistance R_s and g_{seam} . To extract the latter, we used a combination of simulation and experimental data to fit the total, bare cavity loss to a linear model of the form of a line $y = ax + b$

$$\begin{aligned} Q_{\text{bare, tot}}^{-1} &= \frac{y_{\text{seam}}}{g_{\text{seam}}} + R_s \frac{p_{\text{cond}}}{X_s} \\ \frac{Q_{\text{bare, tot}}^{-1}}{y_{\text{seam}}} &= \frac{1}{g_{\text{seam}}} + R_s \frac{p_{\text{cond}}}{X_s y_{\text{seam}}} \end{aligned} \quad (7.7)$$

where $y = Q_{\text{bare, tot}}^{-1}/y_{\text{seam}}$, $x = p_{\text{cond}}/(X_s y_{\text{seam}})$, $a = R_s$, and $b = g_{\text{seam}}^{-1}$. In Figure 7.8, we report the total internal quality factors as a function of the simulated y_{seam} values for four resonances in the unetched cavity.

The line is a least squares fit to the model in (7.7) and the shaded region is the confidence interval on the fit, bounded by $\pm\sigma$, where σ is the standard error from the covariance matrix returned by the fitting routine. From the fit we extracted the surface resistance and seam conductances: $6 \times 10^{-5} \Omega$ and $g_{\text{seam}} = (3 \pm 2) \times 10^3 \text{ S/m}$. The values of y_{seam} are fixed by the geometry, leaving expected improvements from the etch to reductions in R_s and p_{cond} (by smaller λ_L), or increases in g_{seam} .

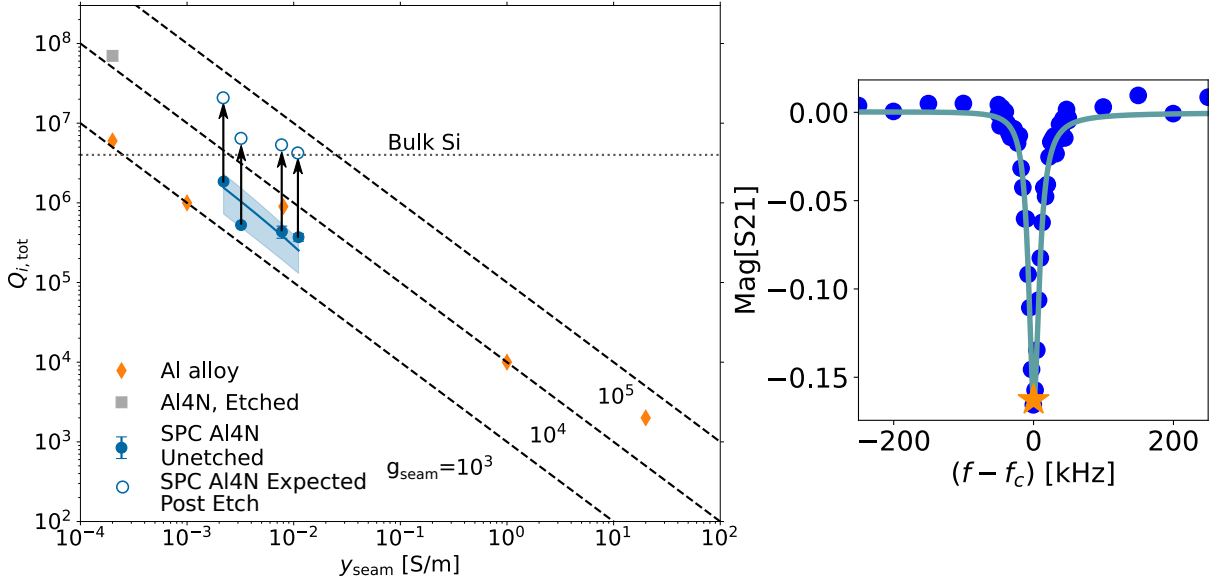


Figure 7.8 Preliminary data showing four modes from the SPC before wet chemical etching. Left: Al4N, etched and Al Alloy (6061) results from [27] to give bounds on the expected improvement in Q_i, tot after etching. Black dashed lines indicate constant g_{seam} values and the gray dotted line shows the value for the bulk loss of high resistivity silicon (2.5×10^{-7}) as estimated by Woods et al. [25]. Open blue circles and black arrows show best case, expected improvements in Q_i following the SPC etch. Right: representative transmission data of the 5.210 GHz split post resonance.

Previous etches of high purity aluminum superconducting cavities have shown a significant reduction in the London penetration, decreasing p_{cond} and the wall loss contribution [50]. Using the extracted values of R_s and g_{seam} we estimated the contributions to Q_{walls}^{-1} and Q_{seam}^{-1} for each mode, and found that all four modes were dominated by seam loss. To improve the estimate of these contributions to the fit of R_s and g_{seam} , we added constraints in the form of penalties with high weights for fits that lead to large deviations from the sum of the seam and wall loss contributions from the experimental, total losses for each mode. We summarize these results in Table 7.1, with the wall and seam loss summing to slightly more than the total measured losses. The differences in mode losses are attributed to the differences in y_{seam} , with the two lower frequency modes occupying the space between the posts and the higher frequency modes existing in the vacuum between the posts and the outer cavity walls.

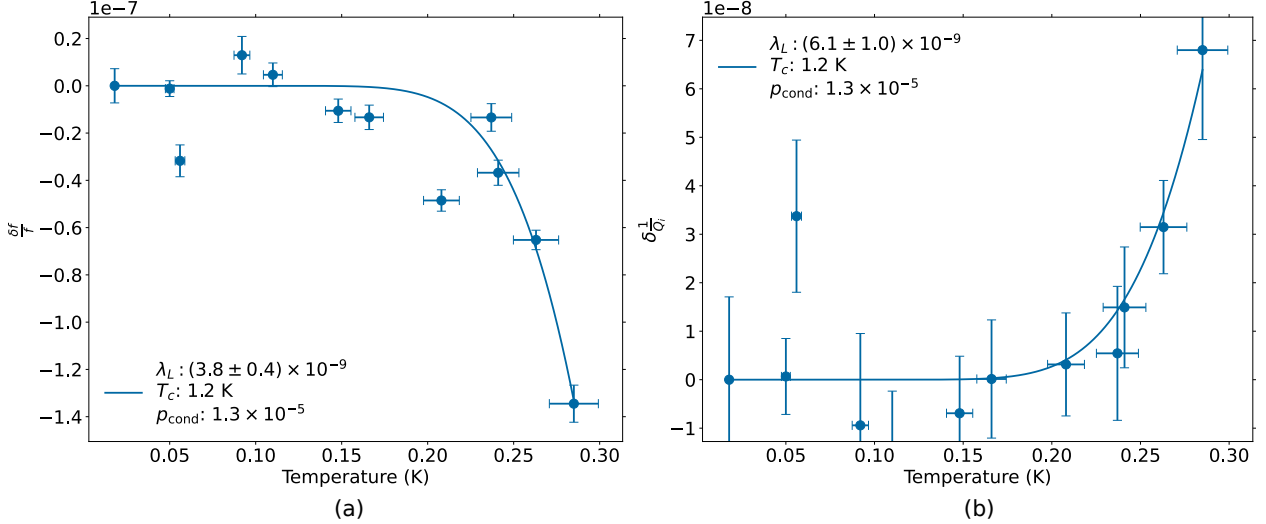


Figure 7.9 Temperature dependent fractional frequency shift in (a) and fractional loss in (b) for the 7.875 GHz resonance of the unetched bare cavity.

We suspect that a miscalculation in the location and depth of the $\lambda/4$ choke led to higher than desired y_{seam} in the lower frequency modes and lower than expected y_{seam} in the higher frequency modes. We performed temperature sweeps of the four resonances studied in Table 7.1, with only the highest frequency mode exhibiting the expected Mattis-Bardeen theory temperature dependence [50, 66, 139]. The fractional frequency shift and quality factor are given by

$$\frac{\delta f}{f} = \frac{f(T) - f(0)}{f(0)} = \frac{X_s(T) - X_s(0)}{X_s(0)} \quad (7.8)$$

$$\delta \frac{1}{Q_i} = \frac{1}{Q_i(T)} - \frac{1}{Q_i(0)} \quad (7.9)$$

where $R_s = \text{Re}\{Z_s\}$ and $X_s = \text{Im}\{Z_s\}$ are the surface resistance and reactance of the superconductor and Z_s is the surface impedance. See Section 1.5 for a detailed description of the Mattis-Bardeen theory, linking the resonant frequency and inverse quality factor shifts to universal properties of conventional BCS-type superconductors. In Figure 7.9, we report the temperature sweep measurements of the 7.875 GHz resonance. The Mattis-Bardeen fits with the transition temperature T_c fixed for pure aluminum at 1.2 K and the conductive participation p_{cond} fixed by simulation. We extracted London penetration depths between 3.8 and 6.1 nm, much smaller than the theoretical value for pure aluminum, 16 nm, and smaller yet than what was extracted by Reagor et al. [50] from etched 5N5 aluminum coaxial stub cavities (65 and 55 nm, respectively).

If we relax the constraint on the critical temperature and conductive participation, fitting those parameters along with the London penetration depth, the fraction frequency shift gives a London penetration depth of 43 nm, $T_c = (1.1 \pm 0.7)$ K, and $p_{\text{cond}} = 5.5 \times 10^{-5}$. This fit more closely agrees with an expected λ_L on the order of tens of nm, although a similar fitting procedure applied to the fractional loss still yields a smaller $\lambda_L = 2.3$ nm (see Figure 7.10).

Table 7.1 Unetched cavity estimated wall and seam losses.

Mode Frequency [GHz]	p_{cond}	y_{seam}	Q_{walls}^{-1}	Q_{seam}^{-1}	$Q_{\text{bare, tot}}^{-1}$
4.657	9.78×10^{-6}	7.75×10^{-3}	1.9×10^{-7}	2.4×10^{-6}	$(2.3 \pm 0.4) \times 10^{-6}$
5.2101	1.15×10^{-5}	1.11×10^{-2}	2.0×10^{-7}	3.4×10^{-6}	$(2.7 \pm 0.3) \times 10^{-6}$
6.551	1.33×10^{-5}	3.21×10^{-3}	1.5×10^{-7}	9.8×10^{-7}	$(1.90 \pm 0.02) \times 10^{-6}$
7.875	1.25×10^{-5}	2.2×10^{-3}	1.5×10^{-7}	6.7×10^{-7}	$(5.4 \pm 0.2) \times 10^{-7}$

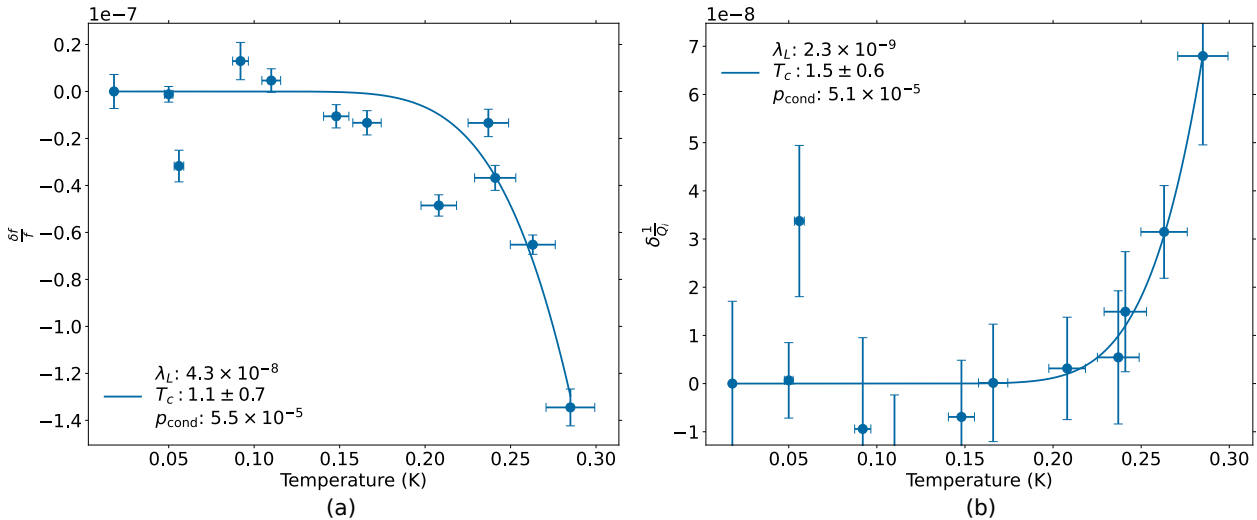


Figure 7.10 Temperature dependent fractional frequency shift (a) and (b) fractional loss with λ_L , T_c , and p_{cond} as free parameters.

7.3 Discussion and Conclusions

The sheer number of superconducting cavity measurements [4, 182, 223, 228] to extract the bulk dielectric losses of substrates at single photon powers and millikelvin temperatures speaks to the progress in the superconducting qubit field in reducing other losses to such a degree that bulk losses will soon limit their performance. Thus, developing high throughput measurement techniques to screen substrates from multiple vendors, different manufacturing processes, and materials is critical to continue improving qubit coherence. We emphasize the high throughput and low barrier to entry as differentiating features of this measurement approach compared to the others.

The cavity was machined by a precision, online machine shop, Zero Hour Parts, and required a wet chemical etch to achieve high quality factors to be sensitive enough to measure low loss sapphire wafers. Future iterations of the cavity could be fabricated from lower purity Al 6061 and diamond turn polished as in [182]. The high participation in the wafer lends itself to future studies of surface defect layers in sapphire identified by McLellan et al. [215] and A/B comparisons of Nb_2O_5 and Ta_2O_5 grown on a wafer with Nb deposited on it.

CHAPTER 8

CONCLUSIONS AND OUTLOOK

8.1 Conclusion

In this thesis, we developed numerical modeling approaches for superconducting 2D and 3D tunable couplers relevant to superconducting quantum computing systems. The 2DEG coupler presented in Chapter 2 was a unique, direct tunable capacitive coupling element, evidenced by the patent [229]. An experimental demonstration of such a coupler remains to be seen in the literature, with a notable experiment performing parametric gates mediated by a gatemon driven with an oscillating gate bias rather than a tunable coupler. We emphasize that the modeling effort presented in our work is substantial on its own, combining multiphysics simulations of the semiclassical semiconductor physics of the 2DEG with full electromagnetic simulations and lumped element circuit models, including parasitic capacitances of the three terminal device. The super-semi field as well as those working to integrate cryogenic complementary metal oxide semiconductor (cryo-CMOS) electronics with superconducting circuits stand to benefit from similar modeling efforts.³⁹

The work presented in Chapter 4 is a significant departure from the conventional capacitive tunable couplers in the literature. To date, there are no experimental or theoretical proposals, apart from an experiment where a diode shorts two electrically isolated low quality-factor rectangular cavity halves in [231], using galvanic coupling in 3D. As we found in our modeling of a two post coupler design, there are challenges in both simulating and physically realizing such systems. Galvanic coupling, at least of the variety that we studied in thesis, poses a high seam conductance requirement to mitigate seam loss introduced by the interface between the cavity structures and the external SQUID circuit. A forthcoming experimental effort to realize such a tunable coupler would benefit the quantum information and particle detection communities, such as the Axion Dark Matter eXperiment (ADMX) search team [232]. ADMX uses a large cavity that is tuned in resonance with candidate dark matter that weakly couple to the electromagnetic field in the cavity by using a dielectric tuning rod to scan the resonance frequency of the cavity. Electronic tuning schemes that encompass a wider range of frequencies and cavities that are free of mode crossings could be a significant boost to future axion searches at higher frequencies.

³⁹There is also significant overlap with our modeling efforts and the spin qubit community. Accurately modeling the spatial profile of their gate-defined quantum wells, as well as the microwave electromagnetic environment, plays a critical role in coordinating the sophisticated base-band pulse sequences required to perform gates on their triplet spin qubits [230].

The field overlap integral method developed to support the galvanic coupler modeling has far-reaching applications as well. By reformulating the problem of extracting bare and parametric rates to integrals calculated offline, that is outside of the Ansys HFSS solver, we can estimate these rates with potentially higher accuracy at a lower computational cost compared to similar calculations performed with the HFSS fields calculator. Similar calculations can also give estimates of the loss rates due to coupling to spurious modes in the packaging of 2D qubits [39] and parasitic resonances in 3D systems.

Our measurements of 2D CPW resonators expanded the understanding of the correlations between materials and losses. In particular, we reported the first A/B comparison study of the effects of grain size in tantalum thin films in Chapter 6, albeit in a restricted regime. The null result, that is a lack of difference in loss observed between the two films, is significant in that we can exclude grain size in that regime as a significant contributor to loss in those films. By combining microwave loss measurements with room temperature materials characterization techniques and cryogenic transport measurements, our work is an example of where the field is moving to systematically link materials properties with device performance [215].

The work in the hydrides study, presented in Section 5.2.1 is a prime example of connecting materials with microwave losses. By carefully accounting for the number and phase of niobium hydrides precipitated following fluoride-based wet chemical etchants, we can tie increases in power-independent losses to the increased presence of hydrides. A heuristic solution that balances hydride formation with oxide removal, a short duration BOE dip, is another outcome from the study, now backed by the evidence of our microwave measurements.

Lastly, the split post cavity design is a unique contribution of this thesis. Namely, no measurements at millikelvin temperatures and single photon powers have been performed on full wafers until this study. The strength of this technique is two-fold. First, it offers a complementary measurement approach to extract the bulk losses of dielectric substrates at the wafer scale. Second, we anticipate that we will be sensitive to variations in wafers of different boules, manufacturers, and pre-deposition processing such as annealing to better quantify the contributions of those processes to the total loss of superconducting devices.

8.2 Outlook

At the advent of this thesis (ca. 2018), the field of superconducting circuit and cavity quantum computing was rapidly growing. There were multiple commercial and academic groups with tens of qubits starting to become accessible through cloud computing and the next year the Google group would demonstrate quantum advantage in a random sampling problem [37].

Some five years later, the commercial players (IBM, Google, Rigetti) continue to push forward with transmon-based, planar qubits with improved coherences and some modifications to connectivity and control on the order of a few hundred physical qubits, with some indications that the surface error correction code at least works in principle – logical error rates improve with increasing size of the surface code or number of physical qubits [56].

A biased perspective might suggest that the work done by 3D superconducting cavity-based bosonic error correction community [58, 113, 220] supersedes the former, as the size and complexity of their logical qubits is dwarfed by the resource requirements of standard surface code estimates [57]. Some smaller companies are taking this approach, investing in higher coherence, fewer qubit systems with error correction built-in from the start. Autonomous error correction was also demonstrated with an equally hardware-efficient implementation: the very small logical qubit star code using a single tunable coupler driven with oscillating fields [233, 234]. The thread that links these works and the large scale systems is the enabling technology of tunable couplers, namely parametrically activated, high fidelity couplers.

This thesis presented designs for two couplers, one in the super-semi domain, compatible with existing transmon and gatemon qubits, and the other in the 3D cavity space. The design and analysis tools used to study these couplers have broad applicability in their respective domains, with the field overlap integral method potentially spanning both the 2D and 3D design space. There are related developments in circuit quantum acoustodynamics (cQAD) field⁴⁰ that extend the EPR method in similar ways as the FOI, calculating couplings between the electromagnetic field and the strain field in coupled finite element simulations [235].

The second half of this thesis focused on the large space of materials loss mechanisms in superconducting qubits as elucidated by superconducting CPW and 3D cavity measurements. Our contributions to the body of knowledge surrounding the materials parameters in 2D superconducting qubit fabrication included the influence of grain size in Ta thin films on c-axis sapphire⁴¹ and various attempts to cap Nb resonators with other superconductors, normal metals, and amorphous silicon. Even the most routine measurements, transmission microwave measurements of superconducting resonators, are open to refinement and debate. As we noted in Section 1.5.2, the point distribution of frequencies used to extract the losses from fits of the transmission frequency responses is an area of active research [122].

⁴⁰cQAD is the mechanical analog of cQED, where the microwave resonator is replaced by a mechanical resonator and the nonlinear element is a transmon qubit. The resulting Hamiltonian, dispersive readout, and control are similar to cQED, with applications in quantum information, transduction, and sensing.

⁴¹The additional qualifiers are both necessary and a nod to the precision of this line of work, where statements about a particular superconductor or crystallographic orientation of a substrate does not necessarily transfer to all other superconducting thin films and substrates or even the same substrate with a different orientation.

With the emergence of 3D cavity measurements, there is still low hanging fruit in characterizing new materials, especially birefringement dielectrics [4, 224] and wafers. These techniques can stand alone as novel metrological systems as well as complement existing methods to construct accurate loss budgets of superconducting resonators and qubits. The use of high throughput measurement systems such as high-Q cavities and multiplexed resonator readout [236] also stands to benefit both small academic groups and industry, where fast feedback between measurement and fabrication can accelerate improvements in device performance. We expect other opportunities for adjacent fields such as the high energy superconducting particle detector and single flux quantum digital logic communities to interface with superconducting qubits for readout, loss metrology, and loss mitigation on the path to fault tolerant digital quantum computing and near term, practical demonstrations of quantum advantage.

REFERENCES

- [1] Jens Koch, Terri M. Yu, Jay Gambetta, A. A. Houck, D. I. Schuster, J. Majer, Alexandre Blais, M. H. Devoret, S. M. Girvin, and R. J. Schoelkopf. Charge-insensitive qubit design derived from the Cooper pair box. *Phys. Rev. A*, 76:042319, Oct 2007. doi: 10.1103/PhysRevA.76.042319.
- [2] P. Krantz, M. Kjaergaard, F. Yan, T. P. Orlando, S. Gustavsson, and W. D. Oliver. A quantum engineer's guide to superconducting qubits. *Applied Physics Reviews*, 6(2):021318, 2019. doi: 10.1063/1.5089550.
- [3] Nicholas Materise. An introduction to superconducting qubits and circuit quantum electrodynamics. In Gianpaolo Carosi, Gray Rybka, and Karl van Bibber, editors, *Microwave Cavities and Detectors for Axion Research*, pages 87–95, Cham, 2018. Springer International Publishing. ISBN 978-3-319-92726-8.
- [4] Alexander P. Read, Benjamin J. Chapman, Chan U Lei, Jacob C. Curtis, Suhas Ganjam, Lev Krayzman, Luigi Frunzio, and Robert J. Schoelkopf. Precision Measurement of the Microwave Dielectric Loss of Sapphire in the Quantum Regime with Parts-per-Billion Sensitivity. *Phys. Rev. Appl.*, 19:034064, Mar 2023. doi: 10.1103/PhysRevApplied.19.034064.
- [5] Hanhee Paik, D. I. Schuster, Lev S. Bishop, G. Kirchmair, G. Catelani, A. P. Sears, B. R. Johnson, M. J. Reagor, L. Frunzio, L. I. Glazman, S. M. Girvin, M. H. Devoret, and R. J. Schoelkopf. Observation of high coherence in josephson junction qubits measured in a three-dimensional circuit qed architecture. *Phys. Rev. Lett.*, 107:240501, Dec 2011. doi: 10.1103/PhysRevLett.107.240501.
- [6] Eric T. Holland, Yaniv J. Rosen, Nicholas Materise, Nathan Woollett, Thomas Voisin, Y. Morris Wang, Sharon G. Torres, Jorge Mireles, Gianpaolo Carosi, and Jonathan L DuBois. High-kinetic inductance additive manufactured superconducting microwave cavity. *Applied Physics Letters*, 111(20):202602, 2017. doi: 10.1063/1.5000241.
- [7] Yu Chen, C. Neill, P. Roushan, N. Leung, M. Fang, R. Barends, J. Kelly, B. Campbell, Z. Chen, B. Chiaro, A. Dunsworth, E. Jeffrey, A. Megrant, J. Y. Mutus, P. J. J. O'Malley, C. M. Quintana, D. Sank, A. Vainsencher, J. Wenner, T. C. White, Michael R. Geller, A. N. Cleland, and John M. Martinis. Qubit Architecture with High Coherence and Fast Tunable Coupling. *Phys. Rev. Lett.*, 113:220502, Nov 2014. doi: 10.1103/PhysRevLett.113.220502.
- [8] Yao Lu, S. Chakram, N. Leung, N. Earnest, R. K. Naik, Ziwen Huang, Peter Groszkowski, Eliot Kapit, Jens Koch, and David I. Schuster. Universal stabilization of a parametrically coupled qubit. *Phys. Rev. Lett.*, 119:150502, Oct 2017. doi: 10.1103/PhysRevLett.119.150502.
- [9] Yvonne Y. Gao, Brian J. Lester, Yaxing Zhang, Chen Wang, Serge Rosenblum, Luigi Frunzio, Liang Jiang, S. M. Girvin, and Robert J. Schoelkopf. Programmable interference between two microwave quantum memories. *Phys. Rev. X*, 8:021073, Jun 2018. doi: 10.1103/PhysRevX.8.021073.
- [10] Fei Yan, Philip Krantz, Youngkyu Sung, Morten Kjaergaard, Daniel L. Campbell, Terry P. Orlando, Simon Gustavsson, and William D. Oliver. Tunable Coupling Scheme for Implementing High-Fidelity Two-Qubit Gates. *Phys. Rev. Appl.*, 10:054062, Nov 2018. doi: 10.1103/PhysRevApplied.10.054062.

- [11] D.K. Weiss, Helin Zhang, Chunyang Ding, Yuwei Ma, David I. Schuster, and Jens Koch. Fast High-Fidelity Gates for Galvanically-Coupled Fluxonium Qubits Using Strong Flux Modulation. *PRX Quantum*, 3:040336, Dec 2022. doi: 10.1103/PRXQuantum.3.040336.
- [12] Benjamin J. Chapman, Stijn J. de Graaf, Sophia H. Xue, Yaxing Zhang, James Teoh, Jacob C. Curtis, Takahiro Tsunoda, Alec Eickbusch, Alexander P. Read, Akshay Koottandavida, Shantanu O. Mundhada, Luigi Frunzio, M.H. Devoret, S.M. Girvin, and R.J. Schoelkopf. High-On-Off-Ratio Beam-Splitter Interaction for Gates on Bosonically Encoded Qubits. *PRX Quantum*, 4:020355, Jun 2023. doi: 10.1103/PRXQuantum.4.020355.
- [13] X. Y. Jin, K. Cicak, Z. Parrott, S. Kotler, F. Lecocq, J. Teufel, J. Aumentado, E. Kapit, and R. W. Simmonds. Versatile parametric coupling between two statically decoupled transmon qubits. *arXiv e-prints*, art. arXiv:2305.02907, May 2023. doi: 10.48550/arXiv.2305.02907.
- [14] Yinqi Chen, Konstantin N. Nesterov, Hugh Churchill, Javad Shabani, Vladimir E. Manucharyan, and Maxim G. Vavilov. Voltage-activated parametric entangling gates based on gatemon qubits. *Phys. Rev. Appl.*, 20:044012, Oct 2023. doi: 10.1103/PhysRevApplied.20.044012.
- [15] Kentaro Kubo and Hayato Goto. Fast parametric two-qubit gate for highly detuned fixed-frequency superconducting qubits using a double-transmon coupler. *Applied Physics Letters*, 122(6):064001, 02 2023. ISSN 0003-6951. doi: 10.1063/5.0138699.
- [16] Yao Lu, Aniket Maiti, John W. O. Garmon, Suhas Ganjam, Yaxing Zhang, Jahan Claes, Luigi Frunzio, Steven M. Girvin, and Robert J. Schoelkopf. High-fidelity parametric beamsplitting with a parity-protected converter. *Nature Communications*, 14(1):5767, Sep 2023. ISSN 2041-1723. doi: 10.1038/s41467-023-41104-0.
- [17] C. R. H. McRae, H. Wang, J. Gao, M. R. Vissers, T. Brecht, A. Dunsworth, D. P. Pappas, and J. Mutus. Materials loss measurements using superconducting microwave resonators. *Review of Scientific Instruments*, 91(9), 09 2020. ISSN 0034-6748. doi: 10.1063/5.0017378. 091101.
- [18] boulder-cryogenic-quantum-testbed/scresonators.
<https://github.com/Boulder-Cryogenic-Quantum-Testbed/scresonators>, 2023.
- [19] Clemens Müller, Jared H Cole, and Jürgen Lisenfeld. Towards understanding two-level-systems in amorphous solids: insights from quantum circuits. *Reports on Progress in Physics*, 82(12):124501, 10 2019. doi: 10.1088/1361-6633/ab3a7e.
- [20] Rógerio de Sousa. Fundamentals of applied superconductivity. In *CMC Microsystems Build Your Own Superconducting Quantum Device Workshop*, 2023.
- [21] William Mayer, Joseph Yuan, Kaushini S. Wickramasinghe, Tri Nguyen, Matthieu C. Dartiallh, and Javad Shabani. Superconducting proximity effect in epitaxial Al-InAs heterostructures. *Applied Physics Letters*, 114(10):103104, 2019. doi: 10.1063/1.5067363.
- [22] J. Shabani, M. Kjaergaard, H. J. Suominen, Younghyun Kim, F. Nicelle, K. Pakrouski, T. Stankevic, R. M. Lutchyn, P. Krogstrup, R. Feidenhans'l, S. Kraemer, C. Nayak, M. Troyer, C. M. Marcus, and C. J. Palmstrøm. Two-dimensional epitaxial superconductor-semiconductor heterostructures: A platform for topological superconducting networks. *Phys. Rev. B*, 93:155402, Apr 2016. doi: 10.1103/PhysRevB.93.155402.
- [23] Kaushini S. Wickramasinghe, William Mayer, Joseph Yuan, Tri Nguyen, Lucy Jiao, Vladimir Manucharyan, and Javad Shabani. Transport properties of near surface InAs two-dimensional heterostructures. *Applied Physics Letters*, 113(26):262104, 2018. doi: 10.1063/1.5050413.

- [24] William M. Strickland, Mehdi Hatifiour, Dylan Langone, S. M. Farzaneh, and Javad Shabani. Controlling fermi level pinning in near-surface inas quantum wells. *Applied Physics Letters*, 121(9):092104, 2022. doi: 10.1063/5.0101579.
- [25] W. Woods, G. Calusine, A. Melville, A. Sevi, E. Golden, D.K. Kim, D. Rosenberg, J.L. Yoder, and W.D. Oliver. Determining Interface Dielectric Losses in Superconducting Coplanar-Waveguide Resonators. *Phys. Rev. Applied*, 12:014012, Jul 2019. doi: 10.1103/PhysRevApplied.12.014012.
- [26] G. L. Ragan. *Microwave Transmission Line Circuits*, volume 9 of *MIT Radiation Laboratory*. McGraw Hill, New York, 1948.
- [27] T. Brecht, M. Reagor, Y. Chu, W. Pfaff, C. Wang, L. Frunzio, M. H. Devoret, and R. J. Schoelkopf. Demonstration of superconducting micromachined cavities. *Applied Physics Letters*, 107(19):192603, 11 2015. ISSN 0003-6951. doi: 10.1063/1.4935541.
- [28] D. Phan, J. Senior, A. Ghazaryan, M. Hatifiour, W. M. Strickland, J. Shabani, M. Serbyn, and A. P. Higginbotham. Detecting Induced $p \pm ip$ Pairing at the Al-InAs Interface with a Quantum Microwave Circuit. *Phys. Rev. Lett.*, 128:107701, Mar 2022. doi: 10.1103/PhysRevLett.128.107701.
- [29] He Ma, Marco Govoni, and Giulia Galli. Quantum simulations of materials on near-term quantum computers. *npj Computational Materials*, 6(1):85, Jul 2020. ISSN 2057-3960. doi: 10.1038/s41524-020-00353-z.
- [30] T. R. Clem, C. P. Foley, and M. N. Keene. *SQUIDs for Geophysical Survey and Magnetic Anomaly Detection*, chapter 14, pages 481–543. John Wiley & Sons, Ltd, 2006. ISBN 9783527609956. doi: <https://doi.org/10.1002/9783527609956.ch14>.
- [31] Jarrod R McClean, Jonathan Romero, Ryan Babbush, and Alán Aspuru-Guzik. The theory of variational hybrid quantum-classical algorithms. *New Journal of Physics*, 18(2):023023, feb 2016. doi: 10.1088/1367-2630/18/2/023023.
- [32] P. J. J. O’Malley, R. Babbush, I. D. Kivlichan, J. Romero, J. R. McClean, R. Barends, J. Kelly, P. Roushan, A. Tranter, N. Ding, B. Campbell, Y. Chen, Z. Chen, B. Chiaro, A. Dunsworth, A. G. Fowler, E. Jeffrey, E. Lucero, A. Megrant, J. Y. Mutus, M. Neeley, C. Neill, C. Quintana, D. Sank, A. Vainsencher, J. Wenner, T. C. White, P. V. Coveney, P. J. Love, H. Neven, A. Aspuru-Guzik, and J. M. Martinis. Scalable quantum simulation of molecular energies. *Phys. Rev. X*, 6:031007, Jul 2016. doi: 10.1103/PhysRevX.6.031007.
- [33] Charles H. Bennett and Gilles Brassard. Quantum cryptography: Public key distribution and coin tossing. *Theoretical Computer Science*, 560:7–11, 2014. ISSN 0304-3975. doi: <https://doi.org/10.1016/j.tcs.2014.05.025>. Theoretical Aspects of Quantum Cryptography – celebrating 30 years of BB84.
- [34] Artur K. Ekert. Quantum cryptography based on bell’s theorem. *Phys. Rev. Lett.*, 67:661–663, Aug 1991. doi: 10.1103/PhysRevLett.67.661.
- [35] John Preskill. Quantum Computing in the NISQ era and beyond. *Quantum*, 2:79, 8 2018. ISSN 2521-327X. doi: 10.22331/q-2018-08-06-79.
- [36] Morten Kjaergaard, Mollie E. Schwartz, Jochen Braumüller, Philip Krantz, Joel I.-J. Wang, Simon Gustavsson, and William D. Oliver. Superconducting qubits: Current state of play. *Annual Review of Condensed Matter Physics*, 11(1):369–395, 2020. doi: 10.1146/annurev-conmatphys-031119-050605.

- [37] Frank Arute, Kunal Arya, Ryan Babbush, Dave Bacon, Joseph C. Bardin, Rami Barends, Rupak Biswas, Sergio Boixo, Fernando G. S. L. Brando, David A. Buell, Brian Burkett, Yu Chen, Zijun Chen, Ben Chiaro, Roberto Collins, William Courtney, Andrew Dunsworth, Edward Farhi, Brooks Foxen, Austin Fowler, Craig Gidney, Marissa Giustina, Rob Graff, Keith Guerin, Steve Habegger, Matthew P. Harrigan, Michael J. Hartmann, Alan Ho, Markus Hoffmann, Trent Huang, Travis S. Humble, Sergei V. Isakov, Evan Jeffrey, Zhang Jiang, Dvir Kafri, Kostyantyn Kechedzhi, Julian Kelly, Paul V. Klimov, Sergey Knysh, Alexander Korotkov, Fedor Kostritsa, David Landhuis, Mike Lindmark, Erik Lucero, Dmitry Lyakh, Salvatore Mandrà, Jarrod R. McClean, Matthew McEwen, Anthony Megrant, Xiao Mi, Kristel Michelsen, Masoud Mohseni, Josh Mutus, Ofer Naaman, Matthew Neeley, Charles Neill, Murphy Yuezhen Niu, Eric Ostby, Andre Petukhov, John C. Platt, Chris Quintana, Eleanor G. Rieffel, Pedram Roushan, Nicholas C. Rubin, Daniel Sank, Kevin J. Satzinger, Vadim Smelyanskiy, Kevin J. Sung, Matthew D. Trevithick, Amit Vainsencher, Benjamin Villalonga, Theodore White, Z. Jamie Yao, Ping Yeh, Adam Zalcman, Hartmut Neven, and John M. Martinis. Quantum supremacy using a programmable superconducting processor. *Nature*, 574(7779): 505–510, Oct 2019. ISSN 1476-4687. doi: 10.1038/s41586-019-1666-5.
- [38] R. Barends, C. M. Quintana, A. G. Petukhov, Yu Chen, D. Kafri, K. Kechedzhi, R. Collins, O. Naaman, S. Boixo, F. Arute, K. Arya, D. Buell, B. Burkett, Z. Chen, B. Chiaro, A. Dunsworth, B. Foxen, A. Fowler, C. Gidney, M. Giustina, R. Graff, T. Huang, E. Jeffrey, J. Kelly, P. V. Klimov, F. Kostritsa, D. Landhuis, E. Lucero, M. McEwen, A. Megrant, X. Mi, J. Mutus, M. Neeley, C. Neill, E. Ostby, P. Roushan, D. Sank, K. J. Satzinger, A. Vainsencher, T. White, J. Yao, P. Yeh, A. Zalcman, H. Neven, V. N. Smelyanskiy, and John M. Martinis. Diabatic gates for frequency-tunable superconducting qubits. *Phys. Rev. Lett.*, 123:210501, Nov 2019. doi: 10.1103/PhysRevLett.123.210501.
- [39] Ziwen Huang, Yao Lu, Eliot Kapit, David I. Schuster, and Jens Koch. Universal stabilization of single-qubit states using a tunable coupler. *Phys. Rev. A*, 97:062345, Jun 2018. doi: 10.1103/PhysRevA.97.062345.
- [40] Y. Nakamura, Yu. A. Pashkin, and J. S. Tsai. Coherent control of macroscopic quantum states in a single-cooper-pair box. *Nature*, 398(6730):786–788, Apr 1999. ISSN 1476-4687. doi: 10.1038/19718.
- [41] Schuster, D.I. *Circuit Quantum Electrodynamics*. PhD thesis, Yale University, 2007.
- [42] T. W. Larsen, K. D. Petersson, F. Kuemmeth, T. S. Jespersen, P. Krogstrup, J. Nygård, and C. M. Marcus. Semiconductor-nanowire-based superconducting qubit. *Phys. Rev. Lett.*, 115:127001, Sep 2015. doi: 10.1103/PhysRevLett.115.127001.
- [43] S. P. Benz. Superconductor-normal-superconductor junctions for programmable voltage standards. *Applied Physics Letters*, 67(18):2714–2716, 1995. doi: 10.1063/1.114302.
- [44] A. W. Kleinsasser and T. N. Jackson. Prospects for proximity effect superconducting fets. *IEEE Transactions on Magnetics*, 25(2):1274–1277, 3 1989. ISSN 1941-0069. doi: 10.1109/20.92528.
- [45] A. W. Kleinsasser, T. N. Jackson, D. McInturff, F. Rammo, G. D. Pettit, and J. M. Woodall. Superconducting ingaas junction field-effect transistors with nb electrodes. *Applied Physics Letters*, 55(18):1909–1911, 1989. doi: 10.1063/1.102166.
- [46] Zhenyi Qi, Hong-Yi Xie, Javad Shabani, Vladimir E. Manucharyan, Alex Levchenko, and Maxim G. Vavilov. Controlled-Z gate for transmon qubits coupled by semiconductor junctions. *Phys. Rev. B*, 97:134518, 4 2018. doi: 10.1103/PhysRevB.97.134518.

- [47] L. Casparis, N. J. Pearson, A. Kringhøj, T. W. Larsen, F. Kuemmeth, J. Nygård, P. Krogstrup, K. D. Petersson, and C. M. Marcus. Voltage-controlled superconducting quantum bus. *Phys. Rev. B*, 99:085434, 2 2019. doi: 10.1103/PhysRevB.99.085434.
- [48] N. Materise, M.C. Dartailh, W.M. Strickland, J. Shabani, and E. Kapit. Tunable capacitor for superconducting qubits using an InAs/InGaAs heterostructure. *Quantum Science and Technology*, 8 (4):045014, 2023. doi: 10.1088/2058-9565/aceb18.
- [49] A. Romanenko, R. Pilipenko, S. Zorzetti, D. Frolov, M. Awida, S. Belomestnykh, S. Posen, and A. Grassellino. Three-dimensional superconducting resonators at $t < 20$ mk with photon lifetimes up to $\tau = 2$ s. *Phys. Rev. Applied*, 13:034032, Mar 2020. doi: 10.1103/PhysRevApplied.13.034032.
- [50] Matthew Reagor, Hanhee Paik, Gianluigi Catelani, Luyan Sun, Christopher Axline, Eric Holland, Ioan M. Pop, Nicholas A. Masluk, Teresa Brecht, Luigi Frunzio, Michel H. Devoret, Leonid Glazman, and Robert J. Schoelkopf. Reaching 10 ms single photon lifetimes for superconducting aluminum cavities. *Applied Physics Letters*, 102(19):192604, 2013. doi: 10.1063/1.4807015.
- [51] E. T. Holland, B. Vlastakis, R. W. Heeres, M. J. Reagor, U. Vool, Z. Leghtas, L. Frunzio, G. Kirchmair, M. H. Devoret, M. Mirrahimi, and R. J. Schoelkopf. Single-photon-resolved cross-kerr interaction for autonomous stabilization of photon-number states. *Phys. Rev. Lett.*, 115:180501, Oct 2015. doi: 10.1103/PhysRevLett.115.180501.
- [52] Xian Wu, S. L. Tomarken, N. Anders Petersson, L. A. Martinez, Yaniv J. Rosen, and Jonathan L. DuBois. High-fidelity software-defined quantum logic on a superconducting qudit. *Phys. Rev. Lett.*, 125:170502, Oct 2020. doi: 10.1103/PhysRevLett.125.170502.
- [53] T. Noh, Z. Xiao, X. Y. Jin, K. Cicak, E. Doucet, J. Aumentado, L. C. G. Govia, L. Ranzani, A. Kamal, and R. W. Simmonds. Strong parametric dispersive shifts in a statically decoupled two-qubit cavity QED system. *Nature Physics*, 19(10):1445–1451, Oct 2023. ISSN 1745-2481. doi: 10.1038/s41567-023-02107-2.
- [54] Andrew D. King, Sei Suzuki, Jack Raymond, Alex Zucca, Trevor Lanting, Fabio Altomare, Andrew J. Berkley, Sara Ejtemaei, Emile Hoskinson, Shuiyuan Huang, Eric Ladizinsky, Allison J. R. MacDonald, Gaelen Marsden, Travis Oh, Gabriel Poulin-Lamarre, Mauricio Reis, Chris Rich, Yuki Sato, Jed D. Whittaker, Jason Yao, Richard Harris, Daniel A. Lidar, Hidetoshi Nishimori, and Mohammad H. Amin. Coherent quantum annealing in a programmable 2,000 qubit ising chain. *Nature Physics*, 18(11):1324–1328, Nov 2022. ISSN 1745-2481. doi: 10.1038/s41567-022-01741-6.
- [55] R. Baumann. Soft errors in advanced computer systems. *IEEE Design & Test of Computers*, 22(3): 258–266, 2005. doi: 10.1109/MDT.2005.69.

- [56] Rajeev Acharya, Igor Aleiner, Richard Allen, Trond I. Andersen, Markus Ansmann, Frank Arute, Kunal Arya, Abraham Asfaw, Juan Atalaya, Ryan Babbush, Dave Bacon, Joseph C. Bardin, Joao Basso, Andreas Bengtsson, Sergio Boixo, Gina Bortoli, Alexandre Bourassa, Jenna Bovaird, Leon Brill, Michael Broughton, Bob B. Buckley, David A. Buell, Tim Burger, Brian Burkett, Nicholas Bushnell, Yu Chen, Zijun Chen, Ben Chiaro, Josh Cogan, Roberto Collins, Paul Conner, William Courtney, Alexander L. Crook, Ben Curtin, Dripto M. Debroy, Alexander Del Toro Barba, Sean Demura, Andrew Dunsworth, Daniel Eppens, Catherine Erickson, Lara Faoro, Edward Farhi, Reza Fatemi, Leslie Flores Burgos, Ebrahim Forati, Austin G. Fowler, Brooks Foxen, William Giang, Craig Gidney, Dar Gilboa, Marissa Giustina, Alejandro Grajales Dau, Jonathan A. Gross, Steve Habegger, Michael C. Hamilton, Matthew P. Harrigan, Sean D. Harrington, Oscar Higgott, Jeremy Hilton, Markus Hoffmann, Sabrina Hong, Trent Huang, Ashley Huff, William J. Huggins, Lev B. Ioffe, Sergei V. Isakov, Justin Iveland, Evan Jeffrey, Zhang Jiang, Cody Jones, Pavol Juhas, Dvir Kafri, Kostyantyn Kechedzhi, Julian Kelly, Tanuj Khattar, Mostafa Khezri, Mária Kieferová, Seon Kim, Alexei Kitaev, Paul V. Klimov, Andrey R. Klots, Alexander N. Korotkov, Fedor Kostritsa, John Mark Kreikebaum, David Landhuis, Pavel Laptev, Kim-Ming Lau, Lily Laws, Joonho Lee, Kenny Lee, Brian J. Lester, Alexander Lill, Wayne Liu, Aditya Locharla, Erik Lucero, Fionn D. Malone, Jeffrey Marshall, Orion Martin, Jarrod R. McClean, Trevor McCourt, Matt McEwen, Anthony Megrant, Bernardo Meurer Costa, Xiao Mi, Kevin C. Miao, Masoud Mohseni, Shirin Montazeri, Alexis Morvan, Emily Mount, Wojciech Mruczkiewicz, Ofer Naaman, Matthew Neeley, Charles Neill, Ani Nersisyan, Hartmut Neven, Michael Newman, Jiun How Ng, Anthony Nguyen, Murray Nguyen, Murphy Yuezhen Niu, Thomas E. O'Brien, Alex Opremcak, John Platt, Andre Petukhov, Rebecca Potter, Leonid P. Pryadko, Chris Quintana, Pedram Roushan, Nicholas C. Rubin, Negar Saei, Daniel Sank, Kannan Sankaragomathi, Kevin J. Satzinger, Henry F. Schurkus, Christopher Schuster, Michael J. Shearn, Aaron Shorter, Vladimir Shvarts, Jindra Skruzny, Vadim Smelyanskiy, W. Clarke Smith, George Sterling, Doug Strain, Marco Szalay, Alfredo Torres, Guifre Vidal, Benjamin Villalonga, Catherine Vollgraff Heidweiller, Theodore White, Cheng Xing, Z. Jamie Yao, Ping Yeh, Juhwan Yoo, Grayson Young, Adam Zalcman, Yaxing Zhang, Ningfeng Zhu, and Google Quantum AI. Suppressing quantum errors by scaling a surface code logical qubit. *Nature*, 614(7949):676–681, Feb 2023. ISSN 1476-4687. doi: 10.1038/s41586-022-05434-1.
- [57] Austin G. Fowler, Matteo Mariantoni, John M. Martinis, and Andrew N. Cleland. Surface codes: Towards practical large-scale quantum computation. *Phys. Rev. A*, 86:032324, Sep 2012. doi: 10.1103/PhysRevA.86.032324.
- [58] Arne L. Grimsmo and Shruti Puri. Quantum Error Correction with the Gottesman-Kitaev-Preskill Code. *PRX Quantum*, 2:020101, Jun 2021. doi: 10.1103/PRXQuantum.2.020101.
- [59] Daniel Gottesman, Alexei Kitaev, and John Preskill. Encoding a qubit in an oscillator. *Phys. Rev. A*, 64:012310, Jun 2001. doi: 10.1103/PhysRevA.64.012310.
- [60] C. Flühmann, T. L. Nguyen, M. Marinelli, V. Negnevitsky, K. Mehta, and J. P. Home. Encoding a qubit in a trapped-ion mechanical oscillator. *Nature*, 566(7745):513–517, Feb 2019. ISSN 1476-4687. doi: 10.1038/s41586-019-0960-6.
- [61] P. Campagne-Ibarcq, A. Eickbusch, S. Touzard, E. Zalys-Geller, N. E. Frattini, V. V. Sivak, P. Reinhold, S. Puri, S. Shankar, R. J. Schoelkopf, L. Frunzio, M. Mirrahimi, and M. H. Devoret. Quantum error correction of a qubit encoded in grid states of an oscillator. *Nature*, 584(7821):368–372, Aug 2020. ISSN 1476-4687. doi: 10.1038/s41586-020-2603-3.
- [62] Dany Lachance-Quirion, Marc-Antoine Lemonde, Jean Olivier Simoneau, Lucas St-Jean, Pascal Lemieux, Sara Turcotte, Wyatt Wright, Amélie Lacroix, Joëlle Fréchette-Viens, Ross Shillito, Florian Hopfmüller, Maxime Tremblay, Nicholas E. Frattini, Julien Camirand Lemyre, and Philippe St-Jean. Autonomous quantum error correction of Gottesman-Kitaev-Preskill states. *arXiv e-prints*, art. arXiv:2310.11400, oct 2023. doi: 10.48550/arXiv.2310.11400.

- [63] Nissim Ofek, Andrei Petrenko, Reinier Heeres, Philip Reinhold, Zaki Leghtas, Brian Vlastakis, Yehan Liu, Luigi Frunzio, S. M. Girvin, L. Jiang, Mazyar Mirrahimi, M. H. Devoret, and R. J. Schoelkopf. Extending the lifetime of a quantum bit with error correction in superconducting circuits. *Nature*, 536(7617):441–445, Aug 2016. ISSN 1476-4687. doi: 10.1038/nature18949.
- [64] Reinier W. Heeres, Philip Reinhold, Nissim Ofek, Luigi Frunzio, Liang Jiang, Michel H. Devoret, and Robert J. Schoelkopf. Implementing a universal gate set on a logical qubit encoded in an oscillator. *Nature Communications*, 8(1):94, Jul 2017. ISSN 2041-1723. doi: 10.1038/s41467-017-00045-1.
- [65] Peter K. Day, Henry G. LeDuc, Benjamin A. Mazin, Anastasios Vayonakis, and Jonas Zmuidzinas. A broadband superconducting detector suitable for use in large arrays. *Nature*, 425(6960):817–821, Oct 2003. ISSN 1476-4687. doi: 10.1038/nature02037.
- [66] Jiansong Gao. *The Physics of Superconducting Microwave Resonators*. PhD thesis, California Institute of Technology, 2008.
- [67] Alex I. Braginski and John Clarke. *Introduction*, chapter 1, pages 1–28. John Wiley & Sons, Ltd, 2004. ISBN 9783527603640. doi: 10.1002/3527603646.ch1.
- [68] H.K. Onnes. The Superconductivity of Mercury. *Comm. Phys. Lab. Univ., Leiden*, page 122, 1911.
- [69] B.D. Josephson. Possible new effects in superconductive tunnelling. *Physics Letters*, 1(7):251–253, 1962. ISSN 0031-9163. doi: [https://doi.org/10.1016/0031-9163\(62\)91369-0](https://doi.org/10.1016/0031-9163(62)91369-0).
- [70] J. E. Mooij and Yu. V. Nazarov. Superconducting nanowires as quantum phase-slip junctions. *Nature Physics*, 2(3):169–172, Mar 2006. ISSN 1745-2481. doi: 10.1038/nphys234.
- [71] Bernard Yurke and John S. Denker. Quantum network theory. *Phys. Rev. A*, 29:1419–1437, 3 1984. doi: 10.1103/PhysRevA.29.1419.
- [72] M. H. Devoret. *Quantum fluctuations in electrical circuits*. Edition de Physique, France, 1997. ISBN 0-444-82593-2.
- [73] W.H. Louisell. *Quantum statistical properties of radiation*. Wiley Series in Pure and Applied Optics Series. John Wiley & Sons Canada, Limited, 1973. ISBN 9780471547853.
- [74] Andrew Osborne, Trevyn Larson, Sarah Jones, Ray W. Simmonds, András Gyenis, and Andrew Lucas. Symplectic geometry and circuit quantization. *arXiv e-prints*, art. arXiv:2304.08531, April 2023. doi: 10.48550/arXiv.2304.08531.
- [75] E.T. Jaynes and F.W. Cummings. Comparison of quantum and semiclassical radiation theories with application to the beam maser. *Proceedings of the IEEE*, 51(1):89–109, 1963. doi: 10.1109/PROC.1963.1664.
- [76] Alexandre Blais, Ren-Shou Huang, Andreas Wallraff, S. M. Girvin, and R. J. Schoelkopf. Cavity quantum electrodynamics for superconducting electrical circuits: An architecture for quantum computation. *Phys. Rev. A*, 69:062320, Jun 2004. doi: 10.1103/PhysRevA.69.062320.
- [77] Yao Lu. *Parametric Control of Flux-Tunable Superconducting Circuits*. PhD thesis, The University of Chicago, 2019.
- [78] C.A. Hamilton, R.L. Kautz, R.L. Steiner, and F.L. Lloyd. A practical Josephson voltage standard at 1 V. *IEEE Electron Device Letters*, 6(12):623–625, 1985. doi: 10.1109/EDL.1985.26253.

- [79] Jared B. Hertzberg, Eric J. Zhang, Sami Rosenblatt, Easwar Magesan, John A. Smolin, Jeng-Bang Yau, Vivekananda P. Adiga, Martin Sandberg, Markus Brink, Jerry M. Chow, and Jason S. Orcutt. Laser-annealing Josephson junctions for yielding scaled-up superconducting quantum processors. *npj Quantum Information*, 7(1):129, Aug 2021. ISSN 2056-6387. doi: 10.1038/s41534-021-00464-5.
- [80] J. M. Raimond, M. Brune, and S. Haroche. Manipulating quantum entanglement with atoms and photons in a cavity. *Rev. Mod. Phys.*, 73:565–582, Aug 2001. doi: 10.1103/RevModPhys.73.565.
- [81] P. J. Leek, M. Baur, J. M. Fink, R. Bianchetti, L. Steffen, S. Filipp, and A. Wallraff. Cavity quantum electrodynamics with separate photon storage and qubit readout modes. *Phys. Rev. Lett.*, 104:100504, Mar 2010. doi: 10.1103/PhysRevLett.104.100504.
- [82] Akash V. Dixit, Srivatsan Chakram, Kevin He, Ankur Agrawal, Ravi K. Naik, David I. Schuster, and Aaron Chou. Searching for dark matter with a superconducting qubit. *Phys. Rev. Lett.*, 126:141302, Apr 2021. doi: 10.1103/PhysRevLett.126.141302.
- [83] Audrey Cottet. *Implementation of a quantum bit in a superconducting circuit*. PhD thesis, Université Paris VI, 2002.
- [84] Peter Groszkowski and Jens Koch. Scqubits: a Python package for superconducting qubits. *Quantum*, 5:583, November 2021. ISSN 2521-327X. doi: 10.22331/q-2021-11-17-583.
- [85] Sai Pavan Chitta, Tianpu Zhao, Ziwen Huang, Ian Mondragon-Shem, and Jens Koch. Computer-aided quantization and numerical analysis of superconducting circuits. *New Journal of Physics*, 24(10):103020, nov 2022. doi: 10.1088/1367-2630/ac94f2.
- [86] Ronald M. Foster. A reactance theorem. *The Bell System Technical Journal*, 3(2):259–267, 1924. doi: 10.1002/j.1538-7305.1924.tb01358.x.
- [87] Otto Brune. *Synthesis of a finite two-terminal network whose driving-point impedance is a prescribed function of frequency*. PhD thesis, Massachusetts Institute of Technology, 1931.
- [88] B. D. O. Anderson and P. J. Moylan. The brune synthesis in state-space terms. *International Journal of Circuit Theory and Applications*, 3(2):193–199, 1975. doi: 10.1002/cta.4490030209.
- [89] Firat Solgun. *Multiport impedance quantization*. PhD thesis, RWTH Aachen University, 2015.
- [90] Firat Solgun, David W. Abraham, and David P. DiVincenzo. Blackbox quantization of superconducting circuits using exact impedance synthesis. *Phys. Rev. B*, 90:134504, Oct 2014. doi: 10.1103/PhysRevB.90.134504.
- [91] B. Gustavsen and A. Semlyen. Rational approximation of frequency domain responses by vector fitting. *IEEE Transactions on Power Delivery*, 14(3):1052–1061, 1999. doi: 10.1109/61.772353.
- [92] B. Gustavsen and A. Semlyen. Enforcing passivity for admittance matrices approximated by rational functions. *IEEE Transactions on Power Systems*, 16(1):97–104, 2001. doi: 10.1109/59.910786.
- [93] Henry Ruston and Joseph Bordogna. *Electric Networks: functions, filters, analysis*, chapter Transfer and Driving-Point Functions. McGraw-Hill, Inc., 1966.
- [94] M. D. Reed, B. R. Johnson, A. A. Houck, L. DiCarlo, J. M. Chow, D. I. Schuster, L. Frunzio, and R. J. Schoelkopf. Fast reset and suppressing spontaneous emission of a superconducting qubit. *Applied Physics Letters*, 96(20):203110, 2010. doi: 10.1063/1.3435463.

- [95] Simon E. Nigg, Hanhee Paik, Brian Vlastakis, Gerhard Kirchmair, S. Shankar, Luigi Frunzio, M. H. Devoret, R. J. Schoelkopf, and S. M. Girvin. Black-box superconducting circuit quantization. *Phys. Rev. Lett.*, 108:240502, 6 2012. doi: 10.1103/PhysRevLett.108.240502.
- [96] N. E. Frattini, U. Vool, S. Shankar, A. Narla, K. M. Sliwa, and M. H. Devoret. 3-wave mixing josephson dipole element. *Applied Physics Letters*, 110(22):222603, 2017. doi: 10.1063/1.4984142.
- [97] Bjorn Gustavsen. Fast Passivity Enforcement for S-Parameter Models by Perturbation of Residue Matrix Eigenvalues. *IEEE Transactions on Advanced Packaging*, 33(1):257–265, 2010. doi: 10.1109/TADVP.2008.2010508.
- [98] S. Grivet-Talocia. Passivity enforcement via perturbation of hamiltonian matrices. *IEEE Transactions on Circuits and Systems I: Regular Papers*, 51(9):1755–1769, 2004. doi: 10.1109/TCSI.2004.834527.
- [99] D. Saraswat, R. Achar, and M. S. Nakhla. Global passivity enforcement algorithm for macromodels of interconnect subnetworks characterized by tabulated data. *IEEE Transactions on Very Large Scale Integration (VLSI) Systems*, 13(7):819–832, 2005. doi: 10.1109/TVLSI.2005.850098.
- [100] Abraham. Savitzky and M. J. E. Golay. Smoothing and Differentiation of Data by Simplified Least Squares Procedures. *Analytical Chemistry*, 36(8):1627–1639, Jul 1964. ISSN 0003-2700. doi: 10.1021/ac60214a047.
- [101] Jean. Steinier, Yves. Termonia, and Jules. Deltour. Smoothing and differentiation of data by simplified least square procedure. *Analytical Chemistry*, 44(11):1906–1909, Sep 1972. ISSN 0003-2700. doi: 10.1021/ac60319a045.
- [102] Savitzky Golay Filtering. <https://scipy-cookbook.readthedocs.io/items/SavitzkyGolay.html>, 2007.
- [103] Zlatko K. Minev, Zaki Leghtas, Shantanu O. Mundhada, Lysander Christakis, Ioan M. Pop, and Michel H. Devoret. Energy-participation quantization of Josephson circuits. *npj Quantum Information*, 7(1):131, Aug 2021. ISSN 2056-6387. doi: 10.1038/s41534-021-00461-8.
- [104] Eric T. Holland. *Cavity State Reservoir Engineering in Circuit Quantum Electrodynamics*. PhD thesis, Yale University, 2015.
- [105] Matthew Reagor, Wolfgang Pfaff, Christopher Axline, Reinier W. Heeres, Nissim Ofek, Katrina Sliwa, Eric Holland, Chen Wang, Jacob Blumoff, Kevin Chou, Michael J. Hatridge, Luigi Frunzio, Michel H. Devoret, Liang Jiang, and Robert J. Schoelkopf. Quantum memory with millisecond coherence in circuit QED. *Phys. Rev. B*, 94:014506, Jul 2016. doi: 10.1103/PhysRevB.94.014506.
- [106] Srivatsan Chakram, Andrew E. Oriani, Ravi K. Naik, Akash V. Dixit, Kevin He, Ankur Agrawal, Hyeokshin Kwon, and David I. Schuster. Seamless high- q microwave cavities for multimode circuit quantum electrodynamics. *Phys. Rev. Lett.*, 127:107701, Aug 2021. doi: 10.1103/PhysRevLett.127.107701.
- [107] Jerry M. Chow, A. D. Córcoles, Jay M. Gambetta, Chad Rigetti, B. R. Johnson, John A. Smolin, J. R. Rozen, George A. Keefe, Mary B. Rothwell, Mark B. Ketchen, and M. Steffen. Simple All-Microwave Entangling Gate for Fixed-Frequency Superconducting Qubits. *Phys. Rev. Lett.*, 107:080502, Aug 2011. doi: 10.1103/PhysRevLett.107.080502.

- [108] I. Ozfidan, C. Deng, A.Y. Smirnov, T. Lanting, R. Harris, L. Swenson, J. Whittaker, F. Altomare, M. Babcock, C. Baron, A.J. Berkley, K. Boothby, H. Christiani, P. Bunyk, C. Enderud, B. Evert, M. Hager, A. Hajda, J. Hilton, S. Huang, E. Hoskinson, M.W. Johnson, K. Jooya, E. Ladizinsky, N. Ladizinsky, R. Li, A. MacDonald, D. Marsden, G. Marsden, T. Medina, R. Molavi, R. Neufeld, M. Nissen, M. Norouzpour, T. Oh, I. Pavlov, I. Perminov, G. Poulin-Lamarre, M. Reis, T. Prescott, C. Rich, Y. Sato, G. Sterling, N. Tsai, M. Volkmann, W. Wilkinson, J. Yao, and M.H. Amin. Demonstration of a nonstoquastic hamiltonian in coupled superconducting flux qubits. *Phys. Rev. Appl.*, 13:034037, Mar 2020. doi: 10.1103/PhysRevApplied.13.034037.
- [109] R. K. Naik, N. Leung, S. Chakram, Peter Groszkowski, Y. Lu, N. Earnest, D. C. McKay, Jens Koch, and D. I. Schuster. Random access quantum information processors using multimode circuit quantum electrodynamics. *Nature Communications*, 8(1):1904, Dec 2017. ISSN 2041-1723. doi: 10.1038/s41467-017-02046-6.
- [110] J. D. Strand, Matthew Ware, Félix Beaudoin, T. A. Ohki, B. R. Johnson, Alexandre Blais, and B. L. T. Plourde. First-order sideband transitions with flux-driven asymmetric transmon qubits. *Phys. Rev. B*, 87:220505, Jun 2013. doi: 10.1103/PhysRevB.87.220505.
- [111] Félix Beaudoin, Marcus P. da Silva, Zachary Dutton, and Alexandre Blais. First-order sidebands in circuit qed using qubit frequency modulation. *Phys. Rev. A*, 86:022305, Aug 2012. doi: 10.1103/PhysRevA.86.022305.
- [112] James D. Teoh, Patrick Winkel, Harshvardhan K. Babla, Benjamin J. Chapman, Jahan Claes, Stijn J. de Graaf, John W. O. Garmon, William D. Kalfus, Yao Lu, Aniket Maiti, Kaavya Sahay, Neel Thakur, Takahiro Tsunoda, Sophia H. Xue, Luigi Frunzio, Steven M. Girvin, Shruti Puri, and Robert J. Schoelkopf. Dual-rail encoding with superconducting cavities. *arXiv e-prints*, art. arXiv:2212.12077, December 2022. doi: 10.48550/arXiv.2212.12077.
- [113] Kevin S. Chou, Tali Shemma, Heather McCarrick, Tzu-Chiao Chien, James D. Teoh, Patrick Winkel, Amos Anderson, Jonathan Chen, Jacob Curtis, Stijn J. de Graaf, John W. O. Garmon, Benjamin Gudlewski, William D. Kalfus, Trevor Keen, Nishaad Khedkar, Chan U Lei, Gangqiang Liu, Pinlei Lu, Yao Lu, Aniket Maiti, Luke Mastalli-Kelly, Nitish Mehta, Shantanu O. Mundhada, Anirudh Narla, Taewan Noh, Takahiro Tsunoda, Sophia H. Xue, Joseph O. Yuan, Luigi Frunzio, Jose Aumentado, Shruti Puri, Steven M. Girvin, Jr. Moseley, S. Harvey, and Robert J. Schoelkopf. Demonstrating a superconducting dual-rail cavity qubit with erasure-detected logical measurements. *arXiv e-prints*, art. arXiv:2307.03169, July 2023. doi: 10.48550/arXiv.2307.03169.
- [114] Alec Eickbusch, Volodymyr Sivak, Andy Z. Ding, Salvatore S. Elder, Shantanu R. Jha, Jayameenakshi Venkatraman, Baptiste Royer, S. M. Girvin, Robert J. Schoelkopf, and Michel H. Devoret. Fast universal control of an oscillator with weak dispersive coupling to a qubit. *Nature Physics*, 18(12):1464–1469, Dec 2022. ISSN 1745-2481. doi: 10.1038/s41567-022-01776-9.
- [115] D.M. Pozar. *Microwave Engineering*, 4th Edition. Wiley, 2011. ISBN 9781118213636.
- [116] R.E. Collin. *Foundations for Microwave Engineering*. McGraw-Hill, Inc., 1966.
- [117] A.F. Harvey. *Microwave Engineering*. by A. F. Harvey. Academic Press, 1963.
- [118] R.E. Collin. *Foundations for Microwave Engineering*, chapter 3. Transmission lines and waveguides, pages 64–72. McGraw-Hill, Inc., 1966.
- [119] R.E. Collin. *Foundations for Microwave Engineering*, chapter 4. McGraw-Hill, Inc., 1966.

- [120] Kaidong Peng, Rick Poore, Philip Krantz, David E. Root, and Kevin P. O'Brien. X-parameter based design and simulation of josephson traveling-wave parametric amplifiers for quantum computing applications. In *2022 IEEE International Conference on Quantum Computing and Engineering (QCE)*, pages 331–340, 2022. doi: 10.1109/QCE53715.2022.00054.
- [121] M. S. Khalil, M. J. A. Stoutimore, F. C. Wellstood, and K. D. Osborn. An analysis method for asymmetric resonator transmission applied to superconducting devices. *Journal of Applied Physics*, 111(5):054510, 2012. doi: 10.1063/1.3692073.
- [122] Paul G. Baity, Connor Maclean, Valentino Seferai, Joe Bronstein, Yi Shu, Tania Hemakumara, and Martin Weides. Circle fit optimization for resonator quality factor measurements: point redistribution for maximal accuracy. *arXiv e-prints*, art. arXiv:2301.06364, 1 2023. doi: 10.48550/arXiv.2301.06364.
- [123] S Probst, FB Song, PA Bushev, AV Ustinov, and M Weides. Efficient and robust analysis of complex scattering data under noise in microwave resonators. *Rev. Sci. Instrum.*, 86(2):024706, 2015.
- [124] K. J. Satzinger, C. R. Conner, A. Bienfait, H.-S. Chang, Ming-Han Chou, A. Y. Cleland, É. Dumur, J. Grebel, G. A. Peairs, R. G. Povey, S. J. Whiteley, Y. P. Zhong, D. D. Awschalom, D. I. Schuster, and A. N. Cleland. Simple non-galvanic flip-chip integration method for hybrid quantum systems. *Applied Physics Letters*, 114(17):173501, 04 2019. ISSN 0003-6951. doi: 10.1063/1.5089888.
- [125] D. Rieger, S. Günzler, M. Spiecker, A. Nambisan, W. Wernsdorfer, and I.M. Pop. Fano Interference in Microwave Resonator Measurements. *Phys. Rev. Appl.*, 20:014059, Jul 2023. doi: 10.1103/PhysRevApplied.20.014059.
- [126] U. Fano. The Theory of Anomalous Diffraction Gratings and of Quasi-Stationary Waves on Metallic Surfaces (Sommerfeld's Waves). *J. Opt. Soc. Am.*, 31(3):213–222, Mar 1941. doi: 10.1364/JOSA.31.000213.
- [127] U. Fano. Effects of Configuration Interaction on Intensities and Phase Shifts. *Phys. Rev.*, 124: 1866–1878, Dec 1961. doi: 10.1103/PhysRev.124.1866.
- [128] A. B. Zorin, F.-J. Ahlers, J. Niemeyer, T. Weimann, H. Wolf, V. A. Krupenin, and S. V. Lotkhov. Background charge noise in metallic single-electron tunneling devices. *Phys. Rev. B*, 53:13682–13687, May 1996. doi: 10.1103/PhysRevB.53.13682.
- [129] John M. Martinis, K. B. Cooper, R. McDermott, Matthias Steffen, Markus Ansmann, K. D. Osborn, K. Cicak, Seongshik Oh, D. P. Pappas, R. W. Simmonds, and Clare C. Yu. Decoherence in Josephson Qubits from Dielectric Loss. *Phys. Rev. Lett.*, 95:210503, Nov 2005. doi: 10.1103/PhysRevLett.95.210503.
- [130] W. A. Phillips. Tunneling states in amorphous solids. *Journal of Low Temperature Physics*, 7(3): 351–360, May 1972. ISSN 1573-7357. doi: 10.1007/BF00660072.
- [131] W A Phillips. Two-level states in glasses. *Reports on Progress in Physics*, 50(12):1657–1708, 12 1987. doi: 10.1088/0034-4885/50/12/003.
- [132] B. I. Halperin P. W. Anderson and c. M. Varma. Anomalous low-temperature thermal properties of glasses and spin glasses. *The Philosophical Magazine: A Journal of Theoretical Experimental and Applied Physics*, 25(1):1–9, 1972. doi: 10.1080/14786437208229210.
- [133] Jiansong Gao, Jonas Zmuidzinas, Benjamin A. Mazin, Henry G. LeDuc, and Peter K. Day. Noise properties of superconducting coplanar waveguide microwave resonators. *Applied Physics Letters*, 90 (10):102507, 03 2007. ISSN 0003-6951. doi: 10.1063/1.2711770.

- [134] Jonathan Burnett. *High Precision readout of superconducting resonators For analysis of slow noise processes*. PhD thesis, Royal Holloway, University of London, 2013.
- [135] Jiansong Gao, Miguel Daal, Anastasios Vayonakis, Shwetank Kumar, Jonas Zmuidzinas, Bernard Sadoulet, Benjamin A. Mazin, Peter K. Day, and Henry G. Leduc. Experimental evidence for a surface distribution of two-level systems in superconducting lithographed microwave resonators. *Applied Physics Letters*, 92(15), 2008. ISSN 00036951. doi: 10.1063/1.2906373.
- [136] SE De Graaf, L Faoro, J Burnett, AA Adamyan, A Ya Tzalenchuk, SE Kubatkin, T Lindström, and AV Danilov. Suppression of low-frequency charge noise in superconducting resonators by surface spin desorption. *Nat. Commun.*, 9(1):1–6, 2018.
- [137] Jonathan Burnett, Andreas Bengtsson, David Niegce, and Jonas Bylander. Noise and loss of superconducting aluminium resonators at single photon energies. *Journal of Physics: Conference Series*, 969:012131, mar 2018. doi: 10.1088/1742-6596/969/1/012131.
- [138] J. Bardeen, L. N. Cooper, and J. R. Schrieffer. Microscopic theory of superconductivity. *Phys. Rev.*, 106:162–164, Apr 1957. doi: 10.1103/PhysRev.106.162.
- [139] D. C. Mattis and J. Bardeen. Theory of the anomalous skin effect in normal and superconducting metals. *Phys. Rev.*, 111:412–417, Jul 1958. doi: 10.1103/PhysRev.111.412.
- [140] F. London, H. London, and Frederick Alexander Lindemann. The electromagnetic equations of the supraconductor. *Proceedings of the Royal Society of London. Series A - Mathematical and Physical Sciences*, 149(866):71–88, 1935. doi: 10.1098/rspa.1935.0048.
- [141] R. Gross, A. Marx, and F. Deppe. *Applied Superconductivity: Josephson Effect and Superconducting Electronics*. De Gruyter Textbook Series. Walter De Gruyter Incorporated, 2016. ISBN 9783110417067.
- [142] Alfred Brian Pippard and William Lawrence Bragg. An experimental and theoretical study of the relation between magnetic field and current in a superconductor. *Proceedings of the Royal Society of London. Series A. Mathematical and Physical Sciences*, 216(1127):547–568, 1953. doi: 10.1098/rspa.1953.0040.
- [143] Daniel Gall. Electron mean free path in elemental metals. *Journal of Applied Physics*, 119(8):085101, 02 2016. ISSN 0021-8979. doi: 10.1063/1.4942216.
- [144] Matthew Reagor. *Superconducting Cavities for Circuit Quantum Electrodynamics*. PhD thesis, Yale University, 2015.
- [145] John Ward, Frank Rice, Goutam Chattopadhyay, and Jonas Zmuidzinas. SuperMix: A Flexible Software Library for High-Frequency Circuit Simulation, Including SIS Mixers And Superconducting Elements. In *Proceedings SPIE—the International Society of Optical Engineering*, 03 1999.
- [146] J. Gao, J. Zmuidzinas, A. Vayonakis, P. Day, B. Mazin, and H. Leduc. Equivalence of the Effects on the Complex Conductivity of Superconductor due to Temperature Change and External Pair Breaking. *Journal of Low Temperature Physics*, 151(1):557–563, Apr 2008. ISSN 1573-7357. doi: 10.1007/s10909-007-9688-z.
- [147] Charles M. Marcus, Peter Krostrup, Thomas Sand Jespersen, Jesper Nygård, Karl Petersson, Thorvald Larsen, and Ferdinand Kuemmeth. Semiconductor Josephson Junction and a Transmon Qubit Related Thereto, 1 2019. US Patent No. US010177297B2.

- [148] Kasra Sardashti, Matthieu C. Dartailh, Joseph Yuan, Sean Hart, Patryk Gummam, and Javad Shabani. Voltage-tunable superconducting resonators: a platform for random access quantum memory. *arXiv e-prints*, art. arXiv:2006.08683, June 2020.
- [149] William D. Oliver and Paul B. Welander. Materials in superconducting quantum bits. *MRS Bulletin*, 38(10):816–825, 2013. doi: 10.1557/mrs.2013.229.
- [150] William M. Strickland, Bassel Heiba Elfeky, Joseph O’Connell Yuan, William F. Schiela, Peng Yu, Dylan Langone, Maxim G. Vavilov, Vladimir E. Manucharyan, and Javad Shabani. Superconducting resonators with voltage-controlled frequency and nonlinearity. *Phys. Rev. Appl.*, 19:034021, Mar 2023. doi: 10.1103/PhysRevApplied.19.034021.
- [151] R. C. Bialczak, M. Ansmann, M. Hofheinz, M. Lenander, E. Lucero, M. Neeley, A. D. O’Connell, D. Sank, H. Wang, M. Weides, J. Wenner, T. Yamamoto, A. N. Cleland, and J. M. Martinis. Fast Tunable Coupler for Superconducting Qubits. *Phys. Rev. Lett.*, 106:060501, 2 2011. doi: 10.1103/PhysRevLett.106.060501.
- [152] A. W. Kleinsasser and T. N. Jackson. Prospects for proximity effect superconducting FETs. *IEEE Transactions on Magnetics*, 25(2):1274–1277, 3 1989. ISSN 1941-0069. doi: 10.1109/20.92528.
- [153] Catherine Leroux, Adrian Parra-Rodriguez, Ross Shillito, Agustin Di Paolo, William D. Oliver, Charles M. Marcus, Morten Kjaergaard, András Gyenis, and Alexandre Blais. Nonreciprocal devices based on voltage-tunable junctions. *arXiv e-prints*, art. arXiv:2209.06194, September 2022.
- [154] The semiconductor module user’s guide. SemiconductorModuleManual.html, 2020.
- [155] William M. Strickland, Mehdi Hatefipour, Dylan Langone, S. M. Farzaneh, and Javad Shabani. Controlling Fermi level pinning in near-surface InAs quantum wells. *Applied Physics Letters*, 121(9), 09 2022. ISSN 0003-6951. doi: 10.1063/5.0101579. 092104.
- [156] B.G. Streetman and S. Banerjee. *Energy Bands and Charge Carriers in Semiconductors*, chapter 5, pages 238–243. Pearson, 2015.
- [157] M. G. Ancona. Density-gradient theory: a macroscopic approach to quantum confinement and tunneling in semiconductor devices. *Journal of Computational Electronics*, 10(1):65–97, Jun 2011. ISSN 1572-8137. doi: 10.1007/s10825-011-0356-9.
- [158] Raseong Kim, Xufeng Wang, and Mark Lundstrom. Notes on Fermi-Dirac Integrals, 2019.
- [159] The AC/DC Module User’s Guide. ACDCModuleManual.html, 2020.
- [160] S. Krinner, S. Storz, P. Kurpiers, P. Magnard, J. Heinsoo, R. Keller, J. Lütolf, C. Eichler, and A. Wallraff. Engineering cryogenic setups for 100-qubit scale superconducting circuit systems. *EPJ Quantum Technology*, 6(1):2, May 2019. ISSN 2196-0763. doi: 10.1140/epjqt/s40507-019-0072-0.
- [161] J. Wenner, R. Barends, R. C. Bialczak, Yu Chen, J. Kelly, Erik Lucero, Matteo Mariantoni, A. Megrant, P. J. J. O’Malley, D. Sank, A. Vainsencher, H. Wang, T. C. White, Y. Yin, J. Zhao, A. N. Cleland, and John M. Martinis. Surface loss simulations of superconducting coplanar waveguide resonators. *Applied Physics Letters*, 99(11):113513, 2011. doi: 10.1063/1.3637047.
- [162] C. Wang, C. Axline, Y. Y. Gao, T. Brecht, Y. Chu, L. Frunzio, M. H. Devoret, and R. J. Schoelkopf. Surface participation and dielectric loss in superconducting qubits. *Applied Physics Letters*, 107(16):162601, 2015. doi: 10.1063/1.4934486.

- [163] Marco Scigliuzzo, Laure E Bruhat, Andreas Bengtsson, Jonathan J Burnett, Anita Fadavi Roudsari, and Per Delsing. Phononic loss in superconducting resonators on piezoelectric substrates. *New Journal of Physics*, 22(5):053027, may 2020. doi: 10.1088/1367-2630/ab8044.
- [164] H. Q. Nguyen, D. Sabonis, D. Razmadze, E. T. Mannila, V. F. Maisi, D. M. T. van Zanten, E. C. T. O'Farrell, P. Krogstrup, F. Kuemmeth, J. P. Pekola, and C. M. Marcus. Electrostatic control of quasiparticle poisoning in a hybrid semiconductor-superconductor island, 2022.
- [165] C. D. Wilen, S. Abdullah, N. A. Kurinsky, C. Stanford, L. Cardani, G. D'Imperio, C. Tomei, L. Faoro, L. B. Ioffe, C. H. Liu, A. Opremcak, B. G. Christensen, J. L. DuBois, and R. McDermott. Correlated charge noise and relaxation errors in superconducting qubits. *Nature*, 594(7863):369–373, Jun 2021. ISSN 1476-4687. doi: 10.1038/s41586-021-03557-5.
- [166] A. Kringhøj, T. W. Larsen, O. Erlandsson, W. Uilhoorn, J.G. Kroll, M. Hesselberg, R.P.G. McNeil, P. Krogstrup, L. Casparis, C.M. Marcus, and K.D. Petersson. Magnetic-field-compatible superconducting transmon qubit. *Phys. Rev. Applied*, 15:054001, May 2021. doi: 10.1103/PhysRevApplied.15.054001.
- [167] C. R. H. McRae, H. Wang, J. Gao, M. R. Vissers, T. Brecht, A. Dunsworth, D. P. Pappas, and J. Mutus. Materials loss measurements using superconducting microwave resonators. *Review of Scientific Instruments*, 91(9):091101, 2020. doi: 10.1063/5.0017378.
- [168] Vinay Ambegaokar and Alexis Baratoff. Tunneling between superconductors. *Phys. Rev. Lett.*, 10: 486–489, Jun 1963. doi: 10.1103/PhysRevLett.10.486.
- [169] Z. K. Minev, S. O. Mundhada, S. Shankar, P. Reinhold, R. Gutiérrez-Jáuregui, R. J. Schoelkopf, M. Mirrahimi, H. J. Carmichael, and M. H. Devoret. To catch and reverse a quantum jump mid-flight. *Nature*, 570(7760):200–204, Jun 2019. ISSN 1476-4687. doi: 10.1038/s41586-019-1287-z.
- [170] T. P. Orlando, J. E. Mooij, Lin Tian, Caspar H. van der Wal, L. S. Levitov, Seth Lloyd, and J. J. Mazo. Superconducting persistent-current qubit. *Phys. Rev. B*, 60:15398–15413, Dec 1999. doi: 10.1103/PhysRevB.60.15398.
- [171] Bassel Heiba Elfeky, Neda Lotfizadeh, William F. Schiela, William M. Strickland, Matthieu Dartialih, Kasra Sardashti, Mehdi Hatefipour, Peng Yu, Natalia Pankratova, Hanho Lee, Vladimir E. Manucharyan, and Javad Shabani. Local control of supercurrent density in epitaxial planar josephson junctions. *Nano Letters*, 21(19):8274–8280, Oct 2021. ISSN 1530-6984. doi: 10.1021/acs.nanolett.1c02771.
- [172] Gioele Consani and Paul A Warburton. Effective Hamiltonians for interacting superconducting qubits: local basis reduction and the Schrieffer–Wolff transformation. *New Journal of Physics*, 22(5): 053040, may 2020. doi: 10.1088/1367-2630/ab83d1.
- [173] María Hita-Pérez, Gabriel Jaumà, Manuel Pino, and Juan José García-Ripoll. Three-Josephson junctions flux qubit couplings. *Applied Physics Letters*, 119(22), 12 2021. ISSN 0003-6951. doi: 10.1063/5.0069530. 222601.
- [174] A. Dutta, A. P. M. Place, K. D. Crowley, X. H. Le, Y. Gang, L. V. H. Rodgers, T. Madhavan, N. P. Khedkar, X. Gui, Y. Jia, L. Baker, A. Head, I. Jarrige, A. Hunt, I. Waluyo, A. Barbour, C. Weiland, S. Hulbert, M. Liu, A. L. Walter, R. J. Cava, A. A. Houck, and N. P. de Leon. Study of material loss channels in tantalum microwave superconducting resonators. In *Quantum 2.0 Conference and Exhibition*, page QTU2A.25. Optica Publishing Group, 2022. doi: 10.1364/QUANTUM.2022.QTU2A.25.

- [175] Joel I-J. Wang, Megan A. Yamoah, Qing Li, Amir H. Karamlou, Thao Dinh, Bharath Kannan, Jochen Braumüller, David Kim, Alexander J. Melville, Sarah E. Muschinske, Bethany M. Niedzielski, Kyle Serniak, Youngkyu Sung, Roni Winik, Jonilyn L. Yoder, Mollie E. Schwartz, Kenji Watanabe, Takashi Taniguchi, Terry P. Orlando, Simon Gustavsson, Pablo Jarillo-Herrero, and William D. Oliver. Hexagonal boron nitride as a low-loss dielectric for superconducting quantum circuits and qubits. *Nature Materials*, 21(4):398–403, Apr 2022. ISSN 1476-4660. doi: 10.1038/s41563-021-01187-w.
- [176] M. Abramowitz and I.A. Stegun. *Handbook of Mathematical Functions: With Formulas, Graphs, and Mathematical Tables*, chapter 9, pages 358–361. Applied mathematics series. Dover Publications, 1965. ISBN 9780486612720.
- [177] Chaitali Joshi, Wenyuan Chen, Henry G. LeDuc, Peter K. Day, and Mohammad Mirhosseini. Strong Kinetic-Inductance Kerr Nonlinearity with Titanium Nitride Nanowires. *Phys. Rev. Appl.*, 18:064088, Dec 2022. doi: 10.1103/PhysRevApplied.18.064088.
- [178] Isaac L. Chuang and Yoshihisa Yamamoto. Simple quantum computer. *Phys. Rev. A*, 52:3489–3496, Nov 1995. doi: 10.1103/PhysRevA.52.3489.
- [179] D. H. Auston, A. A. Ballman, P. Bhattacharya, G. J. Bjorklund, C. Bowden, R. W. Boyd, P. S. Brody, R. Burnham, R. L. Byer, G. Carter, D. Chemla, M. Dagenais, G. Dohler, U. Efron, D. Eimerl, R. S. Feigelson, J. Feinberg, B. J. Feldman, A. F. Garito, E. M. Garmire, H. M. Gibbs, A. M. Glass, L. S. Goldberg, R. L. Gunshor, T. K. Gustafson, R. W. Hellwarth, A. E. Kaplan, P. L. Kelley, F. J. Leonberger, R. S. Lytel, A. Majerfeld, N. Menyuk, G. R. Meredith, R. R. Neurgaonkar, N. G. Peyghambarian, P. Prasad, G. Rakuljic, Y.-R. Shen, P. W. Smith, J. Stamatoff, G. I. Stegeman, G. Stillman, C. L. Tang, H. Temkin, M. Thakur, G. C. Valley, P. A. Wolff, and C. Woods. Research on nonlinear optical materials: an assessment. *Appl. Opt.*, 26(2):211–211, Jan 1987. doi: 10.1364/AO.26.000211.
- [180] Helin Zhang, Chunyang Ding, D. K. Weiss, Ziwen Huang, Yuwei Ma, Charles Quinn, Sara Sussman, Sai Pavan Chitta, Danyang Chen, Andrew A. Houck, Jens Koch, and David I. Schuster. Tunable inductive coupler for high fidelity gates between fluxonium qubits. *arXiv e-prints*, art. arXiv:2309.05720, September 2023. doi: 10.48550/arXiv.2309.05720.
- [181] Teresa Brecht. *Micromachined Quantum Circuits*. PhD thesis, Yale University, 2017.
- [182] Chan U Lei, Suhas Ganjam, Lev Krayzman, Archan Banerjee, Kim Kisslinger, Sooyeon Hwang, Luigi Frunzio, and Robert J. Schoelkopf. Characterization of Microwave Loss Using Multimode Superconducting Resonators. *Phys. Rev. Appl.*, 20:024045, Aug 2023. doi: 10.1103/PhysRevApplied.20.024045.
- [183] G. Calusine, A. Melville, W. Woods, R. Das, C. Stull, V. Bolkhovsky, D. Braje, D. Hover, D. K. Kim, X. Miloshi, D. Rosenberg, A. Sevi, J. L. Yoder, E. Dauler, and W. D. Oliver. Analysis and mitigation of interface losses in trenched superconducting coplanar waveguide resonators. *Applied Physics Letters*, 112(6):062601, 02 2018. ISSN 0003-6951. doi: 10.1063/1.5006888.
- [184] A. Melville, G. Calusine, W. Woods, K. Serniak, E. Golden, B. M. Niedzielski, D. K. Kim, A. Sevi, J. L. Yoder, E. A. Dauler, and W. D. Oliver. Comparison of dielectric loss in titanium nitride and aluminum superconducting resonators. *Applied Physics Letters*, 117(12):124004, 09 2020. ISSN 0003-6951. doi: 10.1063/5.0021950.

- [185] Suhas Ganjam, Yanhao Wang, Yao Lu, Archan Banerjee, Chan U Lei, Lev Krayzman, Kim Kisslinger, Chenyu Zhou, Ruoshui Li, Yichen Jia, Mingzhao Liu, Luigi Frunzio, and Robert J. Schoelkopf. Surpassing millisecond coherence times in on-chip superconducting quantum memories by optimizing materials, processes, and circuit design. *arXiv e-prints*, art. arXiv:2308.15539, 8 2023. doi: 10.48550/arXiv.2308.15539.
- [186] McRae, Corey Rae. *Indium Thin Films in Multilayer Superconducting Quantum Circuits*. PhD thesis, University of Waterloo, 2018. URL <http://hdl.handle.net/10012/12803>.
- [187] Carlos G. Torres-Castanedo, Dominic P. Goronzy, Thang Pham, Anthony McFadden, Nicholas Materise, Paul Masih Das, Matthew Cheng, Dmitry Lebedev, Stephanie M. Ribet, Mitchell J. Walker, David G. Wetten, Cameron J. Kopas, Jayss Marshall, Ella Lachman, Nikolay Zhelev, James A. Sauls, Joshua Y. Mutus, Vinayak P. Dravid, Corey Rae H. McRae, Michael J. Bedzyk, and Mark C. Hersham. Formation and losses of hydrides in superconducting niobium resulting from wet chemical processing. Manuscript in preparation, to be submitted to *Advanced Materials*, 2023.
- [188] Cameron J. Kopas, Ella Lachman, Corey Rae H. McRae, Yuvraj Mohan, Josh Y. Mutus, Ani Nersisyan, and Amrit Poudel. Simple coplanar waveguide resonator mask targeting metal-substrate interface. *arXiv e-prints*, art. arXiv:2204.07202, April 2022. doi: 10.48550/arXiv.2204.07202.
- [189] A. A. Murthy, J. Lee, C. Kopas, M. J. Reagor, A. P. McFadden, D. P. Pappas, M. Checchin, A. Grassellino, and A. Romanenko. TOF-SIMS analysis of decoherence sources in superconducting qubits. *Applied Physics Letters*, 120(4):044002, 01 2022. ISSN 0003-6951. doi: 10.1063/5.0079321.
- [190] F. Barkov, A. Romanenko, and A. Grassellino. Direct observation of hydrides formation in cavity-grade niobium. *Phys. Rev. ST Accel. Beams*, 15:122001, Dec 2012. doi: 10.1103/PhysRevSTAB.15.122001.
- [191] J.-M. Welter and F. J. Johnen. Superconducting transition temperature and low temperature resistivity in the niobium-hydrogen system. *Zeitschrift für Physik B Condensed Matter*, 27(3): 227–232, Sep 1977. ISSN 1431-584X. doi: 10.1007/BF01325532.
- [192] U Laudahn, A Pundt, M Bicker, U v. Hülsen, U Geyer, T Wagner, and R Kirchheim. Hydrogen-induced stress in Nb single layers. *Journal of Alloys and Compounds*, 293–295:490–494, 1999. ISSN 0925-8388. doi: 10.1016/S0925-8388(99)00471-5.
- [193] J. Verjauw, A. Potočnik, M. Mongillo, R. Acharya, F. Mohiyaddin, G. Simion, A. Pacco, Ts. Ivanov, D. Wan, A. Vanleenehove, L. Souriau, J. Jussot, A. Thiam, J. Swerts, X. Piao, S. Couet, M. Heyns, B. Govoreanu, and I. Radu. Investigation of Microwave Loss Induced by Oxide Regrowth in High-Q Niobium Resonators. *Phys. Rev. Appl.*, 16:014018, Jul 2021. doi: 10.1103/PhysRevApplied.16.014018.
- [194] Jaeyel Lee, Zuhawn Sung, Akshay A. Murthy, Matt Reagor, Anna Grassellino, and Alexander Romanenko. Discovery of Nb hydride precipitates in superconducting qubits. *arXiv e-prints*, art. arXiv:2108.10385, August 2021. doi: 10.48550/arXiv.2108.10385.

- [195] Mustafa Bal, Akshay A. Murthy, Shaojiang Zhu, Francesco Crisa, Xinyuan You, Ziwen Huang, Tanay Roy, Jaeyel Lee, David van Zanten, Roman Pilipenko, Ivan Nekrashevich, Daniel Bafia, Yulia Krasnikova, Cameron J. Kopas, Ella O. Lachman, Duncan Miller, Josh Y. Mutus, Matthew J. Reagor, Hilal Cansizoglu, Jayss Marshall, David P. Pappas, Kim Vu, Kameshwar Yadavalli, Jin-Su Oh, Lin Zhou, Matthew J. Kramer, Florent Q. Lecocq, Dominic P. Goronzky, Carlos G. Torres-Castanedo, Graham Pritchard, Vinayak P. Dravid, James M. Rondinelli, Michael J. Bedzyk, Mark C. Hersam, John Zasadzinski, Jens Koch, James A. Sauls, Alexander Romanenko, and Anna Grassellino. Systematic improvements in transmon qubit coherence enabled by niobium surface encapsulation. *arXiv*, 6 2023. URL <http://arxiv.org/abs/2304.13257>. arXiv:2304.13257 [cond-mat, physics:quant-ph].
- [196] Sarah Garcia Jones, Nicholas Materise, Ka Wun Leung, Joel C. Weber, Brian D. Isakov, Xi Chen, Jiangchang Zheng, András Gyenis, Berthold Jaeck, and Corey Rae H. McRae. Grain size in low loss superconducting ta thin films on c axis sapphire. *Journal of Applied Physics*, 134(14):144402, 10 2023. ISSN 0021-8979. doi: 10.1063/5.0169391.
- [197] Morten Kjaergaard, Mollie E. Schwartz, Jochen Braumüller, Philip Krantz, Joel I.-J. Wang, Simon Gustavsson, and William D. Oliver. Superconducting Qubits: Current State of Play. *Annual Review of Condensed Matter Physics*, 11(1):369–395, 2020. doi: 10.1146/annurev-conmatphys-031119-050605.
- [198] Helin Zhang, Srivatsan Chakram, Tanay Roy, Nathan Earnest, Yao Lu, Ziwen Huang, D. K. Weiss, Jens Koch, and David I. Schuster. Universal fast-flux control of a coherent, low-frequency qubit. *Phys. Rev. X*, 11:011010, Jan 2021. doi: 10.1103/PhysRevX.11.011010.
- [199] Eric Hyyppä, Suman Kundu, Chun Fai Chan, András Gunyhó, Juho Hotari, David Janzso, Kristinn Juliusson, Olavi Kiuru, Janne Kotilahti, Alessandro Landra, Wei Liu, Fabian Marxer, Akseli Mäkinen, Jean-Luc Orgiazzi, Mario Palma, Mykhailo Savitskyi, Francesca Tosto, Jani Tuorila, Vasili Vadimov, Tianyi Li, Caspar Ockeloen-Korppi, Johannes Heinsoo, Kuan Yen Tan, Juha Hassel, and Mikko Möttönen. Unimon qubit. *Nature Communications*, 13(1):6895, Nov 2022. ISSN 2041-1723. doi: 10.1038/s41467-022-34614-w.
- [200] Joel Howard, Alexander Lidiak, Casey Jameson, Bora Basyildiz, Kyle Clark, Tongyu Zhao, Mustafa Bal, Junling Long, David P. Pappas, Meenakshi Singh, and Zhexuan Gong. Demonstrating two-qubit entangling gates at the quantum speed limit using superconducting qubits. *arXiv e-prints*, art. arXiv:2206.07716, June 2022. doi: 10.48550/arXiv.2206.07716.
- [201] Frank Arute, Kunal Arya, Ryan Babbush, Dave Bacon, Joseph C Bardin, Rami Barends, Rupak Biswas, Sergio Boixo, Fernando GSL Brandao, David A Buell, et al. Quantum supremacy using a programmable superconducting processor. *Nature*, 574(7779):505–510, 2019.
- [202] Alexander P. M. Place, Lila V. H. Rodgers, Pranav Mundada, Basil M. Smitham, Mattias Fitzpatrick, Zhaoqi Leng, Anjali Premkumar, Jacob Bryon, Andrei Vrajitoarea, Sara Sussman, Guangming Cheng, Trisha Madhavan, Harshvardhan K. Babla, Xuan Hoang Le, Youqi Gang, Berthold Jäck, András Gyenis, Nan Yao, Robert J. Cava, Nathalie P. de Leon, and Andrew A. Houck. New material platform for superconducting transmon qubits with coherence times exceeding 0.3 milliseconds. *Nature Communications*, 12(1):1779, Mar 2021. ISSN 2041-1723. doi: 10.1038/s41467-021-22030-5.

- [203] Kevin D. Crowley, Russell A. McLellan, Aveek Dutta, Nana Shumiya, Alexander P. M. Place, Xuan Hoang Le, Youqi Gang, Trisha Madhavan, Nishaad Khedkar, Yiming Cady Feng, Esha A. Umbarkar, Xin Gui, Lila V. H. Rodgers, Yichen Jia, Mayer M. Feldman, Stephen A. Lyon, Mingzhao Liu, Robert J. Cava, Andrew A. Houck, and Nathalie P. de Leon. Disentangling Losses in Tantalum Superconducting Circuits. *arXiv e-prints*, art. arXiv:2301.07848, January 2023. doi: 10.48550/arXiv.2301.07848.
- [204] Irfan Siddiqi. Engineering high-coherence superconducting qubits. *Nature Reviews Materials*, 6(10): 875–891, 2021.
- [205] Chenlu Wang, Xuegang Li, Huikai Xu, Zhiyuan Li, Junhua Wang, Zhen Yang, Zhenyu Mi, Xuehui Liang, Tang Su, Chuhong Yang, Guangyue Wang, Wenyang Wang, Yongchao Li, Mo Chen, Chengyao Li, Kehuan Linghu, Jiaxiu Han, Yingshan Zhang, Yulong Feng, Yu Song, Teng Ma, Jingning Zhang, Ruixia Wang, Peng Zhao, Weiyang Liu, Guangming Xue, Yirong Jin, and Haifeng Yu. Towards practical quantum computers: transmon qubit with a lifetime approaching 0.5 milliseconds. *npj Quantum Information*, 8(1):3, Jan 2022. ISSN 2056-6387. doi: 10.1038/s41534-021-00510-2.
- [206] Loren D. Alegria, Daniel M. Tennant, Kevin R. Chaves, Jonathan R. I. Lee, Sean R. O’Kelley, Yaniv J. Rosen, and Jonathan L. DuBois. Two-level systems in nucleated and non-nucleated epitaxial alpha-tantalum films. *Applied Physics Letters*, 123(6):062601, 08 2023. ISSN 0003-6951. doi: 10.1063/5.0157654.
- [207] Lili Shi, Tingting Guo, Runfeng Su, Tianyuan Chi, Yifan Sheng, Junliang Jiang, Chunhai Cao, Jingbo Wu, Xuecou Tu, Guozhu Sun, Jian Chen, and Peiheng Wu. Tantalum microwave resonators with ultra-high intrinsic quality factors. *Applied Physics Letters*, 121(24):242601, 2022. doi: 10.1063/5.0124821.
- [208] D. P. Lozano, M. Mongillo, X. Piao, S. Couet, D. Wan, Y. Canvel, A. M. Vadhiraj, Ts. Ivanov, J. Verjauw, R. Acharya, J. Van Damme, F. A. Mohiyaddin, J. Jussot, P. P. Gowda, A. Pacco, B. Raes, J. Van de Vondel, I. P. Radu, B. Govoreanu, J. Swerts, A. Potočnik, and K. De Greve. Manufacturing high-Q superconducting α -tantalum resonators on silicon wafers. *arXiv e-prints*, art. arXiv:2211.16437, November 2022. doi: 10.48550/arXiv.2211.16437.
- [209] Anjali Premkumar, Conan Weiland, Sooyeon Hwang, Berthold Jäck, Alexander PM Place, Iradwikanari Waluyo, Adrian Hunt, Valentina Bisogni, Jonathan Pelliciari, Andi Barbour, et al. Microscopic relaxation channels in materials for superconducting qubits. *Communications Materials*, 2(1):72, 2021.
- [210] Arash Rabbani and Shahab Ayatollahi. Comparing three image processing algorithms to estimate the grain-size distribution of porous rocks from binary 2d images and sensitivity analysis of the grain overlapping degree. *Special Topics & Reviews in Porous Media: An International Journal*, 6(1), 2015.
- [211] See Supplementary Information of the *Grain size in low loss superconducting Ta thin films on c-axis sapphire* in Appendix D., 2023.
- [212] GE McGuire, G Kk Schweitzer, and Thomas A Carlson. Core electron binding energies in some Group IIIA, VB, and VIB compounds. *Inorganic Chemistry*, 12(10):2450–2453, 1973.
- [213] FJ Himpsel, JF Morar, FR McFeely, RA Pollak, and Guy Hollinger. Core-level shifts and oxidation states of ta and w: Electron spectroscopy for chemical analysis applied to surfaces. *Physical Review B*, 30(12):7236, 1984.

- [214] Haolin Jia, Boyi Zhou, Tao Wang, Yanfu Wu, Lina Yang, Zengqian Ding, Shuming Li, Xiao Cai, Kanglin Xiong, and Jiagui Feng. Investigation of the deposition of α -tantalum (110) films on a-plane sapphire substrate by molecular beam epitaxy for superconducting circuit. *Journal of Vacuum Science Technology B: Microelectronics and Nanometer Structures*, 41(5):052210, September 2023. doi: 10.1116/6.0002886.
- [215] Russell A. McLellan, Aveek Dutta, Chenyu Zhou, Yichen Jia, Conan Weiland, Xin Gui, Alexander P. M. Place, Kevin D. Crowley, Xuan Hoang Le, Trisha Madhavan, Youqi Gang, Lukas Baker, Ashley R. Head, Iradwikanari Waluyo, Ruoshui Li, Kim Kisslinger, Adrian Hunt, Ignace Jarrige, Stephen A. Lyon, Andi M. Barbour, Robert J. Cava, Andrew A. Houck, Steven L. Hulbert, Mingzhao Liu, Andrew L. Walter, and Nathalie P. de Leon. Chemical profiles of the oxides on tantalum in state of the art superconducting circuits. *arXiv e-prints*, art. arXiv:2301.04567, January 2023. doi: 10.48550/arXiv.2301.04567.
- [216] Robert Knepper, Blake Stevens, and Shefford P Baker. Effect of oxygen on the thermomechanical behavior of tantalum thin films during the β - α phase transformation. *Journal of applied physics*, 100(12):123508, 2006.
- [217] Sterling Myers, Jianliang Lin, Roberto Martins Souza, William D Sproul, and John J Moore. The β to α phase transition of tantalum coatings deposited by modulated pulsed power magnetron sputtering. *Surface and Coatings Technology*, 214:38–45, 2013.
- [218] Corey Rae McRae and Nicholas Materise. Dataset for "grain size in low loss superconducting ta thin films on c-axis sapphire". <https://zenodo.org/record/8161535>, 2023.
- [219] Aaron Somoroff, Quentin Ficheux, Raymond A. Mencia, Haonan Xiong, Roman Kuzmin, and Vladimir E. Manucharyan. Millisecond Coherence in a Superconducting Qubit. *Phys. Rev. Lett.*, 130:267001, 6 2023. doi: 10.1103/PhysRevLett.130.267001.
- [220] Ofir Milul, Barkay Guttel, Uri Goldblatt, Sergey Hazanov, Lalit M. Joshi, Daniel Chausovsky, Nitzan Kahn, Engin Çiftürek, Fabien Lafont, and Serge Rosenblum. Superconducting Cavity Qubit with Tens of Milliseconds Single-Photon Coherence Time. *PRX Quantum*, 4:030336, Sep 2023. doi: 10.1103/PRXQuantum.4.030336.
- [221] Vladimir E. Manucharyan, Jens Koch, Leonid I. Glazman, and Michel H. Devoret. Fluxonium: Single cooper-pair circuit free of charge offsets. *Science*, 326(5949):113–116, 2009. doi: 10.1126/science.1175552.
- [222] András Gyenis, Pranav S. Mundada, Agustin Di Paolo, Thomas M. Hazard, Xinyuan You, David I. Schuster, Jens Koch, Alexandre Blais, and Andrew A. Houck. Experimental realization of a protected superconducting circuit derived from the $0-\pi$ qubit. *PRX Quantum*, 2:010339, Mar 2021. doi: 10.1103/PRXQuantum.2.010339.
- [223] M. Checchin, D. Frolov, A. Lunin, A. Grassellino, and A. Romanenko. Measurement of the low-temperature loss tangent of high-resistivity silicon using a high- q superconducting resonator. *Phys. Rev. Appl.*, 18:034013, Sep 2022. doi: 10.1103/PhysRevApplied.18.034013.
- [224] Silvia Zorzetti, Changqing Wang, Ivan Gonin, Sergey Kazakov, Timergali Khabiboulline, Alexander Romanenko, Vyacheslav P. Yakovlev, and Anna Grassellino. Millikelvin measurements of permittivity and loss tangent of lithium niobate. *Phys. Rev. B*, 107:L220302, Jun 2023. doi: 10.1103/PhysRevB.107.L220302.

- [225] J. Krupka, K. Derzakowski, A. Abramowicz, M.E. Tobar, and R.G. Geyer. Use of whispering-gallery modes for complex permittivity determinations of ultra-low-loss dielectric materials. *IEEE Transactions on Microwave Theory and Techniques*, 47(6):752–759, 1999. doi: 10.1109/22.769347.
- [226] Daniel L. Creedon, Yarema Reshitnyk, Warrick Farr, John M. Martinis, Timothy L. Duty, and Michael E. Tobar. High Q-factor sapphire whispering gallery mode microwave resonator at single photon energies and millikelvin temperatures. *Applied Physics Letters*, 98(22):222903, 06 2011. ISSN 0003-6951. doi: 10.1063/1.3595942.
- [227] Janka Biznárová. *Electropolishing of superconducting cavities for quantum memory applications*. PhD thesis, Chalmers University of Technology, 2019.
- [228] J. Bourhill, M. Goryachev, D.L. Creedon, B.C. Johnson, D.N. Jamieson, and M.E. Tobar. Low-Temperature Properties of Whispering-Gallery Modes in Isotopically Pure Silicon-28. *Phys. Rev. Appl.*, 11:044044, Apr 2019. doi: 10.1103/PhysRevApplied.11.044044.
- [229] E. Kapit, N. Materise, and J. Shabani. Tunable capacitor for superconducting qubits, 12 2020. U.S. Patent Application No. 17/564,789.
- [230] Aaron J. Weinstein, Matthew D. Reed, Aaron M. Jones, Reed W. Andrews, David Barnes, Jacob Z. Blumoff, Larken E. Euliss, Kevin Eng, Bryan H. Fong, Sieu D. Ha, Daniel R. Hulbert, Clayton A. C. Jackson, Michael Jura, Tyler E. Keating, Joseph Kerckhoff, Andrey A. Kiselev, Justine Matten, Golam Sabbir, Aaron Smith, Jeffrey Wright, Matthew T. Rakher, Thaddeus D. Ladd, and Matthew G. Borselli. Universal logic with encoded spin qubits in silicon. *Nature*, 615(7954):817–822, Mar 2023. ISSN 1476-4687. doi: 10.1038/s41586-023-05777-3.
- [231] Martijn A. Cohen, Mingyun Yuan, Bas W. A. de Jong, Ewout Beukers, Sal J. Bosman, and Gary A. Steele. A split-cavity design for the incorporation of a dc bias in a 3d microwave cavity. *Applied Physics Letters*, 110(17):172601, 2017. doi: 10.1063/1.4981884.
- [232] N. Du, N. Force, R. Khatiwada, E. Lentz, R. Ottens, L. J Rosenberg, G. Rybka, G. Carosi, N. Woollett, D. Bowring, A. S. Chou, A. Sonnenschein, W. Wester, C. Boutan, N. S. Oblath, R. Bradley, E. J. Daw, A. V. Dixit, J. Clarke, S. R. O’Kelley, N. Crisosto, J. R. Gleason, S. Jois, P. Sikivie, I. Stern, N. S. Sullivan, D. B Tanner, and G. C. Hilton. Search for invisible axion dark matter with the axion dark matter experiment. *Phys. Rev. Lett.*, 120:151301, Apr 2018. doi: 10.1103/PhysRevLett.120.151301.
- [233] Ziqian Li, Tanay Roy, David Rodriguez Perez, Kan-Heng Lee, Eliot Kapit, and David I. Schuster. Autonomous error correction of a single logical qubit using two transmons. *arXiv e-prints*, art. arXiv:2302.06707, February 2023. doi: 10.48550/arXiv.2302.06707.
- [234] Ziqian Li, Tanay Roy, David Rodríguez Pérez, David I. Schuster, and Eliot Kapit. Hardware efficient autonomous error correction with linear couplers in superconducting circuits. *arXiv e-prints*, art. arXiv:2303.01110, March 2023. doi: 10.48550/arXiv.2303.01110.
- [235] Hugo Banderier, Maxwell Drimmer, and Yiwen Chu. Unified Simulation Methods for Quantum Acoustic Devices. *Phys. Rev. Appl.*, 20:024024, Aug 2023. doi: 10.1103/PhysRevApplied.20.024024.
- [236] J.B. Mates. *The Microwave SQUID Multiplexer*. PhD thesis, University of Colorado Boulder, 2011.
- [237] S. Adachi. *III-V Ternary and Quaternary Compounds*, pages 725–741. Springer International Publishing, Cham, 2017. ISBN 978-3-319-48933-9. doi: 10.1007/978-3-319-48933-9_30.

- [238] M P C M Krijn. Heterojunction band offsets and effective masses in III-V quaternary alloys. *Semiconductor Science and Technology*, 6(1):27–31, 1 1991. doi: 10.1088/0268-1242/6/1/005.
- [239] V. E. Manucharyan, E. Boaknin, M. Metcalfe, R. Vijay, I. Siddiqi, and M. Devoret. Microwave bifurcation of a josephson junction: Embedding-circuit requirements. *Phys. Rev. B*, 76:014524, Jul 2007. doi: 10.1103/PhysRevB.76.014524.
- [240] Florian Kagerer. *Finite Elements for Maxwell's Equations*. Bachelor's thesis, Johannes Kepler University Linz, 2018.

APPENDIX A
TUNABLE CAPACITOR APPENDICES

A.1 III-V Ternary Alloy Interpolation Formulas

Following the standard linear and quadratic interpolation schemes for III-V ternary alloys $A_xB_{1-x}C$, with composition parameter x and in terms of experimentally measured values of their binary constituents, AB and BC, we have the lattice constant a , energy gap E , and effective mass at the Γ point $m^{\Gamma*}$ as [237]

$$a_{A_xB_{1-x}C} = xa_{AC} + (1 - x)a_{BC}, \quad (\text{A.1})$$

$$E_{A_xB_{1-x}C} = xE_{AC} + (1 - x)E_{BC} + x(1 - x)E_{AB}, \quad (\text{A.2})$$

$$m_{A_xB_{1-x}C}^{\Gamma*} = xm_{AC}^{\Gamma} + (1 - x)m_{BC}^{\Gamma} + x(1 - x)m_{AB}^{\Gamma}. \quad (\text{A.3})$$

Similarly, the hole effective masses follow from a quadratic interpolation scheme of the AB, AC binary components as computed from a spherical band approximation of the valence band edge [237]

$$m_{p,\text{dos}} = \left(m_{lh}^{3/2} + m_{hh}^{3/2} \right)^{2/3}, \quad (\text{A.4})$$

$$m_{p,c} = \frac{m_{lh}^{5/2} + m_{hh}^{5/2}}{m_{p,\text{dos}}}, \quad (\text{A.5})$$

$$m_{p,c,A_xB_{1-x}C} = xm_{p,c,AC} + (1 - x)m_{p,c,BC}, \quad (\text{A.6})$$

$$m_{p,\text{dos},A_xB_{1-x}C} = xm_{p,\text{dos},AC} + (1 - x)m_{p,\text{dos},BC}. \quad (\text{A.7})$$

We recognize that the spherical band approximation may not apply to the III-V materials in our study, but it gives an estimate for density of states and conduction band effective masses that are inputs to the COMSOL Semiconductor Module materials models.

To estimate the conduction band offsets between the $In_xAl_{1-x}As$ and $In_xGa_{1-x}As$ layers, we followed another interpolation scheme that computes the absolute conduction band edges E_c using experimentally measured parameters of InAs, AlAs, and GaAs[238]

$$E_c = E_{v,\text{avg}} + \frac{\Delta_0}{3} + E_g + \Delta E_c^{\text{hy}}, \quad (\text{A.8})$$

$$\Delta E_c = E_c^B - E_c^A, \quad (\text{A.9})$$

where $E_{v,\text{avg}}$ is the average valence band edge, Δ_0 is the spin-orbit splitting in the absence of strain, E_g is the band gap energy, and ΔE_c^{hy} is the shift of the conduction band edge due to hydrostatic strain.

These parameters are calculated from the following expressions with coefficients C_{ij} read-off from Table 3 compiled by Krijn [238]

$$E_{v, \text{avg}} = \sum_{i=1}^2 C_{i0}(E_{v,\text{avg}})x^i, \quad (\text{A.10})$$

$$\Delta_0 = \sum_{i=1}^2 C_{i0}(\Delta_0)x^i, \quad (\text{A.11})$$

$$\Delta E_c^{\text{hy}} = \frac{\Delta a(x)}{a(x)} \sum_{i=0}^1 C_{i0}(\Delta E_c^{\text{hy}})x^i, \quad (\text{A.12})$$

$$\Delta a(x) = a_0 - a(x). \quad (\text{A.13})$$

A.2 Charge–Charge Interaction Matrix Element Derivation

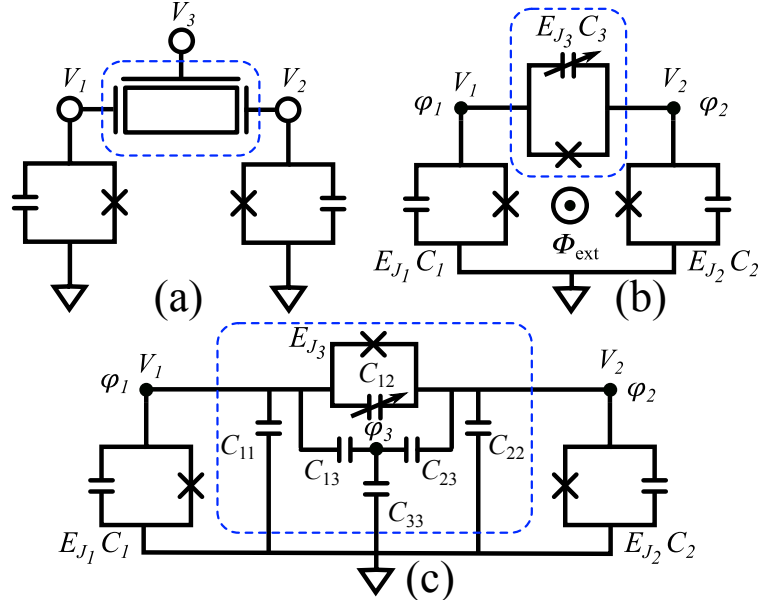


Figure A.1 Coupler circuit models. (a) The 2DEG coupler compact representation with a single gate and a pair of transmon qubits compared with (b) the simplified circuit used in the derivation of the charge-charge interaction matrix in the main text. (c) Parasitic capacitance circuit model of the coupler and two transmons; capacitances taken from (2.14) and (2.17).

Starting from the two transmon circuit coupled by a voltage-controlled Josephson junction (our 2DEG coupler) in figure Figure A.1 (b), with phases $\varphi_1, \varphi_2, \varphi_3$ referring to the left, right, and coupling junctions, respectively, we have [170]

$$\varphi_1 - \varphi_2 + \varphi_3 = -\frac{2\pi}{\Phi_0}\Phi_{\text{ext}} \quad (\text{A.14})$$

In (A.14), Φ_{ext} is the flux threading the loop formed by the three Josephson junctions as in a typical flux qubit circuit. For a finite Φ_{ext} , the potential energy U is given by

$$\begin{aligned} U(\varphi) &= \sum_j E_{J_j} (1 - \cos \varphi_j) \\ &= E_{J_1} (1 - \cos \varphi_1) + E_{J_2} (1 - \cos \varphi_2) \\ &\quad + E_{J_3} (1 - \cos(\varphi_2 - \varphi_1 - 2\pi\Phi_{\text{ext}}/\Phi_0)), \end{aligned} \quad (\text{A.15})$$

with the signs on the phases following figure Figure A.1 (b), preserving the conventions chosen in. [170] We order the phases in a single column vector as

$$\varphi = \begin{pmatrix} \varphi_1 \\ \varphi_2 \end{pmatrix}. \quad (\text{A.16})$$

Setting $\Phi_{\text{ext}} = 0$, we compute the kinetic energy T by using the Josephson equation relating the voltages at nodes with $k = \{1, 2\}$, $V_k = (\Phi_0/2\pi)\dot{\varphi}_k$ and the definition of T in terms of $\dot{\varphi}_k$

$$\begin{aligned} T &= \frac{1}{2} (C_1 V_1^2 + C_2 V_2^2 + C_3 V_3^2) \\ &= \frac{1}{2} \left(\frac{\Phi_0}{2\pi} \right)^2 (C_1 \dot{\varphi}_1^2 + C_2 \dot{\varphi}_2^2 + C_3 (\dot{\varphi}_2 - \dot{\varphi}_1)^2) \\ &= \frac{1}{2} \left(\frac{\Phi_0}{2\pi} \right)^2 \dot{\varphi}^T \mathbf{C} \dot{\varphi}, \end{aligned} \quad (\text{A.17})$$

and reading off the capacitance matrix

$$\mathbf{C} = \begin{pmatrix} C_1 + C_3 & -C_3 \\ -C_3 & C_2 + C_3 \end{pmatrix}. \quad (\text{A.18})$$

Relating the total capacitances (both the intrinsic junction and external capacitance, commonly referred to as C_Σ [41]) shunting the junctions, C_1 , C_2 , to the anharmonicities extracted from the EPR calculations, we have, from the asymptotic expressions derived by Koch et al. [1]

$$C_k = \frac{e^2}{2E_C} \simeq -\frac{e^2}{2\alpha_k} \quad (\text{A.19})$$

and we take $C_3 = C_{12}(V_g)$, the gate voltage-dependent capacitance across the 2DEG coupler.

The classical Lagrangian \mathcal{L} and Hamiltonian \mathcal{H} associated with the kinetic and potential energies above, then read [170]

$$\begin{aligned}\mathcal{L}(\boldsymbol{\varphi}, \dot{\boldsymbol{\varphi}}) &= T - U \\ &= \frac{1}{2} \left(\frac{\Phi_0}{2\pi} \right)^2 \dot{\boldsymbol{\varphi}}^T \mathbf{C} \dot{\boldsymbol{\varphi}} - \sum_j E_{J_j} (1 - \cos \varphi_j)\end{aligned}\quad (\text{A.20})$$

$$\begin{aligned}\mathcal{H} &= \mathbf{P}^T \dot{\boldsymbol{\varphi}} - \mathcal{L} \\ &= \frac{1}{2} \mathbf{Q}^T \mathbf{C}^{-1} \mathbf{Q} + U(\boldsymbol{\varphi})\end{aligned}\quad (\text{A.21})$$

$$P_j = \frac{\partial \mathcal{L}}{\partial \dot{\varphi}_j} = \left(\frac{\Phi_0}{2\pi} \right)^2 \sum_k C_{jk} \dot{\varphi}_k, \quad \mathbf{Q} = \frac{2\pi}{\Phi_0} \mathbf{P} \quad (\text{A.22})$$

We take the form of the quantized Hamiltonian to be the same as the classical one in (A.21) with classical variables promoted to operators, and identify the charge-charge matrix elements as $e^2[\mathbf{C}^{-1}]_{ij}/2$. Similarly, we write the Lagrangian and identify the capacitance matrix corresponding to the parasitic capacitance model given by the circuit in Fig. Figure A.1 (c) as

$$\begin{aligned}\mathcal{L} &= \frac{1}{2} \left(\frac{\Phi_0}{2\pi} \right)^2 [(C_1 + C_{11})\dot{\varphi}_1^2 + (C_2 + C_{22})\dot{\varphi}_2^2 \\ &\quad + C_{33}\dot{\varphi}_3^2 + C_{12}(\dot{\varphi}_2 - \dot{\varphi}_1)^2 \\ &\quad + C_{13}(\dot{\varphi}_3 - \dot{\varphi}_1)^2 + C_{23}(\dot{\varphi}_2 - \dot{\varphi}_3)^2] - U(\boldsymbol{\varphi})\end{aligned}\quad (\text{A.23})$$

$$\mathbf{C} = \begin{pmatrix} \tilde{C}_{11} & -C_{12} & -C_{13} \\ -C_{12} & \tilde{C}_{22} & -C_{23} \\ -C_{13} & -C_{23} & \tilde{C}_{33} \end{pmatrix}, \quad (\text{A.24})$$

where $\tilde{C}_{11} = C_1 + C_{11} + C_{12} + C_{13}$, $\tilde{C}_{22} = C_2 + C_{22} + C_{12} + C_{23}$, and $\tilde{C}_{33} = C_{13} + C_{23} + C_{33}$.

APPENDIX B
BLACK BOX HAMILTONIAN AND CORRESPONDENCE WITH EPR

In Section 1.3.1, we wrote the linear part of the black box Hamiltonian

$$H_0 = \sum_p \left(4E_{C,p}N_p^2 + \frac{1}{2}E_{L,p}\varphi_p^2 \right) \quad (\text{B.1})$$

in terms of number and phase variables and stated that we could quantize the Hamiltonian as a sum of harmonic oscillators. Here, we will give more details of those conversions and discuss the relationship between zero point phase fluctuations and energy participation ratios.

The commutation relations of the phase and number operators follow from the flux and charge commutation relations, equating flux to the position and charge to the momentum of particle of a harmonic oscillator as

$$\begin{aligned} [\Phi_m, Q_n] &= i\hbar\delta_{mn} & (\text{B.2}) \\ \left[\left(\frac{\Phi_0}{2\pi} \right) \varphi_m, 2eN_n \right] &= i\hbar\delta_{mn} \\ \left(\frac{\Phi_0}{2\pi} \right) 2e [\varphi_m, N_n] &= i\hbar\delta_{mn} \\ [\varphi_m, N_n] &= i\delta_{mn} & (\text{B.3}) \end{aligned}$$

with the right hand side of Eq. (B.3) agreeing with the dimensionless operators φ_m and N_n on the left hand side.

The Hamiltonian in Eq. (1.26), is equivalent to the sum of harmonic oscillators with frequencies $\omega_p = (L_p C_p)^{-1/2}$, and we can express the flux and charge operators in terms of bosonic raising and lowering operators a_p, a_p^\dagger [103]

$$\Phi_p = \Phi_p^{\text{ZPF}} (a_p + a_p^\dagger), \quad Q_p = -iQ_p^{\text{ZPF}} (a_p - a_p^\dagger) \quad (\text{B.4})$$

where the zero point flux and charge fluctuations are given by

$$\Phi_p^{\text{ZPF}} = \sqrt{\frac{\hbar\omega_p L_p}{2}}, \quad Q_p^{\text{ZPF}} = \sqrt{\frac{\hbar}{2\omega_p L_p}} \quad (\text{B.5})$$

Substituting Eqs. (B.4), (B.5) into Eq. (1.26), gives

$$\begin{aligned} H_0 &= \sum_p \left(-\frac{1}{2C_p} (Q_p^{\text{ZPF}})^2 (a_p - a_p^\dagger)^2 + \frac{1}{2L_p} (\Phi_p^{\text{ZPF}})^2 (a_p + a_p^\dagger)^2 \right) \\ &= \sum_p \hbar\omega_p (a_p^\dagger a_p + 1/2) \end{aligned} \quad (\text{B.6})$$

To calculate the zero point phase fluctuations $\langle \varphi_m^2 \rangle$ of the m -th mode, we invoke the Virial theorem, where the inductive energy is equal to half the total energy which is in turn equal to the capacitive energy,

$$\mathcal{E}_{\text{ind}} = \mathcal{E}_{\text{cap}} = \frac{1}{2} \mathcal{E}_{\text{tot}} \quad (\text{B.7})$$

$$\Rightarrow \mathcal{E}_{\text{ind}} = \frac{1}{2} \sum_p E_{L,p} \langle \psi_m | \varphi_p^2 | \psi_m \rangle = \frac{1}{2} \langle \psi_m | H_0 | \psi_m \rangle \quad (\text{B.8})$$

Taking the vacuum expectation value of Eq. (B.8), by replacing $|\psi_m\rangle = |0\rangle_m$, gives

$$\begin{aligned} \frac{1}{2} E_{L,m} \langle \varphi_m^2 \rangle &= \frac{1}{4} \hbar\omega_m \\ \Rightarrow \langle \varphi_m^2 \rangle &= \frac{\hbar\omega_m}{2E_{L,m}} \end{aligned} \quad (\text{B.9})$$

Repeating the procedure for the zero point number fluctuations, $\langle N_m^2 \rangle$ of the m -th mode, we find

$$\begin{aligned} \mathcal{E}_{\text{cap}} &= \sum_p 4E_{C,p} \langle \psi_m | N_p^2 | \psi_m \rangle = \frac{1}{2} \langle \psi_m | H_0 | \psi_m \rangle, \\ 4E_{C,m} \langle N_m^2 \rangle &= \frac{1}{4} \hbar\omega_m \\ \Rightarrow \langle N_m^2 \rangle &= \frac{\hbar\omega_m}{16E_{C,m}} \end{aligned} \quad (\text{B.10})$$

We will refer back to these expressions in the following sections, with the energy participation ratios from [103] in terms of the quantities obtained from the black box analysis. Comparing the expressions for the inductive and capacitive EPRs in Section 1.3.4 with the black box expressions for the phase and Cooper number zero point fluctuations, we find

$$\begin{aligned} \langle \varphi_m^2 \rangle &= \frac{\hbar\omega_m}{2E_{L,m}} = \langle \varphi_{mj}^2 \rangle = \frac{p_{mj}^L \hbar\omega_m}{2E_{J,j}} \\ \Rightarrow p_{mj}^L &= \frac{E_{J,j}}{E_{L,m}} = \frac{\left(\frac{\Phi_0}{2\pi}\right)^2 L_{J,j}^{-1}}{\left(\frac{\Phi_0}{2\pi}\right)^2 L_m^{-1}} = \frac{L_m}{L_{J,j}} = \frac{\frac{1}{2} L_{J,j} I_k^2(L_{J,j})}{\frac{1}{2} \mu_0 \int_V \mathbf{H}_k^*(\mathbf{x}, L_{J,j}) \cdot \mathbf{H}_k(\mathbf{x}, L_{J,j}) d^3\mathbf{x} + \frac{1}{2} L_{J,j} I_k^2(L_{J,j})} \end{aligned} \quad (\text{B.11})$$

$$\begin{aligned} \langle N_m^2 \rangle &= \frac{\hbar\omega_m}{16E_{C,m}} = \langle N_{mj}^2 \rangle = \frac{p_{mj}^C \hbar\omega_m}{16E_{C,j}} \\ \Rightarrow p_{mj}^C &= \frac{E_{C,j}}{E_{C,m}} = \frac{\frac{e^2}{2C_{J,j}}}{\frac{e^2}{2C_m}} = \frac{C_m}{C_{J,j}} = \frac{\frac{1}{2} C_{J,j} V_k^2(L_{J,j})}{\frac{1}{2} \epsilon_0 \int_V \mathbf{E}_k^*(\mathbf{x}, L_{J,j}) \cdot \mathbf{E}_k(\mathbf{x}, L_{J,j}) d^3\mathbf{x} + \frac{1}{2} C_{J,j} V_k^2(L_{J,j})} \end{aligned} \quad (\text{B.12})$$

In both the inductive and capacitive EPRs, we arrive at ratios of the mode inductances and capacitances referenced to the Josephson junction inductances and capacitances. These ratios agree with those stated in [95] and derived by Manucharyan et al. [239]. The ratios of inductive energy and capacitive energy stored in the junction relative to the total inductive and capacitive energy are classical quantities that are calculated with the eigenmode solver in HFSS.

APPENDIX C
ANSYS HFSS EIGENVALUE PROBLEM

This appendix gives a derivation of the eigenvalue problem solved by Ansys HFSS as outlined in the documentation of the software. We use the terminology commonly used in the finite element community to construct the weak form of the Helmholtz equation and discuss the consequences of the impedance boundary condition to the eigenvalue problem.

C.1 Maxwell's Equations and Helmholtz Equation

The goal of this section is to start with Maxwell's equations, derive the Helmholtz equation. Later, we will apply Galerkin discretization to the Helmholtz equation and arrive at the eigenvalue problem solved by HFSS in terms of basis and testing functions. Maxwell's equations, in SI units, read

$$\nabla \cdot \mathbf{D} = \rho \quad (\text{C.1})$$

$$\nabla \cdot \mathbf{B} = 0 \quad (\text{C.2})$$

$$\nabla \times \mathbf{E} = -\frac{\partial \mathbf{B}}{\partial t} \quad (\text{C.3})$$

$$\nabla \times \mathbf{B} = \mu\epsilon \frac{\partial \mathbf{E}}{\partial t} + \mu \mathbf{J}_{\text{tot}} \quad (\text{C.4})$$

where $\mathbf{E} = \mathbf{E}(\mathbf{x}, t)$ is the electric field, $\mathbf{D} = \epsilon \mathbf{E}$ is the electric displacement field, $\mathbf{B} = \mathbf{B}(\mathbf{x}, t)$ is the magnetic flux density, and $\mathbf{J}_{\text{tot}} = \mathbf{J}_d + \mathbf{J}_s$, $\mathbf{J}_s = \mathbf{J}_s(\mathbf{x}, t)$ is the source current density, and $\mu = \mu_r \mu_0$ and $\epsilon = \epsilon_r \epsilon_0$ are the magnetic permeability and electric permittivity of the medium where the fields are being solved. Taking the curl of Faraday's law in (C.3) and substituting (C.4), we find

$$\nabla \times \nabla \times \mathbf{E} = -\mu\epsilon \frac{\partial^2 \mathbf{E}}{\partial t^2} - \mu \frac{\partial \mathbf{J}_s}{\partial t} \quad (\text{C.5})$$

Separating time t and space $\mathbf{x} = (x, y, z)$ variables as $\mathbf{E} = \text{Re}\{\mathbf{E}(\mathbf{x})e^{i\omega t}\}$, $\mathbf{J}_s = \text{Re}\{\mathbf{J}_s(\mathbf{x})e^{i\omega t}\}$, using the electric engineering notation $i = \sqrt{-1}$, and identifying the magnetic field in terms of the magnetic flux density, $\mathbf{H} = \mu^{-1} \mathbf{B}$, we rewrite (C.5) as

$$\nabla \times \nabla \times \mathbf{E}(\mathbf{x}) = \omega^2 \mu\epsilon \mathbf{E}(\mathbf{x}) - i\omega \mu \mathbf{J}_s(\mathbf{x}) \quad (\text{C.6})$$

with the common $e^{i\omega t}$ factors dropped from the above expressions.

Dividing (C.6) by μ_r and identifying the magnitude of the wave vector $k_0 = \omega^2 \mu_0 \epsilon_0 = \omega^2/c^2$, we have Helmholtz's equation with a source term $\mathbf{J}_s(\mathbf{x})$

$$\nabla \times \frac{1}{\mu_r} \nabla \times \mathbf{E}(\mathbf{x}) - k_0^2 \epsilon_r \mathbf{E}(\mathbf{x}) = -i\omega \mu_0 \mathbf{J}_s(\mathbf{x}) \quad (\text{C.7})$$

C.2 Galerkin Testing

To construct a linear system of equations, HFSS *tests* the partial differential equation in (C.7) by multiplying by some testing function \mathbf{W}_n and integrating over all vacuum and dielectric regions in the volume V

$$\int_V \mathbf{W}_n(\mathbf{x}) \cdot \left[\nabla \times \frac{1}{\mu_r} \nabla \times \mathbf{E}(\mathbf{x}) - k_0^2 \epsilon_r \mathbf{E}(\mathbf{x}) \right] d^3\mathbf{x} = -i\omega \mu_0 \int_V \mathbf{W}_n(\mathbf{x}) \cdot \mathbf{J}_s(\mathbf{x}) d^3\mathbf{x} \quad (\text{C.8})$$

In this scheme, the electric fields are expanded in terms of basis functions $\mathbf{W}_m(\mathbf{x})$ from the same family as the testing functions. Both the testing and basis functions are curl-conforming, meaning that they preserve the continuity of the tangential component of the electric field on the boundaries of the elements being solved on; as expected for physical electric fields. Substituting $\mathbf{E}(\mathbf{x}) = \sum_m v_m \mathbf{W}_m(\mathbf{x})$ into (C.8), we find

$$\sum_m v_m \int_V \mathbf{W}_n(\mathbf{x}) \cdot \left[\nabla \times \frac{1}{\mu_r} \nabla \times \mathbf{W}_m(\mathbf{x}) - k_0^2 \epsilon_r \mathbf{W}_m(\mathbf{x}) \right] d^3\mathbf{x} = -i\omega \mu_0 \int_V \mathbf{W}_n(\mathbf{x}) \cdot \mathbf{J}_s(\mathbf{x}) d^3\mathbf{x} \quad (\text{C.9})$$

In the interest of deriving the eigenvalue problem, we set $\mathbf{J}_s = 0$ and rearrange (C.9)

$$\sum_m v_m \int_V \mathbf{W}_n(\mathbf{x}) \cdot \left[\nabla \times \frac{1}{\mu_r} \nabla \times \mathbf{W}_m(\mathbf{x}) \right] d^3\mathbf{x} - \sum_m v_m k_0^2 \epsilon_r \int_V \mathbf{W}_n(\mathbf{x}) \cdot \mathbf{W}_m(\mathbf{x}) d^3\mathbf{x} = 0 \quad (\text{C.10})$$

$$A\mathbf{v} - \lambda B\mathbf{v} = 0 \quad (\text{C.11})$$

$$A_{nm} = \int_V \mathbf{W}_n(\mathbf{x}) \cdot \left[\nabla \times \frac{1}{\mu_r} \nabla \times \mathbf{W}_m(\mathbf{x}) \right] d^3\mathbf{x} \quad (\text{C.12})$$

$$B_{nm} = \epsilon_r \int_V \mathbf{W}_n(\mathbf{x}) \cdot \mathbf{W}_m(\mathbf{x}) d^3\mathbf{x} \quad (\text{C.13})$$

$$\lambda = k_0^2 \quad (\text{C.14})$$

If the basis functions \mathbf{W}_n are orthonormal with their normalization built-in to their definition, then B_{mn} reduces to the Kronecker delta δ_{mn} or the identity matrix, and the generalized eigenvalue problem in (C.11) becomes the standard eigenvalue problem. This is an important point, as the form of the equation being solved by HFSS dictates the form of the inner product for eigenvectors of different mode numbers. Moreover, the magnetic fields $\mathbf{H}(\mathbf{x}) = i(\omega\mu)^{-1} \nabla \times \mathbf{E}$ have inherently lower accuracy than the electric fields, being a quantity computed by differentiation rather than integration.

To add an impedance boundary condition to this scheme, we consider the surface impedance Z_s on the surface S_J describing a junction of the form

$$\mathbf{E}_{\tan} = Z_S (\mathbf{n} \times \mathbf{H}_{\tan}) \quad (\text{C.15})$$

where \mathbf{n} is the unit normal vector pointing out of the surface S_J . The tangential components of the fields are given by $\mathbf{E}_{\tan} = \mathbf{E} \times \mathbf{n}$ and $\mathbf{H}_{\tan} = \mathbf{H} \times \mathbf{n}$. Substituting these expressions into (C.15) and multiplying by the basis functions \mathbf{W}_n then integrating over the surface S_J gives

$$\int_{S_J} \mathbf{W}_n(\mathbf{x}) \cdot (\mathbf{E}(\mathbf{x}) \times \mathbf{n}) d^2\mathbf{x} = \int_{S_J} \mathbf{W}_n(\mathbf{x}) \cdot (\mathbf{n} \times (\mathbf{H}(\mathbf{x}) \times \mathbf{n})) d^2\mathbf{x} \quad (\text{C.16})$$

$$\sum_m v_m \int_{S_J} \left\{ \mathbf{W}_n(\mathbf{x}) \cdot \left[\mathbf{W}_m(\mathbf{x}) \times \mathbf{n} + \frac{Z_s}{j\omega\mu} \mathbf{n} \times ((\nabla \times \mathbf{W}_m(\mathbf{x})) \times \mathbf{n}) \right] \right\} d^2\mathbf{x} = 0 \quad (\text{C.17})$$

This integral expression then becomes part of the left hand side matrix A in (C.11), implying that information about the junction boundary condition is already encoded in the eigenfunctions $v_{m,k}$ that constitute the eigenmode electric and magnetic fields.

Taking two particular values for $\lambda = k^2, k'^2$ (we drop the subscript 0 here for brevity) and express the inner product of the electric field solutions at k and k' in terms of the eigenvectors \mathbf{v}_k and $\mathbf{v}_{k'}$

$$\begin{aligned} \int_V \mathbf{E}_k(\mathbf{x}) \cdot \mathbf{E}_{k'}(\mathbf{x}) d^3\mathbf{x} &= \sum_{mn} v_{m,k} v_{n,k'} \int_V \mathbf{W}_m(\mathbf{x}) \cdot \mathbf{W}_n(\mathbf{x}) d^3\mathbf{x} \\ &= \mathbf{v}_k^T B \mathbf{v}_{k'} \end{aligned} \quad (\text{C.18})$$

Similarly the magnetic field inner product follows from its definition above in terms of the curl of the electric field

$$\begin{aligned} \int_V \mathbf{H}_k(\mathbf{x}) \cdot \mathbf{H}_{k'}(\mathbf{x}) d^3\mathbf{x} &= -\frac{1}{\omega_k \omega_{k'} \mu^2} \sum_{mn} v_{m,k} v_{n,k'} \int_V (\nabla \times \mathbf{W}_m(\mathbf{x})) \cdot (\nabla \times \mathbf{W}_n(\mathbf{x})) d^3\mathbf{x} \\ &= \mathbf{v}_k^T \tilde{B} \mathbf{v}_{k'} \end{aligned} \quad (\text{C.19})$$

where we have labeled the integral scaled by the prefactor $-1/\mu^2 \omega_k \omega_{k'}$ as \tilde{B} . To evaluate the matrix \tilde{B} , we return to the integral involving the curl-curl term in (C.12) and integrate by parts [240]

$$\begin{aligned} \int_V \mathbf{W}_n(\mathbf{x}) \cdot [\nabla \times \nabla \times \mathbf{W}_m(\mathbf{x})] d^3\mathbf{x} &= \int_V (\nabla \times \mathbf{W}_n(\mathbf{x})) \cdot (\nabla \times \mathbf{W}_m(\mathbf{x})) d^3\mathbf{x} \\ &\quad - \int_S ((\nabla \times \mathbf{W}_m(\mathbf{x})) \times \mathbf{n}) \cdot \mathbf{W}_n(\mathbf{x}) d^2\mathbf{x} \end{aligned} \quad (\text{C.20})$$

Using the identity $((\nabla \times \mathbf{W}_m) \times \mathbf{n}) \cdot \mathbf{W}_n = ((\nabla \times \mathbf{W}_m) \times \mathbf{n}) \cdot ((\mathbf{W}_n \times \mathbf{n}) \times \mathbf{n})$, we have on the left hand side of the dot product a term that is proportional to the tangential magnetic field on the boundary and another term that is proportional to the cross product of the tangential part of the testing function \mathbf{W}_n and the unit normal \mathbf{n} . If either of these terms vanish, then $\tilde{B} \equiv A$ and the orthonormality condition on the magnetic fields is $\langle \mathbf{H}_k, \mathbf{H}_{k'} \rangle = \mathbf{v}_k^T A \mathbf{v}_{k'}$, otherwise it depends on the sum of the surface term above and A .

In general, A includes the boundary conditions and the curl-curl operator, written explicitly for the case of the impedance boundary condition and using the integration by parts result from above

$$\begin{aligned} A_{mn} &= \int_V (\nabla \times \mathbf{W}_n(\mathbf{x})) \cdot (\nabla \times \mathbf{W}_m(\mathbf{x})) d^3\mathbf{x} \\ &\quad - \int_S ((\nabla \times \mathbf{W}_m(\mathbf{x})) \times \mathbf{n}) \cdot \mathbf{W}_n(\mathbf{x}) d^2\mathbf{x} \\ &\quad + \int_{S_J} \left\{ \mathbf{W}_n(\mathbf{x}) \cdot \left[\mathbf{W}_m(\mathbf{x}) \times \mathbf{n} + \frac{Z_s}{j\omega\mu} \mathbf{n} \times ((\nabla \times \mathbf{W}_m(\mathbf{x})) \times \mathbf{n}) \right] \right\} d^2\mathbf{x} \end{aligned} \quad (\text{C.21})$$

This result highlights the difference in orthogonality properties of the electric and magnetic field eigenmode field solutions. The electric field eigenfunctions depend on the boundary conditions, but their orthonormality condition does not, whereas the magnetic field orthonormality condition is a function of the boundary condition terms. Without access to the explicit form of $\mathbf{W}_{m(n)}$, we do not assume that the \mathbf{E}_k and \mathbf{H}_k overlap integrals introduced in Chapter 3 evaluate to exactly zero at different mode numbers and same junction inductances. This leads to slightly more complicated, yet calculable expressions for the coefficients of interest to design of 3D tunable couplers other monolithic microwave structures.

APPENDIX D

SUPPLEMENTAL MATERIAL OF *GRAIN SIZE IN LOW SUPERCONDUCTING TA THIN FILMS ON C-AXIS SAPPHIRE*

D.1 Ta Grain Size for $T = 600^\circ\text{C}$ Deposition

We used atomic force microscopy in tapping mode to study the grain size distribution of the tantalum films deposited at a substrate temperature of $T = 600^\circ\text{C}$. A typical topography is shown in Figure D.1, with an average grain size of $G = 1732 \pm 92 \text{ nm}^2$.

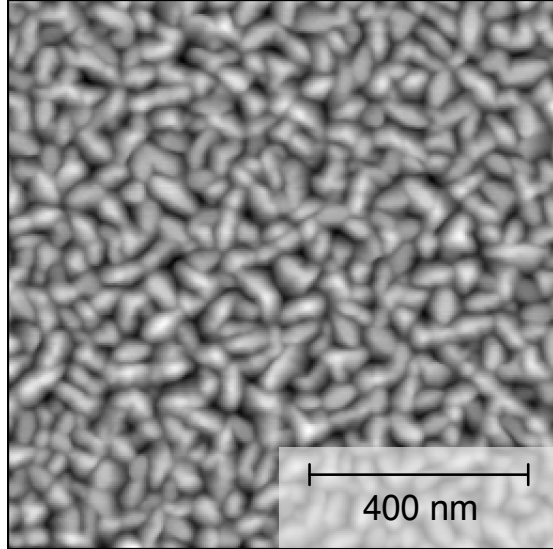


Figure D.1 Typical surface topography recorded with an atomic force microscope of the tantalum film deposited at a substrate temperature of $T=600^\circ\text{C}$.

D.2 Wide Scans

We measured the broadband responses of the devices over multiple cooldowns to compare the variability of the background (Figure D.3). We measured S_{21} , the microwave transmission coefficient, through each device's transmission line with 65,001 points and 100 kHz IF bandwidth to resolve most of the resonator dips over the 4–8 GHz range. Repeated measurements of the same devices show significant similarities, as shown by the two blue curves (SG2) and the two green curves (LGS1). Broad resonances can be attributed to a low-Q spurious environmental mode, which is present for all but LGS2 (purple curve).

D.3 Extracted Resonator Parameters

Table D.1 summarizes the parameters extracted from fitting the TLS and power-independent loss of each resonator. The uncertainties are the 95% confidence intervals returned by a least squares fitting routine.

Figure D.2 compares the loss metrics $F\delta_{\text{TLS}}^0$ with δ_{LP} , δ_{HP} , and $\delta_{\text{LP}} - \delta_{\text{HP}}$. There is excellent agreement between $F\delta_{\text{TLS}}^0$ and $\delta_{\text{LP}} - \delta_{\text{HP}}$, where all measurements lay along the line of 1:1 correlation. The mismatch between $F\delta_{\text{TLS}}^0$ and δ_{LP} highlights that one cannot extract the intrinsic TLS loss with the low power loss alone; the power-independent loss is necessary to accurately compute TLS loss. The scatter in the center plot indicates a lack of correlation between power-independent loss and TLS loss.

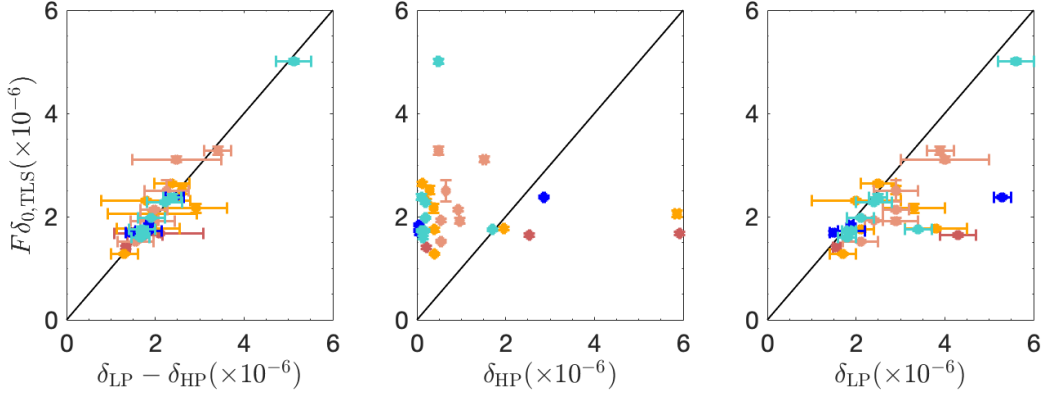


Figure D.2 Correlation of loss metrics. Device-induced intrinsic TLS loss $F\delta_{\text{TLS}}^0$ as a function of three other loss metrics: low power loss δ_{LP} minus power-independent loss δ_{HP} , δ_{HP} , and δ_{LP} . Solid black line indicates a 1:1 relationship between metrics.

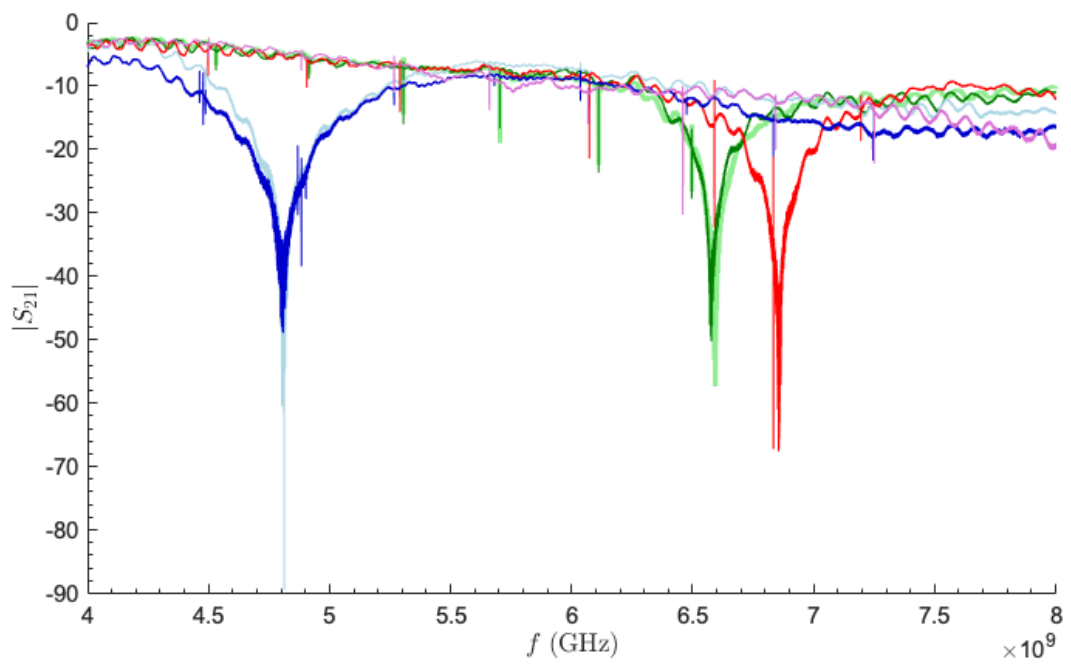


Figure D.3 Background characterization at -100 dBm. Transmission curves for SGS1 cooldown 2 (light blue) and 4 (blue), LGS1 cooldown 1 (light green) and 3 (green), LGS2 cooldown 4 (purple) and SGS2 cooldown 4 (red) are plotted.

Table D.1 Parameters extracted from cryogenic microwave measurements of Ta on Al₂O₃ coplanar waveguide (CPW) resonators. Values are given with their 95% confidence intervals where available. f_0 : resonance frequency. $1/Q_{i,\text{HP}}$: inverse high power internal quality factor. $F\delta_{\text{TLS}}^0$: resonator-induced intrinsic TLS loss. $1/Q_{i,\text{LP}}$: inverse low power internal quality factor. $1/Q_c$: inverse coupling quality factor at high power. Surface treatment labels correspond to small grain size (SGS*) and large grain size (LGS*) devices.

LGS1	5.704	0.05 ± 0.01	1.73 ± 0.02	1.9 ± 0.3	4.658 ± 0.004	0.14 ± 0.02	0.197 ± 0.005
Coldown 1	6.112	0.057 ± 0.005	1.69 ± 0.04	1.5 ± 0.1	5.702 ± 0.002	0.19 ± 0.06	0.24 ± 0.02
LGS1	4.531	0.037 ± 0.008	1.84 ± 0.02	1.89 ± 0.06	1.871 ± 0.004	1.8 ± 0.2	0.237 ± 0.005
Coldown 3	4.915	2.86 ± 0.02	2.38 ± 0.02	5.3 ± 0.2	2.649 ± 0.009	0.34 ± 0.03	0.195 ± 0.002
LGS2	4.501	0.10 ± 0.02	1.73 ± 0.03	1.79 ± 0.1	1.199 ± 0.004	0.4 ± 0.1	0.175 ± 0.009
Cooldown 4	4.884	0.48 ± 0.03	5.01 ± 0.05	5.6 ± 0.4	1.46 ± 0.01	0.17 ± 0.04	0.151 ± 0.006
	5.267	0.110 ± 0.009	2.38 ± 0.05	2.5 ± 0.2	1.892 ± 0.004	0.10 ± 0.04	0.18 ± 0.01
	5.661	0.19 ± 0.02	1.98 ± 0.02	2.1 ± 0.3	3.28 ± 0.01	1.0 ± 0.2	0.212 ± 0.008
	6.068	0.17 ± 0.01	1.73 ± 0.02	1.9 ± 0.1	2.088 ± 0.005	3.6 ± 0.8	0.21 ± 0.01
	6.459	0.13 ± 0.02	1.60 ± 0.03	1.8 ± 0.2	6.14 ± 0.03	1.4 ± 0.4	0.21 ± 0.01
	6.844	1.70 ± 0.02	1.75 ± 0.02	3.4 ± 0.3	5.71 ± 0.02	1.0 ± 0.2	0.207 ± 0.008
	7.250	0.19 ± 0.02	2.28 ± 0.03	2.4 ± 0.4	3.76 ± 0.01	0.13 ± 0.03	0.201 ± 0.008
SGS1	4.488	0.22 ± 0.01	1.41 ± 0.03	1.56 ± 0.08	1.184 ± 0.004	1.5 ± 0.3	0.236 ± 0.008
Cooldown 2	5.682	5.92 ± 0.01	1.68 ± 0.03	8 ± 1	1.631 ± 0.002	0.23 ± 0.05	0.24 ± 0.01
	6.476	2.535 ± 0.006	1.64 ± 0.03	4.3 ± 0.4	1.663 ± 0.002	0.32 ± 0.07	0.26 ± 0.01
SGS1	4.487*	0.38 ± 0.02	2.16 ± 0.09	3.3 ± 0.7	1.244 ± 0.008	9 ± 7	0.27 ± 0.06
Cooldown 4	4.902	0.21 ± 0.01	2.31 ± 0.03	2 ± 1	1.85 ± 0.01	15 ± 3	0.20 ± 0.01
	5.267	0.128 ± 0.010	2.64 ± 0.04	2.5 ± 0.4	1.68 ± 0.01	3.4 ± 0.9	0.29 ± 0.02
	5.681*	5.86 ± 0.06	2.06 ± 0.06	7.8 ± 1.0	1.576 ± 0.004	0.5 ± 0.2	0.25 ± 0.02
	6.037	0.395 ± 0.007	1.28 ± 0.02	1.7 ± 0.3	1.659 ± 0.004	0.9 ± 0.2	0.28 ± 0.02
	6.476*	1.96 ± 0.01	1.77 ± 0.03	3.8 ± 0.7	1.522 ± 0.006	0.9 ± 0.3	0.27 ± 0.02
	6.833	0.29 ± 0.02	2.52 ± 0.08	2.9 ± 0.04	1.99 ± 0.02	0.13 ± 0.06	0.21 ± 0.02
	7.245	0.39 ± 0.01	1.75 ± 0.04	2.1 ± 0.3	1.269 ± 0.008	0.9 ± 0.2	0.29 ± 0.02
SGS2	4.499	0.65 ± 0.01	2.5 ± 0.2	2.9 ± 0.5	2.106 ± 0.006	0.020 ± 0.018	0.21 ± 0.02
Cooldown 4	4.907	0.49 ± 0.01	3.28 ± 0.08	3.9 ± 0.3	2.502 ± 0.007	0.210 ± 0.090	0.21 ± 0.02
	5.292	0.537 ± 0.007	1.93 ± 0.03	2.4 ± 0.2	3.789 ± 0.005	1.0 ± 0.3	0.27 ± 0.02
	6.074	0.93 ± 0.02	2.13 ± 0.03	2.9 ± 0.3	6.609 ± 0.008	0.20 ± 0.05	0.26 ± 0.01
	6.460	0.54 ± 0.02	1.52 ± 0.02	2.1 ± 0.4	5.91 ± 0.01	0.16 ± 0.04	0.20 ± 0.01
	6.591	1.52 ± 0.03	3.11 ± 0.06	4 ± 1	54.9 ± 0.2	0.10 ± 0.03	0.24 ± 0.02
	7.196	0.96 ± 0.02	1.92 ± 0.05	2.9 ± 0.5	4.25 ± 0.03	0.04 ± 0.02	0.21 ± 0.02

D.4 Microwave Setup

In Figure D.5, we give a schematic of the microwave wiring in our Janis JDry 250 dilution refrigerator. A Keysight PNA N5222B vector network analyzer (VNA) transmits signals down input lines A and B, with 60 dB of discrete attenuation supplied by XMA 2082-6418-dB-CRYO cryogenic attenuators. We estimate an additional 10 dB of attenuation from internal and external line losses.

Two Quinstar QCE-060400CM00 circulators separate input and output paths outside of two six-to-one Radiall 583 microwave switches. Additional directionality on the output lines is achieved with two pairs of 20 dB Quinstar QCI-080090XM00 isolators. Two LNF-LNC4.8C high electron mobility transistor (HEMT) amplifiers with average noise temperatures of 1.5 K and gain of 40 dB, mounted at the 3 K stage, set the noise floor of our experiments. Room temperature low noise amplifiers (Miteq AFS4-04001200-48-20P-4), provide an additional 30 dB of gain on the receiver side. DC-blocks (Mini-Circuits BLKD-183-S+) decouple DC currents from the input and output lines at room temperature.

D.5 Resistance Measurements

To collect resistance data, both chips were bonded with aluminum wirebonds on independent four-wire measurement setups. The measurement board was connected to the cold stage of a modified HPD 103 model cryostat. This cryostat consists of a two-stage pulse tube and a two-stage adiabatic demagnetization refrigerator. After loading the samples, but before cooling down, an external mu-metal shield was put in place to reduce the presence of external magnetic fields within the measurement setup. The room temperature resistances of both chips were then taken. Resistance was tracked over several minutes to measure noise. Then the cryostat was pumped out and the compressor turned on to cool to base temperature overnight.

The next morning with the cold FAA stage at ~ 3 K, the chips were now both superconducting. Then turning off the compressor, while tracking the resistance of one chip as the temperature slowly increased to ~ 4.5 K, going through the superconducting transition of Ta.

We use an AC “tickle” current provided by a Linear Research LR-700 to measure the resistance. This minimizes any heating once the device being measured goes normal, preventing a runaway thermal load on the sample stage. Measurements at room temperature and at ~ 4 K were taken with the following LR700 settings chosen to minimize noise for these chips: 1 second filter, 20 μ V excitation, 2 Ω range. Figure D.4 shows the two resistance curves as a function of temperature.

To extract the normal resistance R_n and superconducting transition temperature T_c , we used an empirical expression to fit the transition region (inset of Figure D.4) of the form

$$R(T) = \frac{1}{2} R_n [\tanh((T - T_c)/\Delta T) + 1] \quad (\text{D.1})$$

where ΔT is a free parameter that corresponds to the width of the transition.

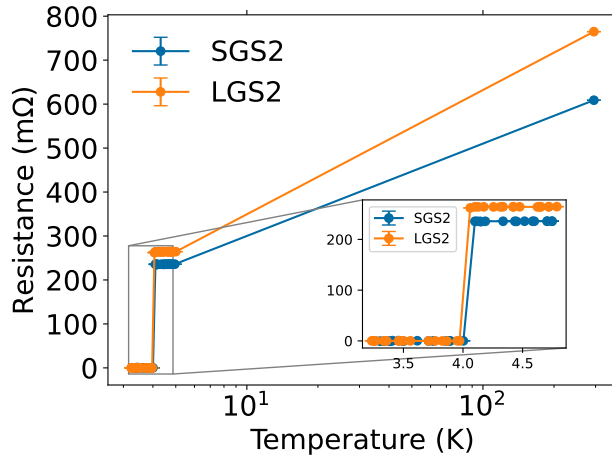


Figure D.4 Temperature sweep of resistance of large grain size (LGS) and small grain size (SGS) films. Inset shows similar transition regions for both films and similar T_c 's.

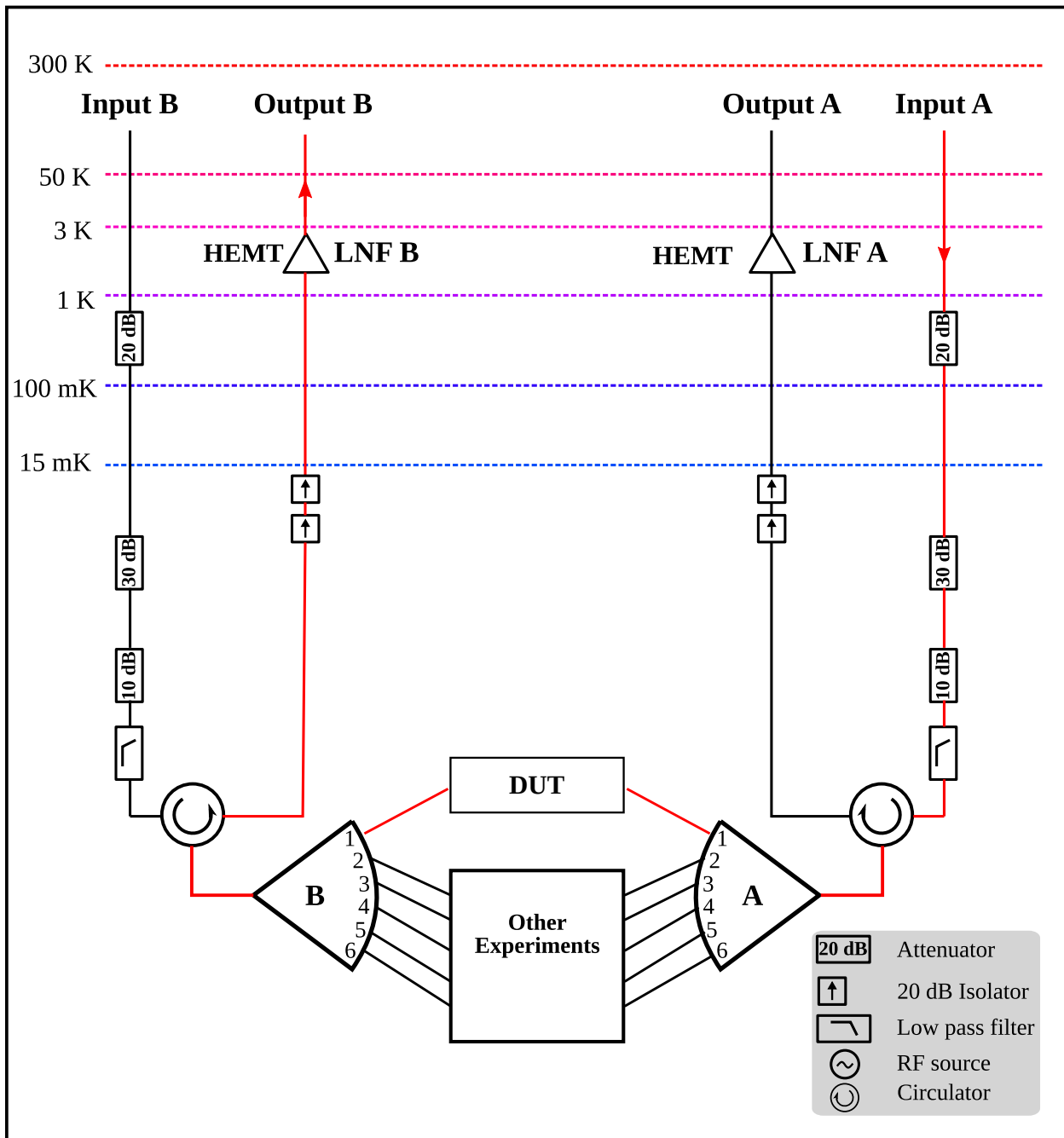


Figure D.5 Microwave wiring diagram. Passive and active components at each stage of a Janis JDry250 cryogen-free dilution refrigerator used to measure the devices reported in this work. Radial six-to-one switches, labeled A and B, allow for multiple samples to be measured on one pair of lines during a single cooldown. Red lines indicate the signal path to measure transmission S_{21} through the devices under test (DUT): LGS1, LGS2, SGS1, and SGS2 resonator chips.

APPENDIX E

PERMISSIONS FOR COPYRIGHTED MATERIAL

E.1 Copyright Permissions for Chapter 1

- Figure 1.5 in Section 1.2.4 is adapted from [2] under the license provided in the supplement to this thesis.
- Figure 1.6 in Section 1.2.4 is adapted from [1] under the license provided in the supplement to this thesis.
- Figure 1.7 in Section 1.3.1 is reproduced from [3] under the license provided in the supplement to this thesis.
- Figure 1.14 in Chapter 1.4 is constructed from three figures, reproduced from [9] in (a), [16] in (b), and [12] in (c), licensed under Creative Commons CC BY 4.0 license. This license grants a worldwide, royalty-free, irrevocable license to reproduce and share the licensed material.
- Figure 1.16 in Section 1.5.2 is based on [17] under the license provided in the supplement to this thesis.
- Figure 1.20 in Section 1.5.3 is reproduced from [19] under the license included in the supplement.

E.2 Copyright Permissions for Chapter 2

- The entirety of Chapter 2 is reproduced from *Quantum Science and Technology*, licensed under Creative Commons CC BY 4.0 license. This license grants a worldwide, royalty-free, irrevocable license to reproduce and share the licensed material [48]. The other authors in [48] give their permission to reproduce this work in the supplement to this thesis.

E.3 Copyright Permissions for Chapter 5

- Figure 5.1 and Figure 5.2 are reproduced from *Physical Review Applied* [25] under the license provided in the supplement.

E.4 Copyright Permissions for Chapter 6 and Appendix D

- The entirety of Chapter 6 and Appendix D are reproduced from *Journal of Applied Physics* [196] under the license provided in the supplement. The other authors in [196] give their permission to reproduce this work in the supplement to this thesis.